University of Warsaw
Faculty of Physics

Paulina Rajchel-Mieldzioć

Dissertation

Tuning light with light: Controlling emission of upconverting nanoparticles via co-excitation

---

Under the supervision of
dr hab. Piotr Fita, prof. UW

Warsaw, 2025

To my husband,
in whose light I have found my way.

Abstract

Among the many remarkable properties of upconverting nanoparticles (UCNPs), perhaps none is more compelling than their ability to shift the boundaries of imagination surrounding light-matter interactions. These nanomaterials—typically doped with trivalent lanthanide ions—are known for their capacity to sequentially absorb multiple low-energy photons, followed by the emission of a single photon of higher energy. The nonlinear character of this process, coupled with the long-lived intermediate states intrinsic to rare-earth ions, has made UCNPs indispensable across applications in microscopy, bioimaging, sensing, and photonics. And yet, despite the breadth of this field, key questions remain—not only about how to extract brighter signals, but how to exert finer control over emission itself.

This work began with a deceptively simple question:

Can light be used not just to drive emission, but to shape it?

This idea became the inspiration—*spiritus movens*—for exploring whether emission pathways could be controlled through **co-excitation**—two independent beams, each resonant with specific transitions, working *together* to sculpt emission in ways a single beam could not.

To pursue this, a dual-beam optical system was developed—featuring collinear excitation from a fixed 975 nm diode laser—resonant with transitions in ytterbium ions present alongside the emitting ions in these materials—and a tunable NIR beam spanning 1050-1875 nm, generated via difference-frequency generation. This system provided not only wavelength precision but also spectral and spatial stability, enabling the exploration of co-excitation across a wide range of conditions.

The journey through the winding pathways of photophysical properties began with thulium-doped nanoparticles, and along the way revealed effects that *exceeded all expectations*. Two spectral regions of the tunable NIR beam—centered around **1213** and **1732 nm**—emerged as particularly cooperative: a beam at each of these wavelengths, when used alone, produced negligible emission; yet when paired with 975 nm, they yielded dramatic enhancements in upconversion. In some cases, the resulting emission surpassed the additive contributions of both beams by **several hundred percent**—that is, their combination yielded *a much higher emission intensity* than the sum of the intensities produced by each beam alone.

A surplus metric was introduced to quantify this excess, and phenomenological models were proposed to describe its dependency on excitation power. Beyond this quantifiable surplus, the low-power regime revealed a more profound phenomenon: ***de novo*** emission—light produced only when both beams acted together, since neither could induce it alone.

To illustrate the implications of this finding, a 1732 nm beam—otherwise invisible to silicon detectors—was directly visualized through co-excitation with 975 nm. Using a microscope slide coated with upconverting nanoparticles as a phosphor and a standard photographic camera, this approach enabled real-time, switchable, and spatially resolved imaging of the beam profile, serving as a practical proof-of-concept for extending spectral conversion—in effect, bringing infrared radiation well beyond the reach of conventional detectors into view.

The study then turned to erbium-based systems, where cooperative behavior was also observed—though with a different texture. A beam at **1523 nm** produced measurable emission on its own, but only a modest surplus when paired with 975 nm. A second region, centered at **1139 nm**, yielded a much more compelling effect: the beam remained dormant in isolation, yet under co-excitation with the 975 nm beam it consistently gave rise to amplified emission. Since 1139 nm photons correspond strictly to excited-state absorption, this wavelength served as a model for co-excitation without ground-state absorption contributions.

Further studies using *only* the 1139 nm beam—without the 975 nm beam—at high power revealed unusual emission behavior that varied with erbium concentration. Sudden shifts in response, along with increased nonlinearity, pointed to feedback effects—perhaps even **energy looping**. While the exact mechanisms remain under investigation, it is already clear that this may be less of a conclusion and more of a prelude to something entirely new.

In the end, the story that began with a question of control leads to one lasting idea: co-excitation is more than just a way to enhance emission—it is a subtle yet powerful tool for shaping it.

Streszczenie

Spośród wielu niezwykłych właściwości nanocząstek konwertujących energię w górę (*ang.* upconverting nanoparticles, UCNPs), chyba żadna nie jest tak fascynująca, jak ich zdolność do poszerzania granic wyobraźni dotyczących interakcji światła z materią. Nanomateriały te – domieszkowane trójwartościowymi jonami lantanowców – znane są ze swojej zdolności do sekwencyjnego pochłaniania kilku niskoenergetycznych fotonów, a następnie emisji pojedynczego fotonu o wyższej energii. Nieliniowy charakter tego procesu, w połączeniu z długożyjącymi pośrednimi stanami wzbudzonymi, które to charakteryzują jony ziem rzadkich, uczynił z nanocząstek konwertujących energię w górę materiał wręcz nieodzowny w wielu zastosowaniach, takich jak mikroskopia, bioobrazowanie, detekcja i fotonika. A jednak, pomimo tak szerokiego zakresu ewentualnych zastosowań, kluczowe pytania wciąż pozostają w mocy – nie tylko o to, jak uzyskać jaśniejsze sygnały, lecz także jak uzyskać precyzyjniejszą kontrolę nad samą emisją.

Ta praca zaczęła się więc od zwodniczo wręcz prostego pytania:

Czy można użyć światła nie tylko do wywołania emisji, lecz także do jej kształtowania?

Idea ta stała się inspiracją – swoistym *spiritus movens* – do zbadania, czy fotofizyczne ścieżki emisji można kontrolować poprzez **ko-wzbudzanie** – gdzie dwie niezależne wiązki, z których każda rezonuje z konkretnymi przejściami elektronowymi, potrafią *razem* ukształtować emisję w sposób nieosiągalny dla pojedynczej wiązki.

Aby to osiągnąć, opracowano dwuwiązkowy układ optyczny, który to wykorzystywał współosiowe wzbudzanie wiązką lasera diodowego pracy ciągłej o długości fali 975 nm – rezonansową z przejściem w jonach iterbu obecnych w badanych materiałach obok innych jonów emitujących i będącą klasyczną długością fali ich wzbudzenia – oraz przestrajalną wiązką w bliskiej podczerwieni w zakresie 1050-1875 nm, generowaną w procesie różnicowej generacji częstotliwości. Układ ten zapewniał nie tylko precyzję wyboru długości fali, ale także stabilność widmową i przestrzenną, umożliwiając przeprowadzenie badań na kanwie ko-wzbudzania w szerokim zakresie warunków.

Podróż poprzez meandry właściwości fotofizycznych rozpoczęto od nanocząstek domieszkowanych tulem – i po drodze odkryto efekty, które *przekroczyły wszelkie oczekiwania*. Dwa zakresy spektralne wiązki przestrajalnej – z maksimum przy **1213** oraz **1732 nm** – okazały się wyjątkowo owocne w ramach ko-wzbudzania: wiązka o każdej z tych długości fali osobno wywoływała niemalże pomijalny sygnał, lecz w połączeniu z 975 nm powodowała dramatyczne wręcz wzmocnienie obserwowanej emisji. W niektórych przypadkach emisja ta przekraczała wkład sumaryczny obu wiązek o **kilkaset procent** – innymi słowy, ich połączenie dawało *znacznie większą intensywność emisji* niż suma intensywności generowanych przez każdą z wiązek osobno. Do ilościowego ujęcia tego efektu wprowadzona została miara nadmiaru emisji, a także zaproponowano fenomenologiczne modele, by opisać zależność rzeczonego nadmiaru od mocy wzbudzenia. Wykraczając poza zakres, gdzie nadmiar emisji pozostawał mierzalny, przejście do reżimu niskich mocy wzbudzenia uzewnętrzniło jeszcze bardziej intrygujące zjawisko: emisję ***de novo*** – światło powstające jedynie przy współdziałaniu obu wiązek, gdy żadna z nich samodzielnie nie jest w stanie go wywołać.

Aby zilustrować konsekwencje tegoż odkrycia, przeprowadzono bezpośrednią wizualizację wiązki 1732 nm – nieuchwytnej dla detektorów krzemowych – poprzez ko-wzbudzanie z wiązką 975 nm. Używając szkiełka mikroskopowego pokrytego nanocząstkami pełniącymi rolę luminoforu oraz standardowego aparatu fotograficznego do rejestracji emisji, doświadczenie to umożliwiło przestrzenne obrazowanie profilu wiązki w czasie rzeczywistym, z możliwością wyłączania – służąc jako praktyczne potwierdzenie, iż możliwe jest znaczące poszerzenie konwersji spektralnej – swoiste zobaczenie promieniowania podczerwonego wykraczającego poza granice konwencjonalnych detektorów.

Następne badania objęły układy na bazie jonów erbu, gdzie również zaobserwowano efekty ujawniające się tylko na kanwie ko-wzbudzania, choć każdy z nich o innym charakterze. Wiązka o długości fali **1523 nm** wzbudzała mierzalną emisję samodzielnie, lecz skutkowała tylko niewielkim nadmiarem emisji przy ko-wzbudzaniu wraz z wiązką 975 nm. Drugi zakres, z maksimum przy **1139 nm**, okazał się znacznie bardziej intrygujący: wiązka ta pozostawała bezczynna w izolacji, lecz w warunkach ko-wzbudzania z wiązką 975 nm prowadziła do wzmocnionej emisji. Ponieważ fotony o długości fali 1139 nm w jonach erbu odpowiadają wyłącznie absorpcji ze stanu wzbudzonego, użycie danej długości fali stało się modelowym przykładem niosącego efekty ko-wzbudzenia bez udziału absorpcji ze stanu podstawowego.

Dalsze badania z użyciem *jedynie* wiązki 1139 nm – czyli bez wiązki 975 nm – przy wysokiej jej mocy ujawniły nietypowe zachowanie intensywności mierzonej emisji, zależne od stężenia jonów erbu. Nagłe zmiany w odpowiedzi oraz zwiększona jej nieliniowość względem mocy wiązki wzbudzającej wskazywały na efekty sprzężenia zwrotnego – a może nawet **pętlę energetyczną**. I chociaż dokładne objaśnienie mechanizmów stojących za rzeczonymi obserwacjami wymaga dalszych badań, już teraz jest w pełni oczywiste, iż nie jest to tylko zakończenie – a preludium do czegoś zupełnie nowego.

Na końcu tej opowieści, która zaczęła się od pytania o kontrolę, pozostaje jedna trwała idea: ko-wzbudzanie to coś więcej niż tylko sposób na wzmocnienie emisji – to subtelne, ale i potężne narzędzie do jej kształtowania.

Acknowledgements

The doctorate is a journey—*and what a journey it is*. Although no one can walk it for you, I cannot say that I walked it alone. There is so much to be grateful for, and to so *many*.

To my advisor, Piotr Fita, who shaped me as a scientist—even though I'm not the easiest to shape. And yet, from now on, my approach to science will always carry your imprint, and I hope it will be something you can be proud of. *For all these years.*

To my parents, for showing me this world and the joy of discovering it, and for making it possible for me to be where I am today.

To my sisters and brothers (in-law, but not really)—for teaching me strength in ways only siblings can.

To my brothers-in-arms—Mateusz Bocheński, Jakub Dobosz, and Paweł Arciszewski—for making bearable the moments that truly weren't. *For always being there.* For being wonderful friends—in science and in life.

To Artur Bednarkiewicz and Katarzyna Prorok, for the fruitful and rewarding collaboration.

And above all, to my beloved husband, Grzegorz. *For everything.*

Proem

Not all those who wander are lost.

— J.R.R. Tolkien, *The Fellowship of the Ring*

One might say that a doctorate is a story threaded with the notion of *homo viator*, where the thesis itself is but a fragment of the journey—crowning, yes, yet never encompassing its entirety. Paper cannot fully capture emotion; it absorbs it like blotting paper, never releasing its full saturation. And though an effort has been made to pour them onto these pages along with the results—for it is unnatural to separate them when science is passion and not mere work—what emerges may at times resemble a stream of consciousness. Let it stand, however, as a reminder that this dissertation was written by a human being of flesh and blood, for whom what is written here is not indifferent.

A fragment of a journey—that is all that can be contained within these pages. Further condensation is possible, though it would strip the work of its personal resonance, and in some respects also of its scientific depth, for even science nowadays is required to be digestible amidst the sheer flood of the new. For this reason, the present work shares much of its material—though treated here in far greater breadth—with the following publication[1], whose significance was further recognized by its place on the cover. Let this stand as a testament that the goals set at the outset were not merely accomplished, but in places even surpassed.

P. Rajchel-Mieldzioć, A. Bednarkiewicz, K. Prorok, and P. Fita, Strong Emission Enhancement via Dual-Wavelength Coexcitation in YbTm-Doped Upconverting Nanoparticles for Near-Infrared and Subdiffraction Imaging, *ACS Nano* **19** (29), 26932–26941 (2025).

The material gathered in the second half of this dissertation has not yet been published, and its encapsulation in manuscript form is still in preparation. This is, however, not the author's only milestone, though perhaps the most profound one. Along the way, the following works have also been published, with others still in preparation.

P. Rajchel-Mieldzioć and P. Fita, Deciphering Photoluminescence in an Aryl Iodides-Gold Nanoparticles System: Au-Mediated Homocoupling Reaction at a Low Temperature, *J. Phys. Chem. Lett.* **15** (14), 3982–3986 (2024).

P. Hanczyc, P. Rajchel-Mieldzioć, B. Feng, and P. Fita, Identification of thioflavin T binding modes to DNA: a structure-specific molecular probe for lasing applications, *J. Phys. Chem. Lett.* **12** (22), 5436–5442 (2021).

T. Kuciel, P. Wieczorek, P. Rajchel-Mieldzioć, M. Wytrwał, S. Zapotoczny, and M. Szuwarzyński, Surface-grafted macromolecular nanowires with pendant fluorescein chromophores by dense non-aggregated nanoarchitectonics as versatile photoactive platforms, *J. Colloid Interface Sci.* **670**, 182–190 (2023).

P. Rajchel-Mieldzioć, R. Tymkiewicz, J. Sołek, W. Secomski, J. Litniewski, and P. Fita, Reaction kinetics of sonochemical oxidation of potassium hexacyanoferrate (II) in aqueous solutions, *Ultrason. Sonochem.* **63**, 104912 (2020).

And though it may appear that the author traversed winding themes across diverse topics, nothing could be further from the truth—for at the foundation of all these endeavors lay the photophysical properties of photoactive materials—properties previously *unknown*. In each of these works, the author ventured—sometimes at the helm, sometimes as a companion—into uncharted territories, an endeavor that demands time and yields not only results, but also experience. For well-trodden paths may offer ease, but they never lead to discovery.

With all that said, there remains nothing more than to invite the reader on this particular journey—a journey that is both scientific and human, marked as much by wonder as by understanding.

Contents

Foundations

Foundations 1

Every piece of research must begin somewhere. Ours began with a question—one that, when stripped of all detail and distilled to its essence, reads as follows: *How can light be used to shape the behavior of a system that emits at shorter wavelengths than it absorbs?* More specifically: how might we influence such a system—and describe that influence—using the tools available to us, those defined by our field: optics?

Yes, the question may appear abstract—perhaps even vague. We could name the materials, mechanisms, and processes involved right here and now. But terminology alone does not reveal meaning—not to those standing at the threshold of a field. And so, this introduction does not begin with outward precision, but with purpose: to render these investigations accessible, to trace the outline of what has been uncovered, and to bring into focus the boundaries of current understanding—boundaries we have not only reached, but also moved beyond.

The rain fell, the floods came, and the winds blew and buffeted the house. But it did not collapse; it had been set solidly on rock.[1]

1: Matthew 7:25

So must it be with any scientific inquiry. Before we speak of what was built—before design, before experiments, before outcomes—we must first acknowledge what already stands. No discovery, however novel, rises in isolation. Ahead of setting new stones, we must lay this work upon solid *foundations*.

1.1 *The material*—upconverting nanoparticles

1.1.1 Mechanisms of upconversion

The material—*our system.* As the central subject of our investigation, it is only fitting that we begin by addressing its general nature. But let us immediately clarify a subtle, yet meaningful distinction: these materials are the *base* of our research, but not its base in *itself*. They are the ink and paper of the spectroscopist—enabling expression, but not defining it.[2]

2: One might argue that they do—just as notes define a musician's performance. Yet the roles of composer and performer, while equally essential, remain fundamentally distinct. It is a distinction worth bearing in mind throughout the pages that follow.

In that spirit, we must state this plainly: the synthesis and nanoscale design of these materials are accomplishments that lie firmly within the domain of materials chemists. This distinction matters—not only in the theoretical introduction, but throughout the experimental sections as well—so as not to obscure the fact that the true contribution of our work lies in analyzing the fruits of *their* labor, and in doing so, producing the fruits of our *own*.

And what are these materials, exactly?

Upconverting nanoparticles (UCNPs) are a type of inorganic luminescent material capable of absorbing photons of lower energy—most often in the near-infrared (NIR) region—and subsequently emitting photons of higher energy in the visible (VIS) or ultraviolet (UV) range.[2]

One may pause here and reflect—anti-Stokes emission[3] can arise from

3: An *anti-Stokes shift* occurs when the energy of the emitted photon exceeds that of the absorbed photon—as opposed to the *Stokes shift*, named after George Gabriel Stokes, where the emitted photon has lower energy.

different mechanisms. The most straightforward mechanism that comes to mind involves thermal population of energy states above the excitation level; however, it produces only a minimal anti-Stokes shift—negligible when compared to the shift from NIR to the visible range. Another possibility is multiphoton absorption, such as two-photon absorption (as illustrated in Fig. 1.1), where excitation occurs via a virtual energy level—rather than a real one—leading to a higher-energy state. This process is simultaneous, meaning the photons are absorbed at the same time, and it can indeed result in higher-energy emission if the excited state is itself emissive—compared to the excitation wavelength.[3–5]

At this point, it's also worth mentioning a process that differs sharply from the previously discussed multiphoton absorption: second-harmonic generation (SHG). SHG is a nonlinear optical process in which two photons of the same frequency interact with a material to produce a single photon with twice the frequency—and thus half the wavelength—of the original light (Fig. 1.1). This results in frequency doubling of the incident beam and can be considered a specific case of three-wave mixing.[6, 7]

Although SHG is frequently cited in discussions of anti-Stokes shifts, the resulting photon does not originate from a luminescent transition. It's important to keep this essential difference in the underlying mechanism in mind when comparing different processes and phenomena.

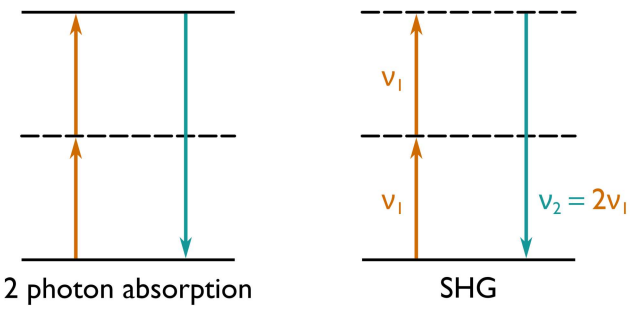

Figure 1.1: Schematic of two-photon absorption and second-harmonic generation (SHG). In two-photon absorption, excitation to a higher energy level occurs through the simultaneous absorption of two lower-energy photons—effectively via a virtual energy state—which may result in anti-Stokes emission. SHG, on the other hand, is a nonlinear optical process in which two photons of the same frequency interact with a material to generate a single photon with twice the frequency. **Neither process represents the mechanism responsible for upconversion in upconverting nanoparticles.**

And yet, all of these serve as clear counterexamples, as they do not reflect the mechanism at work in our case.

What, then, defines this unique behavior? The answer lies in the composition of the nanoparticles in question. Yet to fully understand their design—and the role that composition plays—we must turn to the history that led us here.

It all began with the concept of the *infrared quantum counter*—a proposal to detect infrared photons using a ladder of electronic states in specific dopant ions embedded in a solid matrix. The idea was that such a ladder would allow for selective sequential excitation.[8]

Let us consider this through a simplified schematic (Fig. 1.2a): the material would be illuminated with light matched to a transition between an already excited state and a higher-lying level—a mechanism now recognized as excited-state absorption (ESA). However, this excitation alone would not trigger any emission, as it requires prior population of the lower (initial) excited state.

Herein lies the central concept of infrared detection: if the sample were simultaneously exposed to two light sources—one resonant with a ground-state transition (GSA), the other with an ESA pathway—then excitation followed by emission would become possible.[4] If the GSA-resonant photons originate from the infrared range, this configuration enables their detection: in the absence of IR photons, no emission occurs; in their presence, it *does*. And notably, the resulting emission would be of higher energy—**upconverted**.

4: The idea of **co-excitation**, which lies at the heart of our work, was conceived here on paper—even in the pre-laser era.

Though not the original focus of the concept, this upconverted emission would ultimately become its most significant outcome.

At the time, however, this idea was conceived just before the advent of the laser revolution. Without coherent light sources, sequential excitation of dopant ions remained practically unfeasible, and rigorous experimental validation had to wait.

That soon changed. The breakthrough came with the realization that the distinctive energy-level structure of rare-earth ions held the key. It was discovered that energy could be transferred not only from an excited-state ion to a ground-state one—as previously assumed[9]—but also between two excited ions, allowing one to be promoted to an even higher energy state.[10, 11] This mechanism, now known as energy transfer upconversion (ETU), is illustrated in Fig. 1.2b.[12, 13] The result: *an ion capable of emitting light at a wavelength significantly shorter than that of the original excitation source.*

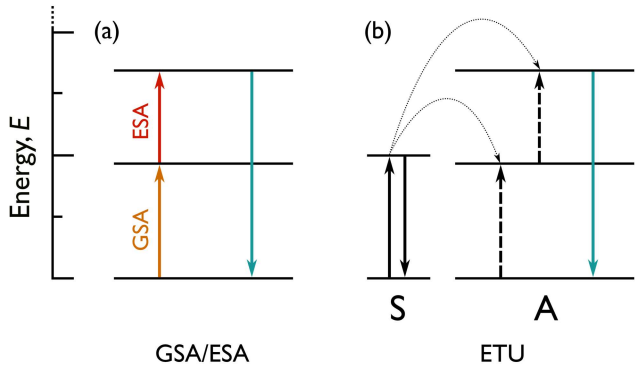

Figure 1.2: Simplified diagrams of the two fundamental upconversion mechanisms. **(a)** Excited-state absorption (ESA), preceded by ground-state absorption (GSA). **(b)** Energy transfer upconversion (ETU)—excitation energy is sequentially transferred between neighboring ions, from sensitizers (S) to activators (A), enabling the activator to reach a higher excited state.

Yet the story told so far omits an important detail: *it all began with bulk crystals.* But while these large structures first revealed the promise of upconversion, their potential for practical use—though still significant—was limited by size and rigidity—constraints that naturally led to a shift toward miniaturization.[2]

The guiding light was the realization that lanthanide ions, even when confined to nanoscale hosts,[5] could still upconvert. Paired with it was the guiding idea: to create structures that could disperse in liquids, form transparent colloids, and offer surfaces accessible to chemical modification and biological integration.

5: The **host** lattice in upconverting materials defines the environment for lanthanide dopants and influences their optical properties. Its phonon energy governs the extent of non-radiative losses experienced by the dopants, while its crystal symmetry defines the local crystal field—shaping radiative transition probabilities and branching ratios—a topic that will be addressed shortly.[14] Among the most widely used hosts is β-$NaYF_4$, valued for its low phonon energy, chemical stability, and resistance to lattice distortion even at high doping levels.[15, 16]

Realizing this vision required overcoming significant challenges, particularly the reduced efficiency at the nanoscale. Yet over time, synthetic strategies advanced, and a new class of materials took shape—in the form of nanocrystals with sub-100 nm dimensions, with ongoing efforts pushing the boundaries of miniaturization even further.[17–19] Thus,

upconverting nanoparticles (UCNPs) were born—and today, they stand as the leading platform for applied upconversion research.

1.1.2 Why rare-earth ions? —*the role of lanthanides*

Picture a theatre of light where most actors—atoms, molecules, even quantum dots—step onto the stage in bright spotlights and promptly exit after a single scene. Lanthanide ions, by contrast, prefer the wings. Their principal characters, the $4f$ electrons, sit hidden behind two thick curtains of $5s^2\ 5p^6$ electrons. That heavy drapery shields them from the external disturbances—and due to that insulation, the lanthanide ions can rehearse extraordinarily long optical routines before the audience notices a single photon.

To understand this, we must first outline the hierarchy of interactions in an isolated Ln^{3+} ion—then introduce the crystal field as the weakest perturbation. The interactions, listed from strongest to weakest, are:

- **Coulomb (electron-electron) repulsion** determines the collective orbital (L) and spin (S) angular momenta emerging from vector-adding of the individual orbital (l) and spin (s) of the $4f$ electrons. Each distinct (L, S) pair is denoted by the term symbol

$$^{2S+1}L \quad (L = 0, 1, 2, \ldots \Leftrightarrow S, P, D, \ldots).$$

- **Spin-orbit coupling** then links L and S to yield the total angular momentum

$$J = L + S$$

  splitting every term into $^{2S+1}L_J$ sub-levels labeled by

$$J = |L - S|, |L - S| + 1, \ldots, L + S.$$

- **Crystal-field interaction** finally perturbs each $^{2S+1}L_J$ level by only a small amount, producing Stark sub-levels that remain extremely narrow.

And why is the crystal-field interaction so weak in this case? In a solid, every lattice point creates an electrostatic potential—called the crystal (ligand) field—that perturbs the energies of an embedded ion. As an example, consider transition-metal ions: their outer $3d$ electrons lie on the periphery of the atom and therefore feel this field strongly, leading to large splittings that broaden spectra and accelerate non-radiative loss.

Lanthanides are different. Their $4f$ shell is radially contracted and lies beneath the filled $5s^2\ 5p^6$ shells—*the curtains*. These outer shells effectively screen the $4f$ electrons, so the crystal-field perturbation that reaches them is typically only a few tens of cm^{-1}—two orders of magnitude smaller than the Coulomb and spin-orbit interactions that primarily define the energy level structure.[2, 20–22]

What remains is a dense ladder of narrow lines—**perfect** for absorbing two or more low-energy photons in sequence, followed by the emission of one of higher energy. Because this ladder is shaped primarily by intra-atomic interactions and only weakly perturbed by the host crystal

field, its structure changes scarcely from one material to another. As a result, upconversion pathways established in one host remain largely applicable across others.[23]

However, this picture is still incomplete. As described earlier, even in its simplest form, upconversion relies on one of two fundamental processes: (i) *excited-state absorption* (ESA), in which a single ion sequentially absorbs multiple photons, or (ii) *energy-transfer upconversion* (ETU), where one ion donates its excitation energy to another. Regardless of the mechanism, two critical physical conditions must be met:

- **Closely spaced intermediate states**, so that each low-energy photon can bridge a realistic energy gap. This condition is naturally fulfilled by the structure of the $4f$ manifold, whose finely spaced levels arise from strong intra-shell Coulomb repulsion and spin-orbit coupling.

- **Long-lived intermediate states**, which allow sufficient time for the second photon to be absorbed or for energy to be transferred from a neighboring ion.

Lanthanides provide both. In a perfectly centrosymmetric crystal field, parity selection rules render $4f \rightarrow 4f$ electric-dipole (ED) transitions forbidden,[6] leaving only magnetic-dipole (MD) emission with very low oscillator strengths. In real materials, however, this restriction is relaxed through two complementary mechanisms:

- **Breaking inversion symmetry**, due to local geometric environment around the lanthanide ion in the host material, which lifts the parity constraint, making ED transitions formally allowed.

- **Parity mixing**, where odd-parity components of the crystal field admix $5d$ character into $4f$ wavefunctions. This gives rise to nonzero ED transition moments, as described by Judd-Ofelt theory.[7]

Together, these effects enable **crystal-field-induced** transitions with oscillator strengths orders of magnitude higher than MD lines. In most upconverting hosts, both mechanisms contribute: the absence of inversion symmetry removes the strict prohibition, while parity mixing enhances the transition probability—so the photon that leaves the nanoparticle is *typically* emitted via such a partially allowed ED transition.[20, 28, 29]

Although brighter, these transitions still exhibit relatively low rate constants, and—more importantly—the intermediate excited states populated during the upconversion process often remain (fully or partly) parity-forbidden. As a result, they exhibit micro- to millisecond lifetimes—*long enough to await the next photon*.

1.1.3 Designing for light

Now that the role of lanthanide ions is understood, one challenge remains—*the art of tailoring it.* And that is no simple matter. A mere glance at the selection rules for optical transitions hints at an uncomfortable truth: without thoughtful design, the brightness of upconverting nanoparticles will be all but lost.

6: The **Laporte rule** is a fundamental selection rule in spectroscopy that governs electronic transitions in centrosymmetric environments—those with a center of inversion, such as many transition-metal complexes or ideal crystal fields. According to this rule, transitions between electronic states of the same parity (either both even, or both odd) are forbidden under the electric-dipole approximation.[24] In practical terms, this means that transitions like $d \rightarrow d$ or $f \rightarrow f$ are disallowed in perfectly symmetric systems, because both initial and final orbitals possess the same inversion symmetry. As a result, these *forbidden* transitions are typically very weak—unless the symmetry is broken, allowing parity to mix and the rule to be relaxed.[25]

7: **Judd-Ofelt theory** is a model used to explain and quantify the optical transitions of lanthanide ions, especially the weak, parity-forbidden $4f \rightarrow 4f$ transitions. It provides a way to calculate the oscillator strength of these transitions using two key ingredients: reduced matrix elements that are characteristic of the specific lanthanide ion, and Judd-Ofelt parameters (Ω) that describe the influence of the surrounding host material. These parameters reflect how much the local crystal field breaks symmetry and enables electric-dipole transitions. By combining these values, one can predict transition intensities and branching ratios with good accuracy.[20, 26, 27]

Consider the effect of dopant concentration. Suppose, for simplicity, the host lattice is doped with ions of a single lanthanide. Increasing their concentration in the host should, in principle, enhance emission intensity. After all, at low concentrations, the ions are too far apart for efficient energy transfer; under such conditions, upconversion can proceed only via excited-state absorption (ESA). But as the ions draw closer, a new set of challenges emerges.

Efficient energy transfer between ions enables non-radiative energy migration—a relay-like process where excitation hops from one ion to another, potentially all the way to the nanoparticle surface. If surface-bound quenchers are present, they can effectively suppress emission.[30] High concentrations also open the door to another non-radiative process: cross-relaxation (Fig. 1.3)—through a coupling between ions with matching energy gaps—which is the principal cause of concentration quenching. This interaction can subsequently lead to non-radiative energy loss, again reducing emission efficiency.

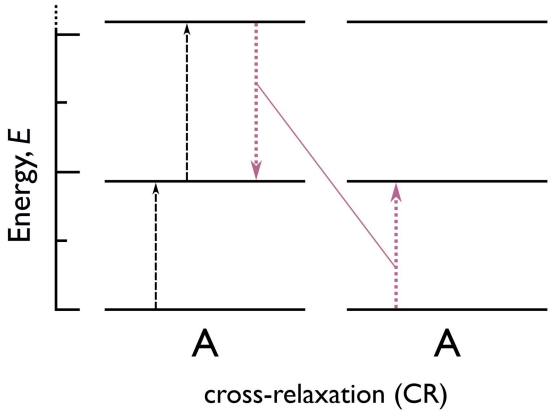

Figure 1.3: Simplified schematic of the cross-relaxation (CR) process between two ions. CR is a non-radiative energy transfer mechanism in which an excited ion transfers part of its energy to a nearby ion in a lower-energy state, promoting the latter to an excited state while the donor ion transitions to a lower-lying excited level.

To make matters worse, many lanthanide ions possess low absorption cross sections in the infrared, undermining the process from the very beginning.

An effective solution is to reimagine the structure of the system entirely by splitting the task between *two lead actors*—one to absorb, one to emit. This division turns out to be a key breakthrough: the concept of a multi-element sensitizer-activator system.[12, 18] The sensitizer ion (for example, Yb^{3+}) is responsible for harvesting incoming light and transferring the energy to an activator ion—such as Er^{3+} or Tm^{3+}—which then performs the emission. Ideally, the sensitizer has a large absorption cross section, a simple energy-level structure, strong energetic resonance with the activator, and minimal back-transfer of energy from the activator to the sensitizer.

But concentration must still be handled with care. In most UCNPs, the sensitizer content—when using Yb^{3+}—can reach up to 20% without major loss, while the activator concentration is kept low to avoid the non-radiative processes described above. Yet with clever structural engineering, these limits can be gently pushed.[31]

Surface quenching can be significantly reduced by surrounding the emitting core with an inert shell, which keeps excitation energy confined

within the nanoparticle.[30, 32] Its optimal thickness is a careful compromise: far enough to minimize non-radiative pathways like Förster resonance energy transfer (which falls off with the sixth power of distance), yet thin enough to preserve efficient excitation and emission.

To further reduce concentration quenching, it is important to ensure a homogeneous distribution of activator ions, avoiding local clusters that locally spike the effective concentration.[33] A larger host lattice constant can also help, by increasing the average distance between ions.[34] Even something as simple as increasing excitation intensity can offer relief: by depopulating the activator's ground state, it reduces the likelihood of unwanted cross-relaxation with excited neighbors.[35, 36]

But what if *one man's meat is another man's poison* could be read in reverse? A limitation in one context may become an advantage in another. To explore this possibility, it helps to consider the kinds of applications envisioned for upconverting nanoparticles.

The purpose

To make invisible—visible. Their core functionality comes from converting low-energy near-infrared (NIR) light into higher-energy visible or ultraviolet emission—a process manifested throughout this section: **upconversion**. NIR excitation is highly attractive for bioimaging because it penetrates several millimeters into soft tissue, minimizes intrinsic autofluorescence, and reduces photothermal damage, thereby enabling high-contrast imaging of living cells and small organisms.

Their fully inorganic lattice renders them essentially photobleach-free and virtually non-blinking—advantages over organic dyes and typical quantum dots for long-term observation.[37] Emission color can be tailored[8] by adjusting dopant identity, concentration,[9] and core-shell architecture, enabling true multicolor labeling and multiplexed detection schemes.[38–40]

It all makes them ideal for bioimaging. Yet what is lacking is brightness. Higher doping brings brighter signals—but also greater losses. **Unless those losses are rerouted.**

Previously, it was discussed how high doping concentrations can promote non-radiative losses, as excitation energy migrates from one ion to another until it is ultimately quenched at surface defects.[31] However, with carefully engineered core@shell architectures, this same migration pathway can be intentionally designed to redirect energy flow toward beneficial outcomes rather than losses.[41] By distributing dopants in separate layers—placing sensitizers, mediators, and activators in distinct spatial zones—researchers can control not only whether energy migrates, but also *where* and *how far* it travels.[42, 43] Focusing on the emission pathway: intermediate ions—distinct from the primary sensitizer, initial acceptor, and final activator—can be incorporated to serve as energy bridges that facilitate long-range energy transfer across interfaces. This enables efficient excitation of activators located in the outer shell, even when they are distant from the initial excitation site, thereby mitigating energy loss and enhancing emission intensity—an especially valuable feature in imaging applications.[38]

Yet in bioimaging the medium is water, and the tool is light—and water absorbs. What if the primary limitation lies not in the emission

8: To curb any overenthusiasm, it's important to note that one should not envision a full rainbow spectrum, but rather a set of narrow emission lines in specific colors, determined by the choice of emitting ion. Additionally, *color tuning* via dopant identity refers to selecting or substituting particular lanthanide ions—each with its characteristic emission—not continuously tuning the output of a fixed composition.

9: The dopant concentration affects cross-relaxation and branching ratios between competing transitions.

pathway, but in the absorption of the excitation light itself—driven by water's strong attenuation at certain wavelengths? What if using an alternative sensitizer, such as Nd^{3+}, offers a more favorable excitation wavelength (e.g., 800 nm),[10] yet introduces the risk of back energy transfer that diminishes overall upconversion efficiency? This is where energy migration strategies can also be applied in reverse, focusing on the excitation pathway. By employing a layered structure in which one sensitizer absorbs the excitation light and another acts as an energy mediator toward the activator located in a different layer, it becomes possible to spatially separate roles and minimize unwanted energy losses—all while enabling excitation under biologically more suitable wavelengths.[44, 45]

10: The commonly used sensitizer Yb^{3+} absorbs light around 980 nm, while Nd^{3+} does so near 808 nm, where the absorption coefficient of water is more than twenty times lower than at 980 nm.

Multicolor emission? In some designs, blocking layers are incorporated to isolate quenching-prone ions or to prevent back energy transfer. This not only enhances upconversion efficiency but also enables dual-mode emission, where different excitation wavelengths selectively address distinct, differently doped regions of the nanoparticle—allowing control over spectral output.[46]

Control. It lies at the heart of this thesis. While much of the current research emphasizes structure-driven strategies—as the literature readily shows—this work also turns to other forms of control, which will be addressed in due course. First, however, we step back to consider the broader context of UCNP applications—both to recognize the full extent of their potential and to clarify why this particular material system was chosen as the foundation for our study.

Thanks to their distinct optical properties, upconverting nanoparticles are being investigated for a growing range of specialized applications—many of which take advantage of their compatibility with biological systems—beyond imaging. For instance, they can be coated with polymers, peptides, or antibodies to ferry drugs while providing simultaneous NIR-driven imaging.[47–49] The same NIR-to-visible conversion may activate photosensitizers for minimally invasive photodynamic therapy[50–52] or deliver patterned light to deep-brain optogenetic actuators.[53–55] Narrow emission lines and micro- to millisecond lifetimes enable time-gated biosensing, and ratiometric pairs[11] allow non-contact luminescent nanothermometry with a high resolution.[56, 57]

11: Two emission peaks from the same ion, whose intensity ratio varies predictably with temperature due to thermal coupling between energy levels, where increased temperature promotes population of the higher-energy excited state according to Boltzmann statistics.

But there's more to life than biomedicine.[12] UCNPs are also gaining attention in fields such as security, energy, and display technologies. Their upconversion behavior makes them ideal for covert pigments in security threads and anti-counterfeiting inks.[58, 59] In the realm of solar energy, UCNPs are being explored as spectral converters for silicon-based photovoltaics: by transforming otherwise unused near-infrared photons into visible light, they have the potential to expand the portion of the solar spectrum that silicon can harvest—although practical quantum yields at one-sun intensity remain limited.[60] And the list doesn't stop there: from using NIR-generated UV to photocatalyze pollutant degradation or pump white-LED phosphors, to leveraging their stable emission for applications in volumetric 3D displays and multi-layer optical data storage, UCNPs continue to find new roles in unexpected places.[61–64]

12: This sentiment resonates with our approach: while our research is rooted in **fundamental science**, we naturally hope that our findings may one day find application across a broad spectrum of fields—biological and beyond.

Beyond the properties discussed above—most notably, their hallmark upconversion—UCNPs possess another remarkable feature, one we have

so far deliberately left unmentioned: their **nonlinear optical response**. Because upconversion relies on the sequential absorption of two or more photons, the emitted intensity scales nonlinearly with the excitation power. *Yet why does that matter?*

Nonlinearity

Nonlinearity opens many doors. It allows for entirely light-driven logic: their emission can act as a threshold-dependent output, enabling all-optical logic operations such as AND, OR, and NOT—executed purely within the optical domain.[65, 66] This same principle extends to optical switching, where light controls light without the need for electronic intermediates.[67]

Beyond logic and switching, nonlinear threshold behavior also finds use in remote activation and sensing. Chemical release, catalytic reactions, or ion signaling can be designed to occur only when local irradiance surpasses a defined threshold, minimizing off-target effects and enabling precise spatial control.[19, 54, 68–70]

Still, perhaps the most compelling application is in super-resolution imaging.[71] But how does nonlinearity make that possible?

A tightly focused laser beam has an intensity that, to first approximation, is Gaussian in the radial coordinate r:

$$I(r) = I_0 e^{-(r/w)^2}, \tag{1.1}$$

where w is the beam waist radius (roughly the diffraction limit), given by $w \approx 0.61\lambda/NA$, where λ is the wavelength of the laser beam and NA is the numerical aperture of the objective lens.

For an ordinary fluorophore, the detected signal is proportional to $I(r)$. But what if our fluorophore is anything but ordinary? For the nanoparticles in question, the emission is proportional to the n^{th} power of the excitation intensity[13] (or power):

$$E(r) \propto I(r)^n = I_0^n e^{-n(r/w)^2}. \tag{1.2}$$

13: In this work, we primarily refer to the excitation beam power, so the expression that more naturally relates the measured emission to excitation power is as follows: $E \propto P^n$.[72]

This leads to a simple but powerful conclusion: the *effective* beam waist radius becomes

$$w_{\text{eff}} = \frac{w}{\sqrt{n}}. \tag{1.3}$$

Assuming the resolution scales with the beam waist, this implies that the resolution improves by a factor of $\sqrt{n}$.

A subtle shift—yet one that literally pushes the boundaries of what can be resolved.

It is only natural to aim for UCNPs with the highest possible degree of nonlinearity. But achieving that is far from trivial.

Upconversion is described as a sequential multiphoton process—which it is. However, the idealized nonlinearity, where the emission scales as the excitation power raised to the number of absorbed photons (P^n),

applies only in the asymptotic limit of vanishingly small upconversion rates—which also corresponds to an extremely low signal.

In practice, any upconversion system that produces a detectable emission will show a lower dependence of intensity on excitation power. As the pump power increases, competition between linear decay pathways and nonlinear upconversion for depopulating the intermediate states reduces the effective slope of the emission curve.

In most cases, when upconversion via energy transfer upconversion (ETU) effectively outcompetes linear decay—as is typically desired when maximizing emission brightness—the luminescence from the final state becomes nearly linear with respect to excitation power. Emission from intermediate states often exhibits sublinear behavior, and in scenarios where excited-state absorption (ESA) dominates, the resulting emission may even become effectively independent of excitation power.[72]

14: Yet typical UCNP nonlinearities reach up to 3.[72]

None of this sounds encouraging—especially when brightness and strong nonlinearity[14] are the ultimate goals. And here enters a once troublesome process—now turned ally: **cross-relaxation**.

Troublesome it may be—after all, cross-relaxation has been cast as the culprit behind concentration quenching. But that doesn't mean it's without redeeming qualities. Its destructive tendencies can be harnessed: cross-relaxation has been used to suppress unwanted emission bands, allowing for clean, single-band emission from ions that would otherwise emit across multiple wavelengths.[73, 74] This form of color tuning can be pushed even further. It turns out that energy transfer between dopant ions can be controlled by adjusting the pulse duration of the excitation laser. In doing so, the extent of cross-relaxation can be finely modulated—and with it, the resulting emission spectrum.[75]

Yet this still isn't the answer to our question. That answer, in fact, has been around for quite some time—but only in bulk materials. In nanomaterials, it began to appear more hesitantly, as an attempt to shift the excitation wavelength into a range more suitable for biological imaging (from the characteristic 980 nm excitation of Yb^{3+} sensitizers to 1064 nm). And it took shape in the form of energy looping, using only the activator ions, without any sensitizer.

Energy-looping

The idea is simple—at least on paper. It involves using an excitation beam tuned to match an ESA (excited-state absorption) transition in the activator ion—while only weakly exciting the GSA (ground-state absorption) transition. The intermediate excited state is then depopulated by resonant excitation to a higher level, again driven by the same excitation beam.

With the help of a cross-relaxation (CR) process, the intermediate state can be repopulated, feeding into a loop: excitation via ESA, followed by CR, and another ESA step—driven by the same resonant beam. This ESA + CR cycle creates a closed feedback loop that, *once a power threshold is reached*, produces a markedly nonlinear response to excitation power—up to the point of saturation. A schematic illustration of this mechanism is shown in Fig. 1.4.

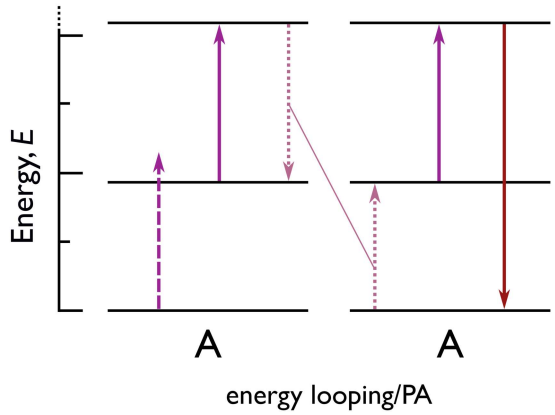

Figure 1.4: A simplified schematic illustrating the mechanistic concept of energy looping and photon avalanche (PA), featuring excitation resonant with the ESA transition (but not with the GSA) and an appropriate cross-relaxation process.

The result? Not only was it possible to use a more biologically friendly excitation wavelength, but the process also enhanced nonlinearity—**within nanomaterials**.[76]

And it turned out to be a breakthrough. Although the process itself was already **known**,[15] translating it into nanoscale systems was far from trivial. It required the precise convergence of multiple factors: the right nanoparticle design, the right activator ion, and a system that worked without a sensitizer—just the activator alone. Building on this, researchers achieved not only energy looping, but also the much more intense phenomenon of *photon avalanche at a nanoscale*.

15: It's worth emphasizing that although high nonlinearities in Pr^{3+}-doped bulk materials were already observed in the 1970s[77–80], achieving comparable results at the nanoscale only became a reality in the second decade of the 21st century.[81]

What is photon avalanche?

It's an avalanche of excited-state population. If energy looping captures the mechanism, then avalanche captures the scale—the extreme nonlinearity of the process.

Just like in basic energy looping, photon avalanche requires a nanoparticle with an appropriate electronic structure in the dopant ion. The necessary—but not sufficient—conditions (as they are shared with energy looping) are evident from the very nature of the process:[81, 82]

- **Resonant** excitation of an **ESA** transition,
- Correspondingly weak or **non-resonant** excitation of the **GSA** transition,
- A suitable **cross-relaxation** process.

But those are just the conditions needed to close the loop. What does it take to set that loop in motion?[14, 83]

- **A dopant concentration high** enough that cross-relaxation outpaces both radiative and non-radiative decay (and here, high dopant content together with the cross-relaxation—previously problematic—becomes an asset),
- **A long-lived intermediate state**, since a low total relaxation rate reduces competition with the ESA + CR loop,

- ❉ And of course, **strong excitation**: resonant with ESA, but still capable—via weak GSA—of seeding initial population in the intermediate level.

Yet how does one know if **true** avalanche has been achieved? That all these conditions are not only fulfilled, but also reflected in the system's observable properties? The most straightforward indicator is, of course, the measured nonlinearity (beyond 10, with the 3-10 range typically associated with energy-looping[14, 84])—*yet far from the only one*:

- ❉ A clear **threshold** must appear in the response curve: when plotting emission vs. excitation power (especially in log-log format, i.e., $\log(E)$ vs. $\log(P_{ex})$), a distinct inflection point should mark the onset of the highly nonlinear regime,

- ❉ Quantifying the ESA/GSA imbalance: to sustain avalanching, the ESA cross-section must exceed the GSA cross-section by at least **four orders of magnitude** (i.e., a ratio > 10000),

- ❉ Emission **rise times** should become significantly **longer** near the avalanche threshold.

Together, these criteria[14, 71, 83] define a rapidly growing subfield in upconversion materials research: the study of avalanche nanoparticles (ANPs)—where optical nonlinearities exceeding factors of 30[16]—and more recently, even *several hundred*[17]—have already been achieved.[67, 81, 85–88] From the perspective of microscopy, this represents a tremendous leap forward.

To understand not just the concept but also its realization, Fig. 1.5 presents a schematic of the avalanche emission process observed at 800 nm in thulium-doped nanoparticles, excited with a 1064 nm laser.[81] One should imagine that, due to the ESA + CR loop, the process quickly outgrows a simple diagram involving just two ions—the number of participating ions increases *avalanche-like*—hence the name. And although the figure shows a seemingly straightforward (at least in theory) example—especially in light of subsequent advancements—it's worth noting that its experimental realization occurred only a few years ago.

16: Achieving a nonlinearity of 31 in thulium-doped β-$NaYF_4$ nanoparticles marked the first demonstration of such a high nonlinear response at the nanoscale.[81]

17: Further enhancements in avalanche behavior have been realized through hetero-doping with multiple lanthanide ions and by modifying the host matrix. The highest reported nonlinearities—surpassing **500**—have been achieved in Tm^{3+}-doped systems, where exceptional optical response was induced by sublattice reconstruction: specifically, substituting Y^{3+} with Lu^{3+} in the commonly used $NaYF_4$ host. This substitution introduces constructive crystal field distortion, amplifying the nonlinear response.[85]

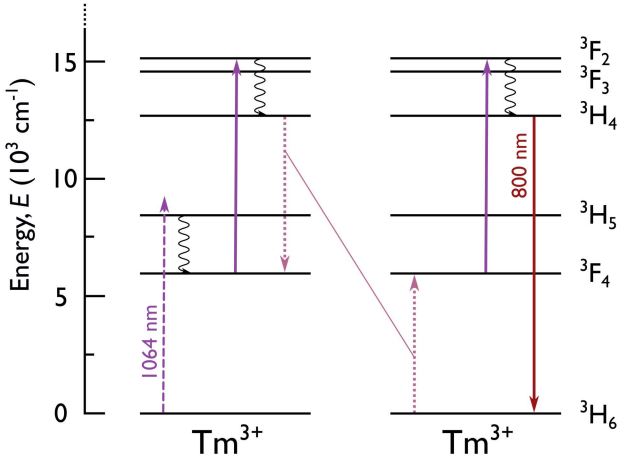

Figure 1.5: A simplified schematic illustrating the mechanism of photon avalanche in Tm^{3+}-doped nanomaterials under 1064 nm excitation, resulting in a highly nonlinear 800 nm emission response.

Challenges remain, of course. The high excitation powers currently required are far from ideal for biological applications. But avalanching

in nanostructures is still a young discipline, with many frontiers left to explore—within the bounds of physics, naturally.

1.1.4 The nanoparticles *herein*

Swept up by the multitude of applications and research directions, let us now return to solid ground. Before we focus on the directions explored in this work, we first introduce the specific nanoparticles that form its foundation. This serves not only as a prelude to the experimental section, but also as a key component of the theoretical discussion—since these are highly *typical* upconverting nanoparticles, based on a widely used host matrix and a well-established dopant composition.[18]

This work builds its narrative around nanoparticles based on the β-$NaYF_4$ matrix,[19] sensitized with $\mathbf{Yb^{3+}}$ ions, and activated by either $\mathbf{Tm^{3+}}$ or $\mathbf{Er^{3+}}$ ions.[20] Every journey forward benefits from knowing the ground already traveled. To set the stage for the developments that follow, we begin by revisiting the familiar terrain, starting with the thulium-doped system.

Thulium and ytterbium co-doped UCNPs

Doping with ytterbium ions enables excitation of the nanoparticles at wavelengths around 975-980 nm—resonant with the $^2F_{7/2} \longrightarrow {}^2F_{5/2}$ transition in Yb^{3+} ions, which possess a relatively high absorption cross-section. Through subsequent energy transfer, the excitation energy is efficiently passed to the activator ion, Tm^{3+}, enabling the cascade of transitions illustrated in Fig. 1.6.[18, 81]

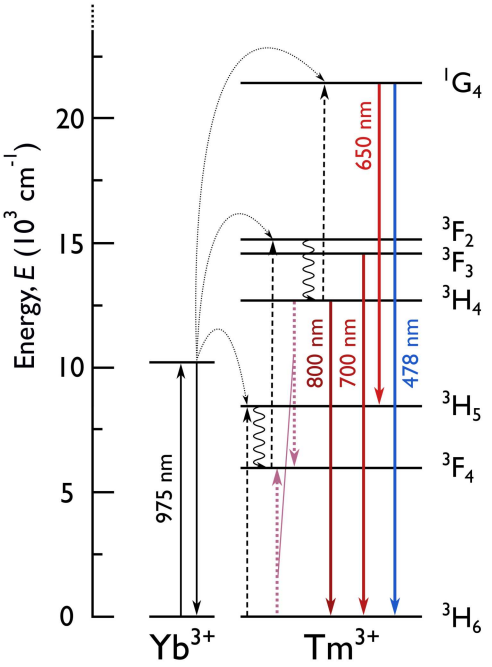

Figure 1.6: A simplified energy level diagram showing the key transitions in YbTm co-doped nanoparticles. For clarity, it has been energetically limited to blue emission only. Line thickness does **not** represent oscillator strengths.

The diagram does not tell the whole story—and for that, we must turn to the emission spectrum. Such a spectrum is presented in Fig. 1.7, recorded under continuous-wave excitation at 975 nm—resonant with the $^2F_{7/2} \longrightarrow {}^2F_{5/2}$ transition in Yb^{3+} ions. Among the array of emission lines, it is the band around **800 nm**—originating from the $^3H_4 \rightarrow {}^3H_6$ transition in Tm^{3+} ions—that unmistakably takes center stage, *asserting*

18: Once synthesized—though not by the present author—these nanoparticles, like any others, demand thorough spectroscopic characterization. That part was firmly in the hands of the present author, and was carried out prior to any further investigation, with the results presented in the experimental section.

19: β-$NaYF_4$ is one of the most widely used host matrices in UCNPs due to its chemical stability, optical transparency, and low maximum phonon energy (approximately 350 cm^{-1}), which suppresses non-radiative multiphonon relaxation. Its crystal structure accommodates a wide range of lanthanide dopants with minimal lattice distortion, helping to prevent defect formation and support efficient upconversion.[15]

20: To be precise, the thulium co-doped nanoparticles used in this work were core-only and contained 20% Yb^{3+} and 0.1% Tm^{3+}. The erbium co-doped nanoparticles were coated with a passive shell and featured a standard composition of 20% Yb^{3+} and 2% Er^{3+}. For additional measurements, the Er^{3+} concentration was also increased to 5% and 10%. Further details are provided in the methodology section (2.3).

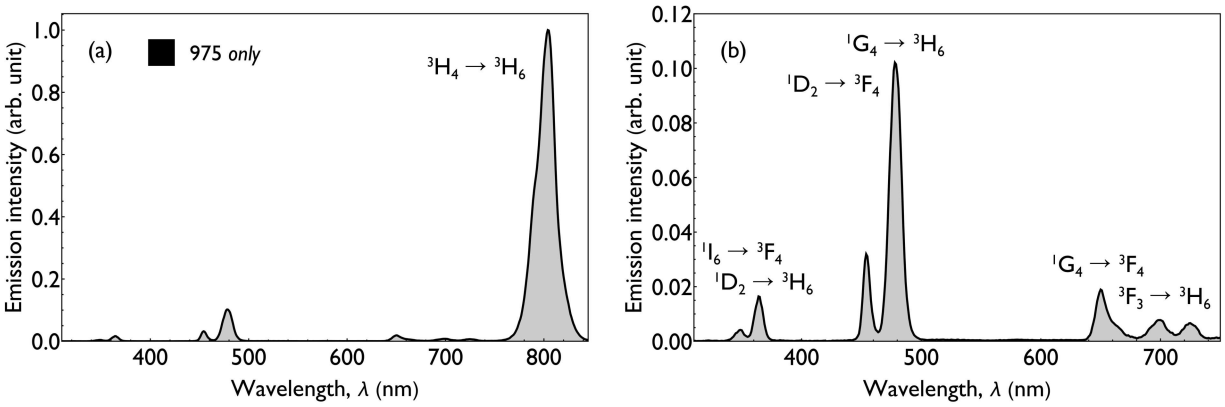

Figure 1.7: The emission spectrum of YbTm nanoparticles under excitation by a continuous-wave 975 nm laser beam. Transitions corresponding to the emission bands are indicated near their respective positions. (a) Spectrum recorded under 10 mW continuous-wave 975 nm excitation, with a clearly dominant band observed near 800 nm. (b) Zoomed-in view of (a), showing emission details below 750 nm.

its dominance over the spectral profile. This observation clearly shows that while the emission palette of thulium-doped nanoparticles is diverse, their *signature* is unmistakably drawn in deep red.

It is therefore only fitting that this particular band—arguably the most defining feature of thulium's emission profile—will serve as our observational window into how the emissive behavior of Tm-doped nanoparticles responds to the variety of stimuli[21] introduced throughout this work.

21: A cryptic remark, but its meaning will soon become clear.

Erbium and ytterbium co-doped UCNPs

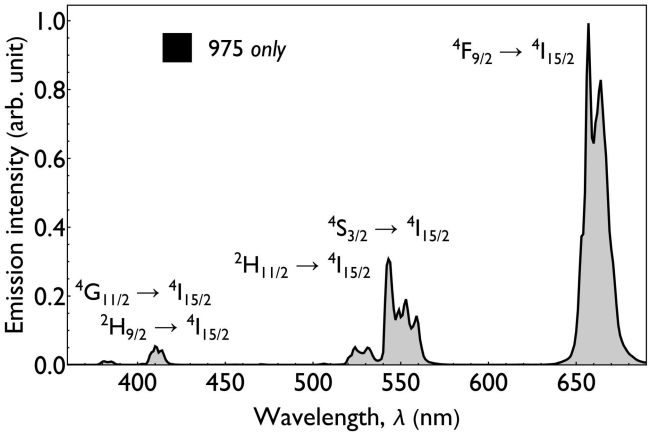

Figure 1.8: The emission spectrum of YbEr (2% Er^{3+}) nanoparticles under excitation by a continuous-wave 975 nm laser beam (10 mW). Transitions corresponding to the emission bands are indicated near their respective positions.

In erbium-doped nanoparticles, as shown in the emission spectrum in Fig. 1.8, the situation is less clear-cut when it comes to identifying a dominant emission band. When excited with a 975-980 nm laser via ytterbium sensitizers, the most characteristic features of Er^{3+} emission are undoubtedly the red band—corresponding to the $^4F_{9/2} \rightarrow {}^4I_{15/2}$ transition—and the green bands, which arise from the $^4S_{3/2} \rightarrow {}^4I_{15/2}$ and $^2H_{11/2} \rightarrow {}^4I_{15/2}$ transitions. For greater clarity, the energy level diagram shown in Fig. 1.9 offers a more intuitive overview.[18, 89, 90]

Yet this intuitive overview quickly reveals its complexity. Even though the presented diagram is simplified, the transitions shown may still not be immediately clear. Take, for example, the ETU process driving the transition from the $^4I_{13/2}$ level to $^4F_{9/2}$, marked in gray (unlike the others, which are shown in black). While this pathway is frequently included

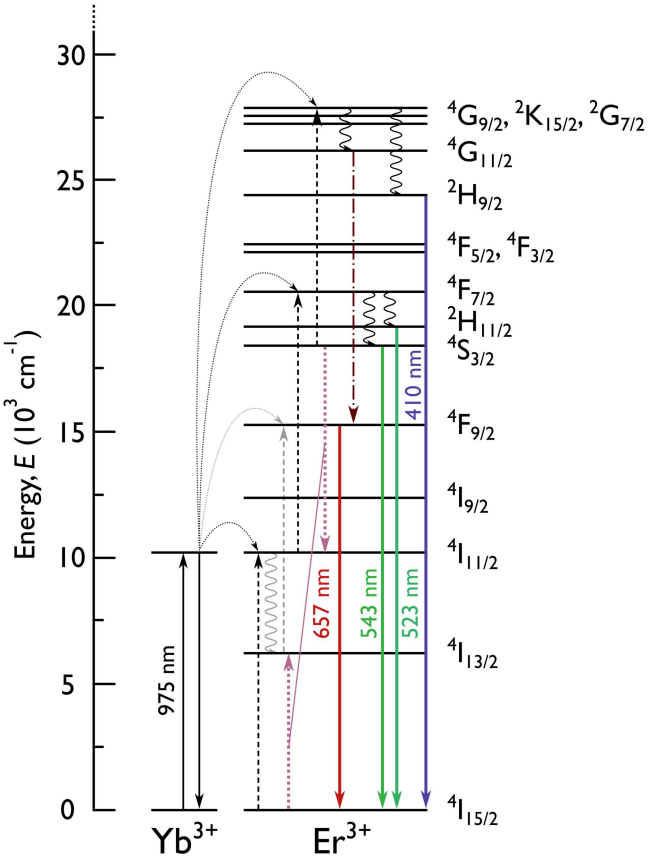

Figure 1.9: A simplified energy level diagram showing the key transitions in YbEr co-doped nanoparticles. Line thickness does **not** represent oscillator strengths.

in the literature, its actual contribution to the overall emission is likely minimal.[90, 91]

Equally unexpected might be the choice to depict the diagram across such a broad energetic range—especially since, for most purposes, the red and green radiative transitions are the most natural indicators of how various factors influence the emission behavior of these nanoparticles. And yet, it is precisely because of the red band that such a broad range becomes necessary: this emission is influenced by an energy transfer process in the opposite direction, where energy is transferred from erbium to ytterbium, leading to a relaxation from $^4G_{11/2}$ to $^4F_{9/2}$—indicated by the burgundy dash-dot arrow.[90, 91]

All that because of the spark coming through ytterbium ions. Yet erbium itself exhibits a relatively high[22] absorption cross section for the $^4I_{15/2} \longrightarrow {}^4I_{13/2}$ ground-state transition, corresponding to direct excitation in the 1510-1550 nm range. This excitation is also capable of driving further excited-state absorption (ESA) transitions, ultimately producing upconverted green and red emission—though with much lower efficiency than Yb-sensitized pathways. Still, this direct route remains well established and represents an important facet of the upconversion behavior of erbium-doped materials.[23][39, 92]

Yet even in a spectrum full of possibilities, a few key bands consistently take center stage. Therefore, in the case of erbium ions, this work focuses on two main bands: the red band, centered around **657 nm**, and one of the green bands, specifically the one at **543 nm**. But as already seen, behind each lies a tangled menagerie of mechanisms and interactions.

22: Relatively—being large only by lanthanide standards—and still more than an order of magnitude smaller than the absorption cross-section of ytterbium ions near 980 nm.

23: Especially useful where telecom-band laser sources are preferred.

1.1.5 Dual-wavelength excitation —*a new lever of control*

Upconversion in lanthanide-doped nanoparticles is most commonly driven by a **single** near-infrared (NIR) excitation. Typically around 975-980 nm, as this wavelength resonates with a ground-state absorption in Yb^{3+} ions, initiating a cascade of energy transfers to activator ions and resulting in visible or ultraviolet emission. However, the rich electronic structure of lanthanides—with multiple long-lived excited states—offers far more.

One can't help but wonder—*must we strain a single lever for change, or might progress lie in reaching for additional ones?*

Introducing **multiple** excitation wavelengths—each carefully tuned to specific electronic transitions—has the potential to unlock new excitation pathways, reshaping population dynamics, thus adding a new layer of **control** over the emitted light intensity.

What has been implicit is now made explicit: the central axis of this work is the search for—and application of—alternative excitation wavelengths, used not only in isolation, but in tandem with the primary 975 nm excitation.

Despite the clear conceptual promise, such multi-wavelength excitation strategies remain largely underexplored.[24] To date, most investigations into the photophysical effects of UCNP co-excitation have concentrated on a specific niche: super-resolution microscopy via stimulated emission depletion (STED).[25] Let us then trace a few illustrative examples—some driven by co-excitation with 975-980 nm light, others using alternative wavelengths—to gain a clearer view of the progress achieved so far.

In the case of thulium, most studies focus on the said *depletion* effect, as the role of the secondary beam is more intuitively *destructive*—and this naturally aligns with its potential use in the aforementioned microscopy applications. For example, it was demonstrated that UCNPs sensitized with Yb^{3+} and co-doped with high concentrations of Tm^{3+} ions can achieve a population inversion at the intermediate $^3H_4$ level under 980 nm excitation. At such doping levels, efficient cross-relaxation between closely spaced ions induces an avalanche-like build-up of excited-state population. When illuminated with a secondary beam at 808 nm—resonant with the $^3H_4 \longrightarrow {}^3H_6$ transition—stimulated emission can be triggered, effectively depleting the intermediate level and suppressing blue upconversion emission—as depletion of the $^3H_4$ state inhibits the subsequent energy transfer upconversion (ETU) process that populates higher-lying blue-emitting states.[26][97]

In another study, a similar approach led to a different line of reasoning. Using nanoparticles co-doped with Yb^{3+} and Tm^{3+} at high concentrations, and simultaneously irradiating with 975 nm (to excite Yb^{3+} and drive subsequent ETU) and 810 nm beams, a depletion of the 455 nm emission—corresponding to the $^1D_2 \longrightarrow {}^3F_4$ transition—was observed. This effect was attributed to stimulated emission from the $^1D_2$ level to the $^3F_2$ level. An important aspect of the overall mechanism was also identified as cross-relaxation (enabled by the high Tm^{3+} concentration) between the

24: It should be clarified that the act of co-excitation, forming the core of our focus, refers to an unconventional approach involving two-beam excitation of nanoparticles typically excited by a single beam. This interpretation excludes nanoparticles specifically engineered for such dual-beam operation, such as those hetero-doped with two types of sensitizers.

25: **STED microscopy** resolves details beyond the diffraction limit by pairing two synchronized laser beams. The first, a diffraction-limited excitation pulse, promotes fluorophores to an excited state. A second, doughnut-shaped *depletion* beam immediately stimulates emission back to the ground state everywhere except at the dark center of the doughnut. Because spontaneous fluorescence can now arise only from the sub-diffraction central zone, the boundary has been crossed over.[93–96]

26: For easier assimilation of the information, the diagram in Fig. 1.6 may serve as a helpful reference for following the described transitions.

ground state and the $^3H_4$ level—populated via relaxation from $^3F_2$. This process led to depopulation of the ground state, effectively suppressing any potential *positive* contribution of 810 nm excitation to blue emission via ground-state absorption (GSA).[98]

A pivotal set of experiments combining 975-980 nm and 808-810 nm excitation in thulium co-doped systems opened the way for this and complementary approaches, laying the groundwork for continued developments—especially as this direction is driven by tangible prospects for practical implementation.[99–102]

While co-excitation strategies have been explored across various other lanthanide-doped systems, they take on particular relevance in the case of erbium—one of the most versatile and widely studied ions in upconversion research.

In fact, the concept of depletion through co-excitation, as described earlier, also emerged in the context of erbium-doped materials.[103] In nanoparticles co-doped with Yb^{3+} and Er^{3+}, it was demonstrated that 1140 nm irradiation can selectively suppress the green emission from Er^{3+} under 795 nm excitation (which populates the $^4I_{9/2}$ state and, after relaxation and subsequent cross-relaxation, results in populating the green-emitting states). This depletion arises from a combination of excited-state absorption (ESA) and interionic energy transfer: the green-emitting $^2H_{11/2}$ state is promoted to higher-lying manifolds (e.g., $^2K_{15/2}$) by 1140 nm light.[27] Subsequent relaxation bypasses the green channel due to inter-ionic energy transfer, populating the red-emitting $^4F_{9/2}$ state instead:

$$^2F_{7/2}\ (Yb^{3+}) + {}^4G_{11/2}\ (Er^{3+}) \longrightarrow {}^2F_{5/2}\ (Yb^{3+}) + {}^4F_{9/2}\ (Er^{3+}).$$

27: For a clearer understanding of the specified transitions, Fig. 1.9 should be used as a foundational reference—though it does not capture all aspects, due to the sheer number of possible transitions.

Yet what makes erbium-doped materials particularly compelling, considering the breadth of work done in this area—is that co-excitation need not always play a destructive role—it can be harnessed *constructively*. Specifically, by exploiting wavelengths above 1500 nm, resonant with the $^4I_{15/2} \longrightarrow {}^4I_{13/2}$ ground-state absorption (GSA) transition of erbium, one can initiate further excited-state absorption (ESA) steps.

The ability to combine this excitation pathway with the conventional Yb^{3+}-mediated route has enabled demonstrations of upconversion color modulation. Unlike single-wavelength excitation, co-excitation with 980 nm and 1550 nm light allowed for dynamic tuning of the red-to-green emission ratio by simply adjusting the power of one beam.[104]

But color modulation is only part of the story. The described strategy enables selective population of specific erbium energy levels—and this carries far-reaching implications. It has been shown, for instance, that simultaneous excitation at 980 nm and 1510-1550 nm efficiently populates the $^4F_{9/2}$ level, resulting in enhanced red emission.[105, 106] In contrast, combining 1510-1550 nm with 790-808 nm excitation (resonant with the $^4I_{15/2} \rightarrow {}^4 I_{9/2}$ GSA transition and simultaneously capable of driving transitions from the $^4I_{13/2}$ state) preferentially populates the $^2H_{11/2}$ and $^4S_{3/2}$ states, leading to the strongest enhancement in green emission.[105, 107] The observed phenomenon has yet to yield any major consequences. Yet even if the enhancement remains subtle, *the true significance lies in the idea itself.*

Two beams—opening a path that one alone could not. Whether to suppress or to enhance, to diminish or to create, co-excitation reshapes the upconversion process. That is the heart of this strategy. And it is the *spiritus movens* behind the work presented herein.

Tools of the trade

Design and methodology 2

The cornerstone has been laid, the foundations set; it is now time to present the full architecture and operational scheme of our approach.

The base beam in our experiments is the already-described 975 nm beam—resonant with the $^2F_{7/2} \longrightarrow {}^2F_{5/2}$ transition in Yb^{3+} ions, which act as sensitizers by transferring energy to the appropriate activator ions (thulium or erbium) via energy transfer upconversion (ETU). This *continuous-wave* beam was generated using a 975 nm diode laser (CNI, MDL-III-975-1000 mW).

Yet a central requirement of our approach is the introduction of a ***second*** *excitation beam.*

The concept of co-excitation inherently demands the introduction of an additional—though in the context of our experiments, *equally essential*—beam, operating within a specific wavelength range of interest. Since our focus is on populating both the lower-lying and the higher, yet closely spaced, electronic states of the activator ions—within the broader terrain of accessible energy levels—this range falls within the near-infrared (NIR) region.[1]

While this tunable range is accessible using specialized pulsed sources or multiple commercially available CW tunable lasers, such equipment was not available in our case. A key step in our methodology, therefore, was to push the boundaries of what was possible with the resources at hand. With our limits set only by physics—and everything else within reach of design—we turned to the well-established technique of *difference-frequency generation (DFG)*,[2] enabling us to generate the desired wavelengths from the sources already available in our system.

1: Importantly, the 975 nm beam is also technically within the NIR domain; however, in this work, we will use the term *NIR beam* exclusively to refer to the tunable beam, while referring to the 975 nm beam explicitly, due to its fixed wavelength.

2: A nonlinear optical process in which two input photons at frequencies ν_1 and ν_2 interact in a nonlinear medium to generate a third photon at the difference frequency $\nu_3 = \nu_1 - \nu_2$. A visual representation is provided in Fig. 2.1.[7]

2.1 Optical setup for *Difference Frequency Generation*

Every experiment begins as an idea; here, it takes shape. The experimental setup we developed—shown schematically in Fig. 2.2—was built to realize this concept. The desired beam is generated via difference-frequency generation by mixing two input beams in a BBO crystal (β-barium borate, β-$Ba(BO_2)_2$).

One of the beams is the output of an optical parametric amplifier (OPA), tunable in the range of **710-1010 nm** (Orpheus, Light Conversion)—which is pumped by a femtosecond amplifier (Carbide, Light Conversion) operating at 1030 nm with a maximum repetition rate of 50 kHz.

The **second** beam used in the mixing process is the *second harmonic* of the femtosecond amplifier output, operating at **515 nm**. This beam is a remnant of the second harmonic previously used to drive parametric amplification in the Orpheus system—an elegant reuse that allows us to recover and repurpose part of the available energy for the DFG process.

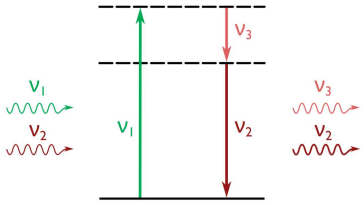

Figure 2.1: A schematic illustrating the concept of difference-frequency generation (DFG), in which the frequency of the generated photon (ν_3) is given by the difference between the input photon frequencies ($\nu_1 - \nu_2$).

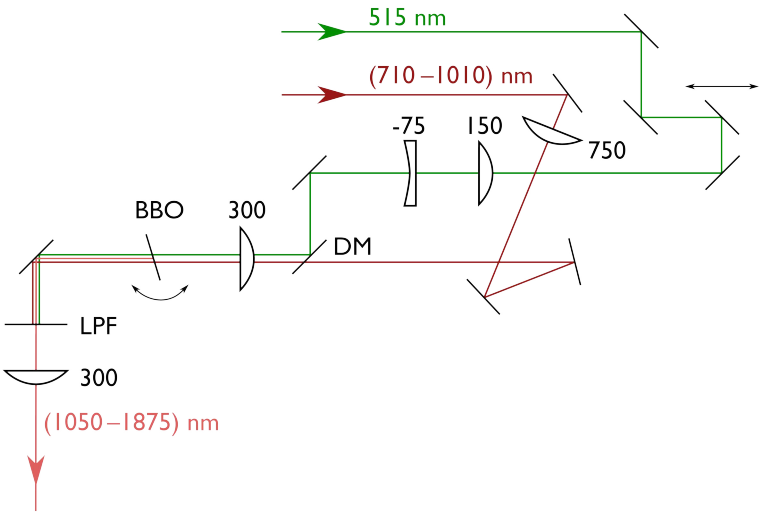

Figure 2.2: Schematic of the optical configuration for generating near-infrared (NIR) radiation via difference-frequency generation (DFG). A pulsed **515 nm** pump beam (green line) and the tunable signal output from an optical parametric amplifier (**710-1010 nm**, red line) are temporally overlapped using a delay line and spatially overlapped at a dichroic mirror (DM). The resulting beam pair is focused near a β-barium borate (BBO) crystal, where, under precise phase-matching conditions, DFG produces tunable NIR output (**1050-1875 nm**, coral line). The resulting beam is filtered using a long-pass filter (LPF) to eliminate residual pump and signal components before being routed to the spectrofluorometric system.

With the component beams defined, we now turn to the specifics of the setup. As illustrated in Figure 2.2, both input beams are properly collimated, and their sizes are adjusted using individual lenses or lens pairs, as needed. **A delay line** is introduced in the path of the 515 nm component to ensure temporal overlap of the pulses. Both beams were guided using dielectric mirrors chosen to match their respective wavelengths: BB1-E02 (Thorlabs) for the green beam, and BB1-E03 (Thorlabs) for the tunable component. The beams are then combined on a dichroic mirror (DMLP550, Thorlabs) and focused slightly ahead of the BBO crystal. Direct focusing onto the crystal would cause damage, so this step requires careful optimization.

Precise adjustment of the crystal angles—using a rotation mount and a micrometer-equipped rotation stage—enables phase matching, which is critical for efficient difference-frequency generation. After this, the residual input beams are filtered out using an appropriate long-pass filter (FELH1000, Thorlabs).

As a result, we obtain femtosecond pulses *centered* at a ***tunable*** wavelength spanning **1050-1875 nm**.

2.1.1 Tunability

Let us take a moment to recognize the exceptional, compared to CW sources, tunability achieved—a major strength of our setup, as it enables comprehensive analysis of co-excitation phenomena in upconverting nanoparticles, *regardless of the specific activator ion involved*. Moreover, throughout the entire accessible spectral range, the generated beam consistently delivers at least 300 mW of power *at the sample plane*—that is, after passing through all required optical elements—which is more than sufficient to reveal any relevant photophysical effects.

This degree of tunability, however, is not solely a product of design, nor is it realized with the *flip of a switch*. Two components are particularly critical: the **phase-matching angle**, the angle between the optical axis

of the crystal and the propagation direction of the beam, and the **delay line**. With each adjustment of the tunable beam's wavelength (710-1010 nm), both must be manually realigned to either optimize—or even enable—difference-frequency generation.

Indeed, the alignment must be performed anew with *every* wavelength adjustment. Such a requirement casts the achieved tuning range in a more demanding light—realizing a 300 nm span[3] and acquiring full co-excitation spectra necessitates persistent, precise intervention. While this presents an undeniable technical challenge, it has not posed a limiting barrier. Even where small margins of imprecision might have been tolerated, we allowed for none—each target wavelength was tuned with the highest possible accuracy,[4] using power measurements as a guiding metric.

3: Spectral tuning range of the red component beam, spanning 710-1010 nm.

4: But how accurate is this so-called *highest possible accuracy* in practice? This was revealed through spectral analysis of the resulting pulses, with the deviations presented in Fig. 2.4 and discussed in the accompanying commentary.

All of this serves to stress that building the system was only the beginning. Its practical operation—without yet accounting for data acquisition and analysis—constituted an equally demanding and indispensable part of the work.

Resulting NIR pulses

To assess the achieved tunability and its practical implications, the generated NIR pulses were examined across a broad spectral range—representative spectra are shown in Fig. 2.3.

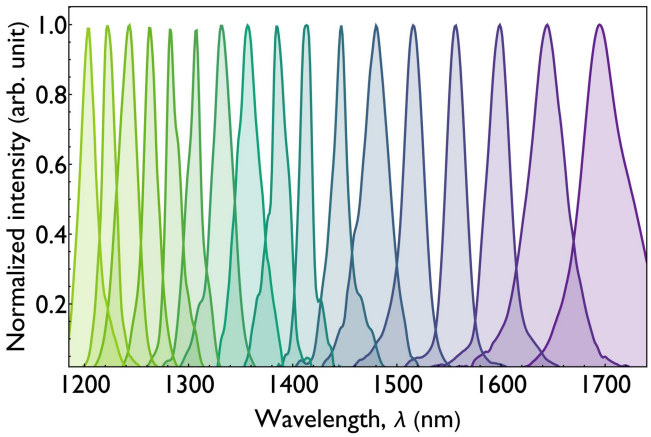

Figure 2.3: Normalized spectra of multiple NIR pulses generated using the constructed DFG system. Spectra acquired with the StellarNET spectrometer in the near-infrared (NIR) range.

Most importantly, the observed spectral maxima are well-defined and correspond *precisely* to the theoretical relationship between the two input beams used for generation.[5]

5: $\frac{1}{\lambda_3} = \frac{1}{\lambda_1} - \frac{1}{\lambda_2}$.

This was confirmed by producing and analyzing pulses across a wide range of central wavelengths. The measured pulse spectra, presented in Fig. 2.3—specifically, the wavelengths at which their maxima occur—were compared against the theoretical wavelengths derived from the output of the OPA. The comparison showed only minor discrepancies—smaller than might have been expected.[6]

Fig. 2.4 presents the residuals based on the measurements, where no deviation exceeded 2 nm, and the mean absolute error is just ±0.5 nm. Even under a more conservative assessment, the root mean square error

6: Every field defines accuracy and the notion of discrepancy differently—and indeed, such assessments are, to some extent, subjective. Subjectively speaking, the discrepancies observed here are unexpectedly small. Let this very sense of *unexpectedness* serve as a measure of how small they truly are.

amounts to only ±0.7 nm—all achieved with a manually tuned DFG setup.

The alignment process is indeed meticulous, and achieving such low errors—especially given the complexity and manual nature of the generation technique—demands attention. Laborious, yes—but with care, such precision is well within reach.

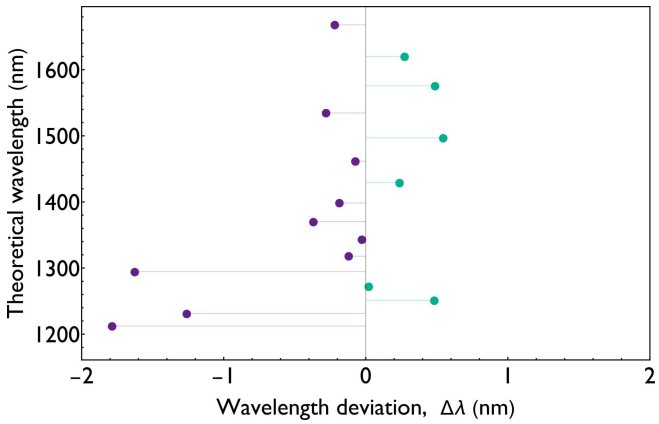

Figure 2.4: Residual plot illustrating the deviation between the generated wavelength and the theoretical wavelength, based on the output of the optical parametric amplifier used in the DFG process. The y-axis indicates the theoretical wavelength, and the x-axis represents the difference between the theoretical and measured wavelengths.

These results indicate that, under the implemented tuning regime—where the generated beam's power is carefully optimized using fine adjustments to the crystal angle and delay line, and verified via power meter readings—the output is consistently dominated by a single spectral band centered at the *expected* wavelength. As a result, the central wavelength can be determined with high confidence directly from the known setting of the tunable component.[7]

7: The set output wavelength of the tunable red component.

Naturally, the resulting pulses exhibit some spectral width—as expected, given that they originate from trains of femtosecond pulses. This apparent spectral width increases with longer output wavelengths, which corresponds to a decreasing difference between the two input wavelengths. It is a well-understood phenomenon and can be approximated through a simple line of reasoning. Let us assume that the spectral width of the input pulses—**in the frequency domain**—remains approximately constant, regardless of their central wavelength.

This assumption is supported by the roughly constant temporal duration of the pulses, approximately 180 fs. The relationship between pulse duration and spectral width (in the frequency domain) is governed by the time-bandwidth product (TBP). To motivate the reasoning that follows, we begin by considering the simple case of Gaussian pulses,[8] for which the time—bandwidth product (TBP) can be expressed in terms of the full width at half maximum (FWHM), as shown in Eq. 2.1.

8: The spectra shown in Fig. 2.3 suggest that the pulses deviate from a Gaussian shape. However, this is merely the starting point of our analysis.

$$\mathrm{TBP} = \Delta\nu \cdot \Delta t = \left(2\sqrt{2\ln 2}\sigma_\nu\right) \cdot \left(2\sqrt{2\ln 2}\sigma_t\right) = 8\ln 2 \cdot \sigma_\nu\sigma_t \tag{2.1}$$

Given that the time-frequency uncertainty for intensity-based Gaussian pulses is $\sigma_\nu\sigma_t = \frac{1}{4\pi}$, the corresponding TBP takes the form presented in Eq. 2.2.

$$\mathrm{TBP} = \frac{2\ln 2}{\pi} \approx 0.441 \tag{2.2}$$

Since this product is constant, a fixed pulse duration implies a *fixed* minimum spectral width in the frequency domain—assuming transform-limited pulses. *Yet the pulses are asymmetric and potentially chirped.* Still, their temporal duration remains **approximately constant**, indicating that the time-bandwidth product, while greater than the transform limit, should be relatively stable.

Consequently, the pulses generated through the difference-frequency generation (DFG) process should also exhibit a constant bandwidth in the frequency domain, as their characteristics are ultimately governed by the spectral widths of the input beams and the phase-matching conditions (with the spectrum limited by whichever imposes the tighter constraint). *But how does this translate into the observed increase in spectral width (in the wavelength domain) as the central wavelength increases?*

The relationship between spectral width in the wavelength and frequency domains is given by Eq. 2.3; it is an approximate expression valid for small spectral widths, but conveys the essential idea.

$$|\Delta\lambda| = \left|\frac{\mathrm{d}\lambda}{\mathrm{d}\nu}\Delta\nu\right| \tag{2.3}$$

Given that the relationship between λ and ν is well established, we may proceed a step further.

$$\lambda = \frac{c}{\nu} \Longrightarrow \frac{\mathrm{d}\lambda}{\mathrm{d}\nu} = -\frac{c}{\nu^2} = -\frac{\lambda^2}{c} \tag{2.4}$$

This allows for a concise estimation of the pulse width in the wavelength domain, with the full reasoning presented in Eq. 2.5, where λ denotes the central wavelength.

$$\begin{aligned} |\Delta\lambda| = \left|\frac{\mathrm{d}\lambda}{\mathrm{d}\nu}\Delta\nu\right| = \left|-\frac{\lambda^2}{c}\cdot\Delta\nu\right| = \\ = \boldsymbol{\lambda^2}\cdot\frac{1}{c}\cdot|\Delta\nu| \end{aligned} \tag{2.5}$$

Taken together, this reasoning leads to a clear conclusion: for a constant spectral width in the frequency domain, the corresponding width in the wavelength domain is a *function of the central wavelength*—and increases with it.

The reasoning presented above explains the shape of the pulse spectra shown in Fig. 2.3. Reversing the argument, however—under the stated assumptions—the spectra we obtained in the wavelength domain should exhibit a constant width when expressed in the frequency domain. To verify this, the data have been reformatted and presented accordingly in Fig. 2.5.

As shown, the differences in spectral widths are significantly **reduced** when transitioning to the frequency domain, as expected. However, the bandwidths of the generated pulses remain relatively broad—*why*? This results from fundamental constraints: the bandwidth of the generated

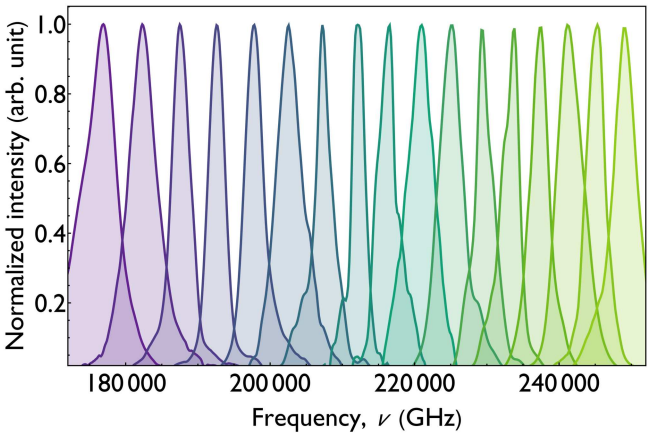

Figure 2.5: Same data as in Fig. 2.3—normalized spectra of multiple NIR pulses generated using the constructed DFG system—presented in the **frequency** domain.

pulses is ultimately determined by the spectral widths of the input pulses and the phase-matching conditions.

If the phase-matching condition is assumed to be always satisfied,[9] then the frequency ranges of the tunable red beam and the 515 nm beam—defined as (ν_1', ν_2') and (ν_1'', ν_2''), respectively—determine the possible frequency span of the difference-frequency signal, which lies within the intervals $(\nu_1'' - \nu_2')$ and $(\nu_2'' - \nu_1')$. In other words, the bandwidth of the generated beam can *exceed* that of either input beam alone.

9: This reasoning holds under the assumption that phase matching is not the limiting factor—i.e., that the effective nonlinear bandwidth is broader than the spectral overlap of the input beams.

In practice, however, this bandwidth is *mostly constrained* by the phase-matching conditions within the nonlinear crystal—conditions that are not uniform across the tuning range. As the generated wavelength shifts deeper into the infrared, the phase-matching bandwidth tends to broaden due to the flattening of the material dispersion curve. This relaxation of phase-matching constraints accounts for the noticeable spectral broadening of the generated pulses in the deeper infrared, even when viewed in the frequency domain.

Together, these explanations fully account for the spectral features seen in Fig. 2.5. Overall, the results support the validity of our reasoning and the explanation provided. They also confirm that the generated output behaves as anticipated, without any unexpected deviations.[10]

10: This applies both to the overall spectral shapes of the pulses, which—despite some minor imperfections—do not exhibit significant deviations, and to the central wavelengths of the generated pulses.

Having established the theoretical basis for the observed behavior, we now return to the baseline and its implications—although the generated pulses exhibit some spectral broadening in the wavelength domain—particularly at longer wavelengths—this has virtually no impact on what matters most: the precise[11] identification of excitation maxima when used as an excitation source.

11: As previously noted, the definition of *precision* varies across disciplines. The level of precision demonstrated here—generating pulses with a central wavelength within ±0.5 nm of the theoretical value calculated from the wavelength of the OPA output beam (see Fig. 2.4)—is, in our honest assessment, high for the domain of ultrafast pulses.

While the broadening may affect the shape of the excitation profiles, it **does not** shift the position of their maxima.

Owing to the stability of the central wavelengths, the key spectral feature in any recorded spectrum—the maximum—should remain well-defined and reliably interpretable across the entire tunable range when the generated beam is used as an excitation or co-excitation source. With this spectral precision assured, we are prepared to integrate the beam into the broader experimental framework.

Having designed, built, and successfully tested the DFG system, we are now ready to take the next step: merging the fixed 975 nm beam with the newly generated tunable NIR beam. This marks the another transition from concept to execution—the construction of a dual-wavelength co-excitation setup that translates our experimental vision into a working reality.

2.2 Experimental arrangement for *dual-wavelength* excitation

With both beams now available—the continuous-wave 975 nm (CNI, MDL-III-975-1000 mW) and the pulsed, tunable 1050-1875 nm beam generated via difference-frequency generation—we can proceed with the next step in our design: their spatial overlap and integration into the final experimental setup, schematically illustrated in Fig. 2.6.

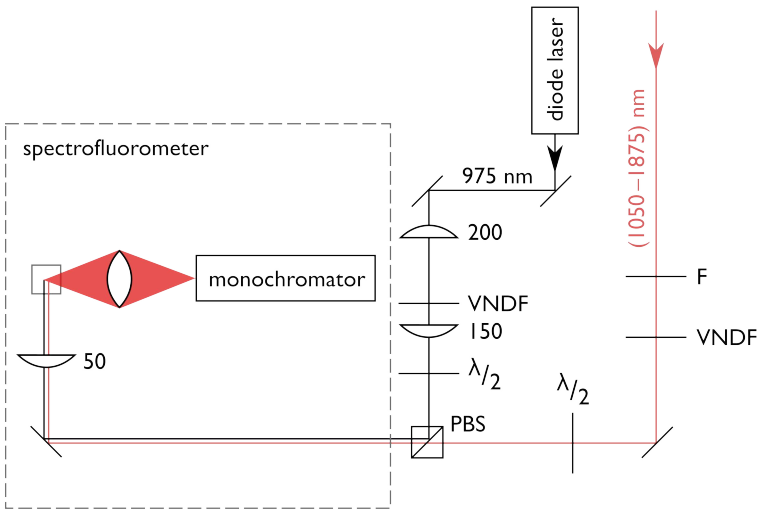

Figure 2.6: Schematic of the optical setup used for co-excitation measurements. A near-infrared tunable beam (1050-1875 nm), produced via difference-frequency generation (DFG), is combined with a continuous-wave 975 nm beam using a polarizing beam splitter. The *spatially overlapped* beams are directed into the spectrofluorometer chamber, where they excite the sample and the resulting emission is detected. Both excitation paths are independently controllable, enabling measurements under single- or dual-beam conditions.

Before the two beams meet, each follows its own carefully controlled path. Along both routes, components are placed to enable independent control—most importantly, each beam can be blocked separately, allowing for single-excitation measurements using only one source. In the path of the tunable NIR beam, a long-pass filter (FELH1050, Thorlabs) removes any residual input beams remaining from the DFG process. Its power is finely adjusted via a variable neutral density filter (NDC-50C-2M, Thorlabs), then passed through an achromatic half-wave plate (AHWP10M-1600, Thorlabs) to align its polarization for transmission through the polarizing beam splitter.

Before detailing the *optical rendezvous point* itself, let us turn to the solitary path of the 975 nm beam. A telescope, composed of appropriate lenses, is introduced to allow for future adjustments—ensuring that both beams, once overlapped, can be precisely focused through the final lens onto the same spot on the sample. Along this path, a variable neutral density filter (NDC-50C-2M, Thorlabs) allows fine control of the 975 nm beam's power, while an achromatic half-wave plate (AHWP05M-980, Thorlabs) sets its polarization for total reflection at the polarizing beam splitter—the designated point of combination.

The selection of an achromatic polarizing beam splitter (1" PBS255, Thorlabs) posed a challenge, as it was tasked with merging beams spanning from 975 to 1875 nm. While the specification of the selected model does not formally cover this entire spectral range, the high power of the NIR beam made the arrangement practically viable across the full tuning range. We thus arrive at the critical point—where the two

beams become **spatially overlapped** and proceed together along a shared, collinear path.

The final destination is the sample chamber of the spectrofluorometer—specifically, the Horiba QuantaMaster 8075-11 system equipped with a PPD850 photomultiplier (sensitivity in the range of 250-850 nm). The combined beams are directed through the final lens and focused onto the sample plane. The resulting emission—determined by the specific activator ion in the tested upconverting nanoparticles—is then collected and recorded.

2.2.1 Focal spot size

Tightly focused onto the sample plane. But just how tightly?

In this work, we primarily refer to power, which we control most precisely. However, in the field we operate in—namely, the study of the emissive properties of upconverting materials—an equally important concept is power density, also referred to as intensity. It is therefore essential to acknowledge this and ensure our results can be translated from the domain of power to that of intensity. To do so, only one additional parameter is required: the focal spot size.

The beam dimensions at the focal point were determined directly within the sample chamber using the well-established knife-edge method. The beam waists, defined at the $1/e^2$ intensity level, were measured for the wavelengths relevant to the study of thulium-doped nanoparticles[12] (in the format: horizontal × vertical):

- at 975 nm: 25 μm × 30 μm,
- at 1213 nm: 18 μm × 33 μm,
- at 1732 nm: 20 μm × 37 μm.

12: It may be something of a reveal, but it's no secret that our investigation did indeed yield meaningful results.

From these, calculating the elliptical beam areas is straightforward—but that's not the whole story. To obtain the actual excitation intensities, it is important to consider that the sample was positioned at an angle of approximately 45° with respect to the beam axis. This tilting increases the effective spot size at the sample surface, i.e., the illuminated area.

Thus, the beam power must be divided by the area of an ellipse (whose vertical semi-axis is equal to the vertical beam waist, and whose horizontal semi-axis is equal to the horizontal waist) **multiplied by $\sqrt{2}$**.This yields the following effective areas:

$$A_{975} = 3.33 \cdot 10^{-5}\ \text{cm}^2 \tag{2.6}$$

$$A_{1213} = 2.64 \cdot 10^{-5}\ \text{cm}^2 \tag{2.7}$$

$$A_{1732} = 3.29 \cdot 10^{-5}\ \text{cm}^2 \tag{2.8}$$

Using Eqs. 2.6, 2.7, and 2.8, our results can therefore be converted into intensity units, or at least interpreted with an *intuition* for intensity—even though they are presented in terms of power. This applies not only to the data concerning thulium-doped nanoparticles but also to other systems. As demonstrated, the effective areas provided here may also serve to estimate values for other NIR wavelengths generated by the

setup—though, of course, only under the assumption that the same optical configuration (specifically, the lens alignment) shown in Fig. 2.6 is used.

These measurements thus complete the preparatory phase—from the design and construction of the system to its full optical characterization.

And so, after a long and carefully engineered optical journey, we reach our destination: a fully realized system for recording excitation spectra of upconverting nanoparticles under **collinear, dual-wavelength co-excitation**.

2.3 Sample preparation

Even the finest instrument is silent without a score to play.

Having assembled the means to probe and measure, we now turn to what gives it meaning: the materials themselves—the preparation of the nanoparticle samples to be investigated.

This study focused on two main types of upconverting nanoparticles with **ytterbium** as the sensitizer—co-doped with either **thulium** or **erbium** ions. These nanoparticles were obtained in an almost ready-to-use form, based on a β-$NaYF_4$ matrix. The thulium co-doped nanoparticles were not coated with an inert shell and contained 20% Yb^{3+} and 0.1% Tm^{3+}. This was the *only* type used for investigating the emission properties of thulium co-doped UCNPs[13] under the dual-excitation scheme and their emission spectrum is shown in Fig. 1.7 in Section 1.1.4.

13: From this point onward, they will be referred to simply as *thulium-doped*, or in a similar manner, without specifying the exact composition.

In contrast, the erbium-based nanoparticles were coated with a neutral shell and contained a standard composition of 20% Yb^{3+} and 2% Er^{3+}. For additional measurements, the erbium concentration was also increased to 5% and 10%. The emission spectrum of nanoparticles containing 2% Er^{3+} is presented in Fig. 1.8 in Section 1.1.4; nanoparticles with higher erbium content exhibit the same set of emission bands.

All nanoparticles were received as suspensions in chloroform, stabilized with oleic acid[14] as a surface surfactant.[15] However, such a solution is far from ideal for co-excitation measurements. The dynamic movement of nanoparticles in suspension, time-dependent concentration gradients, variations in refractive index, and infrared absorption—sometimes leading to thermal lensing—are all factors that undermine the precision, consistency, and reproducibility of spectroscopic measurements, particularly in terms of emission intensity. For this reason, all measurements were conducted **in the solid state**—following the separation of the nanoparticles from their solvent medium.

14: Oleic acid ($C_{17}H_{33}COOH$) is an unsaturated fatty acid that occurs naturally.

15: A surfactant is a surface-active agent. When used to coat nanoparticles, it limits their growth during synthesis and prevents aggregation in solution. In the oleic acid, the more polar component (the carboxylic acid group) attaches to the nanoparticle surface, while the nonpolar alkyl chain extends into the solvent—effectively inhibiting the nanoparticles from sticking together.

Obtaining a dry sample of nanoparticles, however, requires some consideration. In our experiments, we often operate at high power densities due to the use of tightly focused infrared beams. While the nanoparticles themselves are robust under such conditions, *the surfactant is not*. Oleic acid—a flammable organic compound—can burn under high-intensity excitation, and when combustion is incomplete, it leaves behind carbon residues that contaminate the sample. Moreover, in the solid phase, the surfactant serves no practical purpose. Its role in preventing agglomeration is crucial in solution but irrelevant in this context.

Thus, it must be removed.

A straightforward chemical principle offers a practical solution—*similia similibus solvuntur*. Oleic acid, the surfactant coating the nanoparticles, is amphiphilic: it features a polar carboxylic acid head and a long, nonpolar aliphatic tail. In its protonated (acidic) form, however, the molecule behaves largely as a nonpolar compound.

To remove it, the chloroform-based nanoparticle suspension was thoroughly shaken with an immiscible aqueous 0.1 M hydrochloric acid (HCl) solution. At the interface between the two phases, hydrogen ions fully protonate the oleic acid, which, due to its low polarity, remains in the

chloroform phase. The now *uncoated* nanoparticles, no longer stabilized by the surfactant, transfer into the aqueous phase.

After separation, the mixture was left to settle, and the upper aqueous phase—now containing the *clean* nanoparticles—was collected (chloroform, being denser, forms the lower layer). This purified nanoparticle solution was then centrifuged at 16200 rpm, and the resulting pellet was redispersed in a small volume of distilled water.

The final aqueous solution was used to deposit the nanoparticles onto their target substrate—cut glass microscope slides—via drop-casting. Once fully dried, this process yielded ready-to-use solid-state samples, suitable for insertion into the spectrofluorometer and subsequent measurements.

And thus, one drop at a time, every sample investigated in this study came into being.

2.4 Measurement methodology

With the system now complete and operational, we must first outline the measurement methodology to understand the essence of the experiments—and the results—that follow. At the heart of this study lies the recording of **dual-wavelength co-excitation** spectra. In this approach, selected upconverting nanoparticles are simultaneously excited by two collinear beams: a continuous-wave 975 nm laser, resonant with the absorption transition of Yb^{3+} sensitizer ions, and a tunable femtosecond near-infrared (NIR) beam, targeting additional transitions in the activator ions.

As is standard in excitation spectroscopy, the effect of excitation is monitored through the intensity of emission at a selected wavelength. For **Tm-doped** nanoparticles, the emission spectrum is complex (Fig. 1.7), but overwhelmingly dominated by the **800 nm** band. This band—deep in the red—serves as the **primary** indicator of emissive behavior and is thus used as the principal reference also in our measurements.

For **Er-doped** nanoparticles, the emission spectrum (Fig. 1.8) is simpler but involves multiple relevant transitions. While the green emission bands (near 523 and 543 nm) are prominent and often studied, our focus is on the red emission around **657 nm**. This emission originates from lower-lying energy levels, making it particularly sensitive to co-excitation processes involving mid-level excited states. In our experiments, the 657 nm band serves as the main reference for Er^{3+}-based systems, although additional bands—especially the green ones—are also analyzed when needed to clarify underlying mechanisms.

What we refer to as an *excitation spectrum* in the context of co-excitation is obtained by **scanning the wavelength of the tunable NIR beam**, while keeping the 975 nm beam fixed and active, and monitoring the resulting emission intensity.

Each excitation point corresponds to a fixed NIR wavelength, with the emission collected for that setting. As detailed in Section 2.1.1, tuning the NIR beam involves manual adjustment of the DFG setup. For each excitation spectrum, approximately 70-80 measurement points were acquired—with the DFG setup carefully optimized at every point, as confirmed by power meter readings. Denser sampling was used in spectrally interesting regions. Throughout, the power of both excitation beams was kept constant, and each measurement point was repeated and averaged to ensure accuracy.

A crucial element of our methodology is the comparative assessment of the emission response under different excitation conditions. For each measurement point in the co-excitation scan, three configurations were recorded: (i) both beams active (co-excitation), (ii) only the 975 nm beam active,[16] and (iii) only the tunable NIR beam active. This was achieved by physically blocking the appropriate beam before each reading. In this way, every co-excitation spectrum is accompanied by single-beam excitation data, providing immediate context for interpreting any nonlinear or cooperative effects.

16: With the power of the 975 nm beam fixed, each measurement yields the same emission intensity (due to the constant excitation wavelength). However, the measurement was still performed separately for each data point, serving as a reference for assessing the stability of the system.

Beyond spectral scanning, the methodology also allows for power-dependent measurements.

At selected NIR wavelengths, the power of one or both beams is varied systematically, enabling the construction of **intensity-power curves**.

These measurements offer additional insight into the excitation behavior and help *disentangle* the roles of each beam in producing the observed emission.

With the full matrix of measurements in place—meticulously gathered across excitation wavelengths, powers, and configurations—we are now equipped to move from observation to *understanding*. **It is time for analysis.**

2.5 Summa summarum

Every experiment begins not with measurements, but with the tools that make them possible—*we began by building ours*.

At the *technical* core of this research lies the successful realization of a custom optical system, purpose-built for **dual-wavelength co-excitation** of upconverting nanoparticles—a capability that surpasses the limitations of standard commercial instrumentation.

A central component of the setup is the collinear alignment of two complementary excitation sources: a continuous-wave 975 nm diode laser and a tunable near-infrared (NIR) femtosecond beam generated via difference-frequency generation (DFG). The fixed 975 nm wavelength is resonant with the Yb^{3+} sensitizer transition, reliably initiating upconversion through energy transfer. The tunable NIR beam targets additional transitions in Tm^{3+} and Er^{3+} activator ions, granting selective access to both low-lying and higher, closely spaced electronic states. The two beams are **spatially overlapped** and delivered collinearly to the sample, establishing a dual-wavelength excitation regime—an approach essential for probing cooperative excitation mechanisms inaccessible via single-beam excitation. This configuration also supports seamless switching between single- and dual-beam modes, offering high flexibility in experimental design.

The DFG subsystem itself represents a major technical milestone. By combining the 515 nm second harmonic of a femtosecond amplifier with a tunable 710-1010 nm output from an optical parametric amplifier in a β-BBO crystal—and ensuring pulse synchronization via delay line and phase matching through micrometer-precision angular alignment—the system generates stable, high-quality femtosecond pulses.

The resulting setup offers full tunability across the wide **1050-1875 nm** spectral range.

These pulses exhibit well-defined spectral profiles that closely follow theoretical expectations and consistently deliver over 300 mW of output power at the sample—sufficient to expose even subtle nonlinear photophysical phenomena.

A system without samples would be little more than art for art's sake—thus, the preparation of stable solid-state samples forms an equally essential part of the overall design. Starting from oleic acid-coated colloidal suspensions, an acid-based extraction protocol removes the surfactant, yielding clean nanoparticles ready for high-power optical analysis without risk of thermal degradation. Once deposited onto microscope slides via drop-casting and dried, these samples form the foundation for *all* spectroscopic measurements that follow.

And what *does* follow? To answer that, we outlined the measurement methodology—what could be done, and what **was done** using our custom-built setup. This included the recording of dual-wavelength

co-excitation spectra, complemented by single-excitation reference measurements. Key emission wavelengths were defined for each nanoparticle type, along with the rationale for their selection. Finally, power-dependent studies were introduced to probe the system's nonlinear optical response. In doing so, the setup is employed to its fullest extent—delivering on the promise of its design.

In sum, this chapter presents the foundation of a custom-built experimental system—one that integrates tunable NIR beam generation via difference-frequency generation (DFG), precise spatial overlap with a fixed 975 nm excitation source, and their collinear delivery to the sample within a spectrofluorometer chamber. This setup enables not only the recording of dual-wavelength co-excitation spectra across a broad NIR range, but also offers precise control over excitation wavelength and power—allowing for the systematic investigation of co-excitation phenomena under well-defined and reproducible conditions.

With this system, concepts become experiments—and the previously theoretical becomes measurable.

2.5.1 Contributions

Assistance with developing the optical layout—both theoretical design and practical implementation, including precise alignment—as well as setting up the knife-edge method, co-conducting the focal spot size measurements, and analyzing the resulting data — **Piotr Fita**

Construction and alignment of the setup, beam characterization (excluding analysis of knife-edge method results), comprehensive documentation, and all tasks in between — **myself, Paulina Rajchel-Mieldzioć**

Thulium

Co-excitation in Tm-doped upconverting nanoparticles

3

3.1 Two are better than one

They get a good wage for their toil. In the context of co-excitation, we may not always seek something *better*—a notion that is difficult to define in absolute terms. But what we certainly seek is something *different*—an outcome unattainable by either beam alone. And this, precisely, is the essence of our concept, captured most fully by this verse.[1]

1: Ecclesiastes 4:9

From the outset of planning our experiments, we anticipated an observable effect. After all, beyond the commonly used wavelengths that excite upconverting nanoparticles via sensitizer ions, there are others that correspond to specific transitions within the activator ions themselves. One can therefore expect that simultaneous excitation of UCNPs at multiple wavelengths—especially those carefully tuned to particular electronic transitions—will enable new photoexcitation pathways and influence emission intensity, potentially leading to novel effects. Furthermore, the nonlinear nature of UCNPs interactions with light—especially their dependence on the power of multiple excitation beams—can be useful in applications where such behavior offers a practical advantage.

With the introduction complete, we now turn to the results. And let it be said from the outset: what we observed was not only strikingly *different*, but also a tangible and compelling outcome—one that may rightfully be considered an *improvement*.

3.1.1 From theory to practice

Setting the stage

Upon excitation with a 975 nm beam (resonant with the absorption of the sensitizer ion Yb^{3+}), the analyzed co-doped nanoparticles—containing thulium (Tm^{3+}) as the activator—exhibit a characteristic emission spectrum (Fig. 1.7). Although several emission bands can be identified, a prominent maximum appears at the lower-energy region—800 nm. This emission wavelength thus serves as a reference point for evaluating non-standard excitation pathways along the $4f$ manifolds of thulium, particularly when examining the lower-energy levels in the Tm^{3+} energy ladder.

As mentioned earlier in the methodological introduction,[2] from this point onward, this 800 nm emission will simply be referred to as the emission in the context of Tm-doped nanoparticles. It also serves as a direct, visible indicator—a litmus test—for our experimental strategy of co-excitation.[3] This approach has already been described in detail in the methodology section (Section 2.4), but to briefly summarize: here, we present and evaluate a co-excitation scheme involving simultaneous illumination with a continuous-wave beam at a fixed wavelength (975 nm) and a tunable near-infrared pulsed beam spanning the spectral range of 1050-1875 nm.

2: See Section 2.4.

3: The *most* representative litmus test—the very statement evaluated in Section 3.1.3.

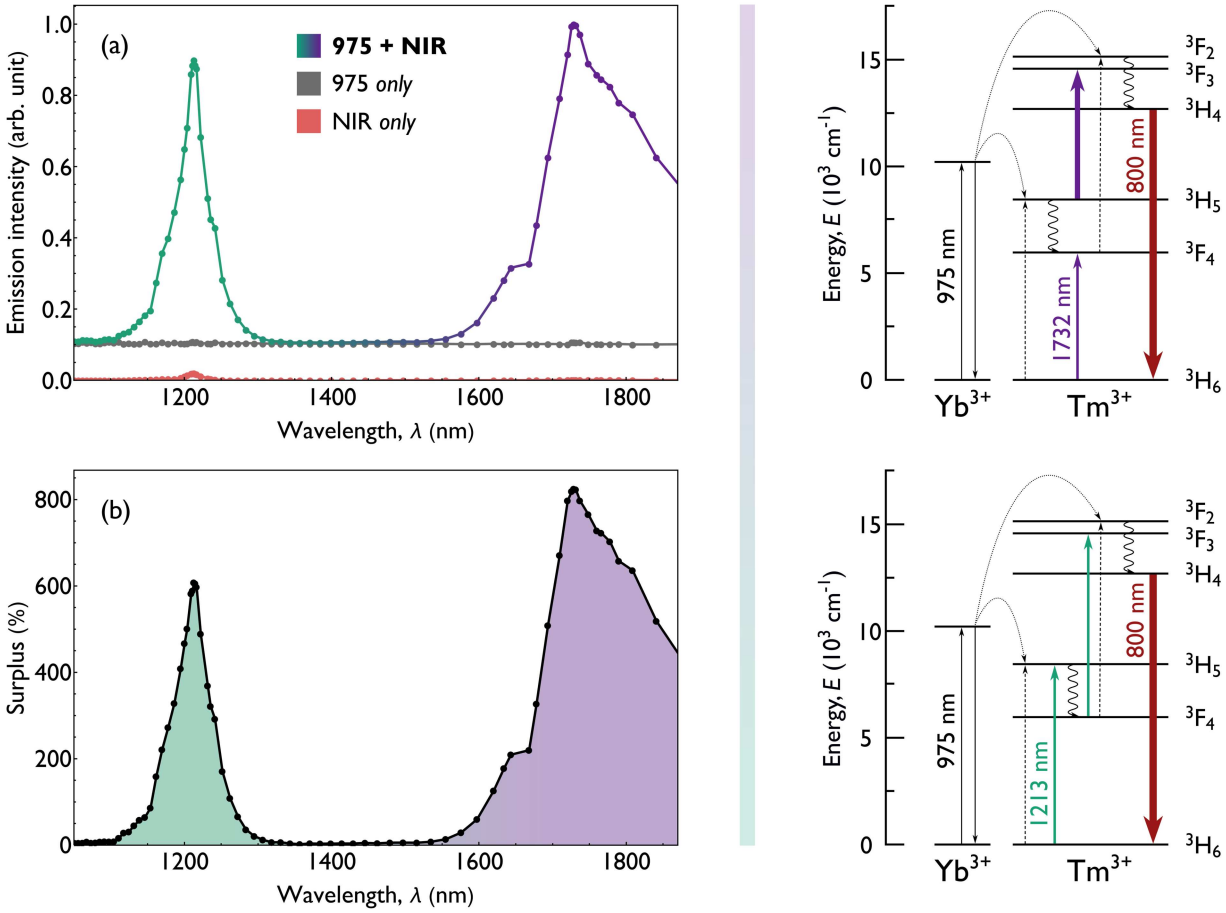

Figure 3.1: Left: Excitation spectra of YbTm nanoparticles recorded at 800 nm emission under simultaneous excitation with two spatially overlapped beams: a continuous-wave 975 nm beam (10 mW) and a tunable pulsed NIR beam (100 mW). **(a)** Excitation spectra measured under three excitation conditions—each plotted on the same scale and normalized to the maximum recorded value: *(i)* co-excitation with both beams (green-violet bichromatic line, used to visually separate the two distinct bands corresponding to color-coded transitions), *(ii)* excitation with the NIR beam only (coral line near the bottom, showing non-zero values only around 1200 nm), and *(iii)* baseline emission generated by the 975 nm beam alone (gray points; a steady level, as the 975 nm beam has a fixed wavelength; however, single-beam measurements with the 975 nm excitation were still performed at each tuning step of the NIR beam). Emission intensity is plotted as a function of NIR excitation wavelength. **(b)** Surplus emission plot under co-excitation, showing the enhancement relative to the **sum** of emission intensities generated by each beam independently. **Right:** Simplified energy-level diagrams of the YbTm system, illustrating ground-state absorption (GSA) and potential excited-state absorption (ESA) processes that govern the observed excitation spectra. The thickness of the absorption lines in thulium ions—corresponding to transitions enabled by the introduction of the NIR beam—serves as an approximate visual indicator of their oscillator strengths, in accordance with Judd-Ofelt theory.

The effect revealed

What follows are the earliest findings—**yet decisive and foundational**. Through manual tuning and alignment of the DFG setup, followed by collinear overlap of the resulting NIR beam with the 975 nm beam—alongside performing comparative single-beam measurements—we obtained a co-excitation spectrum (recorded at an emission wavelength of 800 nm) of the YbTm nanoparticles. This spectrum was measured using a fixed 975 nm excitation (10 mW) in combination with a tunable NIR beam (100 mW) and plotted as a function of the NIR excitation wavelength across the full available range. The results are presented in Fig. 3.1a.

Despite the modest appearance of this figure, it encapsulates a substantial amount of data and insight—representing a key milestone in this work. Crucially, the same plot also includes the baseline emission intensities

obtained from single-beam excitation: both the 975 nm-only and the NIR-only excitation conditions (as comparative references), which are easy to overlook when focusing solely on the co-excitation spectrum. Yet it is precisely this **dramatic difference in emission intensities** that captures the essence of this entire study.

Before we move on to the theoretical considerations[4] that aim to explain what we observe, let us first clearly present what we *actually* see. The co-excitation spectrum reveals two distinct and spectrally broad bands, with maxima centered at 1213 nm and 1732 nm. These peaks indicate enhanced upconversion (UC) emission under simultaneous illumination with both the 975 nm and NIR beams, but they do not correspond to wavelengths that produce substantial emission when used in isolation. This, however, warrants a more emphatic description—one that better conveys the scale of the effect. The 975 nm beam, as expected, induces upconversion[5] emission since it is resonant with the absorption of the sensitizer, which subsequently transfers energy to thulium ions. The NIR beam alone,[6] when held at a fixed and constant power across the entire tuning range, produces mostly negligible emission.

4: See Section 3.1.2.

5: Gray line in Fig. 3.1a.

6: Coral line near the bottom in Fig. 3.1a.

Yet, when these two beams—975 nm and a suitably chosen NIR wavelength—are combined, a **strikingly strong emission emerges**, vastly exceeding the signal produced by either beam on its own.

To fully capture the magnitude of this phenomenon, we introduce the concept of **emission surplus**—a measure of enhancement defined as the extent to which the emission intensity under co-excitation exceeds the **sum** of the intensities generated by the individual beams. The emission surplus, expressed as a function of NIR wavelength and reaching *several hundred percent*, is shown in Fig. 3.1b and quantitatively defined by Eq. 3.1.

$$S_\lambda = \frac{E_{\text{co-ex}}(\lambda) - (E_{\text{NIR}}(\lambda) + E_{975})}{E_{\text{NIR}}(\lambda) + E_{975}} \cdot 100\%. \tag{3.1}$$

In this equation, $E_{\text{co-ex}}(\lambda)$ denotes the emission intensity at 800 nm recorded under co-excitation; E_{NIR} represents the emission intensity under excitation with the NIR beam alone, and E_{975} corresponds to excitation with the 975 nm beam alone. The variable λ (nm) refers to the wavelength of the NIR beam at the time of measurement. As previously noted and shown in Fig. 3.1b, the measured emission surplus—recorded under fixed, non-optimized conditions (i.e., without intentionally maximizing the surplus)—shows a multiple-fold increase relative to the sum of single-beam contributions. This unexpectedly high value prompts further reflection—not only on *how* it might be modulated or controlled, but more fundamentally: *why?*

3.1.2 Photophysical pathways

To understand the origin of these features, we consider the thulium energy-level diagram (Figs. 3.1 and 3.2), which offers several viable

transition pathways capable of interacting with the incident radiation—particularly when assisted by energy transfer upconversion (ETU) from the Yb^{3+} sensitizer.

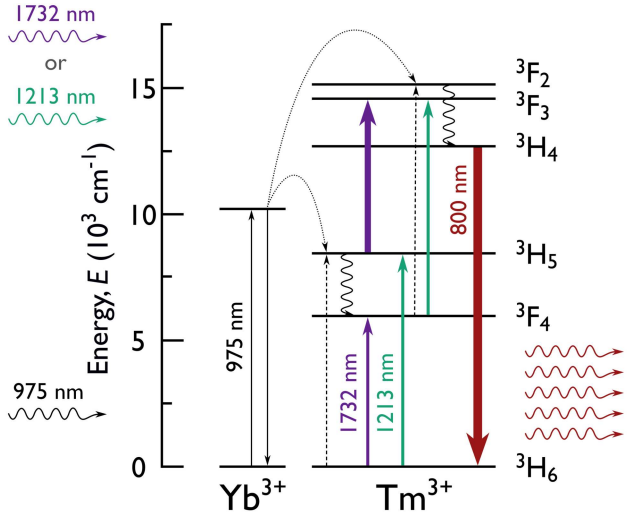

Figure 3.2: Energy level diagram illustrating the observed transitions during the co-excitation experiment with the 975 nm beam and the tunable NIR beam. The diagram marks all likely transitions, color-coded to correspond to different excitation wavelengths used in the experiment. It thus provides a condensed summary of two distinct excitation conditions, as detailed in the course of the experiment and described in Section 3.1.1. The thickness of the absorption transition lines associated with thulium ions—specifically those enabled by the introduction of the NIR beam—approximately reflects the oscillator strength, as described by Judd-Ofelt theory.

According to Judd-Ofelt theory and the associated reduced matrix elements calculated for trivalent thulium transitions, numerous ground-state absorption (GSA) and excited-state absorption (ESA) transitions exhibit significant oscillator strengths. For instance, the GSA transition $^3H_6 \longrightarrow {}^3H_5$ and the ESA transition $^3F_4 \longrightarrow {}^3F_3$ are theoretically expected to possess similar absorption cross-sections. Likewise, the GSA transition $^3H_6 \longrightarrow {}^3F_4$ and the ESA $^3H_5 \longrightarrow {}^3F_3$ pathway are predicted to be comparably efficient. However, under steady-state and room-temperature conditions, excited states such as $^3F_4$ and $^3H_5$ are sparsely populated. As a result, ESA transitions that depend on these states are generally inactive unless additional population is introduced externally.

This is precisely where energy transfer upconversion (ETU) from Yb^{3+} ions plays a critical role. Absorption of 975 nm light by Yb^{3+} ions leads to nonradiative energy transfer to Tm^{3+} ions, partially populating intermediate excited states. While ESA cross-sections are influenced by the host matrix, local crystal field, and temperature—the presence of the sensitizing beam substantially increases the excited-state population, making ESA transitions more accessible.

However, the enhancement observed under co-excitation does not arise from a single mechanism. Alongside enabling ESA from already populated excited levels, the NIR beam can also directly initiate ground-state absorption (GSA) transitions in thulium. These GSA-driven excitations can then be further amplified by subsequent ETU from Yb^{3+} ions. In this way, co-excitation activates two complementary excitation pathways—ESA and GSA-assisted ETU—which together produce a level of upconversion emission that far exceeds what is achieved by either beam alone.

This dual-pathway mechanism also clarifies why NIR excitation alone—particularly at 1732 nm—does not result in significant visible emission. Excitation at 1213 nm, however, yields a weak but detectable signal[7], likely due to excited-state absorption (ESA) from the $^3F_4$ to the $^3F_3$ level. In this

7: See coral points on Fig. 3.1a

scenario, the $^3F_4$ state can be populated through ground-state absorption (GSA) from $^3H_6$, followed by non-radiative relaxation. This weak emission contrasts with the response—or more accurately, lack thereof—when excited with only a 1732 nm beam, which predominantly populates the $^3F_4$ level via GSA but fails to populate the $^3H_5$ state adequately—limiting the effectiveness of the $^3H_5 \rightarrow {}^3F_3$ ESA transition pathway.

The long-lived nature of intermediate excited states in thulium further supports the co-excitation mechanism. Energy transferred from Yb^{3+} ions can be temporarily stored, awaiting subsequent photon absorption via ESA. This temporal separation of excitation events enables a more flexible and efficient population of higher-energy states.

Ultimately, it is this dynamic interplay—between sensitizer-assisted population and wavelength-selective photon absorption—that makes co-excitation a particularly versatile yet complex approach for tuning upconversion emission.

3.1.3 Anchoring the analysis

Before we move on to a deeper analysis of the observed phenomenon, it is worth pausing for a moment to reflect on the selection of the 800 nm emission as our reference point. Previously, this choice was motivated by its overwhelming dominance—emphatically overwhelming—among all emission bands under single-beam excitation, that is, under standard excitation with the 975 nm laser. This rationale was grounded in both the theoretical framework[8] and the methodological section,[9] and is clearly visible in the emission spectrum shown again in Fig. 3.3a.

8: See Section 1.1.4.
9: See Section 2.4.

But does this assumption *still* hold in the dual-beam excitation regime? Is the $^3H_4 \longrightarrow {}^3H_6$ transition still the most valid anchor for our co-excitation analysis?

Fig. 3.3 presents the emission spectra of the YbTm nanoparticles under single-beam excitation at 975 nm (Figs. 3.3a and 3.3b), as well as under co-excitation with either 1732 nm (Figs. 3.3c and 3.3d) or 1213 nm (Figs. 3.3e and 3.3f). For reference, each co-excitation spectrum also includes emission collected under excitation by the long-wavelength beams alone. These individual contributions, however, are negligible compared to the 975 nm excitation and co-excitation conditions; their traces remain close to the baseline.

And here, the answer to our earlier question reveals itself with clarity.

The 800 nm band, already dominant in single-beam excitation, only *strengthens* its position under co-excitation. It exhibits the **highest relative enhancement** among all emission bands—reaffirming its status as the principal transition, both in absolute terms and in its responsiveness to dual-beam excitation.

This makes it abundantly clear why, for the sake of interpretive clarity and consistency, we chose to center our analysis on this most prominent transition ($^3H_4 \longrightarrow {}^3H_6$)—whose enhancement under co-excitation is the most substantial.

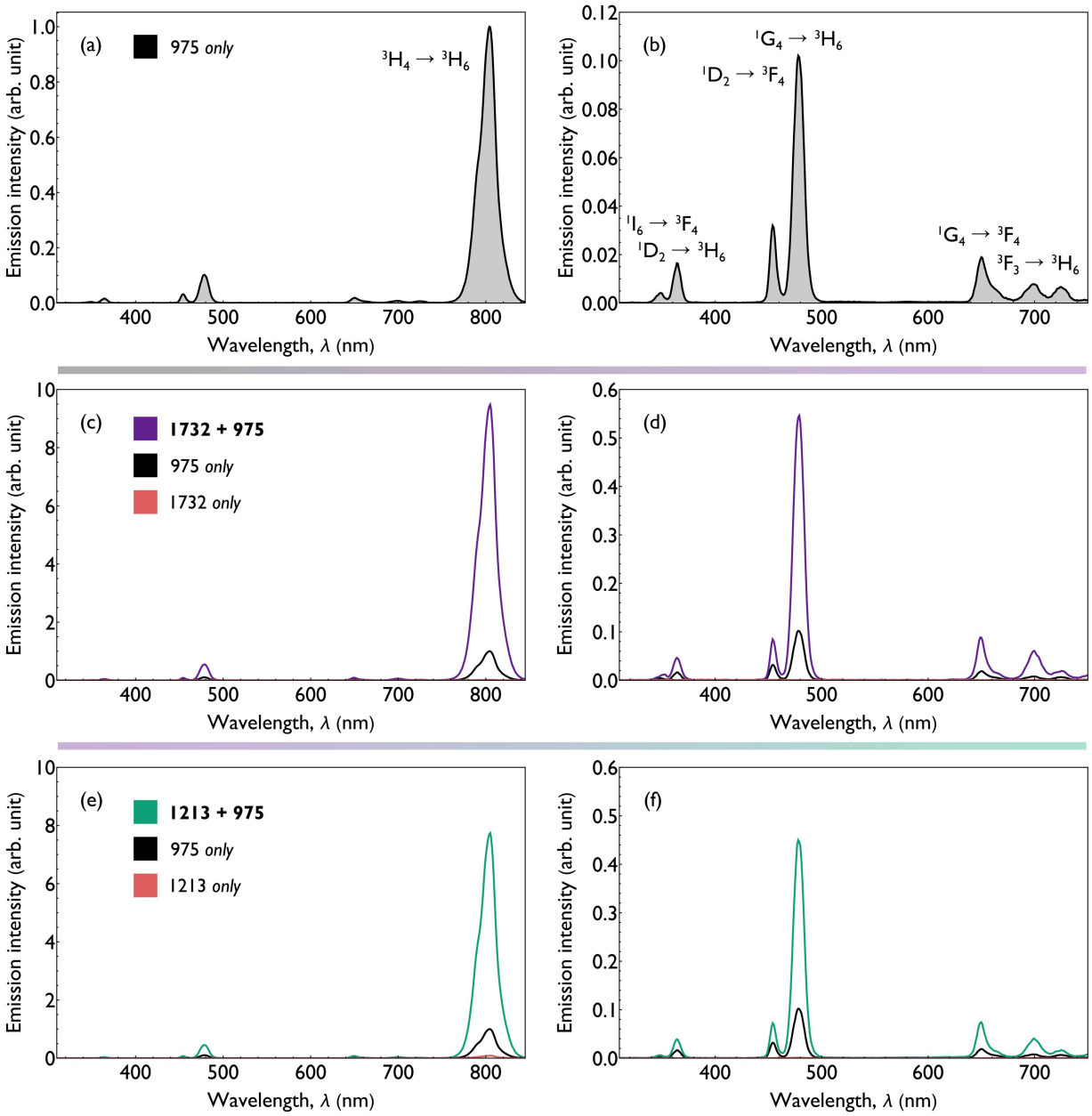

Figure 3.3: Emission spectra of the examined YbTm nanoparticles. **(a)** Spectrum recorded under 10 mW continuous-wave 975 nm excitation, with a clearly dominant band observed near 800 nm. **(b)** Zoomed-in view of (a), showing emission details below 750 nm. **(c)** Emission under co-excitation with 10 mW 975 nm and 100 mW 1732 nm beams. For reference, spectra from 975 nm-only excitation (black) and 1732 nm-only excitation (coral, close to baseline) are also included. **(d)** Magnified segment of (c), highlighting emission features below 750 nm. **(e)** Spectrum under co-excitation with 10 mW 975 nm and 100 mW 1213 nm beams. Emission from single-beam excitation with 975 nm (black) and 1213 nm (coral) is shown for comparison. **(f)** Close-up of (e), limited to the sub-750 nm range. All data are plotted on the same scale to enable direct comparison.

Still, the story of co-excitation does not begin and end with the 800 nm band. Other transitions are also noticeably affected. The ultraviolet emissions ($^1I_6 \longrightarrow {}^3F_4$ and $^1D_2 \longrightarrow {}^3H_6$) are enhanced, especially under co-excitation with the 1732 nm beam. Under 1213 nm excitation, this effect is less pronounced—particularly for the $^1I_6 \longrightarrow {}^3F_4$ transition, which shows minimal enhancement under the given conditions. Yet, due to their already low intensity under 975 nm single-beam excitation, even these amplified UV emissions remain weak in absolute terms.

The blue emission bands ($^1D_2 \longrightarrow {}^3F_4$ and $^1G_4 \longrightarrow {}^3H_6$) also display co-

excitation enhancement—especially the latter, which is more prominent and more responsive under 1732 nm co-excitation. Still, its enhancement remains significantly smaller than that of the 800 nm band, reaching at most about half the relative increase.

A similar trend holds for the red emission bands ($^1G_4 \longrightarrow {}^3F_4$ and $^3F_3 \longrightarrow {}^3H_6$), both of which show increased intensity under co-excitation with either NIR beam. Notably, the $^3F_3 \longrightarrow {}^3H_6$ transition responds more strongly to the 1732 nm excitation.

All these patterns point to a broader insight: while co-excitation amplifies emission across the spectrum, it disproportionately favors the already dominant 800 nm band (compare Fig. 3.3a with Figs. 3.3c and 3.3e). Yet this should not suggest that the other transitions are less worthy of attention—far from it. They, too, show clear—and often considerable—enhancement, presenting further opportunities for mechanistic inquiry and expanding the potential application of the effect beyond the red region and across the entire emission spectrum of YbTm nanoparticles.

Yet to use the effect, one must first understand it. With that in mind—and now equipped with a broader view—we can return to its analysis, focusing, with full confidence, on the behavior of the **800 nm** band: **the most eloquent representative** of the emissive properties of thulium-doped nanoparticles.

3.2 *Emission as a function of power*— single-wavelength excitation

After exploring the possible mechanisms, and affirming the dominance of the chosen emission band, we are still left with a tangible enhancement effect—and a key question: how can this effect be tuned? The answer is straightforward, as only one parameter in the entire system remains freely adjustable: *power*. Before turning to the two-dimensional case—where the interplay of both beams in the co-excitation process is considered—we must first examine the influence of each excitation beam individually.

3.2.1 975 nm

The influence of the 975 nm beam—resonant with the sensitizer ions (Yb^{3+})—on the emission of thulium co-doped upconverting nanoparticles is far from trivial. It depends on a range of structural parameters, including the host matrix, dopant concentration, nanoparticle size, and core-shell architecture. Since these factors differ between nanoparticle systems, the emission response cannot be generalized, making it essential to characterize this dependence specifically for the materials used in our study. The only consistent feature is a certain degree of nonlinearity in the relationship between emission intensity and excitation power, as described by Eq. 3.2.

$$E = a \cdot P^{\xi} \Longrightarrow E \propto P^{\xi} \tag{3.2}$$

Here, E denotes the emission intensity (in our case, measured at 800 nm), P is the excitation power (in mW), a is a proportionality constant (or prefactor), and ξ is the power-law exponent characterizing the degree of nonlinearity. Among these parameters, ξ is of particular interest: it provides insight into the underlying excitation dynamics of the system and serves as the main parameter of focus in the fitting procedure. By contrast, the prefactor a also incorporates contributions from external influences such as *nanoparticle concentration in a non-uniform sample*, detection efficiency, and signal collection geometry—although it remains constant within a given experimental configuration.

In the analysis that follows, we emphasize the interpretation of ξ as an indicator of the system's intrinsic photophysical response, while recognizing that the prefactor a may become relevant in discussions of absolute signal magnitudes or comparative efficiencies between different setups.

Fig. 3.4 shows the emission intensity of YbTm nanoparticles as a function of 975 nm excitation power, ranging from 10 to 200 mW. At first glance, the plot may appear unremarkable, but it reveals a distinct nonlinear behavior—particularly in the low-power regime. And this detail, while subtle, is crucial: the nonlinearity of emission with respect to excitation power is **constant only within specific power ranges**. This is not an unexpected observation—it is, in fact, typical—but it highlights the inherent complexity, and at times the near impossibility, of fully describing the

emission characteristics of UCNPs as a function of power, even under single-beam excitation.

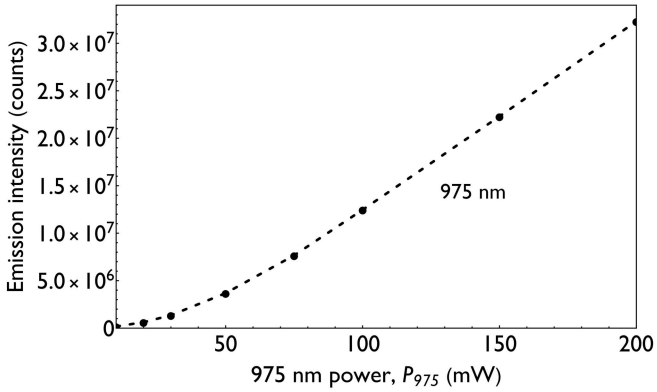

Figure 3.4: Emission intensity (recorded at 800 nm) of YbTm nanoparticles as a function of 975 nm beam power, measured in the range of 10-200 mW under single-beam excitation. The dashed line is included as a visual guide.

To address this challenge, we adopted a methodical approach by dividing the measurement range into distinct power intervals. This strategy is illustrated in Fig. 3.5.

The analyzed power range was divided into two empirical regimes—lower and higher power—with a boundary around 50 mW. It is important to emphasize that this value is empirical; a more universal parameter would be the power density, which depends on the tightness of the beam focus. In the presented case, according to the focal spot size measurements[10] provided in the methodological section, a 50 mW beam at 975 nm corresponds to an intensity of approximately 1.5 kW/cm^2.

10: See Section 2.2.1.

In the lower power regime, the emission behavior of the nanoparticles follows a well-defined power-law dependence, with a pronounced nonlinearity.[11] Crucially, this nonlinearity remains **constant** across the entire regime and is captured by a single exponent: $\xi = \mathbf{1.94}(1)$.

11: Still with the exponent below 2—values above 2-3 are characteristic of energy-looping, a distinct mechanism that involves excitation at a wavelength resonant only with an excited-state transition, which is not the case here; see Section 1.1.3.

As the excitation power increases, this behavior changes—the nanoparticles begin to exhibit self-limiting properties. Although the overall emission intensity still rises, the rate of increase slows down. In this high-power regime, a reduced nonlinearity is observed, best approximated by a fitted exponent of $\xi = \mathbf{1.40}(5)$. However, it is important to note that this fit represents an average: the nonlinearity in this regime is **not constant** but gradually *decreases* as power increases.

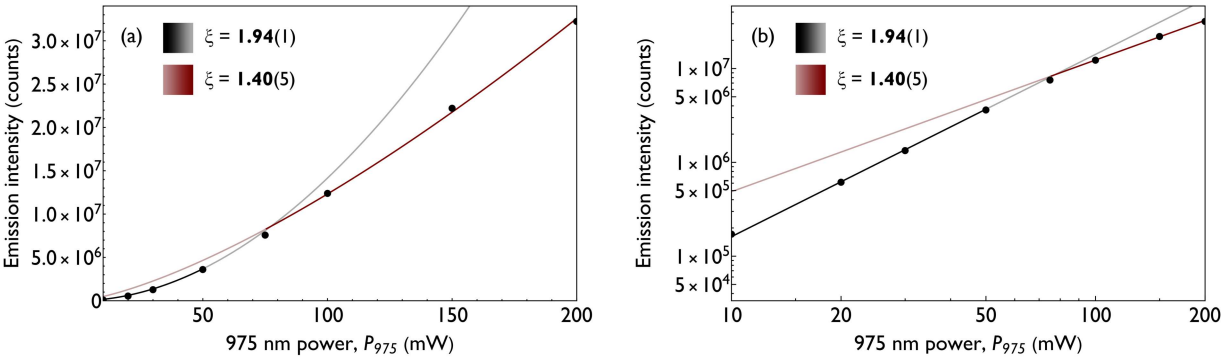

Figure 3.5: Emission intensity (recorded at 800 nm) of YbTm nanoparticles as a function of 975 nm beam power (10-200 mW), measured under single-beam excitation. Fitted trends are included. **(a)** Results shown on a linear scale. **(b)** Results presented on a log-log scale. Black line: fit for the low-power regime of the 975 nm beam, extrapolated across the full range in a lighter shade (gray). Red line: fit for the high-power regime, extended across the full range in a lighter shade (pink).

The observed emission properties—quantitatively described through these fitted exponents—align well with general trends reported for upconverting nanoparticles, including those doped with thulium. Specifically, a consistently superlinear response is followed by saturation and eventual flattening of the curve—driven by photophysical interactions and thermal effects. Thus, the emission behavior observed here is consistent with the current understanding of UCNP photophysics, and the fitted values obtained in our study provide a solid foundation for analyzing the more complex co-excitation phenomena that follow.

3.2.2 NIR: 1213 and 1732 nm

Before we proceed with the analysis of co-excitation, we must first examine the influence of the NIR beam alone—that is, under single-beam excitation. As previously described in Section 3.1.1, this influence is relatively modest when viewed solely from the perspective of the induced emission intensity. While the individual effect of the NIR beam is significantly weaker than that of the 975 nm excitation, it remains a crucial element in the pronounced emission enhancement observed under co-excitation—a phenomenon that underpins the entirety of this work. For this reason, its contribution must be thoroughly examined before we can meaningfully discuss the combined action of both beams.

It is worth emphasizing an important yet easily overlooked point: in the experiments described here, only one beam is used at a time. However, these single-beam experiments were performed separately for two distinct NIR wavelengths—1213 nm and 1732 nm—since it was under co-excitation with the 975 nm base beam that each of these wavelengths (independently) yielded emission enhancements reaching several hundred percent (see Fig. 3.1).

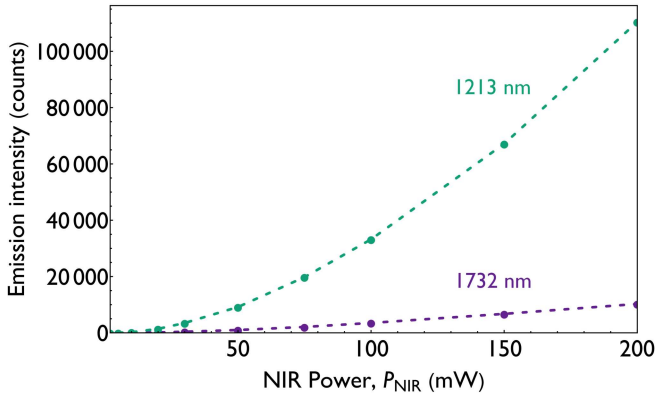

Figure 3.6: Emission intensity (recorded at 800 nm) of YbTm nanoparticles as a function of NIR beam power, measured over the 2-200 mW range under single-beam excitation—performed independently with a 1213 nm beam (green) and a 1732 nm beam (violet). The dashed line is included as a visual guide.

Fig. 3.6 presents the emission intensity at 800 nm as a function of power for the selected NIR beams—1213 nm and 1732 nm—over the range of 2 to 200 mW. For the lower power levels (especially for 1732 nm), no detectable emission was observed, with measurements remaining at the dark count level. It is important to note the scale difference compared to the emission induced by the 975 nm beam alone (see Fig. 3.4): the signal generated by the 975 nm beam is stronger by factors ranging from hundreds (relative to 1213 nm) to thousands (relative to 1732 nm). This weak system response to the NIR beams alone—particularly the even weaker response at 1732 nm

compared to 1213 nm—was previously explained in detail in the analysis of photophysical pathways in Section 3.1.2. Regardless of the functional form describing these responses, it is evident that the prefactor[12] must be smaller than that associated with 975 nm excitation, which is resonant with the ground-state absorption (GSA) of the sensitizer ions.

12: The a in the $a \cdot P^{\xi}$ expression, see Eq. 3.2.

With this context established, we now turn to the actual analysis, which—like before—requires division into distinct power regimes, as illustrated in Fig. 3.7.

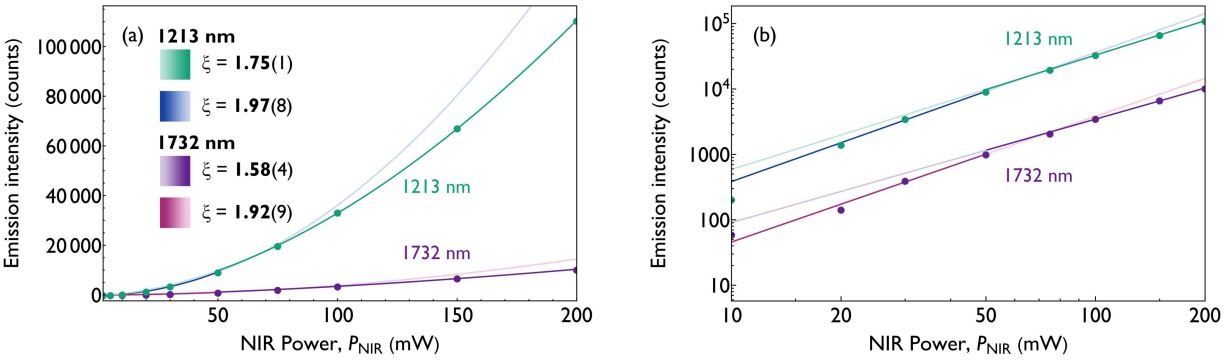

Figure 3.7: Emission intensity (recorded at 800 nm) of YbTm nanoparticles as a function of NIR beam power (2-200 mW), measured under single-beam excitation, independently for a 1213 nm beam (green points) and a 1732 nm beam (violet points). Fitted trends are included. **(a)** Results shown on a linear scale. **(b)** Results presented on a log-log scale. **For the 1213 nm beam:** Green line: fit for the high-power regime, extended across the full range in light green. Blue line: fit for the low-power regime, extrapolated across the full range in light blue. **For the 1732 nm beam:** Violet line: fit for the high-power regime, extended across the full range in light violet. Pink line: fit for the low-power regime, extrapolated across the full range in light pink.

The dependence of emission intensity on NIR beam power—and how it evolves—may initially appear similar to the behavior observed for excitation with the 975 nm beam. At first glance, the relationship exhibits a high degree of nonlinearity, with power-law exponents of **1.97**(8) for the 1213 nm beam and **1.92**(9) for the 1732 nm beam. This nonlinearity seems to decrease with increasing power, eventually reaching values of **1.75**(1) and **1.58**(4), respectively. *However, this similarity is misleading.*

In contrast to the 975 nm excitation, NIR-driven emission does not approach saturation or exhibit self-limiting behavior—where increasing excitation power leads to a continual reduction in nonlinearity. Instead, for the NIR beams, the power-law exponent reaches a lower, yet constant value at higher powers, indicating a stabilization rather than saturation. The fits in the high-power regime are very good, yielding stable exponents of **1.75**(1) and **1.58**(4) for the 1213 nm and 1732 nm beams, respectively.

Why does this happen? Because the NIR beams, when used alone, weakly excite thulium ions—particularly the higher-energy $4f$ manifolds—due to their relatively small absorption cross-sections[13] compared to the more efficient 975 nm excitation of Yb^{3+} ions followed by ETU. Saturation is therefore not approached, especially considering that the NIR beam is pulsed. At most, thermal effects may start to play a role at elevated powers. Thus, the apparent reduction in nonlinearity is actually a stabilization, and true saturation would likely require much higher powers, where both photophysical and thermal processes would come into play.

13: Section 3.1.2 discusses the mechanisms responsible for the limited emission observed with NIR excitation alone.

In the low-power regime, fitting becomes increasingly challenging due to large uncertainties associated with weak—or entirely absent—emission signals. Still, we obtained approximate power-law exponents of **1.97**(8)

and **1.92**(9) for the 1213 nm and 1732 nm beams, respectively.[14] These should be treated as *estimates*, especially since nonlinearity appears to evolve within this regime.

It is important to note that the emission intensity under NIR excitation alone is significantly weaker than under 975 nm excitation—often by several orders of magnitude. This is reflected in the much smaller prefactors of the fitted functions, consistent with the relatively low direct excitation efficiency of thulium ions by a single NIR beam.

Armed with this understanding, we can now turn to the more complex scenario: when two beams—975 nm and NIR—*meet*. Let us now examine co-excitation and how the observed effects depend on the excitation power.

14: It is *highly* important to note that fitting in the low-power regime for the 1732 nm beam naturally omits several initial data points, as they correspond to zero signal. Below several milliwatts, the 1732 nm beam produces no detectable emission, making it **impossible** to extend the fit into the very lowest power range.

3.3 *Emission as a function of power—* dual-wavelength co-excitation

It takes two to tango—and what a tango it is. We have already demonstrated that combining the baseline 975 nm beam with a suitable NIR beam results in a **dramatic surge** in emission intensity, far exceeding what is produced by either beam alone.[15] Now, it is time to examine this phenomenon more closely by analyzing how the effect depends on the power of each individual beam.

15: See Section 3.1.1, especially Fig. 3.1.

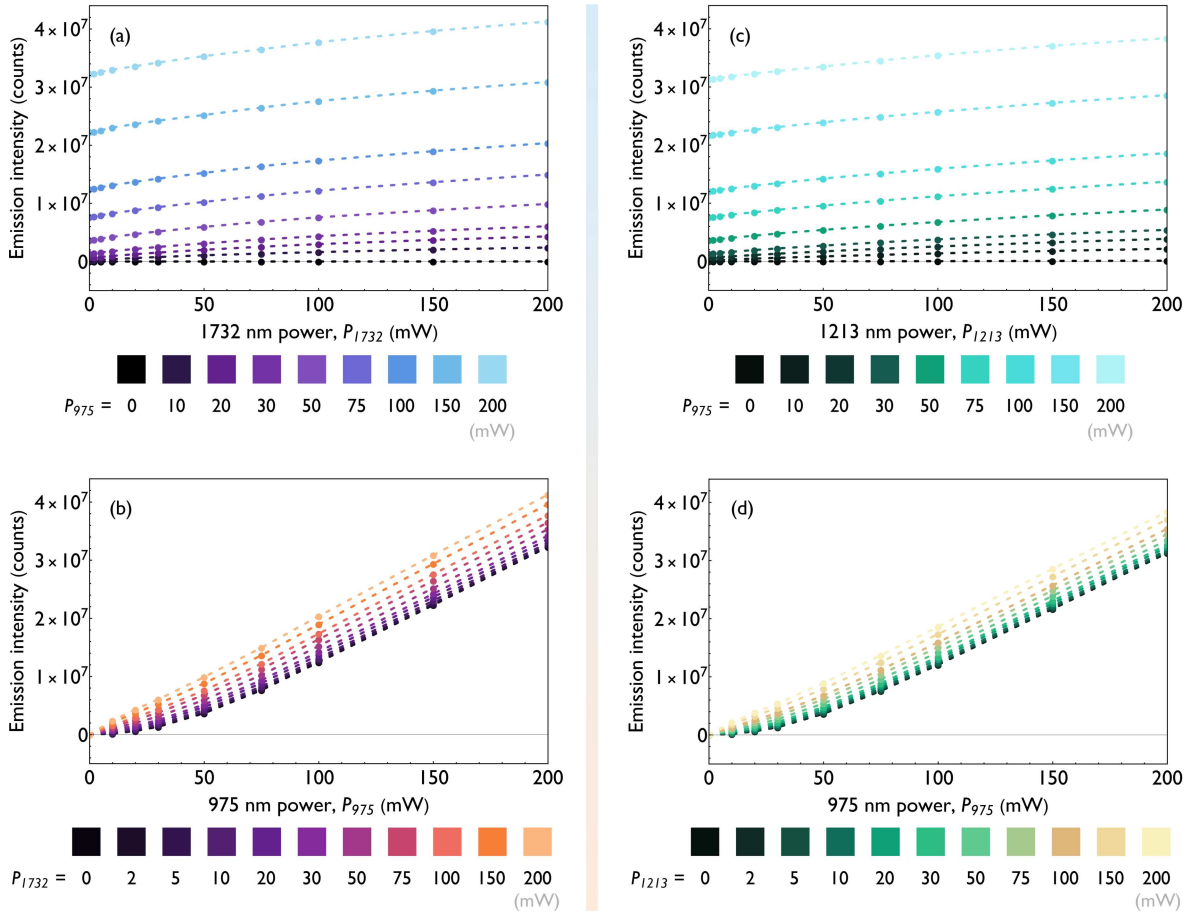

Figure 3.8: Emission intensity at 800 nm from YbTm nanoparticles under dual-wavelength co-excitation with 975 nm and NIR beams, presented as a function of excitation power. **(a)** Emission intensity as a function of 1732 nm beam power at various fixed power levels of the 975 nm beam. **(b)** Complementary plot: emission intensity as a function of 975 nm beam power, shown for multiple fixed 1732 nm power levels. **(c)** Emission intensity as a function of 1213 nm beam power at various fixed power levels of the 975 nm beam. **(d)** Complementary plot: emission intensity as a function of 975 nm beam power, for several fixed 1213 nm power levels. Dashed lines between points are included to guide the eye. Axes are scaled to enhance visibility of low-intensity emission values.

Only two beams—but significantly greater complexity. This means a much larger volume of data, presented in linear scale in Fig. 3.8 and in log-log scale in Fig. 3.9 (displaying the same dataset). Though the richness of the data may seem overwhelming at first glance, we will walk through it step by step to make the insights both clear and accessible—so that the value and importance of the information can be fully appreciated. All considerations presented here are conducted in the medium to high power range—starting from a few milliwatts up to 200 mW.[16]

16: It is important to keep this in mind, as the chosen experimental limits may ultimately define the boundaries of our understanding—limits that **may need to be surpassed**.

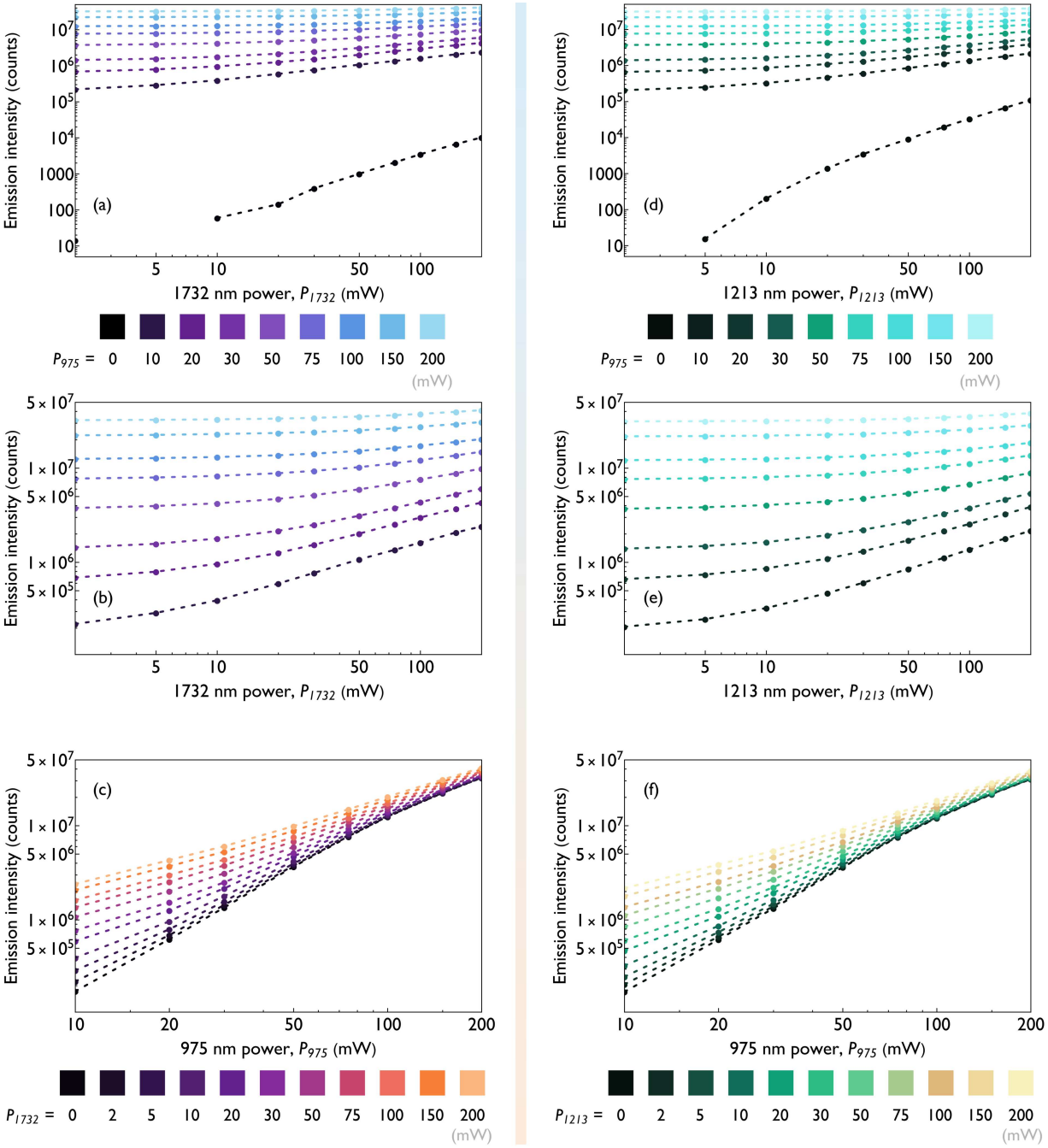

Figure 3.9: Same dataset as in Fig. 3.8, presented here on a log-log scale to highlight nonlinear trends. Emission intensity at 800 nm from YbTm nanoparticles under co-excitation with 975 nm and NIR beams is shown as a function of excitation power. Data points corresponding to zero values on either axis are excluded, as they cannot be represented on logarithmic scales. **(a)** Emission intensity as a function of 1732 nm beam power for various fixed power levels of the 975 nm beam. **(b)** Same as (a), but with the 0 mW 975 nm series omitted for clarity. **(c)** Complementary plot: emission as a function of 975 nm beam power for multiple fixed 1732 nm power levels. **(d)** Emission intensity as a function of 1213 nm beam power for various 975 nm power levels. **(e)** Same as (d), with the 0 mW 975 nm series omitted. **(f)** Complementary plot: emission intensity as a function of 975 nm beam power for different fixed 1213 nm powers. Dashed lines connecting points are included as visual guides.

3.3.1 Seeing the response

Within this defined range, let us first analyze how emission intensity evolves with increasing NIR beam power, while keeping the baseline 975 nm beam power constant. This relationship is shown for the 1732 nm and 1213 nm beams in Figs. 3.8a and 3.8c, respectively, and in logarithmic scale in Figs. 3.9a-b and 3.9d-e (presented twice with different axis scalings). Since the trends for both—1213 and 1732 nm—beams are similar, we refer to them collectively as NIR beams.

As NIR beam power increases, a clear **enhancement** in emission intensity is observed. This enhancement is the **surplus**: the excess emission that emerges exclusively under co-excitation, surpassing what either the 975 nm or NIR beam can generate on its own. It is the central thread running through this entire chapter.[17] Why does it stand out so clearly? Because the NIR beam alone produces negligible emission—especially when compared to single excitation with 975 nm. And yet, once the two are combined, even subtle changes in the NIR beam's power—*on its own, seemingly insignificant*—begin to influence the total emission. That shift, that sudden responsiveness—is the very essence of the surplus.

17: First introduced and defined in Section 3.1.1.

However, the functional form of this dependence differs significantly from that of single-beam excitation.[18] When considering moderate to high NIR beam powers, increasing the power continues to enhance the emission, but with progressively diminishing returns. This is not merely a reduction in superlinearity—rather, the distribution of the data points clearly indicates a distinctly sublinear behavior. These trends are even more evident in the logarithmic plots.

18: Compare with single-wavelength NIR excitation, Figs. 3.6 and 3.7, described in Section 3.2.2.

As stated—at higher NIR powers, the emission intensity shows a clear dependence on the NIR beam power—yet this influence becomes more pronounced as the 975 nm beam weakens. Conversely, at very low NIR powers, its impact on the emission count is minimal, and becomes even less significant as the 975 nm beam intensity increases. This leads us to important conclusions.

As the power of the 975 nm beam *increases*, the relative influence of the NIR beam on the emission intensity *diminishes*—even though the NIR beam remains crucial to the overall effect, its contribution follows a distinctly *sublinear* trend.

Let us briefly summarize: the effect[19] depends on the power of the NIR beam in a sublinear manner, while its influence is further diminished by the increasing power of the 975 nm beam. At the same time, the overall emission intensity is strongly governed by the power of the 975 nm beam—each curve appears elevated with increasing 975 nm power. This is not surprising either, as the 975 nm beam alone produces a measurable emission; thus, when its power increases, the observed enhancement begins from a higher baseline count level.

19: The effect: the **surplus**—an excess emission that arises uniquely under co-excitation. And while at this point it may still seem like a somewhat intangible concept—we are, after all, dealing with overall emission intensity—it already begins to emerge unmistakably, making its presence impossible to ignore.

In essence, increasing the 975 nm beam power leads to a *higher* overall emission intensity but *reduces* the surplus effect observed during co-excitation with the NIR beam.

We arrive here at an important realization: if the goal is to maximize the observed enhancement effect—not merely the total emission intensity—then the power of the 975 nm beam should be kept low. In the experiments presented, the 975 nm beam power started at 10 mW. These results alone provide strong motivation to extend the measurement range even further.[20] However, before proceeding with such efforts, a complete analysis must be carried out to approach future experiments as methodically as possible.

20: Some clarity can already be offered—a fuller explanation awaits in Section 3.5.

It is therefore useful to revisit the same dataset, but now plotted as a function of 975 nm beam power. These data are shown on linear scales in Figs. 3.8b and 3.8d, and in logarithmic form in Figs. 3.9c and 3.9f, corresponding to co-excitation with the 1732 nm and 1213 nm beams, respectively. As seen, the total emission intensity (but not the surplus emission) under co-excitation—when the NIR beam power is held constant—increases superlinearly with the power of the 975 nm beam. This behavior closely resembles the response observed under single-beam excitation with 975 nm, as shown earlier in Figs. 3.4 and 3.5 in Section 3.2.1. This observation allows us to further refine our earlier conclusions.

The influence of the 975 nm beam on total emission intensity—though not on the surplus emission—retains a *superlinear* character when the NIR beam power is held constant, similar to its effect in single-beam excitation.

Before moving on, we must acknowledge an organically emerging bifurcation in how the phenomena should be described. While fundamentally interconnected, total emission intensity—the overall output resulting from co-excitation—and surplus emission[21]—the excess over the sum of emission intensities produced by each beam acting individually—represent distinct metrics. It may seem like a self-fulfilling prophecy to declare that surplus emission is the more informative measure of the effect we aim to understand,[22] but to properly approach it, we must first fully grasp the origins of *total* emission intensity. This is precisely the goal of the mathematical treatment presented in the following sections.

21: Discussed in detail later in this work, in Section 3.4.

22: *Understanding* is a broad concept—it can carry a more reflective, intuitive tone, rather than a strictly mechanistic or formal one. The following discussion aims to deepen understanding in that spirit: not by deriving every step from first principles, but by providing a coherent and structured view of the observed behavior.

3.3.2 Shaping the relationship

Before we begin weaving a coherent perspective from the multitude of observations, one important disclaimer must be clearly stated.

The descriptions presented here are entirely **phenomenological**—that is, they are based on observations and general kinetic relationships, but not derived from rigorous theoretical modeling. Their primary purpose is to quantify the observed reality—without stripping it, of course, of its physical meaning.

Rigorous modeling based on kinetic equations is far from trivial when dealing with custom-made nanoparticles, whose exact parameters are, in practice, unknown. One may attempt to rely on energy levels and cross-sections reported widely in the literature, but for any given batch of

nanoparticles, these values remain approximate and uncertain. Moreover, obtaining such parameters precisely—and using them to construct a full theoretical model—is a research endeavor in its own right, one that lies outside the scope of our current goals. Here, our objective is simply to provide a meaningful description of the effect we observed.

Nonetheless, the proposed phenomenological mathematical description of total emission intensity—though far from exact and more of an approximation—is still not straightforward, as evidenced by the multitude of dependencies outlined in the previous section. That said, this should not discourage us. Instead, we should aim to bring all these observations together into a single, concise framework.

What we know—*but have yet to describe* is that the emission intensity increases sublinearly with the power of the NIR beam, when the 975 nm beam power is held constant. But how exactly does this relationship behave? That remains our unknown. A similar unknown is the observed decrease in excess emission with increasing 975 nm beam power. This reflects a shift toward the dominance of the 975 nm beam's standalone contribution—an additive component that boosts the total emission, yet simultaneously reduces the relative influence of the excess arising from the joint action of both beams.

What we do know with greater certainty—supported by previous single-excitation experiments—is that the 975 nm beam generally maintains a superlinear influence on the total emission intensity. As its power increases, so does the overall emission count. However, its presence concurrently reduces the influence of the NIR beam.

So how can this behavior be described?

We must begin with the realization that co-excitation is inherently a two-beam process involving both the 975 nm and NIR beams. However, this does not rule out individual contributions—what we observe experimentally is a composite effect. It includes the action of each beam independently, their combined interaction, and even some degree of mutual interference—where the action of each beam alone modifies their joint influence, and vice versa.

With this in mind, we now attempt to formulate a coarse, yet descriptive, mathematical expression. First of all, the mutual interplay between the two beams—which can be imagined as enabling a cooperative *climb* up the $4f$ manifolds of thulium via excitation pathways inaccessible to either beam alone—can be mathematically represented as the **product of their respective powers, each raised to an appropriate exponent**.

$$a \cdot P_{\mathrm{NIR}}^{\alpha} \cdot P_{975}^{\varphi} \tag{3.3}$$

The component described by Eq. 3.3 accounts *solely* for the cooperative effect of both beams acting together, excluding the individual contributions of each beam—though such independent excitation pathways still occur. It is also a simplified conceptual model, since excitation channels can be viewed as pathways with limited bandwidth, meaning they influence one another. The expression shown reflects only the isolated[23] cooperative contribution.

23: An adjusted form of this pure relation may—and will—prove essential when we later isolate the relative excess emission arising from co-excitation—all in due time (Section 3.4).

Before analyzing this further, we first present how each beam interacts with the sample individually—that is, how excitation can be described mathematically when the beams act separately through their characteristic pathways, as shown in Eq. 3.4.

$$E_{\mathrm{NIR}} + E_{975} = b \cdot P_{\mathrm{NIR}}^{\gamma} + c \cdot P_{975}^{\delta} \tag{3.4}$$

It looks familiar—*and rightly so*. These equations are simply the well-established models used to describe emission under single-wavelength excitation,[24] applied separately to the 975 nm and NIR beams. This separation is expressed as a **sum**, reflecting their independent contributions via excitation pathways that are accessible to each beam on its own.

24: See Section 3.2.

At this point, an important idea arises: if these terms truly represent the independent excitation contributions of the individual beams, then shouldn't their associated exponents—describing the degree of nonlinearity in the emission response—match those determined from the single-beam experiments?[25] The answer is **yes—they absolutely should**.

25: The results presented in Section 3.2 prove to be highly useful—it is worth revisiting them.

This observation marks a critical milestone in the reasoning developed here, bringing us significantly closer to completing the conceptual framework. However, the foundation must be fully laid before we can place the uppermost bricks.

As previously mentioned, the cooperative interaction within the system—described by Eq. 3.3—is pure;[26] but the independent effects of each beam may influence this interaction. To reflect this more realistically, we incorporate the *entangled* mutual interplay term by dividing the pure interplay term by expressions containing the individual beam contributions. This results in saturating power-law functions that capture the competition between excitation mechanisms—particularly the suppression of mutual interplay by the dominant influence of individual beams as their power increases—culminating in Eq. 3.5.

26: By *pure* we refer to a relationship stripped of secondary effects—akin to analyzing a single chemical reaction pathway under idealized conditions, free from competing reactions, impurities, or side processes. It captures the essence of a direct, distilled interaction.
In our context, a *purely* cooperative relationship refers specifically to the isolated effect arising from the simultaneous action of both beams—excluding any influence stemming from their individual contributions— which would otherwise result in more entangled or mixed terms.

$$E_{\mathrm{interplay}} = a \cdot \frac{P_{\mathrm{NIR}}^{\alpha}}{m + n \cdot P_{\mathrm{NIR}}^{\gamma}} \cdot \frac{P_{975}^{\varphi}}{q + r \cdot P_{975}^{\delta}} \tag{3.5}$$

Just as the sigmoid-like growth with saturation captures the tension between the mutual interplay term and its *eventual* erosion under increasing beam power—it also burdens the model with considerable structural complexity. And yet, the very observations that gave rise to this intricacy offer a path toward its elegant reduction.

It is important to recall that the NIR beam alone generates nearly no measurable emission; its effect emerges only under co-excitation. As a result, its role in competing with the mutual interplay mechanism is negligible. This allows for a simplification of the first term.

$$\frac{P_{\mathrm{NIR}}^{\alpha}}{m + n \cdot P_{\mathrm{NIR}}^{\gamma}} \approx \frac{P_{\mathrm{NIR}}^{\alpha}}{m} \tag{3.6}$$

Here, the constant m is incorporated into the overall prefactor of the main expression.

In contrast, while the 975 nm beam is essential for initiating the mutual interplay, its dominant contribution is evident from the outset. This justifies a distinct simplification of the second term, reflecting its different asymptotic behavior.[27]

$$\frac{P_{975}^{\varphi}}{q + r \cdot P_{975}^{\delta}} \approx \frac{P_{975}^{\omega}}{r} \tag{3.7}$$

In Eq. 3.7, ω reflects the effective exponent after simplification, and r is likewise absorbed into the overall prefactor.

Let us pause here for a moment and ask a very important question—**what if our assumptions are wrong?** What if, in reality, the erosion of the interplay term is much weaker—and even for the 975 nm beam, the dependence reduces simply to a power-law with exponent φ? What if representing the full relationship as initially sigmoidal is, in fact, an overreach?

Fortunately, the answer is clear—**it changes nothing in the final outcome**. As long as one key condition holds—*that we are not traversing between regimes*—then at either extreme, the power dependence for each beam reduces to a basic power-law relationship, with an effective exponent.

It is therefore worth acknowledging that our considerations may indeed overstate the complexity of the system we aim to describe—and that we might, in seeking to represent it, arrive at the correct form by a path not entirely true to its physical simplicity. But what matters most is that we are aware of this.[28] Ultimately, it is the final structure of the expression that takes precedence.

Because—*regardless of the path*—what remains is a streamlined and manageable expression: a re-embodiment of the pure relationship[29] previously introduced as Eq. 3.3, now presented in Eq. 3.8.

$$E_{\text{interplay}} \approx A \cdot P_{\text{NIR}}^{\alpha} \cdot P_{975}^{\omega} \tag{3.8}$$

Thus, we arrive at the conclusion—an overall, approximate description of the total emission intensity ($E_{\text{co-ex}}$) as a function of the excitation beam powers during co-excitation should include a term representing mutual interplay, entangled with the individual contributions of each beam ($E_{\text{interplay}}$), as well as independent terms accounting for their separate effects ($E_{\text{NIR}} + E_{975}$). This leads us to the sum of Eq. 3.4 and 3.8, presented as Eq. 3.9.

$$\begin{aligned} E_{\text{co-ex}} &= E_{\text{interplay}} + E_{\text{NIR}} + E_{975} = \\ &= A \cdot P_{\text{NIR}}^{\alpha} \cdot P_{975}^{\omega} + b \cdot P_{\text{NIR}}^{\gamma} + c \cdot P_{975}^{\delta} \end{aligned} \tag{3.9}$$

The proposed relationship captures all insights *distilled* from observation—without yet introducing any predefined numerical values. An important strength of this formulation lies in its physical consistency: when one of the beams is turned off, the model inherently yields an emission intensity determined solely by the remaining beam[30]—exactly as it must. While it is *certainly* neither exact nor exhaustive, the only way to assess its validity and applicability is by putting it to the test through data fitting.

27: It is important to note that—if our assumptions are true—this approximation should not hold at very low powers of the 975 nm beam—which we are not *yet* considering. Additionally, the exponent δ (see Section 3.2.1) itself depends on power, meaning that the resulting effective exponent may exhibit additional variation beyond its intrinsic variability.

28: It is, after all, a **phenomenological** argument. Even if its formulation is grounded in realistic assumptions, that does not alter its fundamental nature. It is of utmost importance to keep this in mind.

29: And as the sobering remark above indirectly suggests—perhaps it is this fundamental relationship (Eqs. 3.3 and 3.8) that more accurately reflects reality than the proposed (and later simplified) form incorporating saturation (Eq. 3.5). Nonetheless, it was deemed necessary to include a formulation that accounts for potential saturation, as the bandwidth of cooperative mechanism pathways must, in principle, depend on the power of the individual beams—even if, in the regimes considered here, this dependence may in fact be negligible and reduce once again to a simple power-law relationship.

30: Let, for example, $P_{\text{NIR}} = 0$. In this case, Eq. 3.9 simplifies to $E = c \cdot P_{975}^{\delta}$, where this expression—by definition (see Eq. 3.4)—describes the emission behavior driven solely by the remaining 975 nm beam.

Fitting the functional form

Let us begin by considering our limitations.

The number of free parameters in the proposed equation is considerable, and we aim to avoid restricting them unless absolutely necessary. Our primary goal is to establish the functional dependence of the emission intensity on the power of the NIR and 975 nm beams, with particular focus on their mutual interplay—that is, the exclusive effect that arises only under co-excitation.

As previously discussed, the power-law exponents of the individual excitation terms—those corresponding to pathways accessible by each beam independently (without influence from the other)—should be present in the model. Importantly, these terms should exhibit the same or at least comparable degrees of nonlinearity as observed in the single-beam experiments.

This would significantly simplify our task. To that end, we refer back to Section 3.2, where well-defined and *stable* fit parameters were obtained for single-beam excitation experiments using the NIR beams (1213 nm and 1732 nm) and the 975 nm beam.[31] We therefore restate them here and compare them directly with the explicitly defined exponents in Eq. 3.9.

31: What we primarily refer to is the degree of nonlinearity—specifically, the exponent ξ in the expression $a \cdot P^{\xi}$ (see Eq. 3.2)—which remains constant within specific regimes of excitation power.

$$\xi_{1213} = \gamma_{1213} = \mathbf{1.75}(1) \tag{3.10}$$

$$\xi_{1732} = \gamma_{1732} = \mathbf{1.58}(4) \tag{3.11}$$

$$\xi_{975} = \delta = \mathbf{1.94}(1) \tag{3.12}$$

32: See Section 3.2.

However, a critical consideration remains: The fitted nonlinear exponents were constant and reliable only within specific power regimes.[32] For the NIR beams, this applied to higher powers (above 50 mW), although deviations at lower powers were not dramatic. In contrast, for the 975 nm beam, this limitation was decisive—the reported value is valid only in the low-power regime (below 50 mW).

So there they are—our limitations, at least for now. We must constrain ourselves to the defined power ranges: higher powers for the NIR beams and lower powers for the 975 nm beam. Within these regimes, we apply the previously determined exponent values from Equations 3.10, 3.11 and 3.12 directly into the appropriate terms of our model equation. All remaining parameters remain unknown and completely free.

Importantly, we do not set or constrain any prefactors. Imposing limits on the prefactors could distort the fitting, and directly inserting their previously fitted values has no physical justification—while we assume constant nonlinearity for the individual contributions, we do not assume a fixed magnitude of their influence.

33: Just as was done in Section 3.2, where it was clearly shown that the prefactor for the NIR-induced emission was several hundred to even a thousand times smaller than that for the 975 nm excitation. This was evident in the emission count levels recorded at the same excitation power.

Moreover—and this is crucial for clarity—we *deliberately omit the presentation of the prefactors*. While the obtained values were physically reasonable, including them would obscure the key information: **the nonlinearities**. Our focus remains on the relationship between the powers.[33]

The formulation begins as follows.

$$E_{\text{co-ex}} = A \cdot P_{\text{NIR}}^{\alpha} \cdot P_{975}^{\omega} + b \cdot P_{\text{NIR}}^{(1.75\backslash 1.58)} + c \cdot P_{975}^{1.94} \tag{3.13}$$

And through fitting, we ultimately arrive at our results—for co-excitation with 1213 and 1732 nm beams, respectively.

$$P_{1213}^{\mathbf{0.77}(5)} \cdot P_{975}^{\mathbf{0.62}(2)} \tag{3.14}$$

$$P_{1732}^{\mathbf{0.64}(4)} \cdot P_{975}^{\mathbf{0.67}(2)} \tag{3.15}$$

The fitted function (2D surface) is shown in Fig. 3.10—note the limited number of data points, in accordance with the power range constraints applied in the analysis. As shown, the entangled co-excitation term is influenced constructively by both beams—albeit sublinearly—which reflects the real contribution of each beam—regardless of whether it is intrinsic or combined.[34]

More importantly, although the 975 nm beam is essential to enable the co-excitation process, with its increasing power it rapidly dominates the excitation pathways. This not only obscures the co-excitation effect but ultimately dominates the overall emission. Its prefactor (denoted as c in Eq. 3.13) is larger than that of the co-excitation term (denoted A in Eq. 3.13), and significantly greater than that of the NIR beam alone (denoted b in Eq. 3.13). This last observation had also emerged from the single-beam experiments.[35]

From the final point arises a useful simplification of the full equation,[36] and from the first—an obvious but important conclusion. As the power of the 975 nm beam increases, the overall emission intensity increases as well—without exception.

To maintain clarity—co-excitation reveals two distinct power trends.

34: As discussed just before the derivation of the mutual interplay term (Eq. 3.8), the exponents describing the behavior of the beams may—but do not necessarily have to—be interpreted as effective exponents. Effective, in this context, meaning they result from a combined influence that has been simplified to a single exponent, rather than representing an intrinsic property of the system. However, in our specific case—focused on the behavior of thulium-doped nanoparticles—we are primarily interested in the final exponents, which are positive and reflect the net influence of both beams on the co-excitation process. This influence, notably, remains sublinear.

35: See Section 3.2.

36: This idea is further developed—see Eq. 3.17.

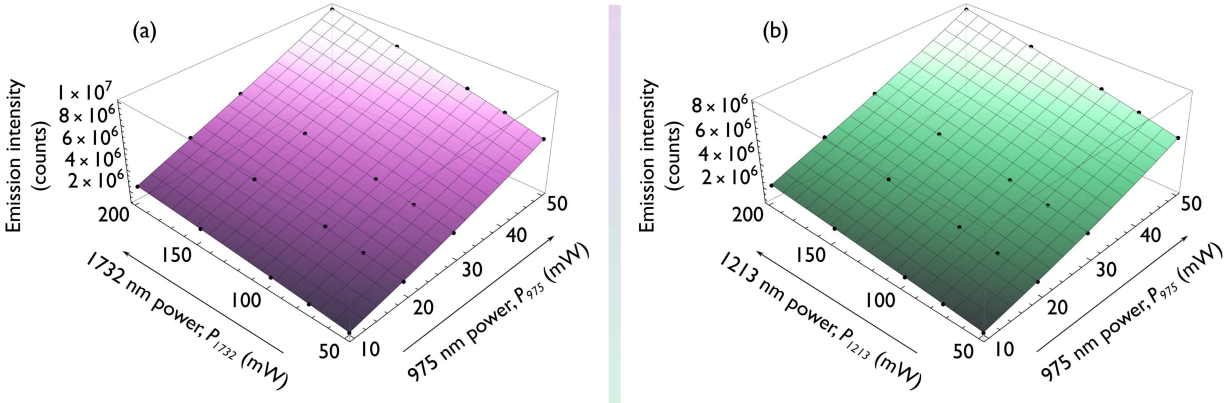

Figure 3.10: Total emission intensity recorded under co-excitation with 975 nm and NIR beams, plotted as a function of the power of each beam (black data points), along with a fitted power-law surface (2D fit, Eq. 3.9). The data included in the fitting and shown here are restricted to cases where the 975 nm beam power does not exceed 50 mW, and the NIR beam power is above 50 mW. **(a)** Co-excitation with a 1732 nm beam—black points represent measured values, while the violet surface corresponds to the fitted function. **(b)** Co-excitation with a 1213 nm beam—black points represent measured values, and the green surface shows the corresponding fit.

- **Interplay term** (co-excitation)—its relative contribution to the total emission *decreases* with rising 975 nm power, due to the growing dominance of the single-beam 975 nm term. However, the interplay component itself *increases* sublinearly with the power of both excitation beams.
- **Total emission**—the overall light output increases *superlinearly* with 975 nm power, primarily due to its standalone contribution, and rises *sublinearly* with increasing NIR power—reflecting the effect of co-excitation, as the standalone NIR term remains negligible.

These opposing behaviors highlight how a stronger 975 nm beam boosts the absolute signal yet steadily erodes the relative impact of the NIR-driven pathway.

Is there a simpler way?

A short and honest answer: **yes**—but this conclusion comes only after fitting the co-excitation data, as relying solely on single-beam measurements is insufficient (even if ultimately accurate). Based on the previously established observation that the contribution from the 975 nm beam (c in Eq. 3.13) far exceeds that of the NIR beam (b in Eq. 3.13), it is possible to simplify Eq 3.9. This simplification is presented in Eq. 3.16.

$$\begin{aligned} b \ll c \implies b \cdot P_{\mathrm{NIR}}^{\gamma} \ll c \cdot P_{975}^{\delta} \\ \implies \left(b \cdot P_{\mathrm{NIR}}^{\gamma} + c \cdot P_{975}^{\delta}\right) \approx c \cdot P_{975}^{\delta} \end{aligned} \tag{3.16}$$

As a result, we arrive at the final, reduced form of the co-excitation equation—Eq. 3.17.

$$\begin{aligned} E_{\mathrm{co-ex}} = A \cdot P_{\mathrm{NIR}}^{\alpha} \cdot P_{975}^{\omega} + c \cdot P_{975}^{\delta} = \\ = A \cdot P_{\mathrm{NIR}}^{\alpha} \cdot P_{975}^{\omega} + c \cdot P_{975}^{1.94} \end{aligned} \tag{3.17}$$

This simplification is not a minor adjustment. While the fitting constraint for the 975 nm beam power range still holds, the term associated with direct NIR beam excitation has been removed. This term was previously subject to validity only within the high-power regime. Does this mean the constraint no longer applies? It certainly still holds for the standalone contribution of the NIR beam. However, that contribution is so negligible across the entire range of measured powers that the corresponding term in the model can be omitted without measurable impact—hence, the fitting results without the data constraint on the NIR beam remain robust and largely consistent.

The results of the fits based on the simplified model[37] (Eq. 3.17), using the restricted power ranges (up to 50 mW for the 975 nm beam and above 50 mW for the NIR beam), are presented in Eqs. 3.18 and 3.19 for the 1213 nm and 1732 nm beams, respectively.

37: When compared to the values obtained using the full (unsimplified) equation (Eqs. 3.14 and 3.15): $P_{1213}^{\mathbf{0.77}(5)} \cdot P_{975}^{\mathbf{0.62}(2)}$ for 1213 nm, and $P_{1732}^{\mathbf{0.64}(4)} \cdot P_{975}^{\mathbf{0.67}(2)}$ for 1732 nm—the results are nearly identical.

$$P_{1213}^{\mathbf{0.71}(2)} \cdot P_{975}^{\mathbf{0.64}(2)} \tag{3.18}$$

$$P_{1732}^{\mathbf{0.62}(2)} \cdot P_{975}^{\mathbf{0.68}(2)} \tag{3.19}$$

Additionally, the results of fits using the simplified model (Eq. 3.17)—now including *the full range of measured NIR beam powers*, while maintaining the earlier constraint of including only data with 975 nm excitation powers up to 50 mW—are shown in Eqs. 3.20 and 3.21. These apply to co-excitation with the 975 + 1213 nm and 975 + 1732 nm beam combinations, respectively. The related experimental data and fitted surfaces are presented in Fig. 3.11.

$$P_{1213}^{\mathbf{0.77}(1)} \cdot P_{975}^{\mathbf{0.60}(1)} \tag{3.20}$$

$$P_{1732}^{\mathbf{0.69}(1)} \cdot P_{975}^{\mathbf{0.63}(1)} \tag{3.21}$$

The fit results obtained across the full measurement range of NIR beam powers (Eqs. 3.20 and 3.21) are slightly higher but remain close to previous values and fully support the conclusions already drawn from the observed (and fitted) dependence of emission intensity on the individual beam powers.

But the story doesn't end here.

In all presented fittings and analyses, the exponent for the 975 nm beam in the term corresponding to its independent contribution (parameter δ in Eq. 3.9) was fixed at **1.94**(1), a value derived from single-beam measurements.[38] This value was then implemented in the fits for the co-excitation experiments, as shown in Eq. 3.13. Subsequent analysis demonstrated, however, that the fits could be limited to just the mixed (co-excitation) term and the independent contribution of the 975 nm beam—the standalone contribution of the NIR beam could be omitted,

38: See Section 3.2.1.

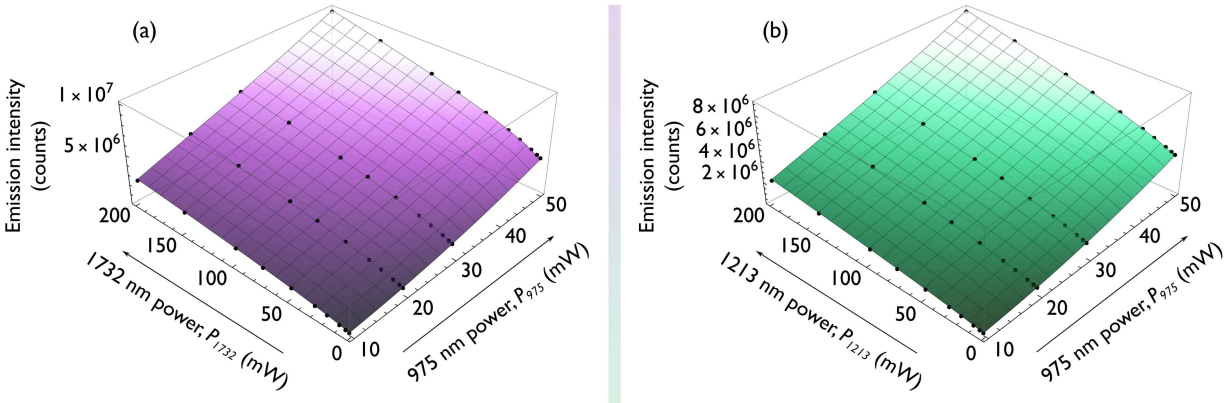

Figure 3.11: Total emission intensity recorded under co-excitation with 975 nm and NIR beams, shown as a function of the power of each beam (black data points), along with a fitted power-law surface (2D fit, Eq. 3.17). **All available NIR beam powers were included**, while the 975 nm beam power was limited to values not exceeding 50 mW. **(a)** Co-excitation with a 1732 nm beam—black points represent measured values; the violet surface corresponds to the fitted function. **(b)** Co-excitation with a 1213 nm beam—black points represent measured values; the green surface shows the corresponding fit.

as illustrated in Eq. 3.17. This equation was already used in fittings and proved to be fully adequate.

This raised a natural question: with the number of parameters already reduced, why not also allow the exponent for the 975 nm beam's independent contribution to vary?

That is precisely what we did. The previously fixed exponent of **1.94**(1), derived from single-beam measurements, was now allowed to vary in the fitting of Eq. 3.17. Under identical power ranges—975 nm beam limited to 50 mW, no restrictions on NIR beam power—the resulting exponents were **1.95**(3) and **1.99**(5) for the 1213 nm and 1732 nm beams, respectively. The remaining parameters (exponents in the mixed term) remained nearly unchanged. Fig. 3.12 illustrates how the fitted surfaces align with the corresponding experimental data.

Beyond serving as a confirmation of the single-beam experiments—where obtaining a consistent value in a completely unconstrained fit reproduces the result derived experimentally from entirely different measurements—this outcome stands as a strong endorsement of the proposed and postulated model.

The fitted parameters align fully with prior observations and assumptions. The total emission under co-excitation consists of two components: independent contributions from each beam—of which only the standalone 975 nm term is substantial, rising *superlinearly* with power in agreement with single-beam excitation results—and a cooperative term, which increases *sublinearly* with the power of both beams but whose relative impact decreases as the 975 nm power grows.

This interplay defines the total emission intensity: due to the intertwined structure of the model (Eqs. 3.9 and 3.17), **the total emission continues to rise superlinearly with increasing 975 nm power**—even though one component, the joint term, actually rises sublinearly. This brings to a close our analysis of how total emission intensity depends on excitation

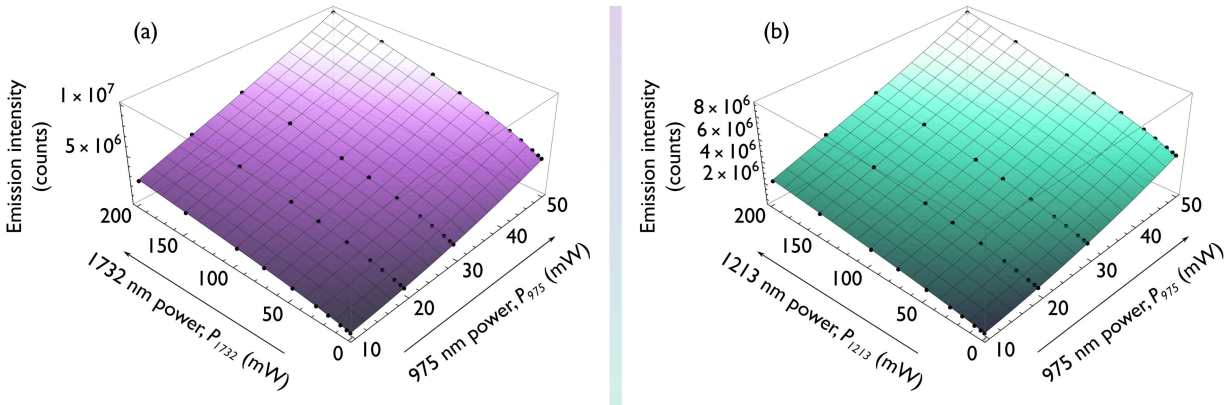

Figure 3.12: Total emission intensity under co-excitation with 975 nm and NIR beams, shown as a function of each beam's power (black data points), along with a fitted power-law surface (2D fit, Eq. 3.17, **with no fixed exponents**). All available NIR beam powers were included; the 975 nm beam power was limited to a maximum of 50 mW. **(a)** Co-excitation with a 1732 nm beam—black points represent measured values; the violet surface shows the fitted function. **(b)** Co-excitation with a 1213 nm beam—black points represent measured values; the green surface shows the corresponding fit.

power in co-excitation experiments. Its behavior has been documented with precision—its rise under co-excitation is, without exaggeration, extraordinary.

But just *how* extraordinary? Paradoxically, the comprehensive view obscures rather than reveals it. Here, the so-called full picture draws attention away from what matters most. From what *is*—and what we never expected. **The surplus.**

3.4 *Surplus emission* under dual-wavelength co-excitation

The totality is not, as it were, a mere heap, but the whole is something besides the parts.

39: Aristotle, *Metaphysics*, VIII, 1045a, 8-10.

Guided by this idea,[39] we now arrive at the point that has been *not-so-quietly* emerging from the data all along. Even when our focus was squarely on total emission intensity, it was impossible not to notice:

> Introducing an NIR beam—one that, on its own, contributes *minimally*—alongside the signal-producing 975 nm beam consistently leads to a striking increase in emission—a **surplus** relative to the effect of either beam alone.

40: See Section 3.1.1.

41: 10 mW for the 975 nm beam and 100 mW for the NIR beam, see Fig. 3.1.

Following our analysis of the total photon count—which incorporates the complex interplay of all excitation beams, as captured in the proposed model (Eqs. 3.13 and 3.17)—the moment has come to focus solely on this enhancement effect. This surplus was introduced early on;[40] indeed, Fig. 3.1 already showed that, for arbitrarily chosen beam powers,[41] this strategy yields a **significant enhancement** in upconverted emission, often surpassing **several hundred percent** relative to single-wavelength excitation. Its mathematical definition is formalized in Eq. 3.1, which is worth recalling here.

$$S_\lambda = \frac{E_{\text{co-ex}}(\lambda) - (E_{\text{NIR}}(\lambda) + E_{975})}{E_{\text{NIR}}(\lambda) + E_{975}} \cdot 100\%.$$

In this expression, $E_{\text{co-ex}}(\lambda)$ represents the emission intensity at 800 nm observed under simultaneous excitation with both beams. E_{NIR} and E_{975} denote the emission intensities resulting from excitation with only the NIR beam and only the 975 nm beam, respectively. The parameter λ (nm) specifies the NIR beam wavelength used during the measurement.

This definition means that the surplus isolates the portion of the total emission arising from the cooperative interaction between the two beams—i.e., photophysical pathways that are either entirely inaccessible—or at least not comparably active—under individual excitation alone. We already know that this enhancement can reach remarkable levels—far exceeding the effects induced by either beam independently. But what *governs* it?

3.4.1 *From input to excess* —surplus emission as a function of power

The answer is simple—sheer *power* of the input beams. The more challenging question, however, is *how*? This calls for a careful analysis.

42: See Section 3.3.

The investigation was conducted over the same power ranges as the total emission intensity analysis, since both are based on the same dataset.[42] To recall: the 975 nm beam power ranged from 10 to 200 mW, while the NIR beam power spanned 2 to 200 mW. Is this range sufficient? The data will tell—but nothing prevents further exploration or future extension.[43]

43: A self-fulfilling prediction, as the results in Section 3.5 now make clear.

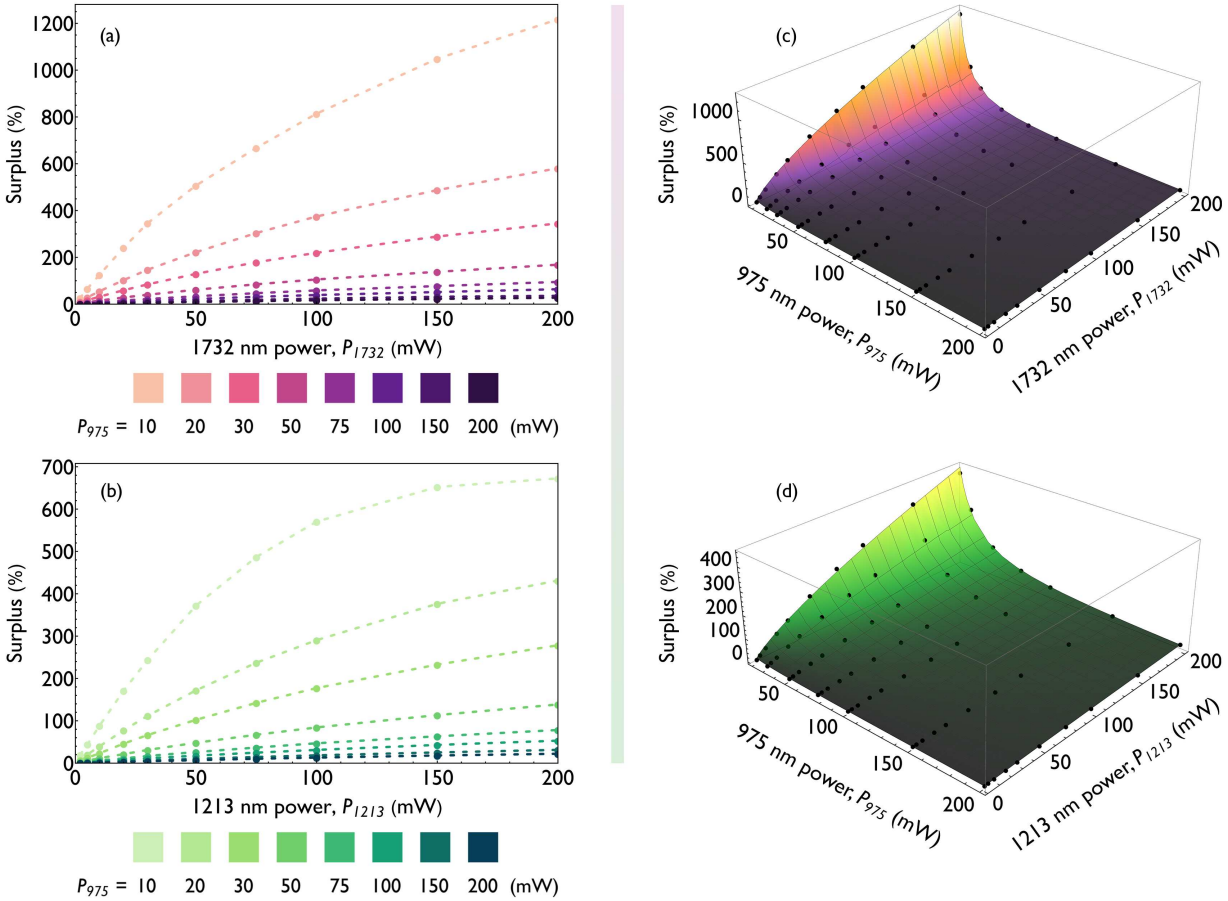

Figure 3.13: Surplus 800 nm emission from YbTm nanoparticles under co-excitation with 975 nm and NIR beams, shown as a function of NIR beam power for various power levels of the 975 nm beam. **(a)** Surplus emission under simultaneous excitation with 975 nm and 1732 nm beams, plotted against the NIR beam power. **(b)** Surplus emission under co-excitation with 975 nm and 1213 nm beams, also shown as a function of NIR beam power. Both (a) and (b) are presented on a linear scale and include results for different power levels of the 975 nm beam; dashed lines connecting individual data points are included for visual guidance. **(c)** Surplus emission under co-excitation with 975 nm and 1732 nm beams (black dots), plotted as a function of both excitation beam powers. A fitted two-dimensional power-law surface is shown in violet. **(d)** Surplus emission under co-excitation with 975 nm and 1213 nm beams (black dots), plotted as a function of both excitation beam powers, with a fitted two-dimensional power-law surface shown in green.

For now, we concentrate on the **mid-to-high** power regime.

Using Eq. 3.1, surplus values were calculated for each measurement point and are presented in Fig. 3.13a and b for the 1732 nm and 1213 nm NIR beams, respectively (log-log versions shown in Fig. 3.14). The initial impression is clear—the values are substantial, in some cases exceeding 1000% within the investigated range.

It is also clearly evident that the surplus effect diminishes with increasing power of the 975 nm beam. This trend had already been observed indirectly in the analysis of total emission intensity—where increasing 975 nm power reduced the contribution of the interplay term while increasing the overall photon count. It is worth stating this explicitly here:

As the power of the 975 nm beam increases, surplus emission *decreases*—highlighting the need to keep this power low in order to maximize the effect.

The NIR beam (either 1213 nm or 1732 nm), on the other hand, has a clearly constructive impact on the surplus emission generated via co-excitation. As previously noted, this influence is sublinear—evident in the shape of the trends traced by the data points. Thus:

> The surplus effect arising from the combination of 975 nm and NIR beams *increases* with higher NIR power—even though the NIR beam alone results in only marginal emission. This increase is characteristically *sublinear*.

As expected—and indeed, as necessary—the observations made earlier in the analysis of the interplay component in total emission intensity reappear here, only now with far greater clarity.

What emerges more distinctly in the context of surplus emission is the prominent role of the 1732 nm beam. This is particularly striking given that excitation at 1732 nm alone produces nearly no measurable emission—unlike the 1213 nm beam, which yields a weak but detectable signal.[44] **And yet, it is the 1732 nm beam that most effectively gives rise to the observed surplus effect**.

44: The mechanistic differences between single excitation by the 1213 nm and 1732 nm beams are discussed in detail in Section 3.1.2, and experimentally examined in Section 3.2.2.

45: See Section 3.1.2, with reference to the energy level diagrams shown in Figs. 3.1 and 3.2.

The underlying mechanism lies in the excitation pathways activated under co-excitation.[45] The 1732 nm beam directly populates the $^3F_4$ state via ground-state absorption (GSA), enabling subsequent energy transfer upconversion (ETU). In contrast, the 1213 nm beam populates the $^3F_4$ state indirectly—via GSA to the $^3H_5$ level, followed by non-radiative relaxation.

> Crucially, under 1732 nm excitation, excited-state absorption (ESA) from the $^3H_5$ level does not depopulate the $^3F_4$ state. This permits concurrent and efficient ESA (from $^3H_5$) and ETU (from $^3F_4$). While similar cooperation is possible with the 1213 nm beam, it originates from the same $^3F_4$ state—rendering the interaction inherently more competitive.

This represents the most important observation derived exclusively from the analysis of surplus emission—from this point onward, the 1732 nm beam will become the focal point of our investigation, both in deeper mechanistic analysis and in potential applications. Yet before we proceed, all these qualitative findings require a quantitative formulation.

Surplus, quantified

The mathematical analysis of the surplus effect was approached from multiple angles, initially without imposing any power constraints—on the assumption that such limitations would be introduced only if necessary. Yet the prologue had barely begun when it revealed itself to be the epilogue.

Fitting the simplest formulation of the interaction between the two beams—originally introduced in Eqs. 3.3 and 3.8, and restated in a generalized form as Eq. 3.22—yielded the most consistent and accurate results.

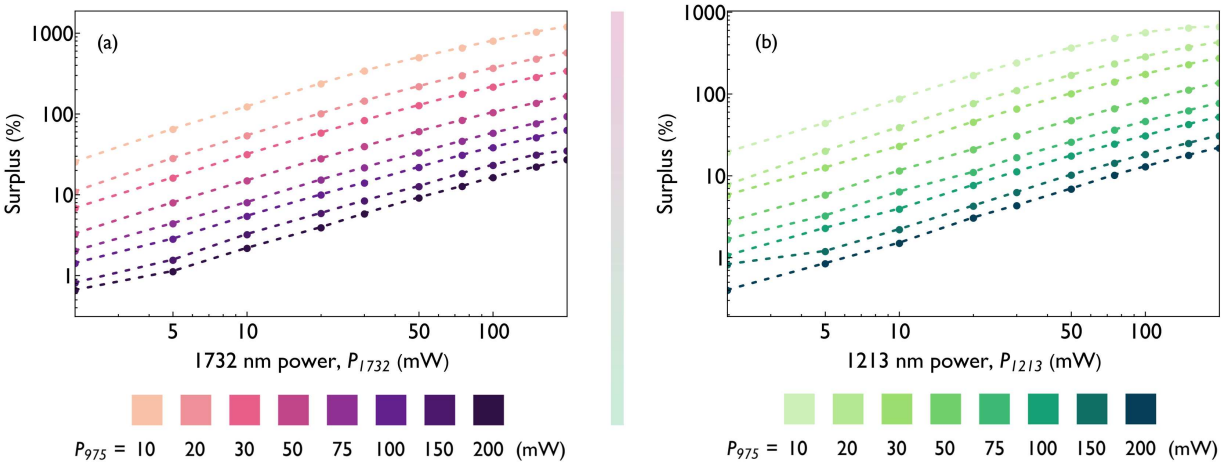

Figure 3.14: The same dataset as in Fig. 3.13 is presented here on a log-log scale. Surplus 800 nm emission from YbTm nanoparticles under co-excitation with 975 nm and NIR beams, shown as a function of NIR beam power for various fixed power levels of the 975 nm beam. **(a)** Surplus emission under simultaneous excitation with 975 nm and 1732 nm beams, plotted against NIR beam power. **(b)** Surplus emission under co-excitation with 975 nm and 1213 nm beams, likewise shown as a function of NIR beam power. Both panels include results for multiple 975 nm beam powers; dashed lines connecting individual data points are included for visual guidance.

$$S = \mathfrak{a} \cdot P_{\mathrm{NIR}}^{\alpha} \cdot P_{975}^{\beta} \tag{3.22}$$

We know this term—this mutual interplay between the two beams, this joined ascent through Tm^{3+} $4f$ manifolds via pathways inaccessible to either beam alone. Represented mathematically as the product of their respective powers, each raised to an appropriate exponent, it was the co-excitation term in the otherwise complex model describing total emission intensity.[46] And yet, it is precisely this short, simple term[47] that describes the surplus emission best—and no addition has made it better.

The fitted two-dimensional power-law surfaces—covering the full power ranges of both the 975 nm and NIR beams—were presented at the beginning of this chapter in Fig. 3.13. The corresponding fit parameters, for the 1213 nm and 1732 nm beams respectively, are given in Eqs. 3.23 and 3.24.

$$S_{1213} \propto P_{1213}^{\mathbf{0.73}(1)} \cdot P_{975}^{\mathbf{-1.30}(2)} \tag{3.23}$$

$$S_{1732} \propto P_{1732}^{\mathbf{0.69}(1)} \cdot P_{975}^{\mathbf{-1.20}(1)} \tag{3.24}$$

When compared with all previously obtained sets of fitted parameters, a striking similarity emerges: the exponent α, describing the influence of the NIR beam on the mutual interplay term, is *nearly identical*[48] across models.[49] While the exponent governing the influence of the 975 nm beam may appear significantly different, *fret not*—for as will become evident, the resulting relation is inherently tied to the cooperative term of the overall emission.

To better understand the nature of this connection, we now turn to the integration of the surplus emission model with the one describing total emission intensity. This begins with the formal definition of surplus emission (Eq. 3.1), which we restate in a simplified form in Eq. 3.25.

46: See Eq. 3.9.

47: Importantly, the proposed mathematical form—being fully **multiplicative**—is physically meaningful: in the absence of either excitation beam, the surplus *cannot* exist, and therefore its value is zero.

48: Compare results from Eqs. 3.14 and 3.15; Eqs. 3.18 and 3.19; and Eqs. 3.20 and 3.21.

49: This is precisely why the same symbol α is retained in the current formulation—a theoretical justification will follow shortly.

$$\begin{aligned} S_\lambda &= \frac{E_{\text{co-ex}}(\lambda) - (E_{\text{NIR}}(\lambda) + E_{975})}{E_{\text{NIR}}(\lambda) + E_{975}} \cdot 100\% \\ \Longrightarrow S &= \frac{E_{\text{co-ex}} - (E_{\text{NIR}} + E_{975})}{E_{\text{NIR}} + E_{975}} \cdot 100\% \end{aligned} \tag{3.25}$$

Next, we substitute into this expression the respective dependencies on power—from the independent contributions of each beam (previously described functionally and defined explicitly in Eq. 3.4) to their combined effect, as proposed in the composite model (Eq. 3.9).

$$\begin{aligned} S &= \frac{\left(A \cdot P_{\text{NIR}}^{\alpha} \cdot P_{975}^{\omega} + b \cdot P_{\text{NIR}}^{\gamma} + c \cdot P_{975}^{\delta}\right) - \left(b \cdot P_{\text{NIR}}^{\gamma} + c \cdot P_{975}^{\delta}\right)}{\left(b \cdot P_{\text{NIR}}^{\gamma} + c \cdot P_{975}^{\delta}\right)} \cdot 100\% = \\ &= \frac{A \cdot P_{\text{NIR}}^{\alpha} \cdot P_{975}^{\omega}}{\left(b \cdot P_{\text{NIR}}^{\gamma} + c \cdot P_{975}^{\delta}\right)} \cdot 100\% = \\ &= \frac{\mathscr{A} \cdot P_{\text{NIR}}^{\alpha} \cdot P_{975}^{\omega}}{\left(b \cdot P_{\text{NIR}}^{\gamma} + c \cdot P_{975}^{\delta}\right)} \end{aligned} \tag{3.26}$$

This is not yet the final form.

As has been demonstrated repeatedly, the independent contribution of the NIR beam is minimal—especially when contrasted with the far more dominant role of the 975 nm excitation.[50] It is equally valid here. Thus, the denominator in Eq 3.26 can be reduced to a function solely of the 975 nm power, paving the way to a final and compact formulation.

50: This assumption has already been applied in earlier modeling; see Eqs. 3.16 and 3.17.

It turns out that when the surplus expression is extracted from the full emission model, only a single term remains: *the mutual dance between the beams*.

$$S \approx \frac{\mathscr{A} \cdot P_{\text{NIR}}^{\alpha} \cdot P_{975}^{\omega}}{c \cdot P_{975}^{\delta}} = \mathfrak{a} \cdot P_{\text{NIR}}^{\alpha} \cdot P_{975}^{\beta} \tag{3.27}$$

In this expression, the exponent α reflects the intrinsic influence of the NIR beam on the cooperative interplay. The exponent β, in turn, represents an effective exponent—capturing the relative contribution of the 975 nm beam to the surplus emission. It is defined as the ratio between the cooperative influence of the 975 nm beam[51] and its standalone effect on the emission yield, in keeping with the definition of the surplus phenomenon.

51: Previously denoted as ω, see Eqs. 3.8 and 3.9.

This interpretation is not only conceptually consistent—it is numerically precise. The previously established value of α holds. Meanwhile, β emerges naturally as the difference between the 975 nm beam's cooperative exponent and its standalone exponent.[52] The alignment is exact, and the structure of the model converges seamlessly—*it all falls together*.

52: Specifically, $\beta = \omega - \delta$, where $\delta = 1.94$—a value that slightly decreases at higher excitation powers; see Section 3.2.1. The cooperative exponent ω ranges from 0.59 to 0.67; see results from Eqs. 3.14 and 3.15; Eqs. 3.18 and 3.19; and Eqs. 3.20 and 3.21. *A perfect match.*

In this way, the complex relationship modeling total emission intensity under co-excitation condenses into an elegant and intuitive distilled expression—one that describes only the observed excess: *the surplus itself*.

Chaos, contained.

Let us condense the findings to consider what the fitted relationship and general observations reveal.

Surplus emission depends *solely* on the product of the beam powers—each raised to an appropriate exponent—and quantifies how strongly co-excitation enhances the emission **beyond** what either beam can achieve alone. It grows sublinearly with NIR power, but falls as 975 nm power increases. Maximizing it demands *low* 975 nm input—with the strongest effects seen under *1732 nm co-excitation*.

Considering the conclusions drawn from the preceding analysis, it is evident that the striking magnitude of the surplus effect is not fully realized when both beams—particularly the primary 975 nm beam—are operated at moderate power levels. As shown in Eqs. 3.23 and 3.24, lowering the 975 nm power results in a substantial enhancement of the surplus emission.

This leads to a natural conclusion: it is time to extend the analysis to include lower 975 nm power levels.

3.5 *When less is more* —exploring the low-power regime

Our motivation is clear—in search of enhanced surplus emission, we explore the depths of low 975 nm beam powers, anticipating—based on the trend captured in Eq. 3.22, where the surplus diminishes as 975 nm power increases—an explosive amplification of the effect, even if relative to an overall lower emission level. And without embellishment—that is precisely what we observe. But that is not all. We have entered a regime where *less* does not simply mean *more*—it means *immeasurably* more.

3.5.1 At the edge of absence

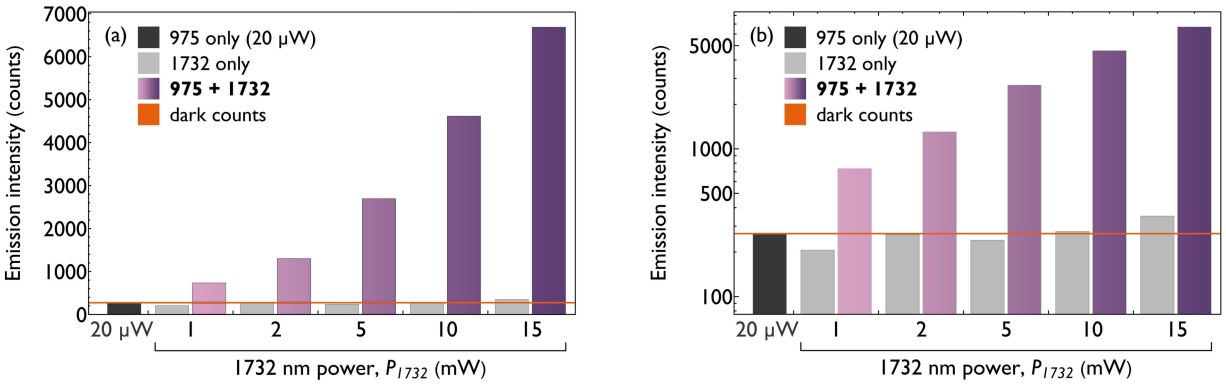

Figure 3.15: Analysis of 800 nm emission intensity under co-excitation with a **weak** 975 nm beam (20 μW) and a 1732 nm beam (purple bars), collected across a **low range** of 1732 nm beam powers. Dark gray bars indicate emission under excitation with the 975 nm beam alone; light gray bars represent excitation with the 1732 nm beam alone. The orange line shows the dark count level. **(a)** Results for the **lowest** 975 nm beam power (20 μW). **(b)** Same data as in (a), shown on a log-log scale. Emission counts are presented in their raw form (without subtracting the dark count level, which is indicated in each graph), and the dark counts were measured separately for each experiment. The fluctuations in counts observed under excitation with the 1732 nm beam alone at the given power levels result from the *absence of actual emission* and variations in the dark count level.

In pursuit of the highest surplus emission, we lowered the excitation powers to levels at which neither beam, on its own, produced any measurable signal. This is not difficult to achieve for the 1732 nm beam—due to the nature of its interaction with Tm^{3+} $4f$ manifolds, it does not generate significant 800 nm emission. In our setup,[53] no detectable signal is observed from this beam alone until its power exceeds approximately 15 mW.

53: See Section 2.2.

The 975 nm beam must be attenuated significantly further—it is ideally matched to excite the Yb^{3+} sensitizer, and its influence becomes noticeable even at very low power levels. In this study, the earliest measurable contribution emerged at approximately 70 μW, marking the boundary below which the regime remains fully sub-threshold.

It is all the more remarkable that the combination of these two sub-threshold—effectively *invisible*—beams **resulted in a clearly visible, strong emission**. The results of this experiment are presented as a bar chart in Fig. 3.15.

Crucially, the observed emission cannot be mathematically described as a surplus, as **no baseline signal exists** against which a surplus can be defined. Within the framework of the mathematical formulation (Eq. 3.1),

this would imply a surplus that diverges—formally, it tends toward infinity.

This leads us to one of the most important conclusions of this work—one that deserves to be stated clearly.

Precisely tuning the power of both excitation beams can result in emission enhancements spanning **several orders of magnitude**—and even yield entirely ***de novo*** emission triggered solely by the combined presence of two individually sub-threshold beams—a ***switchable*** emission.

De novo, indeed.[54] It is therefore possible to tune the excitation beams in such a way that only their mutual cooperation leads to sufficient population of the $^3H_4$ state—the origin of the 800 nm emission.[55] In this configuration, neither independent excitation of ytterbium followed by ETU nor pumping with the low-energy beam alone is sufficient; only their combination opens the most efficient excitation pathway under the given power conditions.

54: Yet not *ex nihilo*—the input beams are present, just incapable of triggering any measurable emission on their own.

55: Photophysical pathways are discussed in detail in Section 3.1.2, with a corresponding schematic provided in Fig. 3.2.

This represents the most tangible evidence for the proposed cooperative mechanism—demonstrating a scenario in which cooperation is not just dominant, but the *only* viable route to emission.

But what about higher 975 nm beam powers—still operating near the edge, where its independent emission remains on the *order* of dark counts?

Figs. 3.16 and 3.17 present results for the threshold level (70 μW) as well as slightly higher powers (up to 150 μW), where the independent contribution of the 975 nm beam begins to emerge—though it remains exceptionally weak.

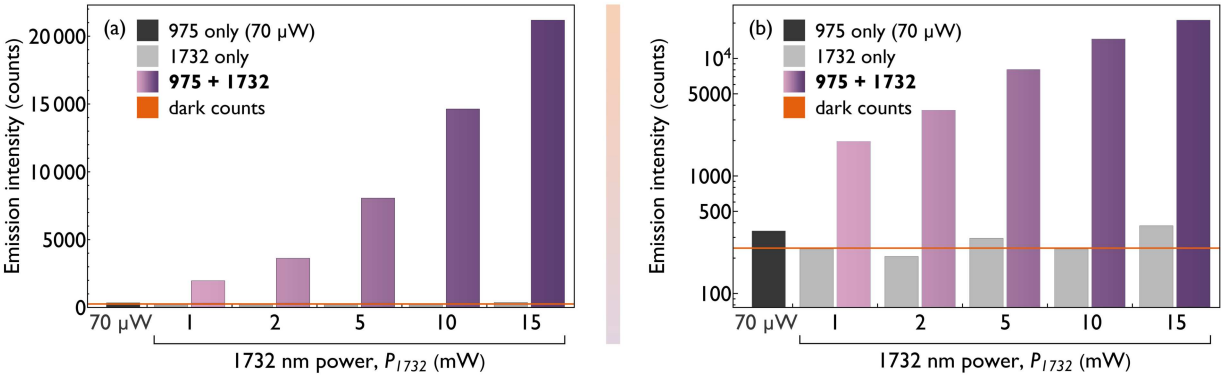

Figure 3.16: Analysis of 800 nm emission intensity under co-excitation with a **weak** 975 nm beam (70 μW) and a 1732 nm beam (purple bars), collected across a **low range** of 1732 nm beam powers. Dark gray bars indicate emission under excitation with the 975 nm beam alone; light gray bars represent excitation with the 1732 nm beam alone. The orange line shows the dark count level. **(a)** Results for the **low** 975 nm beam power (70 μW). **(b)** Same data as in (a), shown on a log-log scale. Emission counts are presented in their raw form (without subtracting the dark count level, which is indicated in each graph), and the dark counts were measured separately for each experiment. The fluctuations in counts observed under excitation with the 1732 nm beam alone at the given power levels result from the *absence of actual emission* and variations in the dark count level.

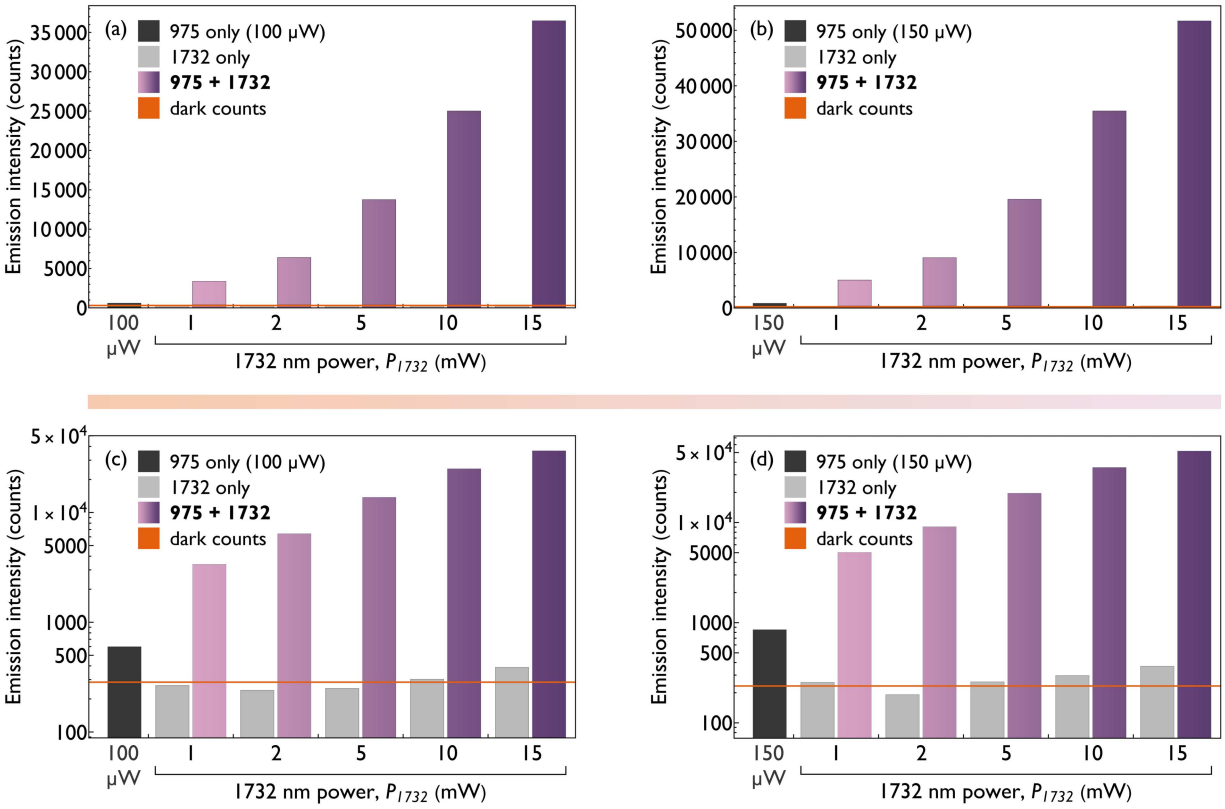

Figure 3.17: Analysis of 800 nm emission intensity under co-excitation with a **weak** 975 nm beam (100 μW or 150 μW) and a 1732 nm beam (purple bars), collected across a **low range** of 1732 nm beam powers. Dark gray bars indicate emission under excitation with the 975 nm beam alone; light gray bars represent excitation with the 1732 nm beam alone. The orange line shows the dark count level. **(a)** Results for the 975 nm beam at 100 μW **(b)** Results for the 975 nm beam at 150 μW. **(c-d)** Same data as in (a-b), shown on a log-log scale. Emission counts are presented in their raw form (without subtracting the dark count level, which is indicated in each graph), and the dark counts were measured separately for each experiment. The fluctuations in counts observed under excitation with the 1732 nm beam alone at the given power levels result from the *absence of actual emission* and variations in the dark count level.

These plots reveal the true scale of the enhancement effect: we observe remarkably strong emission under co-excitation, while the individual beams still contribute only marginally—barely above the detection threshold.

An illumination born not of strength, but of *cooperation*.

3.5.2 Interplay analysis

The low-power regime might seem, at first glance, ideally suited for analyzing mutual dependencies—after all, in this range, the cooperative interplay dominates over the contributions of the individual beams. But this assumption quickly proves misleading.

Let us begin with the fact that the analysis must be carried out on the total emission counts—not on surplus emission. In the low-power regime, calculating the surplus is impossible due to the absence of any measurable signal from the individual beams. And even as power increases and surplus becomes theoretically calculable, the result is plagued by large uncertainty, as the emission from the individual beams remains close to the level of dark counts. Still, it is worth noting that, for some of the data presented here, the calculated surplus can approach nearly **10000%**.

Returning to total emission intensity observed under co-excitation: at the lowest 975 nm powers and low 1732 nm powers, we observe the most *pure* form of interplay—where the total counts arise solely from the beams' cooperative interaction.[56] Yet this regime is left behind very quickly, especially as the power of the 975 nm beam increases, revealing additional pathways accessible to the 975 nm beam alone.[57] A similar transition may occur when the 975 nm power is held low while the 1732 nm beam is strongly increased—though in this case, the individual contribution of the NIR beam to the mechanism is expected to remain minor and largely negligible.[58] As the powers of both beams increase, we transition back toward the regime previously described in earlier sections.[59] In this sense, the low-power regime proves to be surprisingly rich in distinct photophysical extremes—arguably more so than the mid-to-low range. Although the data could, in principle, be subdivided into smaller intervals, the rapid evolution of behavior across power levels means that each subset contains too few data points to draw firm conclusions.

56: See Eq. 3.3 and accompanying commentary.

57: See the diminishing of the cooperative term in Eq. 3.5 and overall formula in Eq. 3.9.

58: This is because its independent climb through the thulium $4f$ manifolds is far less competitive with the interplay pathway than the climb enabled by the 975 nm beam.

59: For a refreshed understanding of these relationships, see Section 3.3.2.

Instead, we adopt a different approach: analyzing the complete set of measurements within the low-power regime—975 nm powers ranging from 20 to 1000 μW, and 1732 nm powers from 1 to 100 mW—while focusing exclusively on the dependence on the 1732 nm beam. The motivation is straightforward: the influence of the NIR beam represents the *novel* element in the analysis of emission behavior in upconverting nanoparticles. Additionally, restricting the analysis to a single beam significantly simplifies the overall relationship. By holding the 975 nm power constant, we can ground the power dependence of total emission in the previously derived model (Eq. 3.9), which then reduces to the simplified form shown in Eq. 3.28.

Yet the key word here is *ground*—not *apply* directly. We also modify the parameterization, particularly the term describing the influence of the 1732 nm beam on the mutual interplay. This adjustment is essential because the original model was derived from data collected at intermediate 975 nm powers, where the exponent governing the NIR beam's role in the interplay (α in the full equation) was stable and well-defined.[60]

60: While investigating 975 nm powers above 10 mW, we observed that it varied only slightly—from 0.64 to 0.69 (see the values derived in Eqs. 3.15, 3.19, 3.21, and 3.24).

In the present context, however, such stability likely holds only within individual measurement series. As the 975 nm power increases, the interplay may evolve, and the exponent itself may shift. This behavior is typical for upconverting nanoparticles, whose nonlinear emission response remains stable only within specific excitation regimes.[61]

61: As previously observed for single-beam excitation—see Section 3.2.

Since our co-excitation measurements begin in the ultra-low power regime—particularly for the 975 nm beam—and extend into medium powers, we are almost certainly traversing a regime where that nonlinearity evolves. For this reason, it is essential to recognize that parameters such as α, determined under higher-power conditions, may not apply across the full range explored here.

That is precisely why Eq. 3.28 must be reconsidered afresh in the present analysis.

$$E_{\text{co-ex}} = d \cdot P_{\text{NIR}}^{\varepsilon} + \mathfrak{b} \cdot P_{\text{NIR}}^{\gamma} + \Lambda(P_{975}) \tag{3.28}$$

In this model, the parameters related to the 975 nm beam—whose power is held constant within each measurement series but varies across series—are absorbed into the constants d and Λ, where Λ denotes the emission intensity measured under excitation by the 975 nm beam alone. Additionally, the parameter α has been replaced with ε, as the exponent governing the NIR beam's role in the interplay remains an unknown in the *uncharted waters* of the low-power regime.

Yet the model still proves too complex to reliably converge—not merely due to the number of free parameters, but because even a reasonable substitution fails to resolve it. The attempted substitution—that is, fixing the parameter at a known value—involves reusing the power-law dependence that describes the isolated influence of the 1732 nm beam (i.e., the exponent γ in Eq. 3.28), previously established in the section on its standalone emission behavior.[62] However, that parameter is only valid above several milliwatts of 1732 nm power, since no measurable emission occurs below that threshold.

And this is precisely where the core difficulty lies: a large portion of the dataset falls into the low-power regime, *where the NIR beam contributes virtually nothing on its own.*[63] This is clearly reflected in the lack of detectable emission from the 1732 nm beam alone at powers below 15 mW.[64]

Given how explicit this observation is, it is more reasonable not to start from the full equation, but rather from the simplified form—Eq. 3.17—which already incorporates this constraint (i.e., treating any individual contribution—aside from the cooperative pathway—as arising solely from the 975 nm beam[65]).

Thus, in Eq. 3.28, the term corresponding to the independent contribution of the NIR beam (i.e., $\mathfrak{b} \cdot P_{\mathrm{NIR}}^{\gamma}$) can be omitted, as it is negligibly small. This leads to Eq. 3.29, where the constant term Λ once again corresponds to the emission measured under excitation with the 975 nm beam alone. Since the analysis examines emission as a function of 1732 nm beam power—while the 975 nm power is held fixed at several discrete levels—this means that, at zero 1732 nm power, the emission arises solely from the baseline contribution of the 975 nm excitation.

$$E_{\mathrm{co-ex}} = d \cdot P_{\mathrm{NIR}}^{\varepsilon} + \Lambda(P_{975}) \tag{3.29}$$

And we *do know* the parameter Λ. For each measurement, the emission induced by the individual beams—including the standalone 975 nm beam—was recorded. Accordingly, the relevant values were incorporated into the fitting procedure (after background subtraction). It is worth noting that for the lowest 975 nm power included—20 μW—no measurable emission was observed, so the corresponding value is set to zero. The measurement results, along with the fitted functions,[66] are presented in Fig. 3.18.

What does all this tell us?

The exponent ε decreases with each fit as the baseline power of the 975 nm beam increases—from 20 to 1000 μW. Starting from an almost linear dependence on the 1732 nm beam power, the overall count rate begins to

62: See Section 3.2.2, where this parameter was established as **1.92**(9) for the low-power regime (but not too low, as the signal was only observed above several milliwatts) of the 1732 nm beam. Similar substitutions were made when modeling total emission in Section 3.3.2, but for the higher-power regime of the NIR beam—see Eq. 3.13 in that section.

63: This means that the 1732 nm beam participates in the cooperative mechanism—co-excitation—but does not induce any measurable excitation on its own.

64: Discussed throughout this work and clearly visible in Figs. 3.6, 3.7, 3.15, 3.16, and 3.17.

65: Even though at very low powers this contribution is also effectively negligible, this holds true only in the extremely low-power regime—unlike the NIR beam, whose independent contribution, as we are currently discussing, is negligible *throughout*.

66: Since we are operating in the uncharted territory of the low-power regime—where the evolution of dependencies takes place—the fittings were performed independently for each power level of the 975 nm beam. This approach allows us to observe how the value of the parameter ε, which describes the influence of the 1732 nm beam, evolves.

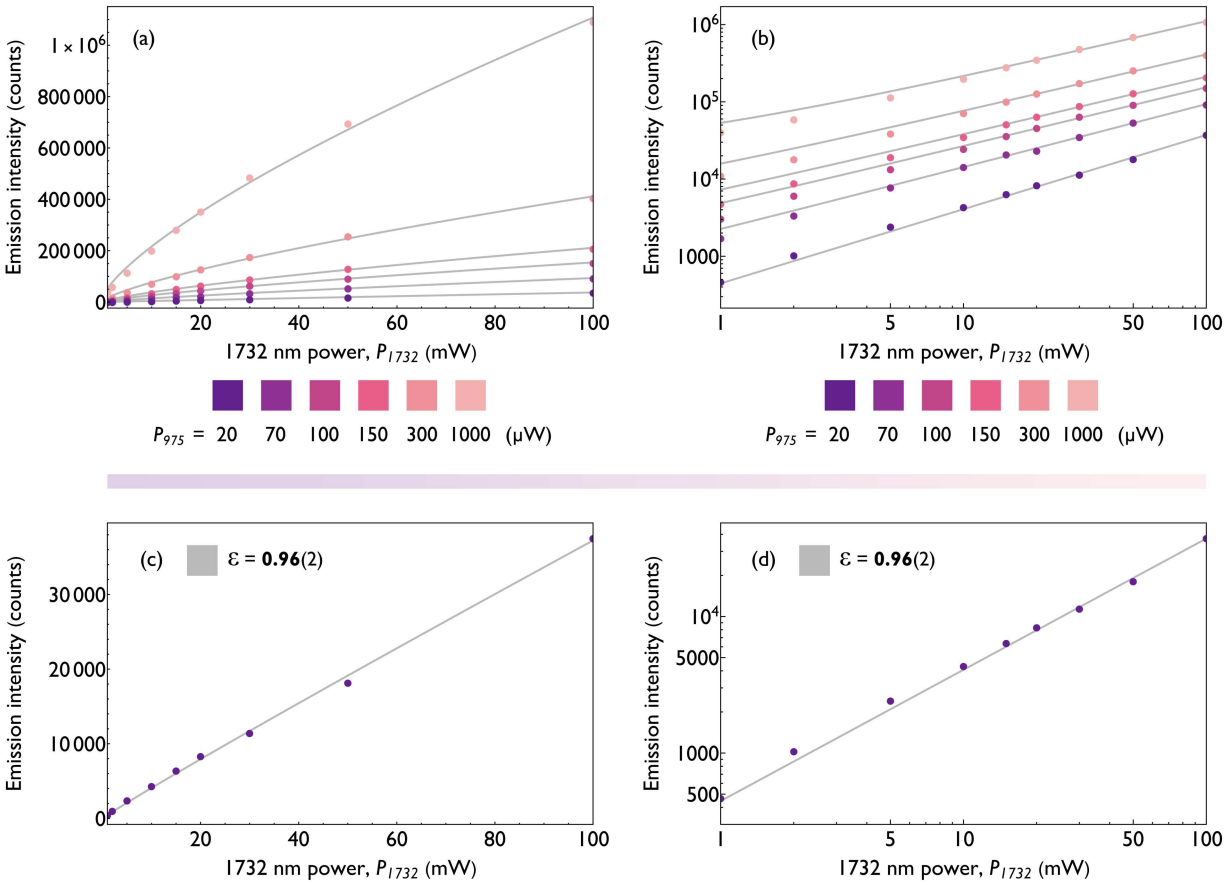

Figure 3.18: Emission intensity at 800 nm from YbTm nanoparticles under dual-wavelength co-excitation with 975 nm and 1732 nm beams **in the low-power regime**, shown as a function of 1732 nm beam power, with fitted curves included (Eq. 3.29). **(a)** Emission intensity plotted against 1732 nm beam power for various fixed power levels of the 975 nm beam. Fitted functions are shown as gray lines. **(b)** Same data as in (a), presented on a log-log scale. **(c)** Emission intensity as a function of 1732 nm beam power at the lowest 975 nm beam power (20 μW), with the fitted curve (gray) and extracted exponent indicated. **(d)** Same as in (c), but shown on a log-log scale.

increase *sublinearly* with 1732 nm power as the co-present 975 nm beam becomes stronger. This trend is clearly shown in the series of values given in Eq. 3.30.

$$\varepsilon = \mathbf{0.96}(2) \rightarrow \mathbf{0.82}(1) \rightarrow \mathbf{0.76}(2) \rightarrow \mathbf{0.75}(2) \rightarrow \mathbf{0.74}(2) \rightarrow \mathbf{0.74}(2) \tag{3.30}$$

It sounds remarkably familiar—*and it should*. When compared with the exponent describing the influence of the 1732 nm beam within the *mutual interplay* term, as determined in the analysis of higher power regimes—where it stabilized around **0.64**-**0.69** across a broad range of moderately high powers[67]—we see a clear convergence. As the 975 nm power increases, we steadily approach that regime, witnessing along the way the evolution of the emission dependence on NIR beam power: from a limiting case, where neither beam alone induces emission, to a state of dynamic equilibrium between their contributions.

67: The derivation is provided in Section 3.3 and detailed in Eqs. 3.15, 3.19, 3.21, and 3.24.

What emerges before us is a bridge—connecting the behavior at ultra-low excitation powers with that of higher regimes, where the

initially *linear* dependence on 1732 nm power gradually evolves into the previously described *sublinear* character.

It all falls perfectly into place.

Still, a critical observation remains. As previously noted—though not emphasized—and as shown in Fig. 3.18c, when operating in the lowest 975 nm power regime, the emission dependence on the 1732 nm beam follows an exponent of **0.96**(2). In other words, in the *de novo* emission regime—where neither beam alone produces measurable emission, but their combination does—the resulting emission scales with 1732 nm power in an almost perfectly *linear* manner.[68]

68: This observation proved useful, as discussed in Section 4.1.3.

This insight is key to understanding the nature of the observed ***switchable*** emission:

By maintaining a sufficiently low 975 nm power, the introduction of the 1732 nm beam **switches on** the emission and allows its intensity to be *precisely controlled*—exhibiting a *linear* response with respect to the 1732 nm beam.

And on this note, we conclude the arc of our exploration.

3.6 Summa summarum

Enhancing emission from upconverting nanoparticles is traditionally approached by increasing excitation power or optimizing composition. But here, we pursue a different strategy—reframing improvement in upconversion as a search for complementarity rather than brute force. This chapter ventures into that pursuit—seeking not only to enhance emission from Tm-doped upconverting nanoparticles, but to unlock regimes of interaction fundamentally inaccessible through single-beam excitation. At its core lies the principle of **co-excitation**: the simultaneous illumination of a thulium and ytterbium co-doped nanoparticle system using two wavelengths—975 nm and a tunable near-infrared (NIR) beam spanning 1050-1875 nm. The idea is elementary: that what neither beam can achieve in isolation, their interplay might reveal.

The baseline excitation at 975 nm, resonant with the sensitizer ion Yb^{3+}, reliably initiates energy transfer upconversion (ETU) to Tm^{3+} activators, producing strong emission at 800 nm. This emission not only serves as a spectroscopic anchor—it also acts as a sensitive indicator of any novel cooperative effects.

Then, the introduction of a tunable NIR beam changes everything—*and leads to a pronounced transformation in the system's emission profile*.

Two broad excitation bands emerge—centered at **1213 nm** and **1732 nm**—that produce negligible emission when applied individually. However, when either is combined with 975 nm excitation, a **striking enhancement** in upconversion is observed: the resulting emission intensity significantly exceeds the combined output of the two beams used separately.

The observed enhancement arises from a set of photophysical processes involving both ground-state absorption (GSA) and excited-state absorption (ESA) in thulium ions. The Judd-Ofelt framework predicts several such transitions, each with a non-negligible oscillator strength. While the NIR beam can directly drive certain GSA transitions, ESA processes depend critically on the initial population of intermediate excited states—levels that, under ambient conditions, remain sparsely occupied. In both scenarios, the 975 nm beam plays a crucial role: through efficient energy transfer upconversion (ETU) from Yb^{3+}, it not only primes the system for subsequent ESA by partially populating intermediate excited states, but also actively sustains the upconversion process by driving transitions that follow from states initially populated via NIR-induced GSA.

To evaluate this interaction quantitatively, a **surplus** emission metric was introduced—defined as the excess signal generated by co-excitation **beyond** what would be expected from the linear sum of the two single-beam contributions.

For the two identified NIR excitation wavelengths—1732 nm and 1213 nm—surplus values reach **several hundred percent**, far exceeding simple summation.

Notably, this surplus is highly sensitive to the balance of beam powers—and so is the total emission intensity. As the 975 nm excitation increases, the total emission continues to grow, but the surplus effect systematically diminishes. This suggests that while the 975 nm beam is essential to enable the cooperative mechanism, it eventually overwhelms the subtle dynamics that make co-excitation unique.

This insight is captured in a mathematical model that partitions total emission into distinct terms: the independent contributions of each beam (each modeled as a power-law function of its respective power) and an interplay term representing their cooperative effect, expressed as a product of the powers with fitted exponents. The model successfully reproduces experimental results across multiple excitation regimes. Crucially, the cooperative term is constructive—though *sublinear*—with respect to the power of both excitation beams. By isolating the mathematical expression for the surplus component from the overall emission model, we arrive at a simple, fully multiplicative relation: one that depends *constructively* and *sublinearly* on the NIR beam power, while exhibiting a *destructive* dependence on the increasing 975 nm power. This behavior aligns with the experimentally observed suppression of surplus emission at higher 975 nm intensities.

To further probe the system's behavior, measurements were extended to the low-power regime—specifically to cases where neither beam, on its own, produced measurable emission. In this domain, the most revealing observations were made.

Careful adjustment of both excitation beam powers in the low-power regime can lead to emission enhancements reaching **several orders of magnitude**—and can even give rise to *de novo* emission, **activated** only through the joint presence of two beams that, on their own, remain below the excitation threshold. The result—a controllable and **switchable** emission process.

This *de novo* emission, arising solely from the presence of both beams, constitutes the clearest evidence for the existence of cooperative excitation pathways that are entirely silent under single-beam operation. In such cases, surplus emission, as formally defined, diverges; with no individual contributions, the combined signal is not enhanced—*it is entirely new*.

Even in this extreme low-power scenario, the system exhibits clear regularity. At the lowest tested 975 nm powers, emission scales nearly linearly with NIR power. As the 975 nm power increases, the response becomes sublinear, gradually converging toward the behavior observed in the moderate-power regime. This smooth evolution demonstrates that the cooperative mechanism persists even as one excitation source becomes increasingly dominant, forming a continuous bridge between regimes.

Across the full power range, emission behavior reflects a delicate balance. The 975 nm beam acts as both enabler and suppressor: essential for initiating energy transfer, yet ultimately limiting the magnitude of surplus emission. The NIR beam, by contrast, contributes little on its own, yet plays a *tremendous* role in shaping the cooperative response when paired effectively.

Altogether, this chapter demonstrates that co-excitation is not merely a means of enhancing emission—it defines a qualitatively distinct mode of nanoparticle excitation. The phenomena observed here—the surplus, the emergence of light from the cooperative action of otherwise inactive beams—highlight a broader principle: that photophysical systems may be shaped not solely by the magnitude of energy, but by the interplay of energies.

The light that results is not simply brighter; it is *different*—revealing new measures of control within systems long known, yet still not fully uncovered.

3.6.1 Contributions

Ongoing support and scientific guidance — **Piotr Fita**

Valuable discussions and assistance with the interpretation of possible transitions in thulium ions —
Artur Bednarkiewicz

Synthesis of the nanoparticles used — **Katarzyna Prorok**

Concept, independent execution of the experiments, analysis, full description, and everything in between — **myself, Paulina Rajchel-Mieldzioć**

Visualization of the NIR beam 4

4.1 To bring the hidden to light

All roads lead to Rome—so let the results be our road, and in this case, let Rome be their application, or at least a practical demonstration of the concept. Regardless of how strongly we might wish the results to stand as a value in themselves—which indeed has been a guiding intention throughout this work—it is worth emphasizing that their significance extends beyond mere novelty.

Beyond the added control over the upconversion process and the potential for tunability when needed (a quality that, while broad in meaning, can be seen as a strength due to the range of possible directions it allows), one particular opportunity emerges with striking clarity—**visualization**.

As demonstrated, it is indeed possible to carefully select the powers of the individual excitation beams such that neither produces detectable emission on its own—even by a highly sensitive detector—yet their combined action results in a clear and measurable signal. This not only confirms the feasibility of such an approach but opens the door to broader implementations.

After all, whether the detector is a photomultiplier tube in a spectrofluorometer, a sensor array in a camera, or the human retina itself, the fundamental principle remains the same: the response depends on sensitivity and appropriate matching of power to the detection threshold.

4.1.1 An idea into action

A sample was prepared by depositing the thulium-doped nanoparticles via drop-casting from an aqueous suspension onto a standard microscope glass slide. After drying under ambient conditions, the sample was ready for the experiment.[1]

1: For a complete description of sample preparation, see Section 2.3.

As in the previous configuration, two lasers were employed: a continuous-wave 975 nm beam and a pulsed near-infrared beam. For this demonstration, the NIR wavelength was set to 1732 nm, chosen in part to highlight a key advantage—extending beyond the primary sensitivity range of conventional InGaAs detectors.

Unlike in the earlier overlapping-beam configuration, the beams were separated in this case. The 975 nm beam was defocused to uniformly illuminate the entire sample area (exceeding 16 mm^2), while the 1732 nm beam was introduced from the side, focused onto the sample at an angle relative to the base beam. The powers of both beams were adjusted using variable neutral density filters. To enable measurements under individual or combined excitation conditions, each beam could be independently blocked as needed using duraluminum shutters. To document the observed effect, a Sony A7 III photographic camera mounted on a tripod was used. The sample was imaged through a combination of optical filters: a 750 nm long-pass and a 900 nm short-pass, effectively isolating the

emission signal. All photographs were taken under identical sensitivity settings and from the same fixed position to ensure consistency.

It is often said that photography is more than the act of capturing an image—it is a way of telling a story. And in this case, the images presented in Fig. 4.1 do just that.

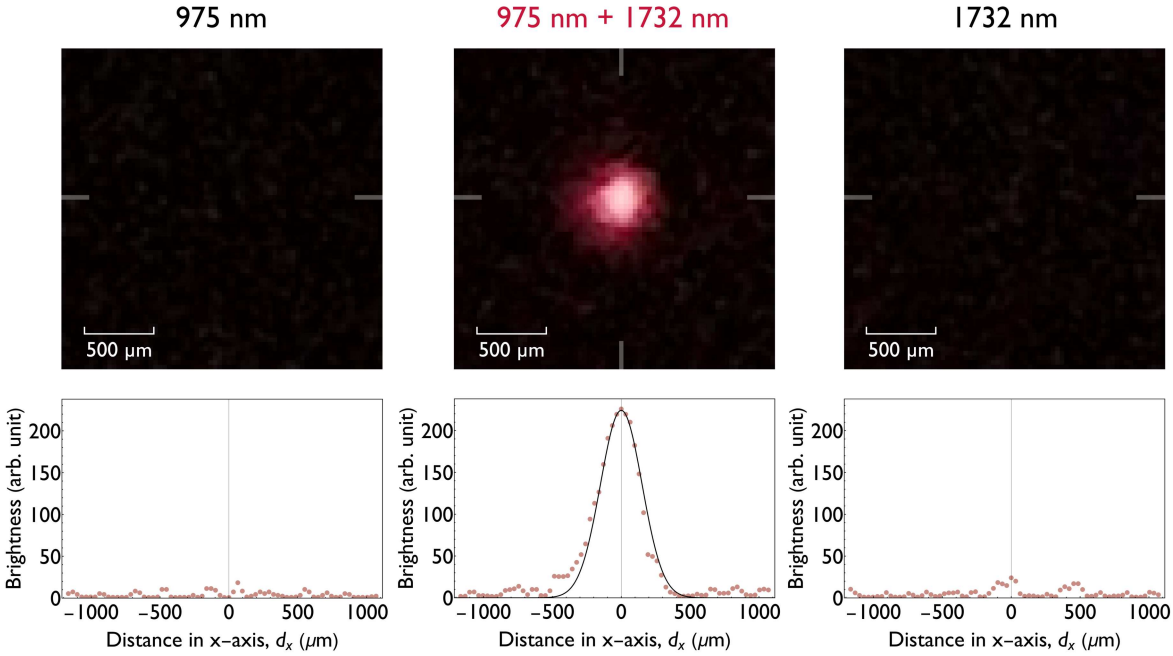

Figure 4.1: Direct visualization of the NIR beam (1732 nm) using thulium-doped nanoparticles under weak illumination with a 975 nm beam. **Left:** A slide containing nanoparticles illuminated with a weak, defocused 975 nm beam, below the threshold for visible emission. **Center:** The sample illuminated simultaneously with both beams. **Right:** The sample illuminated only with the 1732 nm beam, using the same parameters as in the co-excitation case shown in the center image. **Below each image**, a cross-section along the x-axis (horizontal) is shown, extracted through the intensity maximum of the center image (which defines the zero point); the same row was used for analyzing the single-beam cases. The cross-section axis is indicated on the images. The vertical axis of each graph represents pixel brightness from the original, unprocessed image. Emission profiles are plotted as a function of spatial distance, with Gaussian fit applied to the observed signal (FWHM = **355**(13) μm). Images were acquired using Sony A7 III photographic camera with long-pass (750 nm) and short-pass (900 nm) optical filters in front of the camera lens to selectively capture the emission signal.

Before proceeding to a detailed analysis of the presented results, it is essential to emphasize the most important conclusion—one that is, quite literally, visible to the naked eye.

The co-excitation phenomenon, when applied to a phosphor screen coated with upconverting nanoparticles, enables real-time, *switchable*, direct visualization of wavelengths **above 1700 nm**.

Fig. 4.1 presents three images: one of the sample illuminated solely with a defocused 975 nm beam (left), one with only the 1732 nm beam (right), and one under combined illumination with both beams (center), which results in a clearly visible 800 nm emission. Below each image, cross-sections along the x-axis are shown, representing pixel brightness as a function of spatial distance. A detailed discussion of the central cross-section—along with quantitative descriptors such as FWHM—is provided in Section 4.1.2.

Before we turn to the technical and quantitative discussion, two critical features of the observed effect should be appreciated: first, its *switcha-*

bility—the ability to turn the emission on and off via the 975 nm beam; and second, its capacity for fast, direct visualization through upconversion of NIR radiation beyond 1700 nm (notably, a spectral range where conventional phosphors typically fail) into a detectable 800 nm signal.

This naturally raises a question: how does this differ from commercial liquid-crystal-based NIR detection cards? Primarily, in speed. But more importantly—does it differ in *precision*? That answer will become clear as we move into the technical aspects required to analyze the presented images.

4.1.2 Emission intensity analysis

Brightness and spatial distance analysis

Emission intensity was quantified by analyzing pixel brightness in the captured images using the following approach. The original image (70×70 pixels in resolution; an upscaled version is shown in Fig. 4.1, produced via nearest-neighbor resampling, where each new pixel inherits the value of its closest pixel in the original) was evaluated pixel by pixel. For each pixel, the red (R), green (G), and blue (B) channel values were extracted, and their arithmetic mean was calculated to determine brightness (Eq. 4.1), which is assumed to be directly proportional to the local emission intensity.

$$\text{Brightness} = \frac{R + G + B}{3} \tag{4.1}$$

This assumption relies on the RGB sensor response being approximately linear within the dynamic range used. Importantly, no saturated[2] pixels were present in the analyzed images, ensuring that brightness values remained within the linear regime of the detector. As the emission lies within the sensitivity range of all three channels,[3] averaging the RGB values yields a scalar representation of the signal. Additionally, the use of optical filters ensured selective detection of emission light, minimizing background contributions and supporting the validity of this brightness-based method. The dimensions of the sample, glass slide, and holder were measured using a caliper, allowing for the conversion of pixel values into real distances in micrometers. To aid this process, additional images were taken with external flashlight illumination to reveal reference objects lying in the plane of the sample, providing reliable distance markers.

2: Saturation refers to the condition where any one of the RGB channels reaches its maximum value of 255. Since **none** of the channels—particularly the red one—reached this maximum, we confirm that no saturation occurred in our images.

3: Owing to the widespread use of Bayer filter mosaics in photographic cameras, their spectral sensitivity near 800 nm results in signal detection not only by red pixels but also by green and blue pixels. As a result, all color channels contribute to the overall brightness.[108]

Cross-sections

Using the methods outlined above, full mapping of the captured images was made possible. Fig. 4.1 presents x-axis cross-sections from all three images, while Fig. 4.2 shows both x- and y-axis cross-sections of the observed emission. But that's not all—Fig. 4.3 displays a full two-dimensional brightness plot of the emission, revealing its spatial distribution.

To begin with, the cross-sections of the images recorded under single-beam illumination (left and right in Fig. 4.1) clearly show the absence of

detectable emission—pixel brightness remains at the dark-count level, and no structure is observed. In contrast, the cross-sections of the emission captured under co-excitation, as detailed in Fig. 4.2, clearly reveal that the brightness profile reflects the Gaussian nature of the NIR beam.[4]

4: The accuracy and limitations of this representation will be addressed in the following Section 4.1.3.

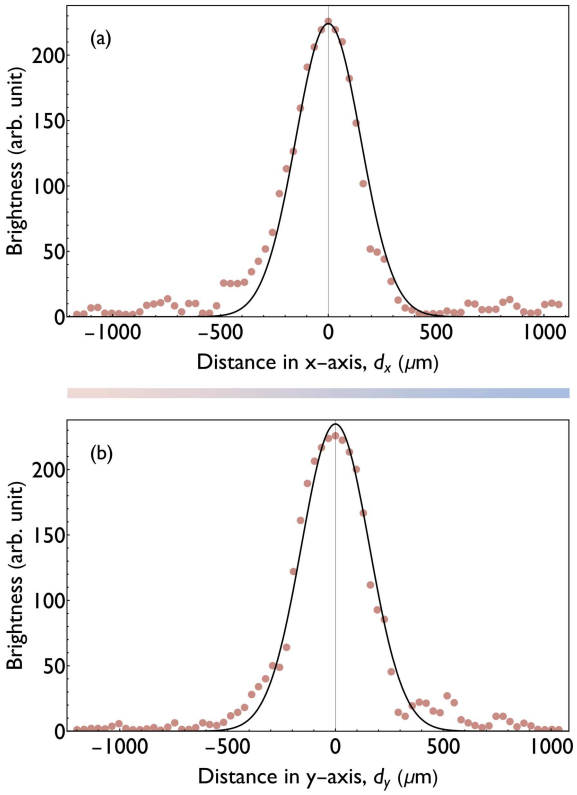

Figure 4.2: (a) Cross-section along the x-axis through the intensity maximum in the visualization image (Fig. 4.1), with a Gaussian fit applied (FWHM = **355**(13) μm); this profile is also shown and described in that figure's caption. **(b)** Analogous y-axis cross-section, taken through the same intensity maximum—guide lines are shown on the main image—and plotted as a function of spatial distance with a Gaussian fit applied (FWHM = **369**(11) μm).

Gaussian functions were fitted to both cross-sections (as shown in the figures, with good agreement), yielding full width at half maximum (FWHM) values of **355**(13) μm for the x-axis (horizontal) profile and **369**(11) μm for the y-axis (vertical). These closely matching values suggest either that the loosely focused infrared beam is spatially symmetric, or conversely—assuming the beam is symmetric—that no significant distortions were introduced during imaging via the upconverting nanoparticles. This symmetry is further supported by the two-dimensional emission map shown in Fig. 4.3.

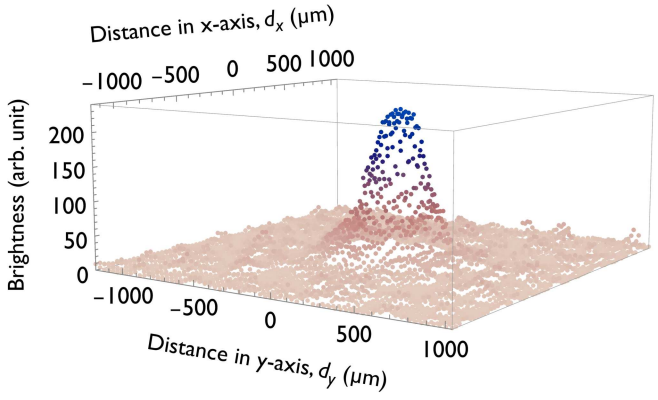

Figure 4.3: Two-dimensional representation of emission intensity (pixel brightness) from the direct visualization of the NIR beam—corresponding to the full central image in Fig. 4.1. Emission intensity is plotted as a function of spatial coordinates, with the origin set at the brightest point (intensity maximum).

SNR analysis

The signal-to-noise ratio (SNR) was calculated as the ratio of the signal maximum to the noise level, with noise estimated as the standard deviation of the first and last 10 pixels in each intensity profile. The analysis was performed for both directions: the x-axis cross-section yielded an SNR of **64**, while the y-axis profile yielded **71**. These high and comparable values confirm that the signal in the presented visualization is clearly and reliably distinguishable from the background.

4.1.3 Reconstruction of the beam profile —the question of *precision*

In the present case, the reconstructed profile retained the Gaussian character of the beam; however, this does not necessarily mean that the fitted parameters accurately reflect the intrinsic properties of the beam itself. At minimum, a preliminary analysis is required to understand how various experimental parameters and nanoparticle characteristics may influence the resulting beam representation.

To begin, let us reiterate the previously stated assumption that pixel brightness is directly proportional to emission intensity—provided there is no saturation.[5] From this point forward, emission intensity will serve as our primary parameter of interest.

5: As stated earlier, in our experiment there is **none**—as none of the RGB channels, including red, reached the full intensity value of 255.

We aim to determine the functional dependence $E(P)$, describing how the emission intensity E varies with the spatial distribution of power of the NIR beam P.[6] This is particularly important, since the fidelity of NIR beam visualization ultimately limits the imaging performance. In contrast, the 975 nm beam is defocused—so within the region corresponding to the NIR beam spot, its intensity can be assumed to be approximately uniform and homogeneous, since the NIR beam's focal spot is much smaller than the overall area illuminated by the 975 nm beam. However, it is important to note that the absolute power level of the 975 nm beam still influences the relationship between NIR power and observed emission, a point which will be addressed after the more general and pressing considerations.

6: The emission intensity depends on the local excitation intensity—but since the camera discretizes the imaged area, it is more practical to speak in terms of power, specifically the power corresponding to the portion of the sample mapped onto a single pixel.

By the nature of upconverting nanoparticles, the relationship $E(P)$ follows a power-law function. When the power exponent remains constant *throughout the entire range of input powers*, the relation can be expressed as $E \propto P^a$.

Assuming a Gaussian beam profile, and recognizing that the detected signal is ultimately discretized by the camera—resulting in a power value per pixel over the imaged area—the simplest case can be described by Eq. 4.2, where $P(x)$ represents the power incident on the area imaged by a single pixel.[7]

7: The continuous approximation holds because the imaged area is sampled by a sufficiently large number of pixels.

$$P(x) \propto \exp\left(\frac{-x^2}{2\sigma_p^2}\right) \tag{4.2}$$

When combined with the established relationship between emission intensity and beam power, this yields an expression describing the spatial distribution of the emission intensity.

$$E(x) \propto \left[\exp\left(\frac{-x^2}{2\sigma_P^2}\right)\right]^a = \exp\left(\frac{-a \cdot x^2}{2\sigma_P^2}\right) \Longrightarrow \sigma_E = \frac{\sigma_P}{\sqrt{a}} \tag{4.3}$$

While the conclusion may seem intuitive, it is nonetheless important to emphasize: nonlinearity—provided it remains constant—does not alter the overall Gaussian nature of the beam profile, which is retained in the resulting emission intensity distribution. However, it does modify the profile shape, including the full width at half maximum (FWHM). Specifically, if the relationship between E and P is superlinear, the reconstructed emission profile becomes narrower than the actual beam profile; conversely, in the case of a sublinear dependence, the emission profile appears broader.

Effect of 975 nm beam power

As previously noted, the power of the 975 nm beam naturally influences the relationship between NIR beam power and the resulting emission intensity. Understanding the true nature of this dependence is essential for analyzing—or at the very least, evaluating—the fidelity of the reconstructed NIR beam profile.

Let us return to Fig. 3.18c in Section 3.5.2, where co-excitation was examined under the lowest applied 975 nm powers, down to 20 μW. In those experiments, the beam was focused, with a focal spot of 0.00333 mm^2 (corresponding to the lowest applied intensity of 0.6 W/cm^2).[8] In the present case, the 975 nm beam operated at a power of 10 mW, but it illuminated an area of approximately 16 mm^2 (corresponding to approximately 0.06 W/cm^2, though this value is subject to uncertainty due to the estimated illuminated area). Notably, this results in a power density that is comparable to—or at most, an order of magnitude lower than—that in the earlier co-excitation experiments. Yet it is precisely those earlier low-power trials that laid the foundation for the NIR beam visualization strategy developed in this work.

8: See Section 2.2.1.

If the purpose of revisiting these previously discussed results is unclear at this point, we now reintroduce the relationship, which describes the dependence of emission intensity E on NIR beam power P_{1732} under constant, low-power 975 nm excitation (20 μW):

$$E \propto P_{1732}^{\mathbf{0.96}(2)}$$

As seen from this expression, when the 975 nm beam operates at sufficiently low power—and only under such conditions—the emission induced by co-excitation depends nearly linearly on the 1732 nm beam power. In light of the earlier discussion, including Eq. 4.3, this leads to a crucial conclusion:

By maintaining a sufficiently low power density of the 975 nm beam—either by reducing its power or by illuminating a sufficiently large area—the NIR beam can be visualized using thulium-doped nanoparticles **without distorting** its spatial profile. As a result, any image formed by NIR light—not just the beam itself—is **linearly** transformed into 800 nm emission, serving as the foundation for faithful and effective visualization.

And this—*this* is what defines our precision.

The answer to a not-so-rhetorical question posed at the end of Section 4.1.1.

4.2 To give shape to the unseen

The successful visualization of the infrared beam serves as a clear proof-of-concept that our findings can be translated into practical implementation. Naturally, this success encouraged us to take the idea further—into more intricate spatial patterns. This time, however, without detailed analysis or parameter extraction, but instead with the intention of letting the image itself demonstrate the power of the approach.

4.2.1 Extending beam visualization through spatial control

A beam path rendering experiment was conducted using a computer-controlled galvanometric scanner programmed to trace an oval shape. The setup closely followed that of the previous experiment,[9] with the primary difference being the dynamic positioning of the 1732 nm beam introduced by the scanning motion. As before, spatial scaling was established using backlit reference images and caliper measurements of the sample and glass slide, which were then used to calibrate the scale in the final images.

9: As described in Section 4.1.1. The filters used in this experiment were a 633 nm long-pass and an 850 nm short-pass, instead of the originally used 750 nm long-pass and 900 nm short-pass, due to availability at the time. However, this substitution has no effect on the results.

It should be noted that the motion of the galvanometric scanner was not perfectly smooth, particularly during brief pauses at direction changes—an imperfection that was clearly captured in the resulting image and may be viewed as an added strength of the visualization method, demonstrating its sensitivity to subtle variations in the illumination pattern.

The outcome of the experiment—a direct spatial rendering of the scanned beam path—is presented in Fig. 4.4.

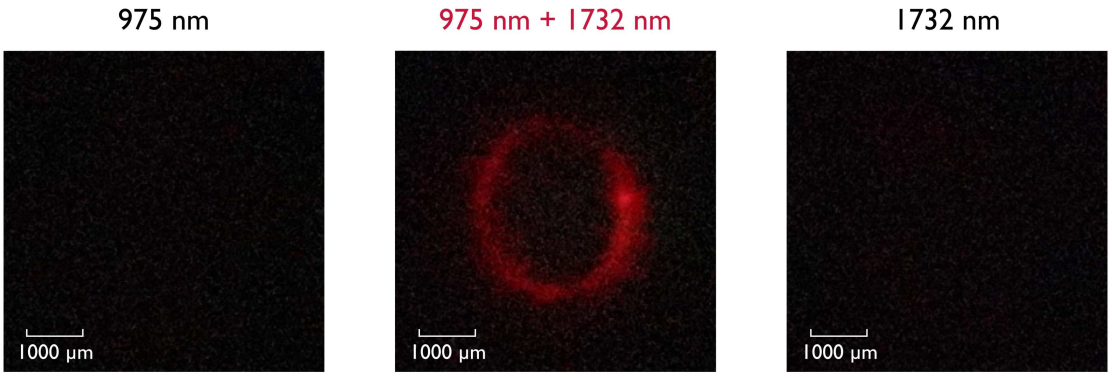

Figure 4.4: 2D direct visualization of the 1732 nm beam using YbTm nanoparticles under weak 975 nm illumination, with beam scanning by a galvanometer scanner. **Left:** Illumination with a defocused 975 nm beam at sub-threshold intensity. **Center:** Simultaneous illumination with both beams; the 1732 nm beam is scanned in an oval pattern. **Right:** Illumination with only the 1732 nm beam, scanned under the same conditions. Images were captured with a Sony A7 III camera equipped with 633 nm long-pass and 850 nm short-pass filters. Each frame is an average of three consecutively acquired photographs.

The Fig. 4.4 shows an image of the sample illuminated with only the defocused 975 nm beam (left), only the 1732 nm beam scanned in an oval pattern by the galvanometric scanner (right), and with both beams applied simultaneously without changing their parameters (center), resulting in visible emission. These results fully reflect those presented in Fig. 4.1 and serve as a complementary extension—now expanded

into a second spatial dimension. This extension is intended not merely as a literal or aesthetic elaboration, but as a meaningful step toward demonstrating the practical applicability of the observed effect—where real-time *spatial* and *switchable* visualization of near-infrared light beyond 1700 nm may serve a valuable role.

4.3 Summa summarum

From results, through concept, to realization—this work builds on earlier findings[10] demonstrating the possibility of generating strong 800 nm emission *de novo* under co-excitation of thulium-doped upconverting nanoparticles. This emission appears only when both the 975 nm and 1732 nm NIR beams are combined at appropriate power levels, and is absent when either beam is used alone. We sought to translate those dry (though inherently valuable) facts into something more visually intuitive: a practical, image-based representation. In short, we aimed to visualize the beam directly, to more vividly illustrate what we had already proven.

10: As described in Section 3.5.

This chapter presents the direct visualization of a near-infrared beam through co-excitation—first as a beam profile reconstruction, and then by extending beam visualization through spatial control using a galvanometric scanner. These images were captured using a standard photographic camera, under conditions where neither excitation beam alone produced a measurable signal—only their combination did. This approach serves as a direct analog to our earlier detector-based measurements, though with a different sensitivity threshold—adapted to entirely different detection hardware, much closer to the characteristics of human vision. It also opens the door to real-time visualization of beams beyond 1700 nm in a more practical setup—well outside the typical detection range of standard InGaAs sensors.

Importantly, this visualization was not only a compelling demonstration—it was shown that, under carefully selected power conditions, the recorded beam profile preserves its Gaussian shape. That is, the emission intensity, linearly related to pixel brightness, accurately reflects the beam's spatial profile without distortion or broadening. This outcome is particularly notable given the inherently nonlinear nature of light-nanoparticle interactions. However, when the power density of the 975 nm beam is kept sufficiently low, the emission becomes nearly linearly dependent on the power of the 1732 nm beam. This offers an additional advantage: the emission remains switchable, and its spatial distribution can be modulated as well—adding a new layer of control to the overall effect.

Through this experiment, we have demonstrated that co-excitation enables direct, real-time, **switchable**, and **spatially-resolved** visualization of infrared wavelengths above 1700 nm—bridging the gap between advanced photophysical phenomena and practical, accessible imaging techniques.

4.3.1 Contributions

Ongoing support and scientific guidance, as well as the idea to extend the beam visualization through spatial control — **Piotr Fita**

Galvanometer scanner setup and assistance with its operation — **Przemysław Słota**

Synthesis of the nanoparticles used — **Katarzyna Prorok**

Concept, independent execution of the experiments, analysis, full description, and everything in between — **myself, Paulina Rajchel-Mieldzioć**

Erbium

Co-excitation in Er-doped upconverting nanoparticles

5

5.1 In the mine of *Ytterby*

It was in the mine near the Swedish village of Ytterby that mineral deposits were discovered containing a wealth of new elements—several of which were named in its honor: terbium (Tb), yttrium (Y), **erbium (Er)**, and **ytterbium (Yb)**.

Encouraged by the results of our analysis of thulium co-doped nanoparticles, we now turn to the investigation of erbium co-doped systems—starting with the typical doping level of 2%. Yet do we know what to expect?

Here, it must be stated clearly—*partially, yes*. Erbium-based nanoparticles, as one of the flagship materials in upconversion research, have been the subject of an impressive number of studies.[1] However, this does not mean the final word has been spoken on the subject.

1: Condensed information on this subject is included in the theoretical introduction, see Sections 1.1.3, 1.1.4 and 1.1.5.

And that, we might add—somewhat enigmatically—serves as a kind of self-fulfilling prophecy. Not because the last word will come from us, **but because *the next one* might**.

5.1.1 Words into action

And what do we know?

Before we proceed into the intricacies of co-excitation, let us first recall that erbium co-doped nanoparticles—when excited with a 975-980 nm beam resonant with the $^2F_{7/2} \longrightarrow {}^2F_{5/2}$ transition in ytterbium ions acting as sensitizers—exhibit a characteristic emission spectrum (Fig. 1.8). Most notably, this includes distinct green emission bands (with maxima near 523 and 543 nm) and a red emission region (with one of its prominent peaks around 657 nm).

Our primary focus lies on the red band—centered at 657 nm—due to the relatively low-lying nature of the $^4F_{9/2}$ state. However, the green bands (in our case, particularly the one at 543 nm) cannot be ignored, as any changes in their intensity reflect the influence of co-excitation on the population of higher-lying electronic states.

Unlike with thulium-doped systems, where the behavior under co-excitation was largely unknown, the case of erbium offers at least a partially clarified foundation. As discussed in the theoretical introduction,[2] co-excitation of these nanoparticles with a beam around 1530 nm—resonant with the ground-state absorption (GSA) transition $^4I_{15/2} \longrightarrow {}^4I_{13/2}$ in erbium (see Fig. 5.1)—is well documented. It is therefore reasonable to expect that in our system as well, excitation at this specific wavelength should produce some observable effect.

2: See Section 1.1.5.

The remainder of the NIR spectral range,[3] however—when paired with the baseline 975 nm beam[4]—remains *uncharted territory*.

And, as it turns out, it is far from being empty.

3: As a reminder, we work in the NIR range of 1050-1875 nm.

4: It is also worth noting that co-excitation involving two beams—one from the NIR region of interest and the other in the visible range, also resonant with erbium transitions—has already been explored (see Section 1.1.5.).

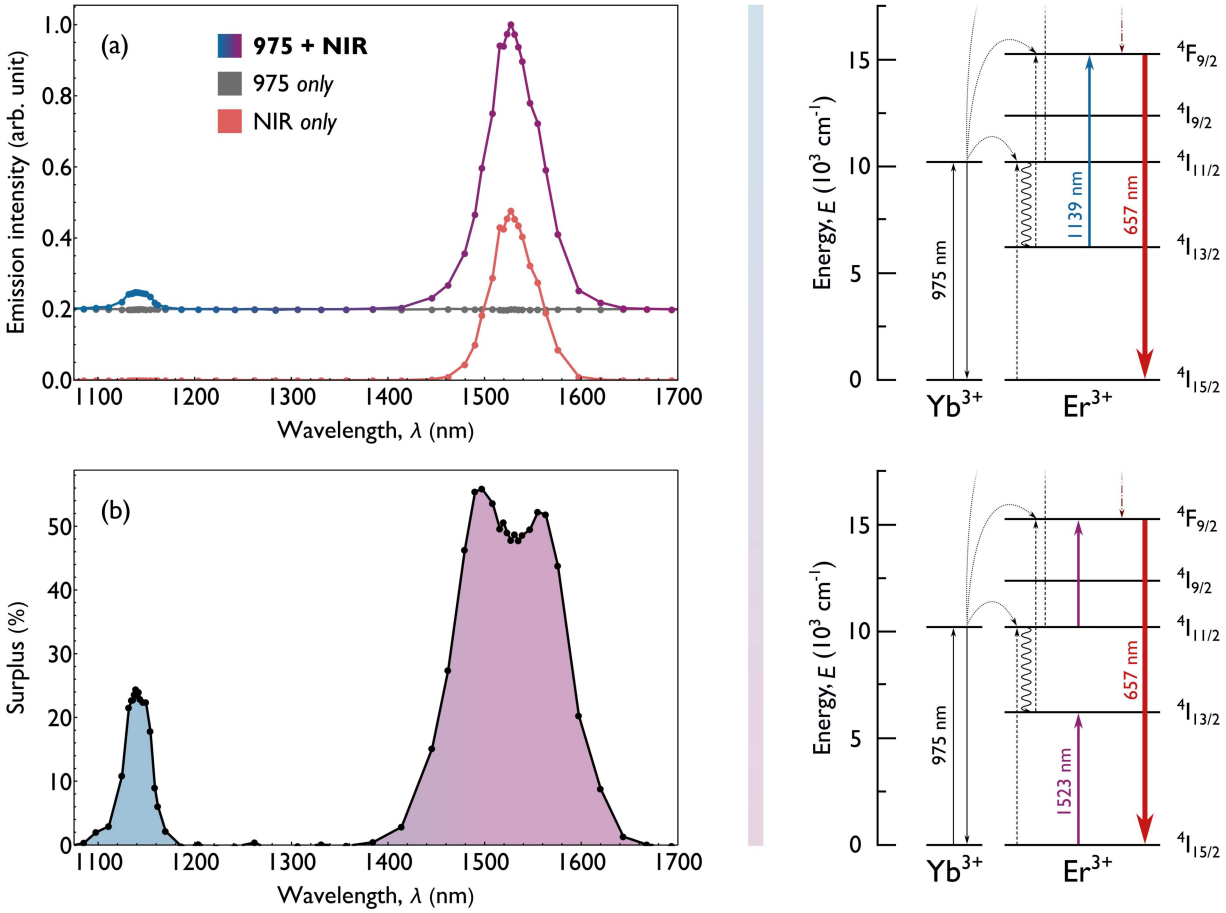

Figure 5.1: Left: Excitation spectra of YbEr nanoparticles recorded at 657 nm emission under simultaneous excitation with two spatially overlapped beams: a continuous-wave 975 nm beam (10 mW) and a tunable pulsed NIR beam (100 mW). **(a)** Excitation spectra measured under three excitation conditions—each plotted on the same scale and normalized to the maximum recorded value: *(i)* co-excitation with both beams (blue-pink bichromatic line, used to visually separate the two distinct bands corresponding to color-coded transitions), *(ii)* excitation with the NIR beam only (coral line near the bottom, showing non-zero values around 1520-1530 nm), and *(iii)* baseline emission generated by the 975 nm beam alone (gray points; a steady level, as the 975 nm beam has a fixed wavelength; however, single-beam measurements with the 975 nm excitation were still performed at each tuning step of the NIR beam). Emission intensity is plotted as a function of NIR excitation wavelength. **(b)** Surplus emission plot under co-excitation, showing the enhancement relative to the **sum** of emission intensities generated by each beam independently. Visible saturation effects near the NIR absorption maximum at 1523 nm. **Right:** Simplified energy-level diagrams of the YbEr system, illustrating ground-state absorption (GSA) and potential excited-state absorption (ESA) processes that govern the observed excitation spectra. These are restricted to lower-lying energy levels; more comprehensive diagrams can be found in Figs. 5.4 and 5.5. For clarity, line thickness *does not* reflect oscillator strength; refer to Fig. 5.3 for that information.

Action into results

5: By manual tuning of the DFG setup—see Sections 2.1 and 2.4.

By collinearly overlapping the generated NIR beam[5] with the 975 nm beam, a co-excitation spectrum was obtained for YbEr nanoparticles, recorded at the 657 nm emission wavelength (i.e., the red band). The spectrum was measured using a fixed 975 nm excitation at 10 mW in combination with a tunable NIR beam at 100 mW, and plotted as a function of the NIR excitation wavelength across the full range used. During the acquisition, comparative single-beam measurements were simultaneously performed—using only the 975 nm beam and only the NIR beam. The results are presented in Fig. 5.1.

We begin on a high note—with what is perhaps the most important finding: **the emergence of a band centered at 1139 nm**. While the

presence of a band around 1530 nm (in our case, centered at **1523 nm**) was highly expected, the appearance of a higher-energy band under exactly these conditions was less obvious. And yet, this is precisely the aim of our work—to detect *more unexpected* excitation wavelengths, enabled by a custom-build setup, that contribute[6] in combination with the 975 nm beam.

Yet it would be incorrect to claim that the excitation band around 1140 nm is entirely unknown or exotic—the sheer idea of it arises directly from the energy of the transition $^4I_{13/2} \longrightarrow ^4 F_{9/2}$. In fact, its influence on green emission has been discussed in the literature[103], where it was used in combination with a 795 nm beam to modulate green output by exciting the $^2H_{11/2} \longrightarrow ^2 K_{15/2}$ transition—thereby, in theory, depleting the green-emitting states that are populated by the 795 nm beam through absorption and subsequent cross-relaxation processes.[7]

In our case, however, the 1139 nm excitation is applied in combination with a 975 nm beam—a pairing that, to our knowledge, **has not been previously explored**.

But are these cases truly so different? In some ways, absolutely—different experimental designs, different types of co-excitation, and, as will soon become clear, even different conclusions. And yet, *nihil novi sub sole*—nothing new under the sun. We are still probing the same transitions, perhaps through different pathways, but the same nonetheless. This makes prior literature invaluable, helping us place our own observations into a coherent framework.

Therefore, determining the influence of the 1139 nm band on red emission in our system naturally calls for an analysis of its effect on other emission wavelengths characteristic of YbEr nanoparticles. Here, we arrive at another crucial—and unobvious—observation.

The 1139 nm beam—when combined with the 975 nm beam—leads to a noticeable enhancement of the 657 nm emission band of Er^{3+}-doped nanoparticles, even though it induces no measurable emission on its own. However, it produces *no enhancement or depletion of higher-energy emission bands*, including the green ones.

In other words, in excitation spectra recorded at emission wavelengths shorter than those corresponding to the red region (e.g., 543 nm), the 1139 nm band is **entirely absent**. This is a particularly intriguing observation with direct implications for the analysis of the photophysical pathways enabled by the 1139 nm beam.

In the literature just discussed, excitation around 1140 nm had a significant effect on green emission—in YbEr co-doped nanoparticles, this effect was negative, leading to depletion of green emission. Yet in our case—under co-excitation with a 975 nm beam—we observe no such effect. This striking difference must be carefully considered in the analysis of the relevant photophysical pathways.

As is now becoming clear, the effects associated with the addition of the 1139 nm beam represent the most compelling component of our investigation into the photophysical behavior of YbEr nanoparticles

6: Where *contribution* need not necessarily imply enhancement—it may also signify any noticeable interaction. In our case, however, only enhancement effects were observed.

7: This case was discussed in the theoretical introduction (Section 1.1.5), but we will revisit it here as well—to draw clear comparisons and contrasts with our own findings.

under co-excitation. Accordingly, this wavelength—1139 nm—will serve as the central axis of this chapter.[8]

8: This axis, however, will have its branches—nothing will go without commentary. Yet it must be emphasized that this stands as the most valuable discovery presented in this chapter.

For now, however, to more fully understand each aspect of the nanoparticles' behavior within a given spectral regime, let us take a broader look at the collected results. And although these particles are fundamentally distinct from their thulium-doped counterparts, it is still instructive to assess their behavior through at least a minimal comparison—bringing us to one of the first key observations.

In erbium-doped nanoparticles, we observe significantly smaller enhancements, on the order of several *tens of percent*—as compared to the several hundred percent increases seen for thulium-doped nanoparticles, under identical excitation powers.

This is particularly evident in the surplus 657 nm emission plot shown in Fig. 5.1b. It is useful here to recall that the surplus is defined as the difference between the emission intensity obtained under co-excitation and the sum of the emission intensities measured when each excitation beam is used on its own—this difference is then normalized to that sum. The mathematical form of this definition is given in Eq. 3.1.

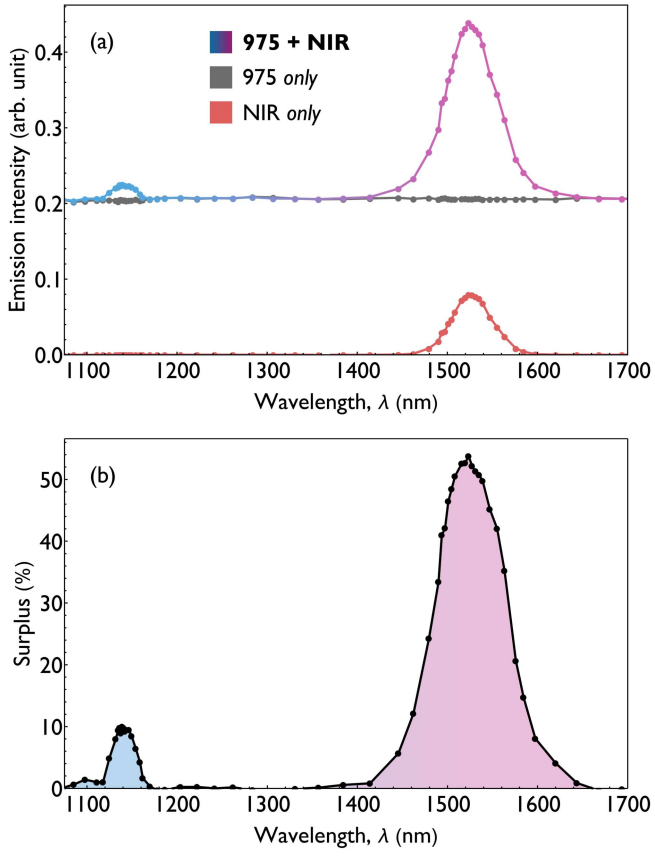

Figure 5.2: Excitation spectra of YbEr nanoparticles recorded at 657 nm emission under simultaneous excitation with two spatially overlapped beams: a continuous-wave 975 nm beam (10 mW) and a tunable pulsed NIR beam with **reduced** power (40 mW). **(a)** Excitation spectra measured under three excitation conditions—each plotted on the same scale and normalized to the maximum recorded value: *(i)* co-excitation with both beams (blue-pink bichromatic line, used to visually separate the two distinct bands corresponding to color-coded transitions), *(ii)* excitation with the NIR beam only (coral line near the bottom, showing non-zero values around 1520-1530 nm), and *(iii)* baseline emission generated by the 975 nm beam alone (gray points; a steady level, as the 975 nm beam has a fixed wavelength; however, single-beam measurements with the 975 nm excitation were still performed at each tuning step of the NIR beam). Emission intensity is plotted as a function of NIR excitation wavelength. **(b)** Surplus emission plot under co-excitation, illustrating the enhancement relative to the **sum** of emissions from each beam individually—*with no visible obvious signs of saturation*.

The analysis of YbEr nanoparticles using the tunable NIR beam alone also yields important insights. While the 1139 nm beam, at the given power level, does not independently induce measurable emission, the 1523 nm beam *most certainly does*—and significantly so. This is by no

means a new discovery, as it is well established and has already been discussed in the theoretical introduction,[9] but it remains relevant in the broader context of what follows.

9: See Sections 1.1.4 and 1.1.5.

It also relates to the particular shape of the co-excitation spectrum involving the 1523 nm beam (Fig. 5.1a), where a dip appears at the peak—possibly indicative of saturation. This saturation *may* involve a thermal component due to the strong absorption of the 1523 nm beam, though it is unclear whether, or to what extent, this is the case.[10]

10: We cannot rule this out—the 1523 nm beam, after all, is a femtosecond pulsed source (unlike the strongly absorbed 975 nm beam, which is a continuous-wave beam of moderate power).

To see results clear of potential saturation effects—or at least less affected by them, a comparable spectrum was recorded using a reduced NIR power—40 mW instead of 100 mW. As shown in Fig. 5.2a, this yielded a spectrum without *obvious* signs of saturation—with a pronounced co-excitation maximum located at a wavelength of 1523 nm. Despite the reduced power, the surplus emission caused by co-excitation with the 1523 nm beam remained at a similar level, whereas the surplus from co-excitation with the 1139 nm beam diminished significantly.

To better understand these intricacies, we must now view them through the lens of the relevant energy levels. Let us proceed to the possible excitation pathways that ground all we have observed so far.

5.1.2 Photophysical pathways

The diagram in Fig. 5.3 presents the most probable NIR-beam-driven transitions in erbium ions responsible for the observed enhancement during co-excitation with the 975 nm beam, with consideration restricted to lower-lying energy levels. The 1523 nm beam is primarily resonant with the ground-state absorption (GSA) transition $^4I_{15/2} \longrightarrow {}^4I_{13/2}$, which is characterized by a high oscillator strength. However, this is not the full extent of its contribution. The beam also has the potential to drive several higher-energy transitions via excited-state absorption (ESA). Among these, the most relevant in the context of co-excitation with 975 nm and the resulting 657 nm emission is the highly probable $^4I_{11/2} \longrightarrow {}^4F_{9/2}$ transition.

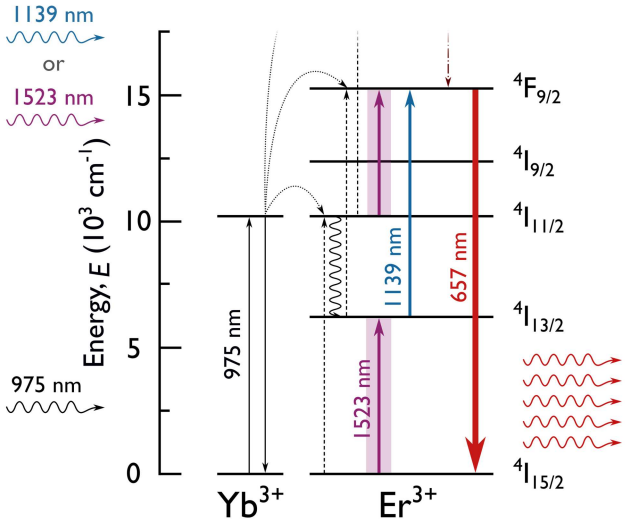

Figure 5.3: Energy level diagram illustrating the most probable observed transitions during the co-excitation experiment with the 975 nm beam and the tunable NIR beam, limited to lower-lying energy levels. The diagram marks most likely transitions in the considered region, color-coded to correspond to different excitation wavelengths used in the experiment. It thus provides a condensed summary of two distinct excitation conditions, as detailed in the course of the experiment and described in Section 2.4. The thickness of the absorption lines for erbium ions—particularly those accessible via the NIR beam—roughly reflects oscillator strengths, as described by Judd-Ofelt theory. Due to their significantly higher value, the transitions driven by the 1523 nm beam are displayed as a transparent overlay for clarity.

Even independently—without the sensitizing effect of ytterbium ion excitation by the 975 nm beam—the 1523 nm beam is capable of inducing upconversion, producing not only red emission but also higher-energy bands. This is illustrated in Fig. 5.4, which marks all possible transitions driven by the 1523 nm beam.

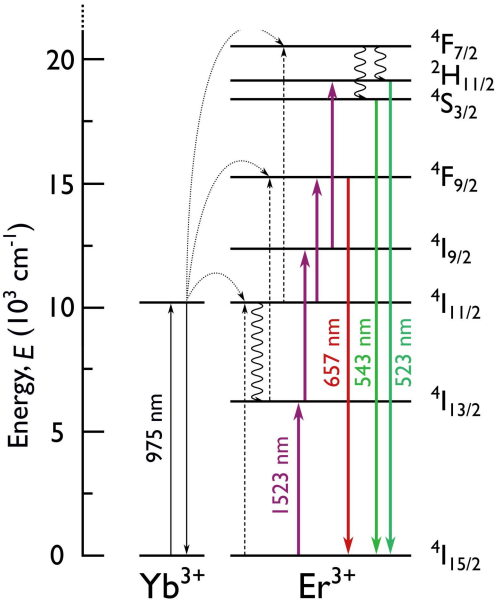

Figure 5.4: Energy level diagram illustrating all probable transitions during single-beam excitation at 1523 nm, as well as co-excitation with 975 nm and 1523 nm beams, extending up to the levels associated with the 657 nm red emission and the green emissions at 543 and 523 nm. For clarity, line thickness *does not* reflect oscillator strength.

Given this information, one cannot help but ask: why, despite its strong resonance with GSA and the high likelihood of ESA transitions, does the 1523 nm beam produce *only a moderate surplus* in emission during co-excitation? The answer, however, is relatively straightforward—its high oscillator strengths become a *limiting* factor for the cooperative effect. This is because significant competition arises from the 1523 nm beam's independent ability to excite emission on its own. In other words, the bandwidth for mutual cooperation is constrained not only by the upconversion pathways driven by the 975 nm beam, but also by those driven solely by the 1523 nm beam.

However, it is not the 1523 nm beam—despite the abundance of transitions it makes possible—that constitutes the most compelling aspect of our investigation. A far more intriguing insight emerges from the diagram in Fig. 5.3: a newly uncovered excitation pathway enabled by co-excitation with the 1139 nm beam.

According to the energy level analysis, the 1139 nm beam corresponds to an excited-state absorption (ESA) transition: $^4I_{13/2} \longrightarrow {}^4F_{9/2}$. It does not contribute meaningfully to ground-state absorption (GSA) due to significant energy mismatch.

The $^4F_{9/2}$ level is associated with red emission at 657 nm, which shows a clear enhancement when the 1139 nm beam is added to the 975 nm excitation. This also explains why, within the examined power regime, the 1139 nm beam alone produces virtually no detectable emission. One might attempt to attribute this to a low-probability GSA transition; however,

as previously noted, the energy mismatch is also considerable—and without an efficient GSA process, the $^4I_{13/2}$ state remains too sparsely populated for subsequent ESA to proceed effectively.

This makes for an important—and genuinely fascinating—observation. The 1139 nm beam appears to be perfectly tailored for co-excitation: it contributes meaningfully in tandem, yet should not, on its own, reduce the bandwidth of mutual interplay—which, of course, remains influenced by upconversion from the 975 nm beam alone.

The moderate surplus observed with this beam is also easily explained—its absorption probability is low, and it drives only a single transition under the considered conditions.

But *does* it?

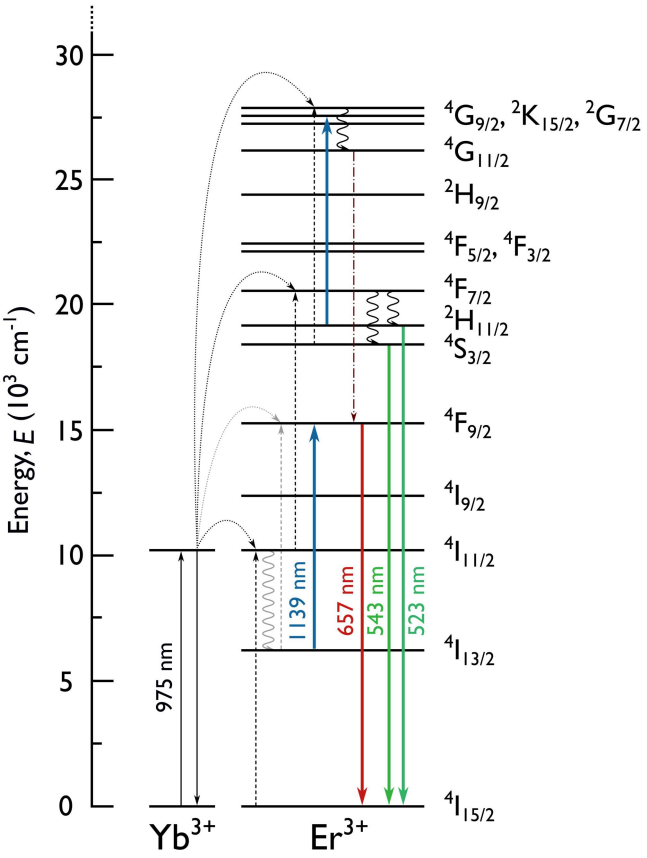

Figure 5.5: Energy-level diagram illustrating the most relevant transitions under single-beam excitation at 975 nm and co-excitation with 975 nm and 1139 nm beams. The diagram includes higher-lying states associated with 1139 nm absorption and interionic (ytterbium-erbium) energy transfer pathways leading to the $^4G_{11/2} \longrightarrow {}^4F_{9/2}$ transition in erbium. For clarity, line thickness does *not* represent oscillator strength.

Let us consider an expanded energy-level diagram (Fig. 5.5), now including states involved in higher-energy green emission and beyond. The 1139 nm beam corresponds also to the $^2H_{11/2} \longrightarrow {}^2K_{15/2}$ transition, which should, in theory, lead to a depletion of green emission by depopulating the $^2H_{11/2}$ state.[103] This effect becomes particularly relevant in the presence of ytterbium ions, which enable an additional energy transfer pathway[90]:

$$^4G_{11/2}\,(Er^{3+}) + {}^2F_{7/2}\,(Yb^{3+}) \longrightarrow {}^4\mathbf{F_{9/2}}\,(Er^{3+}) + {}^2F_{5/2}\,(Yb^{3+}),$$

as marked on the diagram by a maroon dashed-dotted arrow. Through this mechanism, population is funneled away from green-emitting levels,

favoring a lower-energy endpoint.

Which leads us—inevitably and intriguingly—to **red emission**. At first glance, the connection between ytterbium ions, the 1139 nm beam, and the population of the $^4F_{9/2}$ state may seem tenuous. But in reality, this pathway represents a previously underappreciated route for populating the red-emitting state.

And yet, the green emission shows no sign of depletion—*why?* In our view, the answer lies in the choice of co-excitation wavelength. The depletion was previously reported under co-excitation with a 795 nm beam. In contrast, we employ a 975 nm beam, resonant with the $^2F_{7/2} \longrightarrow {}^2F_{5/2}$ transition in Yb^{3+}. While this wavelength facilitates ETU and supports efficient population of erbium levels, it simultaneously inhibits the aforementioned energy transfer by pre-populating the $^2F_{5/2}$ state in Yb^{3+}.

As a result, the $^4G_{11/2} \longrightarrow {}^4F_{9/2}$ relaxation pathway—normally a contributor to red emission and a suppressor of green—is attenuated. The system is effectively steered away from energy redistribution via energy transfer, and toward a slower, less selective trickle-down through the excited-state ladder.

Thus, the 975 nm beam serves a dual role: it enables population of erbium states while simultaneously suppressing competing routes. The $^4I_{13/2} \longrightarrow {}^4F_{9/2}$ transition, driven by the 1139 nm beam, enhances red emission. Meanwhile, the higher-energy $^2H_{11/2} \longrightarrow {}^2K_{15/2}$ transition, in the presence of 975 nm excitation, no longer selectively suppresses green emission—its effect is softened, absorbed into the broader dynamics of energy relaxation.

What of the other, *less tailored* transitions?

From the standpoint of energy matching and transition probability, possible ESA transitions such as $^4I_{11/2} \rightarrow {}^4S_{3/2}$ and $^4I_{11/2} \rightarrow {}^2H_{11/2}$ appear viable (Fig. 5.6). These are directly linked to green emission bands at 543 nm and 523 nm, respectively.

Based solely on theoretical considerations, one might predict that the 1139 nm beam could participate in these ESA processes and thus partially influence the green emission observed under co-excitation. But theory, as always, must defer to experiment—and experiment tells a different story.

Across the entire range of excitation powers studied, co-excitation with the 1139 nm beam shows **no effect** on green emission at either 523 nm or 543 nm. This confirms that the only probable transitions enabled by the 1139 nm beam are the ESA transitions $^4I_{13/2} \longrightarrow {}^4F_{9/2}$ and $^2H_{11/2} \longrightarrow {}^2K_{15/2}$.

This suggests that a combination of low oscillator strengths and slight energy mismatch forms a barrier that cannot be overcome—leaving just two active transitions, precisely energy-matched, to dominate the interaction.

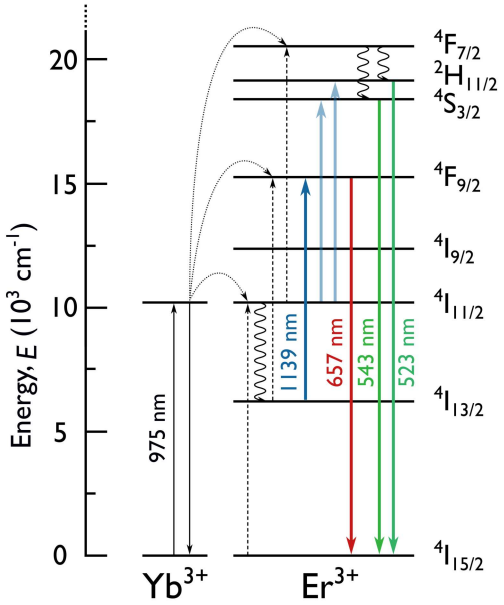

Figure 5.6: Energy level diagram illustrating all transitions that are energetically plausible—though not necessarily occurring—during co-excitation with the 975 nm and 1139 nm beams, extending up to the levels associated with the 657 nm red emission and the green emissions at 543 and 523 nm. Transitions originating from the $^4I_{11/2}$ level are shown in a lighter color, reflecting our experimental conclusion that the 1139 nm beam **does not influence** the green emission bands. For clarity, line thickness *does not* reflect oscillator strength.

Thus, in our experiment, we observe two fundamentally distinct modes of NIR beam interaction with erbium-doped nanoparticles under co-excitation with 975 nm: the 1523 nm beam, characterized by its broad and multifaceted engagement across numerous accessible transitions, and the 1139 nm beam, more selective and narrowly focused, contributing primarily through well-defined ESA pathways under the given conditions.

5.2 *Emission as a function of power*— single-wavelength excitation

To grasp the effects arising from the combined action of the beams, we must first examine their individual contributions—particularly in the context of our specific case. Let us recall that we are working with typical nanoparticles doped with 2% erbium ions, where the inclusion of ytterbium (at 20%) serves as the gateway for inducing emission via excitation with a resonant 975 nm beam, followed by energy transfer to the erbium ions. Accordingly, we begin with the 975 nm beam.

5.2.1 975 nm

As previously mentioned, our primary focus is on the emission band peaking at 657 nm—after all, it serves as the key indicator of the influence exerted by the additional excitation band at 1139 nm. However, since we also take a comprehensive approach and briefly examine co-excitation with the 1523 nm beam—which does affect other emission bands, including the green region—it is essential to consider those as well. Accordingly, the analysis of the 975 nm beam's power dependence was extended and is presented through the lens of emission measured not only at 657 nm, but also at 543 nm.

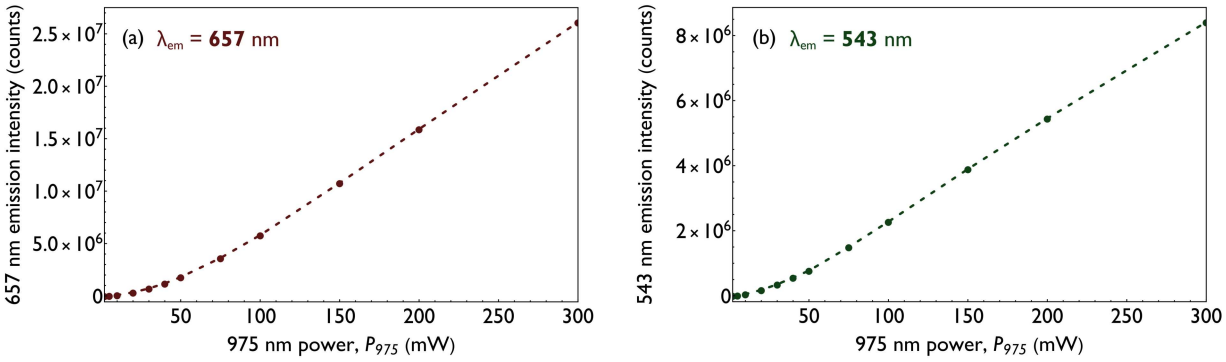

Figure 5.7: Emission intensity recorded at **(a)** 657 nm and **(b)** 543 nm of YbEr nanoparticles as a function of 975 nm beam power, measured in the range of 2-300 mW under single-beam excitation. The dashed line is included as a visual guide.

Fig. 5.7 presents the dependence of selected emission intensities on the power of the 975 nm excitation beam. Using a well-established approach[11]—analyzing nonlinear response by fitting a simple power-law function (where ξ is the exponent)—we can immediately observe that the response falls within the typical[12] range for upconverting nanoparticles and varies with the applied power range. Figs. 5.8a and b show the plots of the best-fit functions for the emission intensity measured at 657 nm across three power regimes. As seen, the nonlinearity decreases with increasing power, a typical behavior associated with saturation. While dividing the data into three regimes is informative, it is not practically necessary—it should be emphasized that these values are approximate, intended to provide qualitative understanding rather than precise description. Accordingly, the fitting was repeated over a restricted power range of 10-200 mW (Figs. 5.8c and d). Within this interval, a two-regime division proved entirely sufficient: the low-to-moderate power region is well

11: As described in the theoretical introduction (Section 1.1.3) and presented during the analysis of the emissive properties of thulium-doped nanoparticles—see Section 3.2.1, particularly Eq. 3.2 along with its accompanying commentary.

12: As described in the theoretical introduction, see Section 1.1.3.

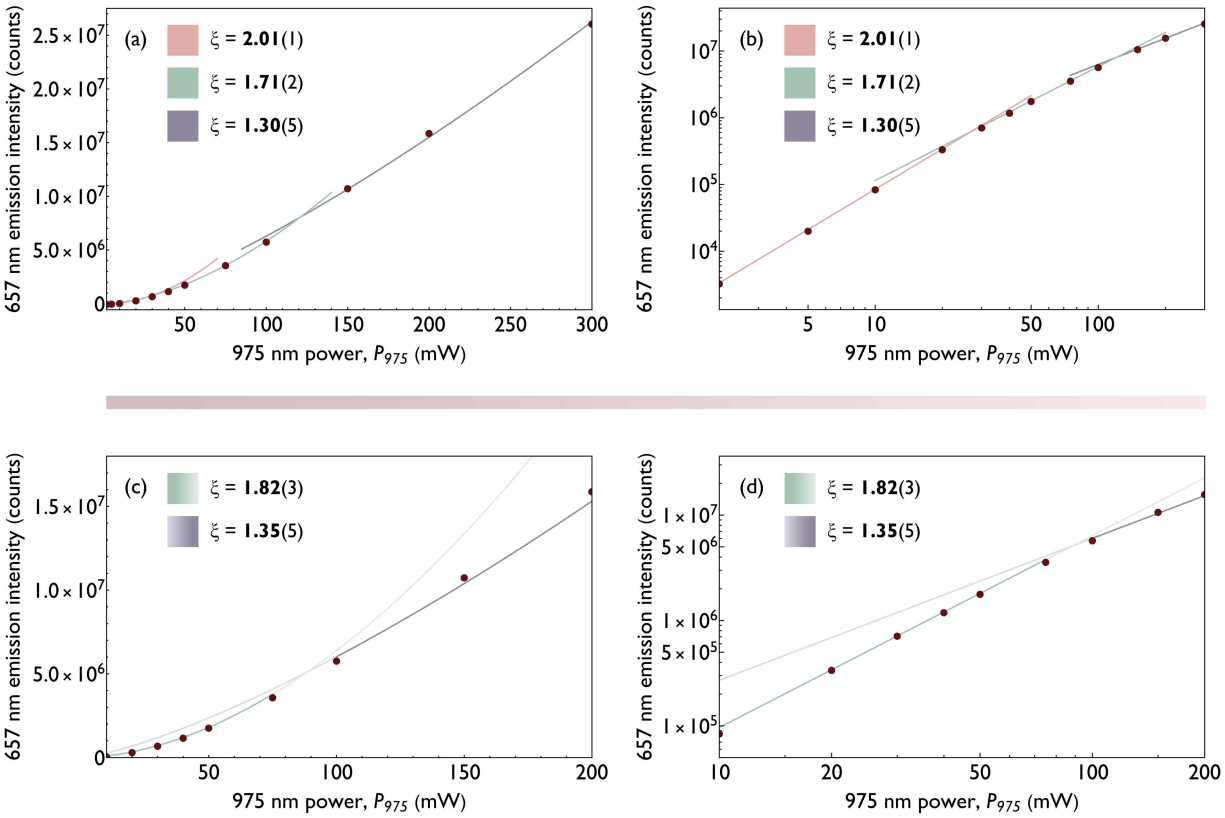

Figure 5.8: Emission intensity (recorded at 657 nm) of YbEr nanoparticles as a function of 975 nm beam power (2-300 mW), measured under single-beam excitation. Fitted trends are included. **(a)** Results shown on a linear scale. **(b)** Results presented on a log-log scale. The fitting was divided into three power regimes: the pink line corresponds to the lowest power range, the green to the moderate, and the gray to the high-power regime. When the analysis is limited to the 10-200 mW range, a satisfactory fit can be achieved using only two regimes. **(c)** Results for the restricted power range shown on a linear scale. **(d)** Results presented on a log-log scale. Green line: fit for the low-power part of constrained regime of the 975 nm beam, extended across the full range in a lighter shade. Gray line: fit for the high-power part of constrained regime, extended across the full range in a lighter shade.

described by a nonlinearity of **1.82**(3), while the high-power regime is characterized by a lower exponent of **1.35**(5).

A similar analysis was performed for the green emission, recorded at 543 nm. Once again, the full power range was initially divided into three regimes (Figs. 5.9a and b), and subsequently reduced to two when fitting was limited to a narrower interval (Figs. 5.9c and d). Here, the moderate-power regime exhibited a nonlinearity of **1.57**(5), while the high-power regime was fit with an exponent of **1.19**(5). The most notable distinction is that the nonlinearity with respect to 975 nm excitation power is slightly *lower* for the green emission. One might (not entirely accurately) argue that both the red (657 nm) and green (543 nm) emissions arise from comparable processes in terms of the number of absorption and energy transfer steps.[13]

For the 657 nm emission, two energy transfers occur with an intermediate relaxation from the $^4I_{11/2}$ to the $^4I_{13/2}$ level. In contrast, the 543 nm emission pathway involves two consecutive energy transfers, followed by relaxation from $^4F_{7/2}$ to $^4S_{3/2}$ prior to photon emission.

But this interpretation may be misleading—or at least incomplete. As shown in the diagram in Fig. 5.5, an additional, more complex pathway must be considered: one involving **three sequential acts** of absorption and energy transfer, reaching as high as the ^2G, ^2K manifold.[90] This

13: Refer to Fig. 1.9 in the theoretical introduction, or focus specifically on the ytterbium-mediated energy transfer pathway illustrated in Fig. 5.5.

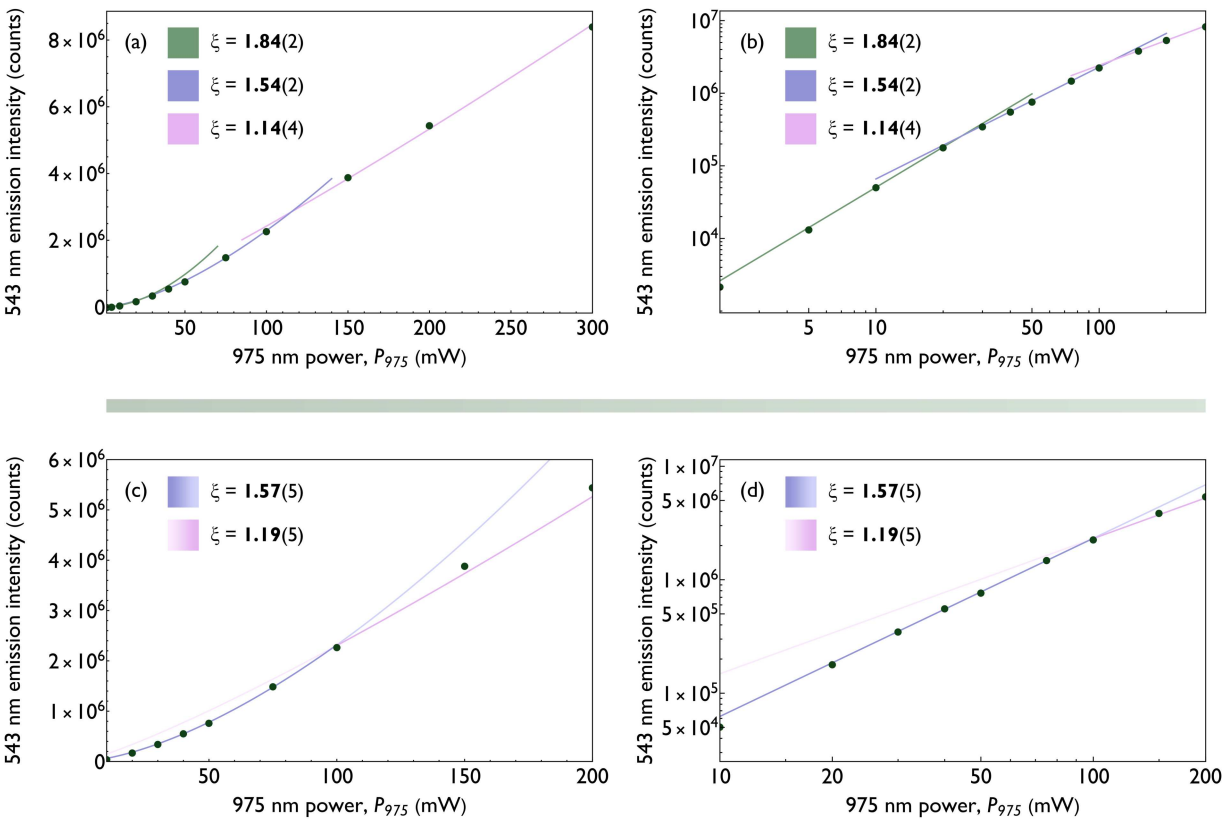

Figure 5.9: Emission intensity (recorded at 543 nm) of YbEr nanoparticles as a function of 975 nm beam power (2-300 mW), measured under single-beam excitation. Fitted trends are included. **(a)** Results shown on a linear scale. **(b)** Results presented on a log-log scale. The fitting was divided into three power regimes: the green line corresponds to the lowest power range, the violet to the moderate, and the pink to the high-power regime. When the analysis is limited to the 10-200 mW range, a satisfactory fit can be achieved using only two regimes. **(c)** Results for the restricted power range shown on a linear scale. **(d)** Results presented on a log-log scale. Violet line: fit for the low-power part of constrained regime of the 975 nm beam, extended across the full range in a lighter shade. Pink line: fit for the high-power part of constrained regime, extended across the full range in a lighter shade.

is followed by an energy transfer step that ultimately populates the red-emitting state: $^4F_{9/2}$.

It has also been postulated that direct energy transfer from the $^4I_{13/2}$ level to $^4F_{9/2}$ is inefficient.[90] Instead, population of $^4F_{9/2}$ likely occurs via relaxation from higher states such as $^4F_{7/2}$, or through the aforementioned energy transfer after excitation to the ^2G,^2K manifold.[90, 91]

This mechanistic complexity explains why the red emission—despite originating from a lower-lying level—exhibits a **higher degree of non-linearity** under 975 nm excitation than the green emission. And indeed, this aligns fully with our experimental observations.

Thus, the results presented here characterize the emission response of the analyzed nanoparticles to 975 nm excitation and establish a baseline for interpreting more complex co-excitation behaviors discussed in the following sections.

5.2.2 1523 nm

As discussed in the theoretical considerations and at the beginning of this chapter, the 1523 nm beam holds a unique position: it is exceptionally effective—by the standards of direct excitation[14]—at exciting erbium ions without the involvement of ytterbium ions, leading to a clearly observable upconversion effect. This time, therefore, the notably high emission intensities (for a beam in the NIR range) warrant particular attention.

14: It is worth keeping in mind that, as with all upconversion processes, the efficiency remains inherently low.

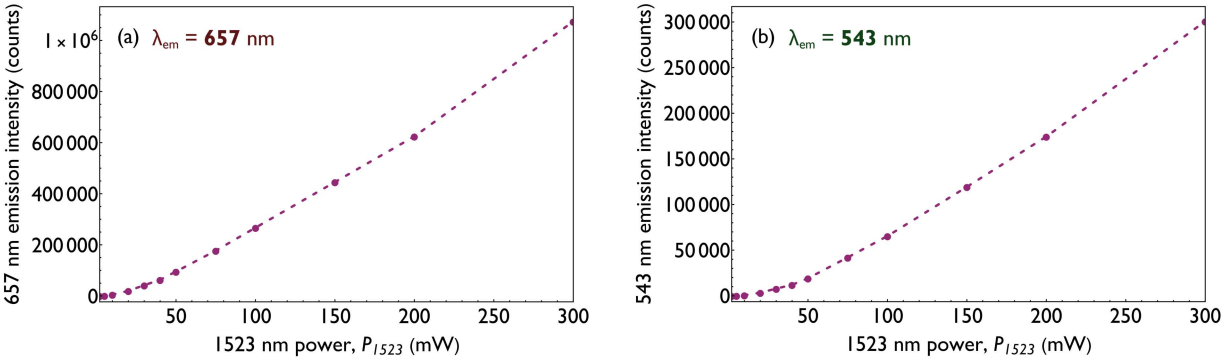

Figure 5.10: Emission intensity recorded at **(a)** 657 nm and **(b)** 543 nm of YbEr nanoparticles as a function of 1523 nm beam power, measured up to 300 mW under single-beam excitation. The dashed line is included as a visual guide.

Fig. 5.10 presents the power dependence of emission measured at both 657 nm and 543 nm under excitation solely by the 1523 nm beam. One can immediately observe a familiar trend, similar to that seen with the 975 nm beam: a slight decrease in nonlinearity with increasing power. To quantify this behavior, the full range of excitation powers was divided into two regions—an approach that proved sufficient. The resulting plots of the best-fit functions and corresponding exponents are shown in Fig. 5.11: Figs. 5.11a and b relate to emission recorded at 657 nm, while Figs. 5.11c and d correspond to 543 nm. For the red emission, the extracted power-law exponents were **1.60**(3) for moderate powers and **1.29**(2) for higher powers. For the green emission, the values were **1.92**(3) and **1.37**(2), respectively.

The most notable observation—beyond the values themselves, which may serve as useful references—is the reversed relationship between the exponents for 657 nm and 543 nm emission compared to those obtained under single-beam excitation with the 975 nm source. This time, the nonlinearity is *higher* for the green emission.

And this should come as no surprise. Let us briefly return to the energy level diagram illustrating the upconversion pathway enabled by the 1523 nm beam alone (Fig. 5.4). Without any concurrent energy transfer from ytterbium ions, generating green emission requires at least four absorption events, while red emission can be achieved with only three. This aligns well with the observed difference—and the direction of that difference—in nonlinearity: a more complex photophysical pathway naturally corresponds to a more complex response, and nonlinearity serves as a direct measure of that complexity. These results not only align with theoretical expectations but also reinforce the validity of the extracted parameters as reliable reference points for further analysis—well grounded in both observation and mechanism.

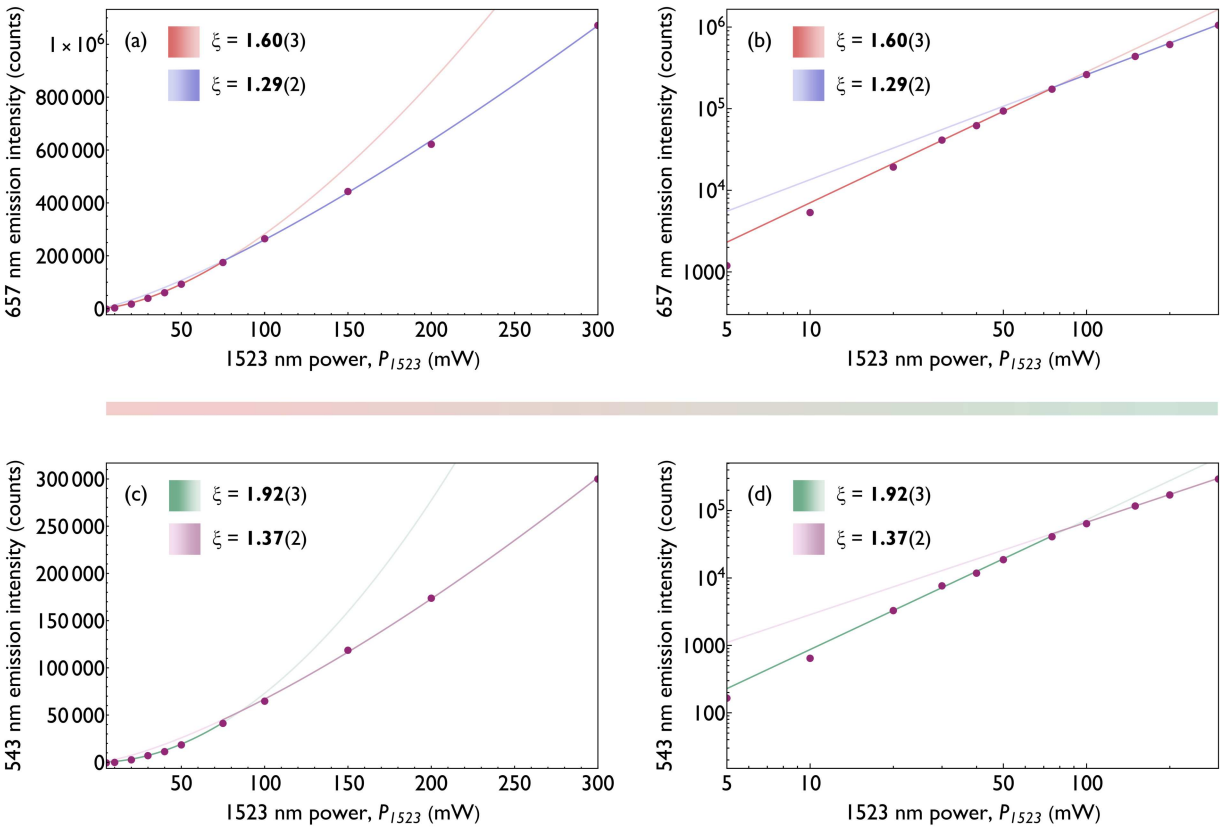

Figure 5.11: Emission intensity of YbEr nanoparticles as a function of 1523 nm beam power (5-300 mW), measured under single-beam excitation. Fitted trends are included. **(a)** Emission recorded at 657 nm, shown on a linear scale. **(b)** Emission recorded at 657 nm, shown on a log-log scale. Red line: fit for the low-power regime of the 1523 nm beam, extended across the full range in a lighter shade. Blue line: fit for the high-power regime, extended across the full range in a lighter shade. **(c)** Emission recorded at 543 nm, shown on a linear scale. **(d)** Emission recorded at 543 nm, shown on a log-log scale. Green line: fit for the low-power regime of the 1523 nm beam, extended across the full range in a lighter shade. Pink line: fit for the high-power regime, extended across the full range in a lighter shade.

5.2.3 1139 nm

Here—instead of detailed plots, fittings, or extended discussion—a brief but illustrative remark will suffice. Nearly all emission intensity data points recorded under excitation with the 1139 nm beam alone remained at or near background level—*across the entire range of applied power*, or more importantly, *power density*.[15] As a result, under the measurement conditions used (i.e., those matching the co-excitation experiments), it is not possible to determine a meaningful power dependence for the 1139 nm beam alone, as no measurable emission occurs.

This is a key observation—previously noted and now explicitly reaffirmed—providing full justification for excluding the independent contribution of this beam from further analysis. With the single-beam experiments now concluded and this understanding in hand, we can shift our focus to the next stage: the co-excitation experiments.

15: **A prophetic statement**—soon to be expanded upon in Chapter 6.

5.3 *Surplus emission* under dual-wavelength co-excitation

Yes, we begin somewhat unconventionally—at least differently than in the analysis of thulium ions. To avoid disrupting the momentum of the unfolding narrative—and to keep the spotlight firmly on the central discovery embodied in the 1139 nm band—we have chosen to introduce, already at this stage of the co-excitation experiments with the 1523 nm beam, the central to this study concept of emission surplus. This choice is particularly fitting, as the surplus presents a strikingly different picture here compared to the emission behavior of thulium-doped upconverting nanoparticles.[16]

16: It is **strongly** recommended that all findings presented here be considered in comparison with those obtained for thulium-doped nanoparticles—which formed the core of our investigation and serve as a foundational reference point. Accordingly, in the context of emission surplus, it is useful to refer back to Section 3.4 for comparison.

Surplus also serves as an indirect measure of total emission intensity—and it was, in fact, through the analysis of total emission that we were led to this concept, ultimately establishing it as a cornerstone of our investigation. With that groundwork laid, we now move past preliminary considerations and turn our attention to what truly matters: *the effect itself*.

Let us briefly recall that surplus emission is defined as the relative increase in emission under co-excitation, compared to the combined emissions produced by the individual beams when used separately. The corresponding mathematical expression was presented in Eq. 3.1, but for convenience, it is restated below:

$$S_\lambda = \frac{E_{\text{co-ex}}(\lambda) - (E_{\text{NIR}}(\lambda) + E_{975})}{E_{\text{NIR}}(\lambda) + E_{975}} \cdot 100\%.$$

In the case of co-excitation with the 1523 nm beam, the analysis was conducted by monitoring emission at both 657 nm and 543 nm—whereas for the 1139 nm beam, due to its inherent lack of influence on green emission, only the 657 nm emission was examined. Let us therefore begin our account with the 1523 nm beam, which proves to be unexpectedly intricate—and distinctly *different*.

5.3.1 1523 nm

What goes up must come down.

And not always gently. The trend of surplus emission in both the red and green regions of erbium-doped nanoparticles, recorded under co-excitation with 975 nm and 1523 nm beams as a function of the latter's power, reveals a distinctly different behavior, shown in Fig. 5.12. Drawing on the analysis of thulium-doped nanoparticles, one might expect a steady increase—after all, the additional NIR beam in that case did not compete with the 975 nm excitation, and its contribution was limited almost entirely to mutual interplay.

But the 1523 nm beam is a different story. As emphasized from the outset,[17] this beam has a strong, independent capacity to excite Er^{3+} $4f$ manifolds. When both beams are combined, we indeed open the door to cooperative interaction—but it turns out to be a narrow one, quickly overshadowed by the dominant individual contributions of each beam. As illustrated in

17: See Sections 5.1.2 and 5.2.2.

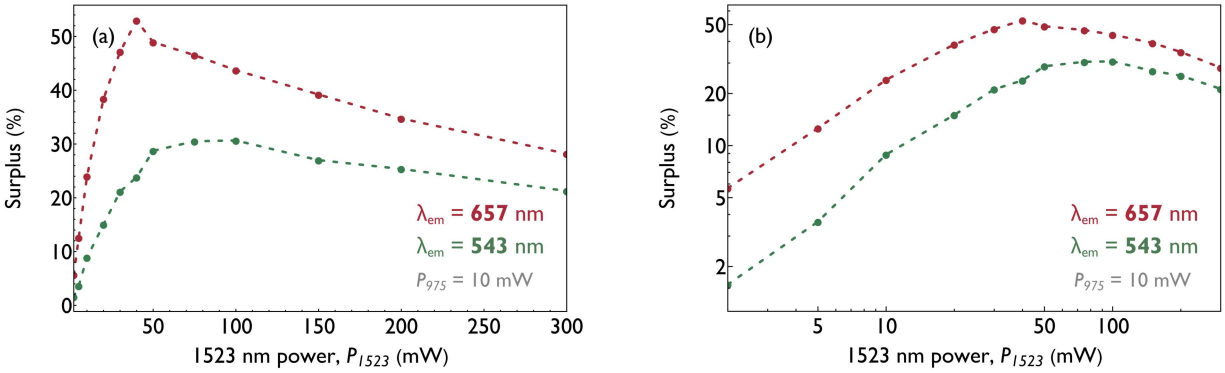

Figure 5.12: Surplus emission obtained at 657 nm and 543 nm from YbEr nanoparticles as a function of 1523 nm beam power, measured up to 300 mW under dual-beam excitation with the 975 nm beam held constant at 10 mW. **(a)** Results shown on a linear scale. **(b)** Results shown on a log-log scale. The dashed line is provided as a visual guide

Fig. 5.12, with the 975 nm beam power held constant, we initially observe an increase in surplus emission at low powers of the 1523 nm beam. However, this rise is short-lived.

As the 1523 nm beam power increases, surplus reaches a peak and then begins to **decline**.

Indeed, we see a clear drop in surplus emission with increasing NIR power—an effect driven by the 1523 nm beam's growing dominance in exciting Er^{3+} ions independently. This increasing independence begins to overpower the mutual interplay with the 975 nm beam. This dynamic also explains the saturation effect observed in the surplus dependence on NIR excitation wavelength in Fig. 5.1b, which appeared to diminish in a subsequent measurement performed at reduced NIR power (Fig. 5.2b). The first dataset, acquired at 100 mW, was already within the regime where the surplus—particularly the 657 nm surplus emission—had begun to decline (notably, the decline in green emission surplus occurs at higher NIR powers). The second dataset, recorded at 40 mW, was obtained closer to the optimal excitation conditions for the nanoparticles under study.

The dip observed in the first of these plots (Fig. 5.1b) can be attributed to the underlying behavior of the surplus curve. It is essential to emphasize that this is not a case of the surplus merely settling into a plateau, but rather a true maximum being reached and subsequently followed by a decline (see Fig. 5.12). Thus, when using resonant excitation at high power—1523 nm in our case—the observed surplus was actually lower than what was achieved using slightly detuned pulses, which due to their spectral width[18] still encompassed 1523 nm but delivered it at a lower effective power.

18: A description of the obtained pulses is provided in the methodology section; see Section 2.1 and Fig. 2.3.

Thus, what we observe is a form of *self-inhibition* of the cooperative effect by the 1523 nm beam itself. Cooperation does occur, but it is swiftly overwhelmed by the 1523 nm beam's strong independent excitation capacity.

Not every blossom comes to full bloom.

Tracing lines

Tracing, more than fitting—since we're working with more limited datasets than in the case of thulium-doped[19] nanoparticles. Yet the analysis for erbium-based nanoparticles was also carried out thoroughly, though across a narrower scope. Without a full power-matrix dataset, it's difficult to provide a complete picture of the dependencies—but we can still attempt to outline the general trend.

19: Which remain the core focus of this work.

Fig. 5.13 presents the dependence of surplus emission in the red (Figs. 5.13a and b) and green (Figs. 5.13c and d) regions as a function of 1523 nm beam power, with the 975 nm beam held constant at 10 mW. The included segmented fits serve a descriptive role rather than a rigorous one. What stands out immediately—both visually and numerically—is the trend: at low powers of the 1523 nm beam, surplus increases with power. However, this trend shifts, and after reaching a certain maximum, the surplus begins to decline as 1523 nm power continues to rise.

Let us now revisit the extended formulation that successfully described the surplus behavior in thulium-based nanoparticles—Eq. 3.26, which is reproduced below for convenience.

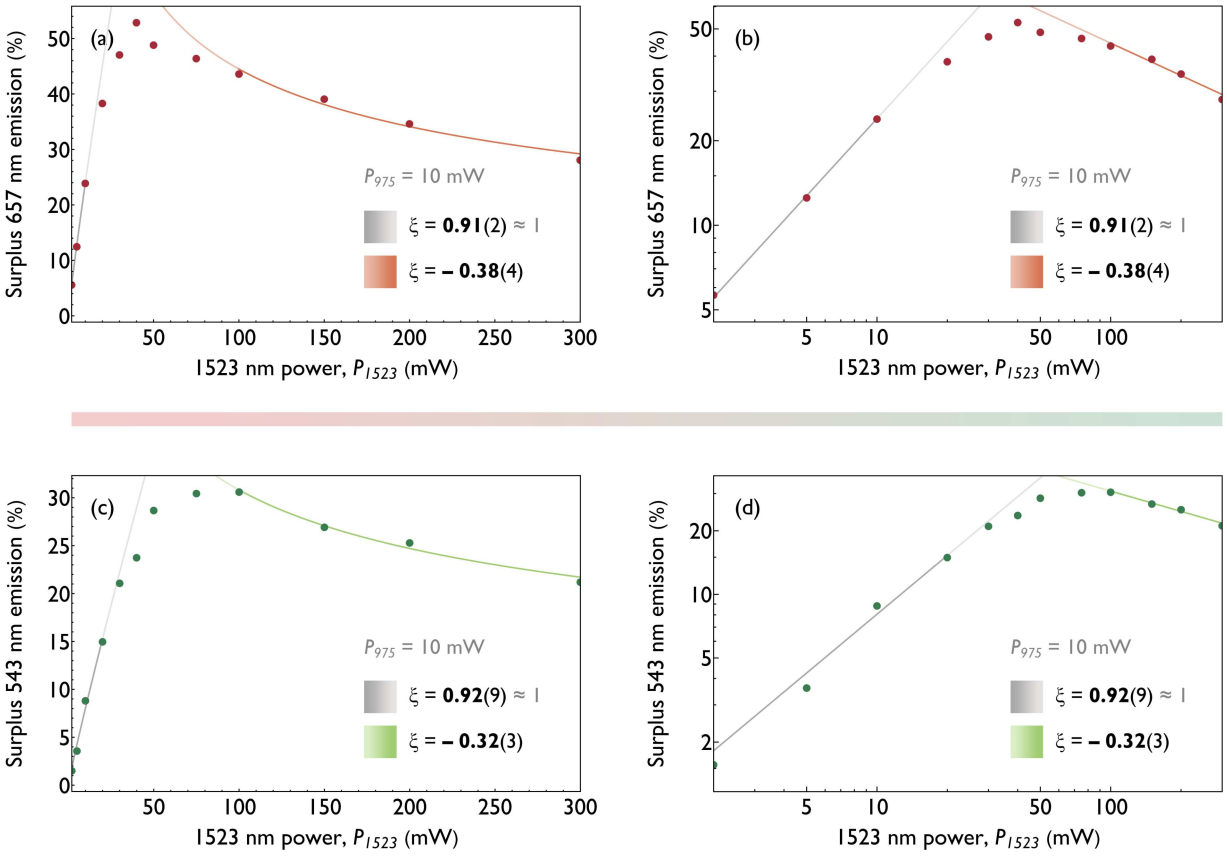

Figure 5.13: Surplus emission of YbEr nanoparticles as a function of 1523 nm beam power, obtained under dual-beam excitation with a 975 nm beam held constant at 10 mW. Fitted trends are included. **(a)** Surplus 657 nm emission, shown on a linear scale. **(b)** Surplus 657 nm emission, shown on a log-log scale. Orange line: fit for the high-power regime of the 1523 nm beam, extended across the full range in a lighter shade. Gray line: fit for the low-power regime, extended across the full range in a lighter shade. **(c)** Surplus 543 nm emission, shown on a linear scale. **(d)** Surplus 543 nm emission, shown on a log-log scale. Green line: fit for the high-power regime of the 1523 nm beam, extended across the full range in a lighter shade. Gray line: fit for the low-power regime, extended across the full range in a lighter shade.

$$S = \frac{\mathcal{A} \cdot P_{\mathrm{NIR}}^{\alpha} \cdot P_{975}^{\omega}}{\left(b \cdot P_{\mathrm{NIR}}^{\gamma} + c \cdot P_{975}^{\delta}\right)}$$

In this equation, the exponents α and ω describe the power dependence of the mutual interplay term with respect to each beam, while δ and γ capture the independent contributions of the individual beams—i.e., the system's response to single-beam excitation.

When we limit ourselves to analyzing the behavior as a function of NIR beam power alone (in this case, 1523 nm), this equation simplifies to the following form:

$$S = \frac{B \cdot P_{\mathrm{NIR}}^{\alpha}}{\left(b \cdot P_{\mathrm{NIR}}^{\gamma} + C\right)} \tag{5.1}$$

Now let's pause and reflect using our earlier phenomenological considerations.[20] We previously assumed that the exponents describing cooperative influence might vary with power (see Eq. 3.5 and later Eqs. 3.6 and 3.7). However, this remained a theoretical possibility, as the analysis of thulium-based nanoparticles showed no clear need to account for such variation.[21]

Instead, we adopted fixed functional forms over specific power regimes—not necessarily justified by rigorous derivation, but crucially, characterized by constant exponents (Eqs. 3.6 and 3.7). This led us to Eq. 3.26, which in turn produced Eq. 5.1.

While the earlier assumption proved valid for thulium, whether it holds for erbium remains to be seen. We will let the data speak to that shortly. But before doing so, let us focus on a more immediate aspect: the structure of the denominator.

In the denominator of Eq. 5.1, as applied to erbium-doped materials, a genuine competition unfolds. At first—meaning at low powers of the 1523 nm beam—the 975 nm beam (represented in our formulation in the constant C) clearly dominates. In this low-power regime, the equation simplifies to the following form:

$$S \approx \frac{B \cdot P_{\mathrm{NIR}}^{\alpha}}{C} = \mathfrak{C} \cdot P_{\mathrm{NIR}}^{\alpha}. \tag{5.2}$$

However, the 1523 nm beam is far from passive. As previously discussed in detail, it couples efficiently to erbium's $4f$ manifolds—particularly at higher excitation powers.[22] *How efficiently?* Sufficiently so to eventually overtake the influence of the 10 mW 975 nm beam and assert dominance in the excitation process. This transition becomes apparent in the single-excitation measurements, particularly in the red emission observed at 657 nm. For the green emission at 543 nm, the 1523 nm beam can also exceed the contribution of the 975 nm beam alone—though this occurs only at considerably higher excitation powers.[23]

Once the 1523 nm beam establishes clear dominance—which occurs only at the highest measured powers, and only for red emission—the equation should be further reduced to the following form:

20: See Section 3.3.2 and the relevant parts on fitting in Section 3.4.1.

21: Perhaps somewhat ambitiously, we previously introduced the term of *entangled* mutual interplay for thulium-doped nanoparticles (Eq. 3.5)—a formulation that was, in the end, simplified. We now return to the equation built on that streamlined reasoning. Still, it must be kept in mind that such a simplification may not necessarily hold for erbium-based systems. *The data will decide.*

22: It is worth revisiting Section 5.2.2, which quantifies the effect of the 1523 nm beam on the analyzed erbium-doped nanoparticles, especially since the conclusions drawn there prove to be particularly relevant in the present context.

23: Compare the results in Fig. 5.8 and Fig. 5.9 for nanoparticles excited with the 975 nm beam alone, with those in Fig. 5.11 under excitation by the 1523 nm beam.

$$S \approx \frac{B \cdot P_{\mathrm{NIR}}^{\alpha}}{b \cdot P_{\mathrm{NIR}}^{\gamma}} = \mathfrak{B} \cdot P_{\mathrm{NIR}}^{\alpha-\gamma} = \mathfrak{B} \cdot P_{\mathrm{NIR}}^{\kappa}. \tag{5.3}$$

We must now consider the indicative exponents[24] obtained through fitting, and particularly their difference.[25] The results of this reflection are presented below.[26]

$$\begin{aligned} \xi_{657(i)} &= \alpha_{657} = \mathbf{0.91}(2) \\ \xi_{657(ii)} &= \kappa_{657} = -\mathbf{0.38}(4) \\ \Delta_{657} &= \alpha_{657} - \kappa_{657} = \mathbf{1.29}(4) \end{aligned} \tag{5.4}$$

$$\begin{aligned} \xi_{543(i)} &= \alpha_{543} = \mathbf{0.92}(9) \\ \xi_{543(ii)} &= \kappa_{543} = -\mathbf{0.32}(3) \\ \Delta_{543} &= \alpha_{543} - \kappa_{543} = \mathbf{1.24}(9) \end{aligned} \tag{5.5}$$

Here, α represents the intrinsic contribution of the 1523 nm beam within the mutual interplay term—a pure and initially dominant influence in the overall picture at low 1523 nm powers—while κ captures its effective impact once the significant independent excitation pathways of the 1523 nm beam come into play at higher powers.

But what truly draws our attention is the difference between these two exponents.

A quick glance at Eqs. 5.2 and 5.3 is enough to see that, in the ideal case, the difference[27] between these limiting scenarios should equal γ—the exponent characterizing the independent effect of the 1523 nm beam, that is, the part not entangled in cooperative excitation channels, but arising from transitions accessible through the 1523 nm beam alone.

This is easily verified by revisiting the single-beam excitation measurements.[28] Drawing on the fits shown in Fig. 5.11, we find that the exponents describing the emission intensity as a function of 1523 nm power under single-beam excitation (**at high powers**—precisely the regime where Eq. 5.3 becomes physically meaningful) are presented in Eq. 5.6.

$$\begin{aligned} \gamma_{657} &= \mathbf{1.29}(2) \\ \gamma_{543} &= \mathbf{1.37}(2) \end{aligned} \tag{5.6}$$

And the match is remarkably precise—between the observed differences (Δ) provided in Eqs. 5.4 and 5.5, particularly for the 657 nm emission, and the independently determined γ value.[29] For the 543 nm emission, the Δ_{543} is smaller than γ_{543}, but this is entirely expected and further reinforces our earlier observations—importantly, ones drawn from completely independent single-beam measurements described in Section 5.2.2. In the case of green emission, the 1523 nm beam never fully dominates, and as a result, we do not reach a regime where Eq. 5.3—rather than its intermediate form—emerges as the most appropriate phenomenological description.[30]

24: For clarity, ξ in this work serves as a symbol representing an apparent power-law exponent, without specifying its exact nature. It appears as such in the figures. In the listings of the extracted exponents below (Eqs. 5.4 and 5.5), more specific symbols are used to associate the obtained powers with the corresponding model expression (Eq. 5.3)—thus, marking the transition from the generic ξ to concrete notation.

25: Denoted as Δ in Eqs. 5.4 and 5.5.

26: The uncertainties associated with the differences were calculated using error propagation.

27: Note that the aforementioned exponent difference was denoted as Δ in Eqs. 5.4 and 5.5—and it is this quantity that we compare to the exponents γ obtained from the single-beam excitation measurements (Section 5.2.2).

28: See Section 5.2.2.

29: Compare γ from Eq. 5.6 and Fig. 5.11 with Δ_{657} in Eq. 5.4—both yield the exact value of **1.29**. And although the fitting is employed here primarily for interpretive insight, the alignment between these two independent measurements is striking.

30: This is precisely why the *smaller* difference Δ_{543} (compared to γ_{543}) does not come as a surprise.

All of these insights lead us to a succinct conclusion.

The surplus emission of erbium-doped nanoparticles grows **constructively** with increasing 1523 nm beam power in the lower range. Yet, as the power continues to rise, its net contribution turns **destructive**—with regard to surplus alone—as the beam's independent role in the photophysical pathways begins to prevail.

This phenomenological description of surplus emission as a function of 1523 nm beam power can thus be distilled into a simple expression—presented in Eq. 5.7.

$$\frac{B \cdot P_{\mathrm{NIR}}^{\alpha}}{C} \xrightarrow[\text{1523 nm power}]{\text{higher}} \frac{B \cdot P_{\mathrm{NIR}}^{\alpha}}{\left(b \cdot P_{\mathrm{NIR}}^{\gamma} + C\right)} \xrightarrow[\text{1523 nm power}]{\text{higher}} \frac{B \cdot P_{\mathrm{NIR}}^{\alpha}}{b \cdot P_{\mathrm{NIR}}^{\gamma}} \tag{5.7}$$

All of this leads to one more conclusion—subtly nestled beneath the layers of fitting and inference, yet brought to light precisely by them. At the outset, we wondered whether the notably overwhelming behavior of the 1523 nm beam—as far as NIR excitation goes—might alter its influence within the mutual interplay term, that is, the numerator in Eq. 5.3.[31] However, our findings suggest otherwise. If such a change were indeed occurring, we would expect to see a shift in the exponent **greater** than the parameter γ derived from the single-beam measurements.

In other words, if the numerator in Eq. 5.3 were to transition from the form inferred in Eq. 3.6 to that suggested by Eq. 3.7, the expected change would involve a decrease in the effective exponent from α to $\alpha - 2\gamma$.[32] And yet, we observe no such shift. This serves as evidence that—even if still a simplification[33]—the more modest description of the system may in fact be closer to reality than the more elaborate scenarios we initially proposed.[34]

Influence of 975 nm beam power on surplus emission

This issue warrants only brief attention—because it is, in fact, already *familiar*.

A brief retrospective is in order. In thulium-doped materials, the emission surplus increased constructively with rising NIR beam power throughout the entire examined range. Such behavior is due to the NIR beam never independently exciting thulium ions strongly enough to rival mutual interplay. In contrast, the erbium-doped systems just explored revealed the opposite tendency—a shift from one regime to the other.

The case of the 975 nm beam is considerably more straightforward—both in YbTm and YbEr nanoparticles. Its influence asserts dominance over the excitation pathways almost immediately.[35] While it is indispensable for enabling *mutual* interplay, its independently accessible excitation channels begin contributing competitively right away.

Fig. 5.14 shows the dependence of the emission surplus at 657 nm and 543 nm for YbEr nanoparticles as a function of 975 nm beam power, with the 1523 nm beam held constant at 40 mW. As the figure illustrates, at very low 975 nm powers, one can still observe a constructive influence

31: To better understand why the numerator in the surplus expression reflects the mutual interaction, one should refer back to our earlier considerations of this term, as discussed in Eqs. 3.4, 3.5 and 3.8 with commentary, and in the derivation of the general surplus formula presented in Eq. 3.26.

32: As the evolution of the denominator in Eq. 5.7 with increasing power results in a transition from the effective exponent α to $\alpha - \gamma$—not due to a change in α itself, but because the overall exponent describing the full expression shifts—it's important to also consider the potential more intrinsic evolution of α (a possibility incorporated in Eqs. 3.6 and 3.7). Such a case would lead to a total change of 2γ, but this is not observed here.

33: After all, these remain **purely phenomenological** considerations, intended more to aid in understanding and predicting the system's behavior than to provide a rigorous description.

34: That said, those earlier possibilities remain worth keeping in mind.

35: In the case of thulium-doped nanoparticles, the trend was evident from the very outset. In *slight* contrast, for the erbium-doped counterparts, we observe a sharp initial increase followed by a decline. This can be explained by the co-excitation framework: while in YbTm the NIR co-excitation beam had virtually no independent effect, the 1523 nm beam in YbEr does. As a result, in its presence, the 975 nm beam does not immediately dominate, but rather gains influence more gradually—picking up momentum.

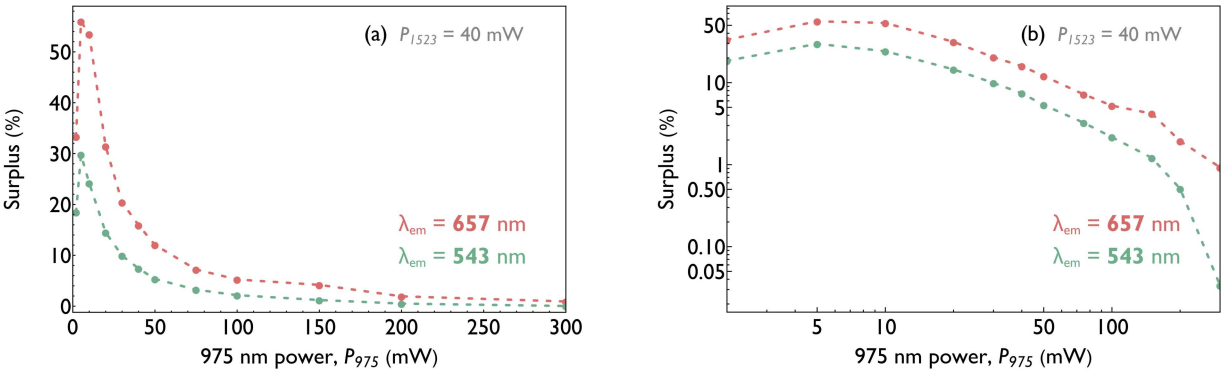

Figure 5.14: Surplus emission obtained at 657 nm and 543 nm from YbEr nanoparticles as a function of 975 nm beam power, measured up to 300 mW under dual-beam excitation with the 1523 nm beam held constant at 40 mW. **(a)** Results shown on a linear scale. **(b)** Results shown on a log-log scale. The dashed line is provided as a visual guide.

on surplus emission. However, this quickly gives way—as expected—to a clearly destructive contribution as the power increases.

This behavior can also be phenomenologically described using a modified version of Eq. 3.26, accounting for the constant 1523 nm beam power, yielding Eq. 5.8.

$$S = \frac{F \cdot P_{975}^{\omega}}{\left(G + c \cdot P_{975}^{\delta}\right)} \tag{5.8}$$

Since the dominance of the 975 nm beam emerges quite early within the considered power range, the equation should asymptotically approach the simplified form presented in Eq. 5.9.

$$S \approx \frac{F \cdot P_{975}^{\omega}}{c \cdot P_{975}^{\delta}} = \mathfrak{F} \cdot P_{975}^{\omega-\delta} = \mathfrak{F} \cdot P_{975}^{\rho} \tag{5.9}$$

Quantifying this behavior numerically proves challenging for a simple reason: the surplus decays rapidly with increasing 975 nm power, such that the final measurements correspond to very low surplus values—approaching zero. Fig. 5.15 therefore presents the only feasible plots of fitted functions to this decay behavior, which serve an illustrative and descriptive purpose rather than a definitive one.

We thus arrive—within the range of moderate 975 nm beam powers—at a dependence that is nearly inversely proportional. Given that the extracted exponents are intended only as estimates, a strictly quantitative analysis is not viable. However, by drawing on these fitted values and the previously determined parameters δ, obtained from single-beam excitation experiments using the 975 nm beam,[36] we can at least *approximate* the influence of the 975 nm beam on the mutual interplay term (i.e., the numerator in Eq. 3.26).

Since the best-fit function in Fig. 5.15 was obtained using data restricted to the moderate-power regime of the 975 nm beam, we refer to the second of the three fitted exponents (corresponding to this specific regime) describing the influence of the power of the 975 nm beam alone on emission intensity (see Fig. 5.8a for the 657 nm emission and Fig. 5.9a

36: Refer to Section 5.2.1, especially Figs. 5.8 and 5.9. In this study, the symbol δ denotes the exponent describing the relationship between the measured emission and the power of the standalone 975 nm beam (in single-beam experiments). However, care should be taken in the forthcoming discussion—while the figures use the placeholder symbol ξ to represent all exponent values, the interpretation of each specific exponent and the assignment of its corresponding symbol are provided in the main text.

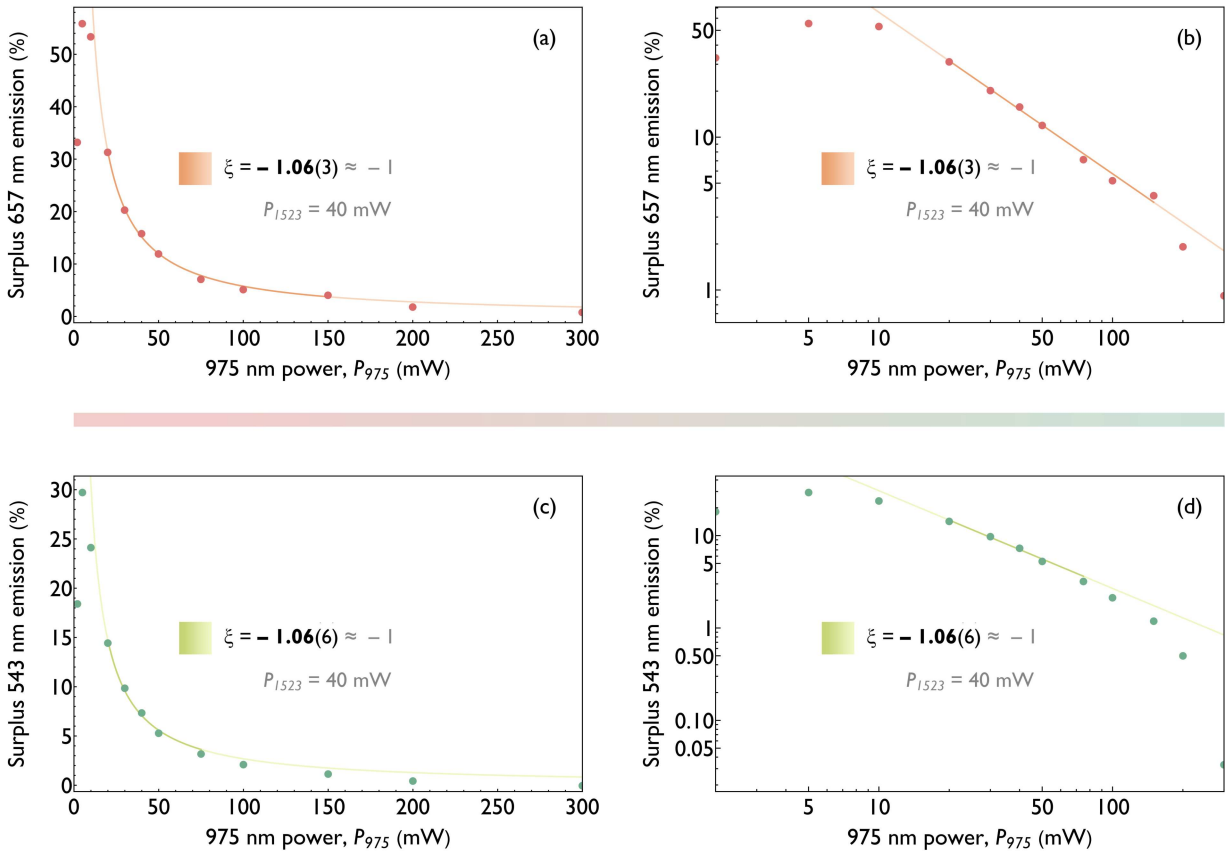

Figure 5.15: Surplus emission of YbEr nanoparticles as a function of 975 nm beam power, obtained under dual-beam excitation with a 1523 nm beam held constant at 40 mW. Fitted trends are included. **(a)** Surplus 657 nm emission, shown on a linear scale. **(b)** Surplus 657 nm emission, shown on a log-log scale. Orange line: fit for the moderate and high power regime of the 975 nm beam, extended across the full range in a lighter shade. **(c)** Surplus 543 nm emission, shown on a linear scale. **(d)** Surplus 543 nm emission, shown on a log-log scale. Green line: fit for the moderate and high power regime of the 975 nm beam, extended across the full range in a lighter shade.

for the 543 nm emission). These fitted exponent values are **1.71**(2) and **1.54**(2) for the red and green emissions, respectively.

Following the relationship outlined in Eq. 5.9, the parameter ω, which estimates the contribution of the 975 nm beam within the cooperative interaction term, should equal the fitted exponents (ξ from Fig. 5.15, now denoted as ρ in accordance with Eq. 5.9), each incremented by the corresponding δ value previously determined and referenced in this paragraph. This yields the following **estimated** values.[37]

$$\begin{aligned} \omega_{657} &\approx \rho_{657} + \delta_{657} = -1.06 + 1.71 = \mathbf{0.65}(4) \\ \omega_{543} &\approx \rho_{543} + \delta_{543} = -1.06 + 1.54 = \mathbf{0.48}(6) \end{aligned} \tag{5.10}$$

A rigorous treatment of these values is not required—indeed, such precision would be unwarranted given their approximate nature. Yet even a cursory examination is sufficient to draw the most important and meaningful conclusions.

The contribution of the 975 nm beam to the mutual interplay under co-excitation conditions is both *constructive* and *sublinear*. This, in

37: The uncertainties associated with the results were calculated using error propagation. Yet it should be noted that these results are to be understood as descriptive rather than physically rigorous, serving primarily as a qualitative guide; thus, the true uncertainties are likely much larger than reported.

turn, results—throughout nearly the entire power regime, save for the very lowest values—in a *destructive* influence on the emission surplus, owing to the competing effect of the 975 nm beam via its independently accessible excitation pathways.

Both experiments—those examining the influence of the 1523 nm beam and the 975 nm beam—though conducted in a more limited scope, have yielded descriptive insights that we now aim to summarize concisely and coherently.

The effect of the 1523 nm beam on mutual interplay is nearly linear, yet still falls within the *sublinear* regime. This behavior carries over to the emission surplus at low powers, into a *constructive* contribution to the effect. At higher powers, however, the beam's independently accessible excitation pathways begin to dominate, leading to a *destructive* influence on the surplus. A similar trend is observed with the 975 nm beam—its influence on mutual interplay is *sublinear*, but its strong individual excitation channels quickly translate it into a *negative* impact on the emission surplus.

What emerges in the case of erbium-doped nanoparticles—particularly when contrasted with their thulium-doped counterparts[38]—is a relative convergence of the roles played by the 975 nm and 1523 nm beams in shaping the emission behavior of the material.[39] This results in a closer resemblance between the observations made as a function of the power of both beams—an important consideration in the broader context of the photophysical properties of the materials under investigation.

38: Compare with the emission surplus results for thulium-doped nanoparticles in Section 3.4.

39: Compared to the 975 nm and 1213/1732 nm excitation pairings used with thulium-doped systems, the 1523 nm beam here demonstrates a notably greater impact, see Sections 3.3 and 3.4.

5.3.2 1139 nm

Like a mustard seed. Such is the role of the 1139 nm beam—on its own, at the given power densities, it does not induce any measurable emission. This is explained by its selective resonances with excited-state transitions, rather than one from the ground state. While this quiet behavior is reminiscent of the 1213 nm and 1732 nm beams in thulium-doped materials, those beams were also resonant with ground-state transitions[40]—unlike the 1139 nm beam in erbium-doped systems.[41]

40: See Section 3.1.2.

41: See Section 5.1.2.

Yet, the 1139 nm beam makes its presence known when combined with the 975 nm beam—but only for low-energy emissions,[42] where the additional excitation channels it opens result in a moderate enhancement. Due to its inability—under the given conditions—to excite erbium ions independently, we can expect it to pose no competition to mutual interplay. This stands in contrast to the 975 nm beam, whose competitive role is expected, and the 1523 nm beam, whose competitive influence, though less intuitive, was clearly demonstrated in the preceding discussion. Consequently, no saturation or decline in the emission surplus is expected within the tested power regime of the 1139 nm beam.

42: The effect of introducing the 1139 nm beam is evident in the red emission intensity (657 nm), but it is not observed in the analysis of green emission (e.g., 543 nm). This was described in the initial observations concerning the emission properties of Er-doped nanoparticles (Section 5.1.1), as well as in the discussion of possible photophysical pathways (Section 5.1.2).

This is precisely what is observed in Fig. 5.16. As shown, the 657 nm emission surplus increases steadily with the power of the 1139 nm beam, when the 975 nm beam power is held constant. Moreover, for lower powers of the 975 nm beam—at the same 1139 nm beam power—the observed

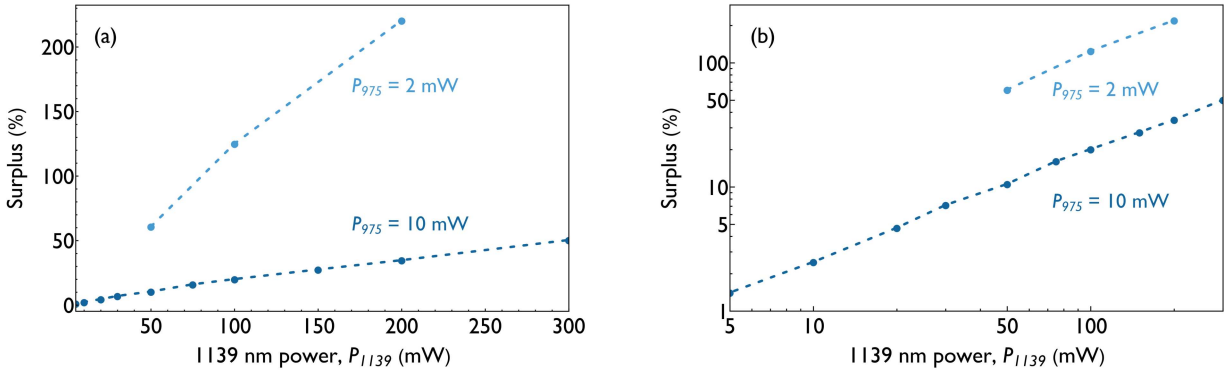

Figure 5.16: Surplus emission obtained at 657 nm from YbEr nanoparticles as a function of 1139 nm beam power under dual-beam excitation, with the 975 nm beam held constant at 10 mW, and with additional measurements performed at 2 mW for comparison. **(a)** Results shown on a linear scale. **(b)** Results shown on a log-log scale. The dashed line is provided as a visual guide

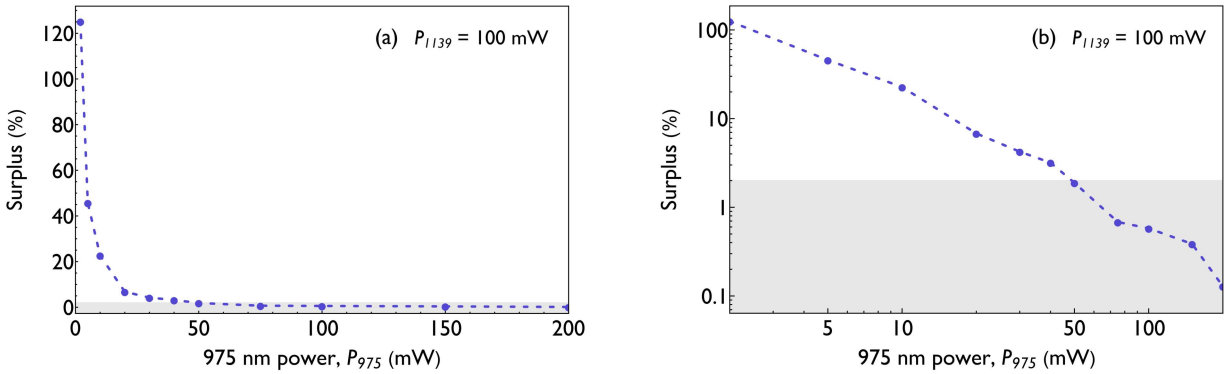

Figure 5.17: Surplus emission obtained at 657 nm from YbEr nanoparticles as a function of 975 nm beam power under dual-beam excitation with the 1139 nm beam held constant at 100 mW **(a)** shown on a linear scale; **(b)** shown on a log-log scale. The gray area indicates surplus values below 2%. The dashed line is provided as a visual guide.

surplus values are higher. In addition, Fig. 5.17 carries complementary information—the influence of the 975 nm beam is destructive to the emission surplus from the very beginning—a result that aligns with expectations. This is due to the strong competition introduced by the 975 nm beam as its power increases: the absolute contribution of the beam quickly outweighs its role within the mutual interplay. In other words, as the 975 nm beam power grows, its independent excitation of erbium-doped nanoparticles increasingly surpasses the cooperative mechanism, causing the relative metric—namely, the emission surplus—to decline.[43]

43: This phenomenon was consistently observed across all analogous experiments conducted and documented in the present study; hence, it should not be regarded as unexpected.

From points to patterns

Let us now direct our attention to the influence of the 1139 nm beam on the measured emission surplus. Given the well-supported assumption that the 1139 nm beam contributes solely through mutual interplay and does not independently influence the photophysical pathways, it is fully justified to model the surplus using Eq. 3.27. This expression already incorporates the destructive influence of the 975 nm beam, and under conditions of fixed 975 nm power, it reduces to Eq. 5.11 (identical to Eq. 5.2).

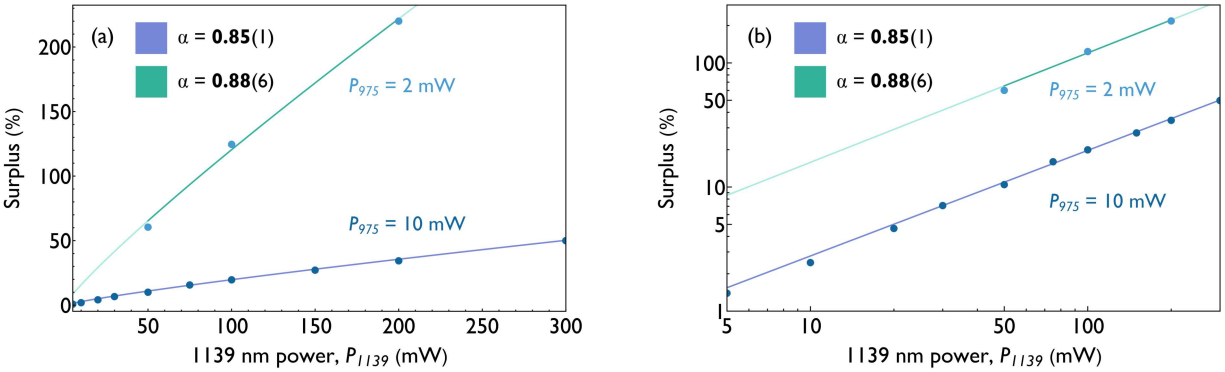

Figure 5.18: Surplus emission of YbEr nanoparticles as a function of 1139 nm beam power, obtained under dual-beam excitation with a 975 nm beam held constant at 10 mW, and with additional measurements performed at 2 mW. Fitted trends are included. **(a)** Surplus 657 nm emission, shown on a linear scale. **(b)** Surplus 657 nm emission, shown on a log-log scale. Blue line: fit for co-excitation with 10 mW 975 nm beam. Green line: fit for co-excitation with 2 mW 975 nm beam, extended across the full range in a lighter shade.

$$S = \mathfrak{a} \cdot P_{\mathrm{NIR}}^{\alpha} \cdot P_{975}^{\beta} = \mathfrak{C} \cdot P_{\mathrm{NIR}}^{\alpha} \tag{5.11}$$

By applying the phenomenological Eq. 5.11, we can attempt to fit the observed trend to the measured data points. However, due to the limited number of measurements at 2 mW of 975 nm power, this particular fit serves a primarily illustrative purpose. In an ideal scenario, the fitted exponents should be identical—meaning that the intrinsic dependence of emission surplus on the 1139 nm beam power should not vary with the power of the 975 nm beam, under the assumptions made. *And indeed, this appears to be the case.*

The analysis of the fits presented in Fig. 5.18 allows us to draw more specific conclusions.

The 657 nm emission surplus, obtained under co-excitation, exhibits a *constructive* and *sublinear* dependence on the 1139 nm beam power. Moreover, this relationship shows no significant variation with changes in the accompanying 975 nm beam power.

Naturally, one must keep in mind the relatively limited dataset. Nevertheless, the described observations—now cast in a more quantitative form—remain internally consistent, and consistent as well with the original assumptions regarding the phenomenological description, specifically the presumed lack of an independent contribution from the 1139 nm beam. Assuming the fitted coefficients are effectively identical, we can also extract from our data a complementary relationship: the surplus as a function of the 975 nm beam power.

Using Eq. 3.27, we arrive at the straightforward expression Eq. 5.12, in which coefficient $\mathfrak{C}$, encoding the entangled dependence on the 975 nm beam power, acts as the prefactor in Eq. 5.11, and coefficient $\mathfrak{a}$ serves as the prefactor in the more general Eq. 3.27. While the exact value of coefficient $\mathfrak{a}$ is unknown, this poses no issue—under identical experimental conditions and fixed excitation wavelengths, it is expected to remain *relatively* constant regardless of beam power. This expectation, though intuitive, is far from trivial.[44]

44: Under typical circumstances, prefactors are disregarded, as they depend on measurement conditions, sample alignment, and detector sensitivity—*and may also shift with transitions between power regimes and changes in dominant mechanisms.* In a limited situation, however, they should remain at least relatively stable. Such is this case—as with the emission surplus in thulium-doped nanoparticles (See Section 3.4)—the appropriate phenomenological model is fully multiplicative with a *constant* prefactor, owing to the absence of any shift in beam dominance (the 975 nm beam being dominant from the outset). Let the similarity between the behavior of the 1139 nm beam in erbium-doped nanoparticles and that of NIR beams in thulium-doped ones serve as our justification.

$$\mathfrak{a} \cdot P_{\mathrm{NIR}}^{\alpha} \cdot P_{975}^{\beta} = \mathfrak{C} \cdot P_{\mathrm{NIR}}^{\alpha} \Longrightarrow P_{975}^{\beta} = \frac{\mathfrak{C}}{\mathfrak{a}} \tag{5.12}$$

Assuming, however, that it remains constant, we can extract the values of the parameter $\mathfrak{C}$ from the fits presented in Fig. 5.18 and obtain the following system of equations. Since our analysis is intended for illustrative purposes only, uncertainties have been omitted for clarity.

$$\begin{cases} \mathfrak{a} = \dfrac{\mathfrak{C}_{10}}{P_{975}^{\beta}} = \dfrac{0.39}{10^{\beta}} \\ \mathfrak{a} = \dfrac{\mathfrak{C}_{2}}{P_{975}^{\beta}} = \dfrac{2.08}{2^{\beta}} \end{cases} \tag{5.13}$$
$$\beta \approx -1.04$$

And thus, we obtain an approximate exponent characterizing the dependence of emission surplus—under co-excitation with 975 nm and 1139 nm beams—on the power of the former. This value aligns well with our developed intuition: it is negative, reflecting the fact that increasing the power of the 975 nm beam has a negative effect on a relative metric such as surplus. However, we are not limited to the preliminary estimate—the picture is further clarified by the fitting presented in Fig. 5.19, which is restricted to the lower power range of the 975 nm beam, as the surplus drops to very low values at higher powers.

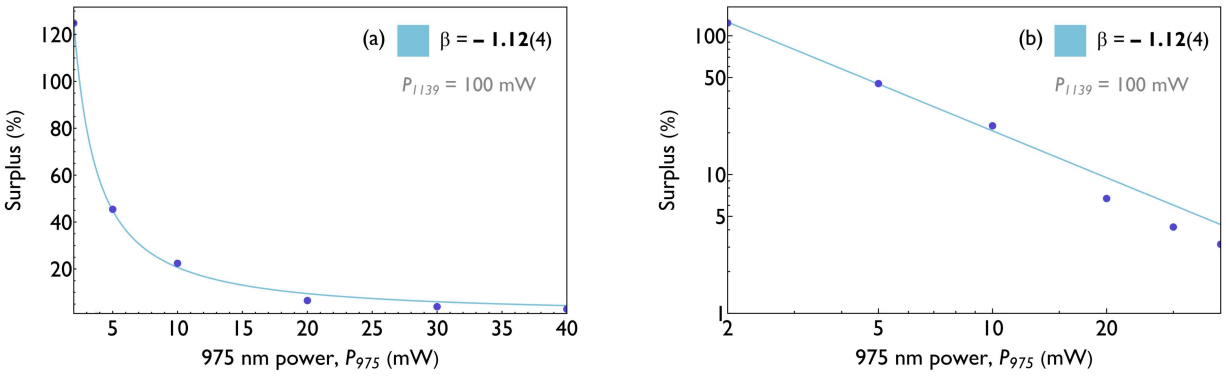

Figure 5.19: Surplus emission of YbEr nanoparticles as a function of 975 nm beam power, obtained under dual-beam excitation with a 1139 nm beam held constant at 100 mW. The 975 nm beam power was restricted to 40 mW, as higher excitation levels resulted in negligible surplus emission. Fitted trends are included. **(a)** Surplus 657 nm emission, shown on a linear scale. **(b)** Surplus 657 nm emission, shown on a log-log scale. Blue line: fit for the restricted power regime of the 975 nm beam.

$$S = \mathfrak{a} \cdot P_{\mathrm{NIR}}^{\alpha} \cdot P_{975}^{\beta} = \mathfrak{H} \cdot P_{975}^{\beta} \tag{5.14}$$

To carry out this analysis, we used Eq. 5.14, which corresponds to the form of Eq. 3.27 under conditions of constant 1139 nm beam power. The resulting exponents are shown in Fig. 5.19. *While not exact, the agreement is remarkably close.* Given that the exponent derived from Eq. 5.13 serves only as a rough estimate, the observed convergence of parameters—derived from complementary yet entirely independent measurements—is reassuring.

To estimate (and only estimate) the intrinsic influence of the 975 nm beam on mutual interplay (as opposed to merely its effect on the surplus), we

refer to the fitting parameters from the single-excitation experiments (Section 5.2.1) as well as to Eq. 3.27, which expresses surplus with the mutual interplay term in the numerator—prior to simplification. This derivation yields the form described in Eq. 5.15.

$$S = \frac{\mathfrak{A} \cdot P_{\mathrm{NIR}}^{\alpha} \cdot P_{975}^{\omega}}{c \cdot P_{975}^{\delta}} \approx \frac{F \cdot P_{975}^{\omega}}{c \cdot P_{975}^{\delta}} = \mathfrak{H} \cdot P_{975}^{\omega-\delta} = \mathfrak{H} \cdot P_{975}^{\beta} \tag{5.15}$$

The exponent δ, characterizing the power dependence of 657 nm emission intensity under 975 nm single-beam excitation (specifically for low power[45]), was determined to be **2.01**(1) (first of the three fits in Fig. 5.8a). We adopt this value for our considerations. Based on Eq. 5.15, we can now estimate the parameter ω[46]—providing at least a qualitative sense of how the 975 nm beam contributes to cooperation, as distinct from its already established destructive effect on the surplus itself.

$$\omega = \beta + \delta = -\mathbf{1.12}(4) + \mathbf{2.01}(1) = \mathbf{0.89}(4) \tag{5.16}$$

We can now, with a clear conscience, formulate the final and general conclusions.

The 1139 nm beam contributes to both the 657 nm emission surplus and the mutual interplay in a *constructive* and *sublinear* manner. Owing to the absence of competition from independently accessible excitation pathways, its influence in both expressions is effectively identical. In contrast, the 975 nm beam exerts a *destructive* effect on the emission surplus, driven by the competing influence of its independent excitation channels. Nevertheless, its contribution to the mutual interplay remains *constructive* and *sublinear*.

This concludes our investigation into the **phenomenological** description[47] of the emission properties of erbium-doped upconverting nanoparticles under co-excitation with a 975 nm beam and either a 1523 nm or 1139 nm beam. Though both NIR beams induce only moderate emission surplus, the roles they play along the upconversion ladder could not be more distinct—from the 1523 nm beam, capable of independently exciting erbium ions, to the 1139 nm beam, resonant solely with excited-state absorptions. These differences shape the emission characteristics and their evolution with excitation power—forming the core of our inquiry.
To reveal the subtle architecture beneath the surface.

45: Since the data points used for fitting in Fig. 5.19 are shown only up to 40 mW, any parameters related to the sole influence of the 975 nm beam must therefore also apply to this range.

46: The uncertainties associated with the results were calculated using error propagation.

47: One should not place too much weight on the numerical values themselves, but rather on the **general trends they outline**. This has been stated before, but it is worth emphasizing once again.

5.4 Summa summarum

Rather than approaching enhancement in erbium-based upconversion through the familiar routes of composition or sheer excitation intensity, this chapter seeks something subtler: an examination of how interplay between beams of distinct wavelengths might reveal cooperative regimes previously obscured. Having already introduced the conceptual framework and methodology in earlier sections, we now turn to its application in a new material system.

The study begins with the co-excitation spectrum—an experiment designed to map the response of erbium-doped nanoparticles under simultaneous illumination with a fixed 975 nm beam and a tunable NIR beam. This primary beam, resonant with Yb^{3+} sensitizer absorption, primes the system. The tuning of the second beam, however, reveals the core findings.

Two NIR regions emerge as influential. The first, centered at **1523 nm**, is a known player—resonant with the $^4I_{15/2} \longrightarrow {}^4I_{13/2}$ ground-state absorption (GSA) in Er^{3+}, it produces measurable emission even in isolation.

The second, less expected, lies at **1139 nm**. It induces no emission alone but, when combined with 975 nm excitation, yields a marked enhancement in red emission centered at 657 nm. Crucially, this enhancement is confined to that band; no effect is seen at higher energies such as the 543 nm green line, indicating a selective contribution via excited-state absorption (ESA) channels—specifically, the $^4I_{13/2} \longrightarrow {}^4F_{9/2}$ transition, and possibly also the $^2H_{11/2} \longrightarrow {}^2K_{15/2}$ transition.

With the bands identified, their behavior under varying excitation conditions was systematically explored.

The 1523 nm beam proves dual-natured. At low power, its influence is constructive—enhancing surplus emission through cooperative action. However, as its power increases, the beam's own capacity to independently excite Er^{3+} begins to dominate. This competition causes a decline in surplus, even as total emission continues to rise. This inflection point is a hallmark of the system's nonlinear dynamics and was captured through both spectral analysis and power-dependent measurements. It reveals a crucial insight: that surplus enhancement is not merely a matter of adding energy, but of maintaining the conditions under which cooperative channels remain dominant.

By contrast, the 1139 nm beam serves as a model of cooperative fidelity. Resonant only with ESA transitions, and lacking GSA capabilities, it introduces no independent competition. Thus, its contribution to mutual interplay—and by extension to surplus emission—is consistently constructive and sublinear. Surplus grows steadily with power, and no saturation or decline is observed across the measured range. Moreover, the response remains stable across different fixed powers of the 975 nm beam, underscoring the intrinsic nature of its contribution.

The behavior of the 975 nm beam itself is also revisited. As expected, its individual channels dominate nearly from the outset. This leads to

a destructive effect on surplus, even though the beam is indispensable for initiating upconversion via energy transfer to erbium. Phenomenologically, the beam contributes constructively to the mutual interplay term—but destructively to surplus, due to the increasingly overwhelming role of its own excitation pathways.

Taken together, the results reinforce a conceptual distinction. The 1523 nm beam, while effective, walks a narrow line—its cooperative potential easily suppressed by its own independent strength. The 1139 nm beam, by contrast, exemplifies the ideal co-excitation partner: invisible alone, but enabling in tandem.

This chapter revisits and extends the investigation begun with thulium-based systems. In that case, the cooperative mechanism proved strong and the surplus effect substantial. In contrast, the erbium-based systems present a more limited but equally informative case. What emerges is not a generalized recipe for enhancement, but a more nuanced principle: that in designing multi-beam excitation systems, the goal is not always to maximize individual power, but to sculpt conditions where cooperation—not competition—leads the way.

5.4.1 Contributions

Ongoing support and scientific guidance — **Piotr Fita**

Valuable discussions and assistance with the interpretation of possible transitions in erbium ions —
Artur Bednarkiewicz

Synthesis of the nanoparticles used — **Katarzyna Prorok**

Concept, independent execution of the experiments, analysis, full description, and everything in between — **myself, Paulina Rajchel-Mieldzioć**

Energy looping in Er-doped upconverting nanoparticles

6

6.1 What goes around comes around

Though your beginning was small,
your future will flourish indeed.[1]

1: Job 8:7

The 1139 nm beam—resonant with the ESA transitions $^4I_{13/2} \longrightarrow {}^4F_{9/2}$ and $^2H_{11/2} \longrightarrow {}^2K_{15/2}$, yet energetically mismatched with any ground-state absorption (GSA) transition—initially appears inert. At moderate excitation intensities, it fails to generate measurable emission.[2] *A silence before the storm?*

2: The lack of measurable emission at moderate intensities does not preclude its emergence at higher ones—a notion that sets the stage for the discussion and experiments to follow.

The facts at hand suggest there may be dormant potential.

Let us return for a moment to the theoretical introduction,[3] to shed more light on our otherwise elusive considerations. Among the most striking phenomena in upconverting materials is their potential for high nonlinearity, whether through the energy-looping mechanism—which yields a moderate enhancement beyond standard upconversion—or by reaching the photon avalanche, where the response becomes truly explosive. These effects—most clearly demonstrated in thulium ions—rely primarily on excitation at a wavelength non-resonant with the ground-state absorption (GSA), yet resonant with an excited-state absorption (ESA) transition.

3: See Section 1.1.3.

In light of this, does the reasoning behind our reference to the 1139 nm beam—resonant with ESA but not GSA in *erbium* ions—begin to reveal its deeper intent?

In previously reported observations of enhanced nonlinearity in thulium-doped systems, achieving the effect (along with the right sequence of transitions and suitable doping concentrations) required high excitation intensities. This is something that, to date, has not been systematically tested in erbium-doped systems under 1139 nm excitation. **Yet.**

And this is precisely our idea. To carry out experiments at high intensities of the 1139 nm beam—and **only** the 1139 nm beam, since the excitation is targeted solely at erbium ions, without any co-excitation—to see whether it is possible to induce emission with any degree of enhanced nonlinearity in erbium-doped nanoparticles.

Let us be clear from the outset: we **do not yet know** whether the conditions for avalanche-like[4] behavior in erbium-doped materials are even met.[5] The ESA-to-GSA cross-section ratio is unknown—though we can reasonably assert that ESA dominates, given the energy mismatch involved. *But is it enough?*

It also remains unclear whether a cross-relaxation mechanism exists that reinforces positive feedback by efficiently populating the $^4I_{13/2}$ state. **Why focus on $^4I_{13/2}$?** This is the very level from which the transition resonant with the 1139 nm beam originates[6]—namely, $^4I_{13/2} \longrightarrow {}^4F_{9/2}$. If a strongly nonlinear population buildup of this state can be achieved, it may—via the ESA transition driven by the 1139 nm beam—lead to enhanced

4: We refrain from using the term *avalanche*; our focus is instead on the broader class of processes exhibiting stronger nonlinear behavior than ETU alone can account for under 975 nm excitation.

5: The necessary conditions for the onset of energy-looping (which are also required—though not sufficient—for the photon avalanche effect) were introduced in the theoretical background (Section 1.1.3), but are briefly reiterated here for clarity:
(i) Resonant excitation of an excited-state absorption (ESA) transition,
(ii) Weak or non-resonant excitation of the ground-state absorption (GSA) transition,
(iii) A suitable cross-relaxation process that repopulates the intermediate state following ESA, thus completing the CR+ESA feedback loop.
Additional constraints apply—such as a sufficiently long lifetime of the intermediate state. To unambiguously confirm that a photon avalanche has occurred, further criteria must be met: the ESA-to-GSA cross-section ratio should exceed 10,000; a sharp threshold behavior must be present; and prolonged rise times near the threshold should be observed.

6: To avoid relying solely on imagination, it is recommended to base those considerations on an energy level diagram—such as one of those shown in Fig. 6.1.

occupation of the emissive $^4F_{9/2}$ level. Yet to realize this nonlinear mechanism in erbium ions alone—*a novel concept in itself*—a suitable cross-relaxation pathway is essential to complete the feedback loop with ESA that would drive the entire process. The propriety or efficiency of such a cross-relaxation pathway, however, remains uncertain.[7]

7: If the reader—seeking a better understanding of the processes described here—refers to literature on thulium ions (also see Fig. 1.5), it may be helpful to note that in our discussion, the 1139 nm beam in erbium is treated as analogous to the 1064 nm beam in thulium. Both are resonant with transitions from specific excited states: $^4I_{13/2}$ in erbium and $^3F_4$ in thulium, respectively.

Given this, it is only natural to revisit previously reported processes even tangentially related to our focus.

One known process[90, 109] of this type takes place between the $^4I_{15/2}$ and $^4S_{3/2}$ levels:

$$^4I_{15/2} + {}^4S_{3/2} \longrightarrow {}^4I_{13/2} + {}^4I_{11/2}.$$

This process[8] populates two states simultaneously. While the $^4I_{11/2}$ level is relatively long-lived, the $^4I_{13/2}$ state is even more so.[110–112] Yet, this alone does not yield efficient population transfer. The relaxation from $^4I_{11/2}$ to $^4I_{13/2}$ may still be insufficient to noticeably affect the overall population of the latter. A greater limitation, however, lies in the initial population of the $^4S_{3/2}$ level, which is expected to be extremely weak under excitation with the 1139 nm beam alone.

8: All cross-relaxation processes between erbium ions discussed in the text are shown in Fig. 6.1b.

A similar challenge arises when considering alternative cross-relaxation processes[90, 109] such as:

$$^4I_{9/2} + {}^4I_{15/2} \longrightarrow {}^4I_{13/2} \quad \text{and} \quad {}^4I_{11/2} + {}^4I_{15/2} \longrightarrow {}^4I_{13/2}.$$

In both cases, sufficient population of the initial states is questionable. The $^4I_{11/2}$ level is difficult to populate either directly (due to insufficient photon energy) or indirectly (via low-probability relaxation from higher-lying states) using only 1139 nm beam. Likewise, the population of the $^4I_{9/2}$ level is likely inadequate. Even assuming a relatively strong population of the $^4F_{9/2}$ state, its relaxation branching ratios are unfavorable for this pathway.[111]

Let us therefore consider other possible cross-relaxation routes[113, 114], such as:

$$^4F_{7/2} + {}^4I_{15/2} \longrightarrow {}^4I_{11/2} \quad \text{and} \quad {}^4F_{7/2} + {}^4I_{15/2} \longrightarrow {}^4F_{9/2} + {}^4I_{13/2}.$$

Here, the main difficulties *once again* include populating the relatively high-lying $^4F_{7/2}$ state, as well as the fact that these processes also populate either the non-targeted $^4I_{11/2}$ state or both the desired $^4I_{13/2}$ and the emitting $^4F_{9/2}$ states simultaneously.

While still focusing solely on the population of the $^4I_{13/2}$ state, another possible mechanism is interionic energy transfer[115], namely:

$$^2F_{7/2}\,(Yb^{3+}) + {}^4S_{3/2}\,(Er^{3+}) \longrightarrow {}^2F_{5/2}\,(Yb^{3+}) + {}^4I_{13/2}\,(Er^{3+}).$$

However, this process[9] requires sufficient population of the green-emitting states in erbium ions. Moreover, it is typically followed by a subsequent energy transfer event that populates the $^4F_{9/2}$ state in erbium—without any involvement of the 1139 nm beam:

9: All interionic energy transfer processes between erbium and ytterbium ions discussed in the text are shown in Fig. 6.1a.

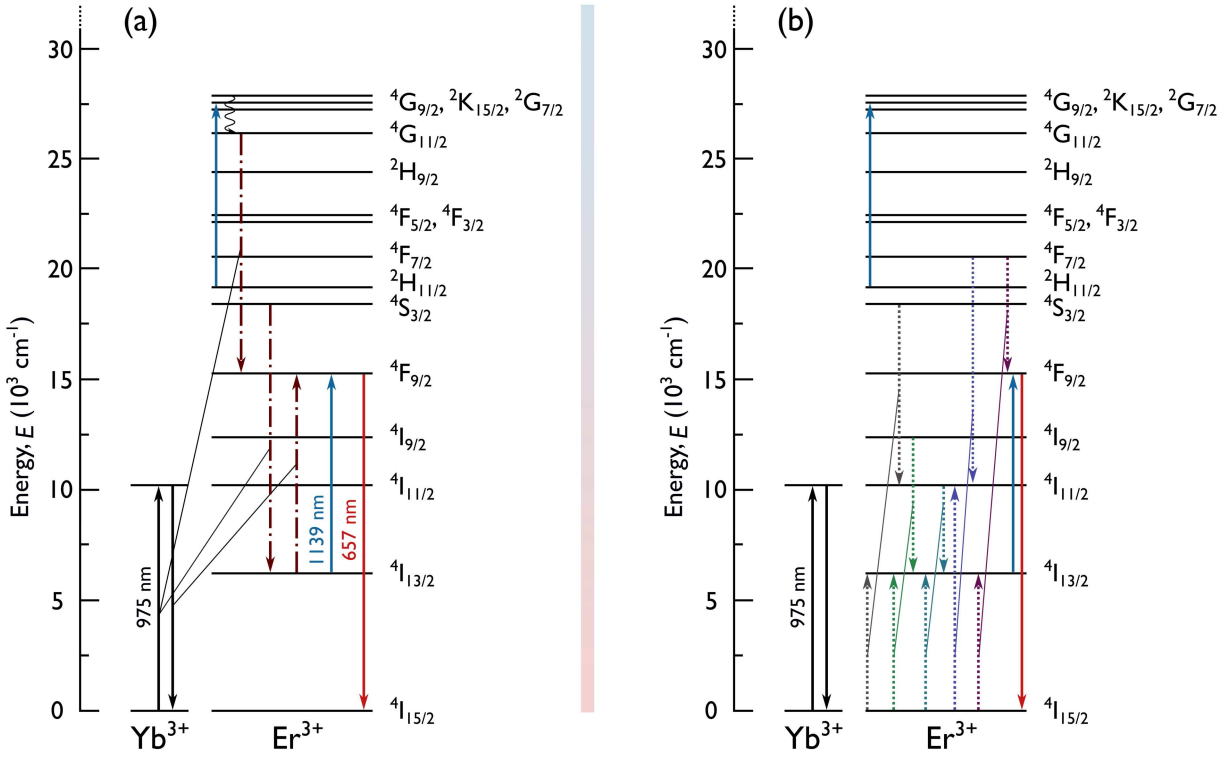

Figure 6.1: Simplified energy-level diagrams highlighting the transitions discussed in the main text. Arrow thickness does *not* indicate transition probability. Transitions enabled by 1139 nm excitation are shown as solid blue arrows, while red emission at 657 nm is indicated with a solid red arrow. **(a)** Interionic energy transfer processes between erbium and ytterbium ions. **(b)** Schematic representation of cross-relaxation processes between erbium ions. For illustrative clarity, the processes are depicted on a single diagram, though they of course occur between separate ions.

$$^2F_{5/2}\,(Yb^{3+}) + {}^4I_{13/2}\,(Er^{3+}) \longrightarrow {}^4F_{9/2}\,(Er^{3+}) + {}^2F_{7/2}\,(Yb^{3+}).$$

Yet the $^4I_{13/2}$ state—our primary focus up to this point—is not the only potential starting point from which the 1139 nm beam can populate the red-emitting $^4F_{9/2}$ level. Earlier in our discussion of YbEr doped materials, we noted that $^4F_{9/2}$ can also be populated via transition from $^4G_{11/2}$, following excitation of the ^2G, ^2K manifolds. While only excitation driven by the 1139 nm beam is of interest here, this wavelength proves exceptionally well-suited to the role.

As previously discussed, the 1139 nm beam can promote transitions from green-emitting levels to these high-energy manifolds, such as:

$$^2H_{11/2} \xrightarrow{1139\text{ nm}} {}^2K_{15/2}.$$

This brings us to a key point: the interaction between the 1139 nm beam and the system may depend not only on the population of the $^4I_{13/2}$ level—as previously emphasized—but also, in theory, on the population of the green-emitting states, which could likewise act as gateways to the $^4F_{9/2}$ state via a 1139 nm-driven pathway through higher-energy manifolds.

However, as already noted, under 1139 nm illumination alone, these green-emitting states are insufficiently populated[10] to significantly engage

10: Recognizing these limitations can serve as a catalyst for designing new experiments—*not yet performed, and thus not subject to evaluation*—but the ideas behind them will be outlined following the presentation of the current results.

additional mechanisms involving the upper manifolds in shaping the emission characteristics of the investigated materials.

This *surface-level* analysis does not provide strong reasons for optimism, but neither does it rule out the possibility entirely. After all, *the goal of this work is neither to model nor to exhaustively trace the mechanistic pathways*.[11] As this is a **deeply experimental study**, there may well be an overlooked or mischaracterized pathway hidden within the apparent complexity.

And what of the remaining requirements?[12] Our measurements—which we will now present—do indeed show clearly defined thresholds. And yet, both their number (yes, *plural*) and precise locations raise further questions. Rise times of the emission, another critical indicator, remain unexamined in the present work. That, of course, lies ahead. For while the current study offers a conclusive chapter, it is also a **prelude**.

Thus, a conclusive assessment of the possibility that the 1139 nm beam induces avalanche phenomena in erbium-doped materials is, at this stage, not possible. What is possible, however, is a phenomenological assessment: *can we approach a regime of heightened nonlinearity?*

We begin with the observations themselves—for only through them can we trace a path toward understanding, and from there, begin to draw conclusions.

6.1.1 Emission as a function of power—*an opening inquiry*

Preliminary measurements were performed on three samples of $NaYF_4$-based nanoparticles co-doped with 20% Yb^{3+} and varying concentrations of Er^{3+} ions: 2%, 5%, and 10%. **Only the 1139 nm** excitation beam was employed—while perhaps obvious given the nature of the measurement, this is still worth explicitly stating. The 975 nm beam was not used.

Yet how can such an analysis even begin, given that earlier single-beam measurements[13] showed that the 1139 nm beam alone does not produce measurable emission?

The answer lies in excitation power *density*. To take on this challenge, the excitation intensity was significantly increased—specifically, the focusing lens was replaced with one of shorter focal length (from 50 mm to 35 mm; see Fig. 2.6), and the sample was not tilted (remaining nearly perpendicular to the incident beam) to ensure a much smaller focal spot. Let us pause here to state this clearly: **the measurements presented in this chapter are strictly preliminary in nature**. Accordingly, a full characterization of the resulting focal spot has not yet been performed,[14] and the results are therefore given simply as a function of the applied power—which, of course, is directly proportional to intensity.

With all these adjustments in place, one final comment is in order: emission intensities between measurements are not directly comparable, given the variability in local nanoparticle concentrations across the sample—and even more so between different samples. That said, we may now begin our analysis: *the emission intensity recorded at 657 nm as a function of 1139 nm excitation power*.

11: This is an important point. While analyzing mechanisms is, of course, essential—we should not reinvent the wheel—it must be emphasized that our work is rooted in, and derives its greatest value from, **experiment**. It is only afterward that we attempt to situate our findings within a mechanistic framework, and even then, with caution, *as this lies outside our core area of expertise.* Our goal and hope is that our results will prove valuable and informative to those approaching these topics from a theoretical standpoint.

12: The requirements for energy-looping and avalanche behavior are outlined at the beginning of this chapter and discussed in full detail in the theoretical introduction of this work (Section 1.1.3).

13: See Section 5.2.3.

14: That said, a rough estimation is warranted—to equip the reader with some intuition. In the previous setup, the *effective* area of the 1213 nm beam was approximately $2.64 \cdot 10^{-5}$ cm^2 (Section 2.2.1). Assuming a similar beam area for the 1139 nm beam under comparable conditions, the combination of a higher focusing power and the absence of sample tilt would reduce the focal spot to **roughly** $1.3 \cdot 10^{-5}$ cm^2. To put this into perspective, a power of 100 mW would correspond to an intensity of about 8 kW/cm^2. To further increase this value, the beam should be expanded just prior to the focusing lens in future experiments.

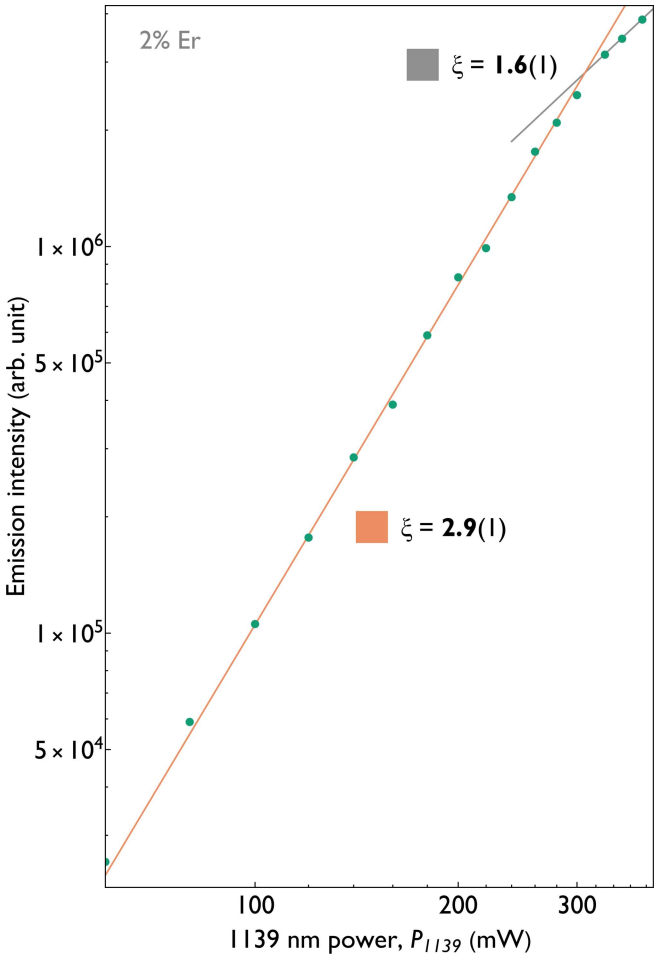

Figure 6.2: Emission intensity at 657 nm as a function of excitation power, using only the 1139 nm beam. Measurements were performed on nanoparticles co-doped with 20% Yb^{3+} and **2%** Er^{3+}. Fitted trends are included.

The case of the sample doped with 2% Er^{3+} begins our story modestly. As shown in Fig. 6.2, the full measurement range can be divided into two regions, with the majority of the data falling within a regime characterized by a nonlinearity of **2.9**(1), as defined by the exponent of a power-law fit without an offset term. This is already a notable value, and one that clearly exceeds the nonlinearity observed for the same sample under 975 nm excitation.[15]

As the power increases, however, we reach a point at which the nonlinearity undergoes a transition to a lower value (**1.6**(1)). While the boundary is somewhat arbitrary, it is worth noting that this change occurs around 300 mW of 1139 nm excitation power—a reference point useful for comparing subsequent results.

This higher nonlinearity of **2.9**(1)—though still within the range typically associated with upconversion processes—nevertheless stands out, especially in light of the lower values for 975 nm excitation. It offers a *cautious* indication that 1139 nm illumination may give rise to some form of energy feedback loop within the sample.

It is only natural, then, to shift our focus to the sample with a higher erbium concentration. Fig. 6.3 presents the results for the 5% Er^{3+}-doped sample. At first glance, the behavior appears distinct: the curve begins with a moderate nonlinearity of **3.1**(1), transitions to a regime characterized by a lower value (**1.6**(1)), and then shifts again into a region exhibiting an even higher nonlinearity of **4.5**(2). Before turning our

15: For 657 nm emission under 975 nm excitation, the response nonlinearity ranged from **2.01**(1) at low powers to **1.30**(5) at higher powers (see Section 5.2.1 and Fig. 5.8).

attention to this final regime, let us first compare the earlier portions of both curves. The nonlinearities characterizing the initial and later segments—**2.9**(1) and **1.6**(1) for the 2% sample, and **3.1**(1) and **1.6**(1) for the 5% sample—are remarkably consistent.

This permits us to cautiously propose—*though not assert*—that we may be observing analogous processes, with thresholds[16] that decrease as erbium concentration increases.

16: In the 2% sample, the described inflection was observed at 300 mW, whereas in the 5% sample it emerged as early as 170 mW.

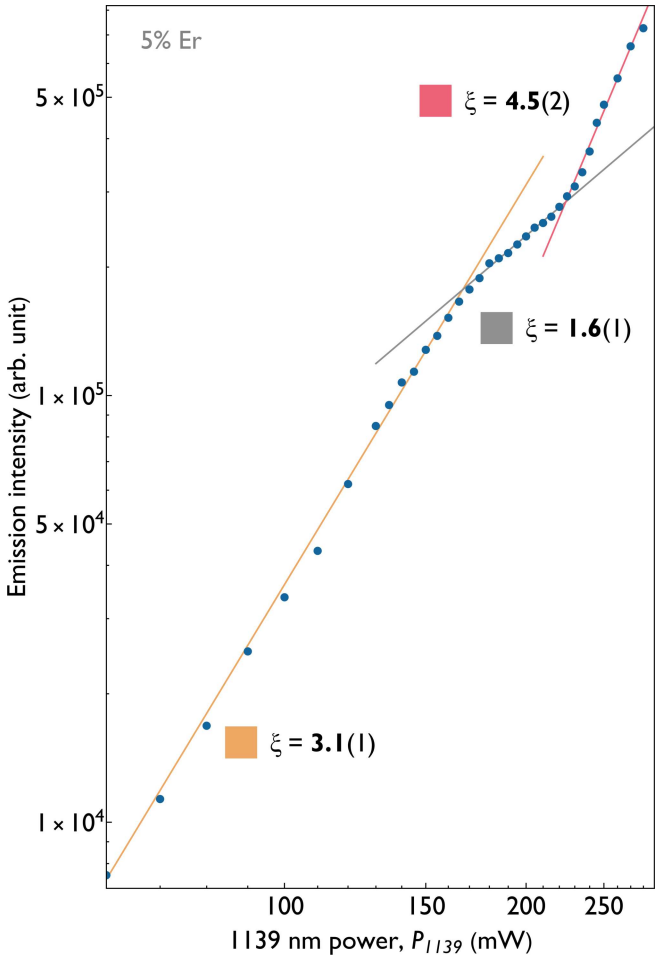

Figure 6.3: Emission intensity at 657 nm as a function of excitation power, using only the 1139 nm beam. Measurements were performed on nanoparticles co-doped with 20% Yb^{3+} and **5%** Er^{3+}. Fitted trends are included.

Yet perhaps most striking is the emergence of a third regime in the 5% sample—absent in the 2% sample, where the measurement range concluded within the region of reduced nonlinearity.

This final regime is characterized by a nonlinearity of **4.5**(2), which more boldly suggests the possibility of energy looping processes occurring under excitation solely by the ESA-resonant 1139 nm beam.

Without detailed modeling, we cannot speculate with confidence on the exact transitions responsible for the observed behavior—but we do see enough to say that something nontrivial is indeed unfolding.

Following these breadcrumbs, it is not unreasonable to expect that a further increase in erbium concentration might lead to a lowering of activation thresholds—and possibly to even higher nonlinearities—as greater doping should, within limits, enhance Er^{3+}-Er^{3+} cross-relaxation.

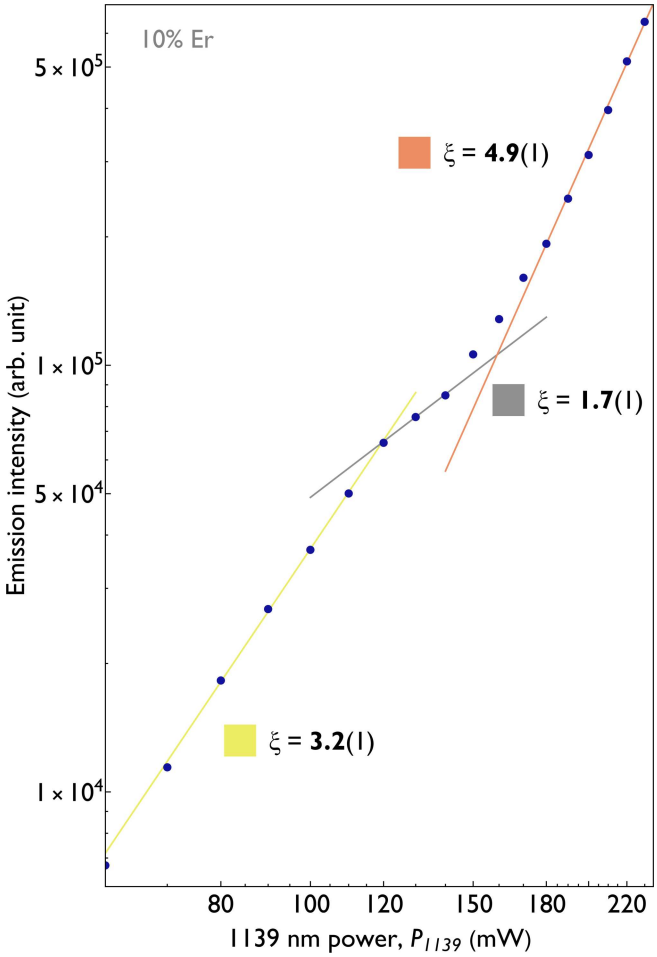

Figure 6.4: Emission intensity at 657 nm as a function of excitation power, using only the 1139 nm beam. Measurements were performed on nanoparticles co-doped with 20% Yb^{3+} and **10%** Er^{3+}. Fitted trends are included.

And indeed, upon increasing the erbium content to 10%, we observe a power-emission relationship closely resembling the previous case, yet with the inflection points clearly shifted toward lower[17] excitation powers (Fig. 6.4). The nonlinearities themselves show a modest further increase (reaching up to **4.9**(1)), although the transition into the higher-nonlinearity regime—the second inflection point—is less sharply defined. *And while our preliminary measurements end here, the investigation itself is only beginning.*

17: For the sample with 5% erbium content (Fig. 6.3), the inflection points occurred at approximately 170 mW and 220 mW. In the case of the 10% sample, they shifted to lower values—around 120 mW and 160 mW, respectively (Fig. 6.4).

6.1.2 Emission as a function of power—*the outlook*

Before we proceed to brief and admittedly speculative reflections, let us first *distill* from our findings the central hypothesis.

The results *suggest* that excitation with an **ESA-resonant 1139 nm** beam in Er^{3+} and Yb^{3+} co-doped nanoparticles gives rise to **energy-looping processes**—as indicated by the elevated nonlinearity in the relationship between excitation power and the emission intensity at 657 nm, originating from the $^4F_{9/2}$ state. Increasing the erbium concentration clearly lowers the activation threshold for the onset of these processes.

And yet, without an appropriate model, we are not in a position to speculate meaningfully on the precise mechanism behind the observed emission behavior. More data must be gathered—both by extending the accessible power-density range (which will require adjustments to the setup), and by expanding the menagerie of studied samples, in order to better understand how erbium concentration shapes the dynamics at play.

The role of ytterbium ions also remains an open question. Even in our preliminary discussion, we noted the existence of known Yb^{3+}-Er^{3+} interactions that could plausibly contribute to the observed effects—and it is almost certain that not all possible pathways have been accounted for. Thus, future investigations must include samples with varying ytterbium content, including those entirely devoid of it.

Our early consideration of ytterbium-related mechanisms has also inspired a separate experimental proposal. While our present analysis is far from exhaustive, several of the hypothesized processes involve population dynamics of the green-emitting states. This is especially true if the 1139 nm beam engages the system not only through transitions originating from the $^4I_{13/2}$ state, but also from $^2H_{11/2}$—which in turn can influence the population of the $^4F_{9/2}$ state through ytterbium-mediated interactions.

We therefore intend to explore the system's response when illuminated not only with 1139 nm light, but also with a distinctly shorter wavelength—just enough to gently perturb the population of green-emitting levels, and observe what changes this induces in the system's interaction with the 1139 nm beam.

On this front, we carry no expectations—we wish to leave the speaking entirely to the *experiment*. The same holds true for all subsequent studies involving the 1139 nm beam alone. Still, we can't help but hope: **there may indeed be something worth waiting for.**

6.2 Summa summarum

While much of the mechanistic discussion remains necessarily speculative, one core idea emerges from our initial reflections: the 1139 nm beam, resonant with excited-state absorption (ESA) but not ground-state absorption (GSA), may enable conditions conducive to energy-looping behavior in Er^{3+} and Yb^{3+} co-doped nanoparticles. The precise nature of this potential feedback remains unconfirmed—cross-relaxation routes, ESA-to-GSA ratios, and population pathways were considered, though the treatment remains necessarily limited. Nonetheless, we now turn from theoretical framing to the heart of our contribution: *experimental* observation.

Our measurements focused on emission at 657 nm as a function of excitation power from a single 1139 nm beam. Using samples co-doped with 20% Yb^{3+} and varying concentrations of Er^{3+} (2%, 5%, and 10%), we observed clear, concentration-dependent nonlinearities. In the 2% sample, the emission intensity followed a power-law behavior with a notable exponent of **2.9**(1) across most of the range, before transitioning sharply to a lower nonlinearity of **1.6**(1). This behavior already surpasses what is typically observed under 975 nm excitation for the same material and hints—however tentatively—at underlying feedback mechanisms potentially related to energy looping.

The 5% sample revealed a more complex profile: an initial region of moderate nonlinearity (**3.1**(1)), a similar dip to **1.6**(1), and a subsequent shift to a higher nonlinearity regime reaching **4.5**(2).

The emergence of this third regime—absent in the 2% sample—points more assertively to the onset of **energy looping processes** under ESA-only excitation.

In the 10% sample, these regimes persisted, with both inflection points shifting to lower powers, and the nonlinearity reaching up to **4.9**(1).

These results suggest that increasing Er^{3+} concentration lowers the activation threshold of this particular nonlinear behavior—possibly due to enhanced Er^{3+}-Er^{3+} cross-relaxation.

However, the role of Yb^{3+} ions remains unresolved. Known Yb-Er energy transfer pathways may contribute to the observed effects, and it is likely that not all interactions have been accounted for. Further studies involving variable Yb^{3+} content—including Yb-free samples—are essential to untangle this influence.

Finally, one proposal emerges from the green-emitting pathways implicated in some hypothesized mechanisms: introducing a second, shorter-wavelength excitation source may selectively perturb the green-state populations and reveal new insights into the system's nonlinear response to 1139 nm excitation. Whether this will confirm or contradict current intuition is not for us to predict. We leave that question to the experiment itself.

For now, we have outlined a phenomenon that clearly warrants further investigation. Though many questions remain, the potential significance offers strong motivation for continued exploration—after all, discovery begins where certainty ends.

This may be only the beginning.

6.2.1 Contributions

Ongoing support and scientific guidance — **Piotr Fita**

Synthesis of the nanoparticles used — **Katarzyna Prorok**

Concept, independent execution of the experiments, analysis, full description, and everything in between — **myself, Paulina Rajchel-Mieldzioć**

Summa summarum

Summa summarum

Two wavelengths, one purpose—**control.**

This control—of emission itself—is both the motivation and the axis of this work, realized through an exploration of co-excitation as a practical method for *reshaping* the upconversion pathways of lanthanide-doped materials across the near-infrared (NIR) excitation. Rather than focusing on a handful of known transitions, the study builds a tunable, wavelength-resolved approach that identifies where an auxiliary NIR beam is quiet on its own yet effective in tandem with the 975 nm excitation. The aim is straightforward: map cooperative windows, quantify how cooperation behaves with power, and translate that understanding into useful control of emission.

Yet the light had much more to say.

Achieving that required more than an idea—it required infrastructure. The studies presented here were conducted within the framework of a custom-built dual-wavelength excitation setup, where a 975 nm beam is combined **collinearly** with a tunable near-infrared beam (1050-1875 nm) generated via difference frequency generation (DFG). The DFG setup—designed, assembled, and integrated as a *vital* part of this work—delivers a well-defined beam with sufficient power at the sample plane, enabling precise scanning, identification, and exploration of cooperative excitation windows with the required spectral resolution.

With this system in place, we turned first to thulium-doped nanoparticles—a well-studied yet far from exhausted platform. While the 975 nm excitation pathway is well characterized, our interest lay in what unfolds when a second beam—one that on its own produces minimal to no measurable emission—is introduced alongside it. Can what seems *inert* light the way? The results—recorded at the 800 nm emission band—revealed something far more intriguing than just additive enhancement. Through systematic co-excitation using the tunable NIR beam alongside the 975 nm excitation, two distinct excitation bands emerged.

The excitation within these bands—centered at **1213** and **1732 nm**—produces negligible to no emission on its own. Yet when either one is paired with 975 nm excitation, a **surge** in upconversion emerges: the resulting signal **far surpasses** the mere *sum* of the individual effects of the two beams used separately.

To fully capture and appreciate the observed phenomenon, a measure of **surplus** was introduced—quantifying the excess emission generated by co-excitation beyond the sum of the two individual beams (975 nm and NIR) when applied separately.

Yet its magnitude defied all expectations.

For the two identified NIR excitation wavelengths—1732 nm and 1213 nm—surplus values reached **several hundred percent**, greatly surpassing a simple additive response.

This effect—strictly cooperative in nature—is strongly dependent on the power ratio between the two beams, and the shape of this dependency is far from trivial. Rather than avoiding complexity, the thesis embraces it as a source of insight. *Phenomenological* models were proposed not to replace mechanistic ones, but to bridge understanding—to provide structure where mechanisms remain elusive, and to offer predictive power where full theoretical clarity is not yet attainable.

Such a description was constructed for the surplus phenomenon, revealing a distilled dependency: a *constructive* and *sublinear* relationship with NIR power; a destructive influence from the 975 nm beam—yet still a *constructive* trend in total emission intensity under its excitation.

Yet the system's most compelling behavior emerged in the low-power regime—where neither beam, alone, is sufficient to produce measurable light. It is in this domain that cooperation takes on its most expressive form.

Careful tuning of both beams at low power results in emission increases of **several orders of magnitude**—and, in certain cases, ***de novo*** emission emerges: light where *neither* beam produces a signal individually, but where both together give rise to it.

From there, the research turned toward visualizing this concept in action. Using one of the key wavelengths—1732 nm—an optical setup was designed to make the invisible—*visible*.

By employing co-excitation, we demonstrated **real-time imaging** of a near-infrared beam, typically *inaccessible* to silicon detectors, via an upconverted signal revealed only through the interplay of both beams.

This result was more than aesthetic. It served as a tangible proof that co-excitation, when precisely tuned, can reveal wavelengths *far beyond* the reach of conventional detection.

Yet thulium-doped nanoparticles were not our only focus. After a series of experiments that not only met but surpassed expectations, our attention shifted—to erbium-based materials. And while we had some sense of what to expect, not everything could be predicted—thankfully so. For it is not in full clarity, but in the half-light, that real progress begins to take shape.

Using the same co-excitation framework, we carried out a parallel investigation—and two key spectral regions emerged. The first, centered at **1523 nm**, was partly anticipated, as this wavelength produces emission even in isolation. Still, the detailed characterization of this

cooperative window—examined across varying power combinations of both beams—offers a meaningful contribution to the field.

But it was the second region that shifted the narrative.

1139 nm. Alone, it yields nearly no signal—but when paired with 975 nm excitation, it selectively amplifies red emission, pointing to a cooperative mechanism based entirely on excited-state absorption.[18]

18: That is, the 1139 nm beam does not resonate with any ground-state absorption transitions in erbium ions—an absence that opens *certain possibilities*.

The intricate dance of these two wavelengths in co-excitation with the 975 nm beam—each marked by contrasting behavior—has been studied and rendered in detail. And given the *certain possibilities* arising from the distinct way in which the 1139 nm beam interacts with the erbium manifolds, one question insists on being asked: what can this beam do on its own?

Far more than expected.

Further investigation under 1139 nm excitation alone, pushed into the high-power regime, revealed complex, nonlinear emission patterns that shifted systematically with Er^{3+} concentration. At elevated doping levels, the system crossed sharp thresholds, transitioning into new regimes of optical behavior. Emission grew increasingly dynamic, as if internal feedback had taken root.

These findings, though still open to interpretation, point toward the emergence of energy feedback phenomena—possibly even energy looping. Yet the investigation is far from over.

This thesis set out to explore the boundaries of co-excitation potential—and ended up redefining them. What began as a study in control grew into something broader—not a mere confirmation of expectations, but an unveiling of the intricate interplay between light and matter, captured on these pages with all the fidelity words can offer.[19] In surpassing its initial goals, this work uncovered more than new excitation windows or measures of surplus; it uncovered a principle—that light, in union with light, becomes more than itself.

19: And—*let me, just once, step through the fourth wall and speak plainly*—with all I could give.

Here, the thesis ends. The work **does not**.

The last word here is the first of what follows.

Bibliography

Here are the references in citation order.

[1] P. Rajchel-Mieldzioć et al. 'Strong Emission Enhancement via Dual-Wavelength Coexcitation in YbTm-Doped Upconverting Nanoparticles for Near-Infrared and Subdiffraction Imaging'. In: *ACS Nano* 19.29 (2025), pp. 26932–26941. DOI: 10.1021/acsnano.5c08510 (cited on page i).

[2] F. Auzel. 'Upconversion and Anti-Stokes Processes with f and d Ions in Solids'. In: *Chem. Rev.* 104.1 (2004), pp. 139–174. DOI: 10.1021/cr020357g (cited on pages 3, 5, 6).

[3] M. Göppert-Mayer. 'Über Elementarakte mit zwei Quantensprüngen'. In: *Annalen der Physik* 401.3 (1931), pp. 273–294. DOI: 10.1002/andp.19314010303 (cited on page 4).

[4] W. Kaiser and C. G. B. Garrett. 'Two-Photon Excitation in CaF_2: Eu^{2+}'. In: *Phys. Rev. Lett.* 7.6 (1961), pp. 229–231. DOI: 10.1103/PhysRevLett.7.229 (cited on page 4).

[5] W. Denk, J. H. Strickler, and W. W. Webb. 'Two-Photon Laser Scanning Fluorescence Microscopy'. In: *Science* 248.4951 (1990), pp. 73–76. DOI: 10.1126/science.2321027 (cited on page 4).

[6] P. A. Franken et al. 'Generation of Optical Harmonics'. In: *Phys. Rev. Lett.* 7.4 (1961), pp. 118–119. DOI: 10.1103/PhysRevLett.7.118 (cited on page 4).

[7] J. A. Armstrong et al. 'Interactions between Light Waves in a Nonlinear Dielectric'. In: *Phys. Rev.* 127.6 (1962), pp. 1918–1939. DOI: 10.1103/PhysRev.127.1918 (cited on pages 4, 23).

[8] N. Bloembergen. 'Solid State Infrared Quantum Counters'. In: *Phys. Rev. Lett.* 2.3 (1959), pp. 84–85. DOI: 10.1103/PhysRevLett.2.84 (cited on page 4).

[9] L. G. Van Uitert and L. F. Johnson. 'Energy Transfer Between Rare-Earth Ions'. In: *J. Chem. Phys.* 44.9 (1966), pp. 3514–3522. DOI: 10.1063/1.1727258 (cited on page 5).

[10] F. Auzel. 'Compteur quantique par transfert d'énergie entre deux ions de terres rares dans un tungstate mixte et dans un verre'. In: *C. R. Acad. Sci. (Paris)* 262 (1966), pp. 1016–1019 (cited on page 5).

[11] F. Auzel. 'Compteur quantique par transfert d'énergie de Yb^{3+} à Tm^{3+} dans un tungstate mixte et dans un verre germanate'. In: *C. R. Acad. Sci. (Paris)* 263 (1966), pp. 819–821 (cited on page 5).

[12] F. Auzel. 'Materials and devices using double-pumped-phosphors with energy transfer'. In: *Proc. IEEE* 61.6 (1973), pp. 758–786. DOI: 10.1109/PROC.1973.9155 (cited on pages 5, 8).

[13] J. C. Wright. 'Up-conversion and excited state energy transfer in rare-earth doped materials'. In: *Radiationless Processes in Molecules and Condensed Phases*. Springer, 1976, pp. 239–295. DOI: 10.1007/BFb0111143 (cited on page 5).

[14] M. Szalkowski et al. 'Advances in the photon avalanche luminescence of inorganic lanthanide-doped nanomaterials'. In: *Chem. Soc. Rev.* 54.2 (2025), pp. 983–1026. DOI: 10.1039/D4CS00177J (cited on pages 5, 13, 14).

[15] S. Heer et al. 'Highly Efficient Multicolour Upconversion Emission in Transparent Colloids of Lanthanide-Doped NaYF4 Nanocrystals'. In: *Adv. Mater.* 16.23-24 (2004), pp. 2102–2105. DOI: 10.1002/adma.200400772 (cited on pages 5, 15).

[16] B. Szefczyk, R. Roszak, and S. Roszak. 'Structure of the Hexagonal $NaYF_4$ Phase from First-Principles Molecular Dynamics'. In: *RSC Adv.* 4.43 (2014), pp. 22526–22535. DOI: 10.1039/C4RA00211C (cited on page 5).

[17] G. Yi et al. 'Synthesis, Characterization, and Biological Application of Size-Controlled Nanocrystalline NaYF4:Yb,Er Infrared-to-Visible Up-Conversion Phosphors'. In: *Nano Letters* 4.11 (2004), pp. 2191–2196. DOI: 10.1021/nl048680h (cited on page 5).

[18] F. Wang and X. Liu. 'Recent advances in the chemistry of lanthanide-doped upconversion nanocrystals'. In: *Chem. Soc. Rev.* 38.4 (2009), pp. 976–989. DOI: 10.1039/B809132N (cited on pages 5, 8, 15, 16).

[19] G. Chen et al. 'Upconversion Nanoparticles: Design, Nanochemistry, and Applications in Theranostics'. In: *Chem. Rev.* 114.10 (2014), pp. 5161–5214. DOI: 10.1021/cr400425h (cited on pages 5, 11).

[20] A. Kaminskii. *Crystalline Lasers: Physical Processes and Operating Schemes*. 1st. CRC Press, 1996 (cited on pages 6, 7).

[21] G. H. Dieke. *Spectra and Energy Levels of Rare Earth Ions in Crystals*. Ed. by H. M. Crosswhite and H. Crosswhite. Interscience Publishers, 1968 (cited on page 6).

[22] W. T. Carnall et al. 'A systematic analysis of the spectra of the lanthanides doped into single crystal LaF_3'. In: *J. Chem. Phys.* 90.7 (1989), pp. 3443–3457. DOI: 10.1063/1.455853 (cited on page 6).

[23] M. Haase and H. Schäfer. 'Upconverting Nanoparticles'. In: *Angew. Chem. Int. Ed.* 50.26 (2011), pp. 5808–5829. DOI: 10.1002/anie.201005159 (cited on page 7).

[24] O. Laporte and W. F. Meggers. 'Some Rules of Spectral Structure'. In: *J. Opt. Soc. Am.* 11.5 (Nov. 1925), pp. 459–463. DOI: 10.1364/JOSA.11.000459 (cited on page 7).

[25] P. Atkins, J. de Paula, and J. Keeler. *Atkins' Physical Chemistry*. 12th ed. Oxford University Press, 2022 (cited on page 7).

[26] B. R. Judd. 'Optical Absorption Intensities of Rare-Earth Ions'. In: *Phys. Rev.* 127.3 (1962), pp. 750–761. DOI: 10.1103/PhysRev.127.750 (cited on page 7).

[27] G. S. Ofelt. 'Intensities of Crystal Spectra of Rare-Earth Ions'. In: *J. Chem. Phys.* 37.3 (1962), pp. 511–520. DOI: 10.1063/1.1701366 (cited on page 7).

[28] S. V. Eliseeva and J.-C. G. Bünzli. 'Lanthanide luminescence for functional materials and bio-sciences'. In: *Chem. Soc. Rev.* 39.1 (2010), pp. 189–227. DOI: 10.1039/B905604C (cited on page 7).

[29] H. Dong, L.-D. Sun, and C.-H. Yan. 'Energy transfer in lanthanide upconversion studies for extended optical applications'. In: *Chem. Soc. Rev.* 44.6 (2015), pp. 1608–1634. DOI: 10.1039/C4CS00188E (cited on page 7).

[30] N. J. J. Johnson et al. 'Direct Evidence for Coupled Surface and Concentration Quenching Dynamics in Lanthanide-Doped Nanocrystals'. In: *J. Am. Chem. Soc.* 139.8 (2017), pp. 3275–3282. DOI: 10.1021/jacs.7b00223 (cited on pages 8, 9).

[31] S. Wen et al. 'Advances in Highly Doped Upconversion Nanoparticles'. In: *Nat. Commun.* 9.1 (2018), p. 2415. DOI: 10.1038/s41467-018-04813-5 (cited on pages 8, 9).

[32] F. Wang, J. Wang, and X. Liu. 'Direct Evidence of a Surface Quenching Effect on Size-Dependent Luminescence of Upconversion Nanoparticles'. In: *Angew. Chem. Int. Ed.* 49.41 (2010), pp. 7456–7460. DOI: 10.1002/anie.201003959 (cited on page 9).

[33] X. Li et al. 'Engineering Homogeneous Doping in Single Nanoparticle To Enhance Upconversion Efficiency'. In: *Nano Lett.* 14.6 (2014), pp. 3634–3639. DOI: 10.1021/nl501366x (cited on page 9).

[34] J. Wang et al. 'Enhancing multiphoton upconversion through energy clustering at sublattice level'. In: *Nat. Mater.* 13.2 (2014), pp. 157–162. DOI: 10.1038/nmat3804 (cited on page 9).

[35] J. Zhao et al. 'Single-nanocrystal sensitivity achieved by enhanced upconversion luminescence'. In: *Nat. Nanotechnol.* 8.10 (2013), pp. 729–734. DOI: 10.1038/nnano.2013.171 (cited on page 9).

[36] D. J. Gargas et al. 'Engineering bright sub-10-nm upconverting nanocrystals for single-molecule imaging'. In: *Nat. Nanotechnol.* 9.4 (2014), pp. 300–305. DOI: 10.1038/nnano.2014.29 (cited on page 9).

[37] S. Wu et al. 'Non-blinking and photostable upconverted luminescence from single lanthanide-doped nanocrystals'. In: *Proc. Natl. Acad. Sci. U.S.A.* 106.27 (2009), pp. 10917–10921. DOI: 10.1073/pnas.0904792106 (cited on page 9).

[38] F. Wang et al. 'Tuning upconversion through energy migration in core–shell nanoparticles'. In: *Nat. Mater.* 10.12 (2011), pp. 968–973. DOI: 10.1038/nmat3149 (cited on page 9).

[39] J. Zuo et al. 'Employing shells to eliminate concentration quenching in photonic upconversion nanostructure'. In: *Nanoscale* 9.23 (2017), pp. 7941–7946. DOI: 10.1039/C7NR01403A (cited on pages 9, 17).

[40] Y. Lu et al. 'Tunable lifetime multiplexing using luminescent nanocrystals'. In: *Nat. Photon.* 8.1 (2014), pp. 32–36. DOI: 10.1038/nphoton.2013.322 (cited on page 9).

[41] S. Wilhelm. 'Perspectives for Upconverting Nanoparticles'. In: *ACS Nano* 11.11 (2017), pp. 10644–10653. DOI: 10.1021/acsnano.7b07120 (cited on page 9).

[42] S. Liu et al. 'Controlling upconversion in emerging multilayer core–shell nanostructures: from fundamentals to frontier applications'. In: *Chem. Soc. Rev.* 51.5 (2022), pp. 1729–1765. DOI: 10.1039/D1CS00753J (cited on page 9).

[43] H. Wen et al. 'Upconverting Near-Infrared Light through Energy Management in Core–Shell–Shell Nanoparticles'. In: *Angew. Chem. Int. Ed.* 52.50 (2013), pp. 13419–13423. DOI: 10.1002/anie.201306811 (cited on page 9).

[44] Y.-F. Wang et al. 'Nd^{3+}-Sensitized Upconversion Nanophosphors: Efficient In Vivo Bioimaging Probes with Minimized Heating Effect'. In: *ACS Nano* 7.8 (2013), pp. 7200–7206. DOI: 10.1021/nn402601d (cited on page 10).

[45] X. Xie et al. 'Mechanistic Investigation of Photon Upconversion in Nd^{3+}-Sensitized Core–Shell Nanoparticles'. In: *J. Am. Chem. Soc.* 135.34 (2013), pp. 12608–12611. DOI: 10.1021/ja4075002 (cited on page 10).

[46] J. Lai et al. 'An Upconversion Nanoparticle with Orthogonal Emissions Using Dual NIR Excitations for Controlled Two-Way Photoswitching'. In: *Angew. Chem. Int. Ed.* 53.52 (2014), pp. 14419–14423. DOI: 10.1002/anie.201408219 (cited on page 10).

[47] B. Yan et al. 'Near Infrared Light Triggered Release of Biomacromolecules from Hydrogels Loaded with Upconversion Nanoparticles'. In: *J. Am. Chem. Soc.* 134.40 (2012), pp. 16558–16561. DOI: 10.1021/ja308876j (cited on page 10).

[48] L. Zhao et al. 'Near-Infrared Photoregulated Drug Release in Living Tumor Tissue via Yolk-Shell Upconversion Nanocages'. In: *Adv. Funct. Mater.* 24.3 (2014), pp. 363–371. DOI: 10.1002/adfm.201302133 (cited on page 10).

[49] H. Wang et al. 'Design and Synthesis of Core–Shell–Shell Upconversion Nanoparticles for NIR-Induced Drug Release, Photodynamic Therapy, and Cell Imaging'. In: *ACS Applied Materials & Interfaces* 8.7 (2016), pp. 4416–4423. DOI: 10.1021/acsami.5b11197 (cited on page 10).

[50] S. Cui et al. 'In Vivo Targeted Deep-Tissue Photodynamic Therapy Based on Near-Infrared Light Triggered Upconversion Nanoconstruct'. In: *ACS Nano* 7.1 (2013), pp. 676–688. DOI: 10.1021/nn304872n (cited on page 10).

[51] N. M. Idris et al. 'In vivo photodynamic therapy using upconversion nanoparticles as remote-controlled nanotransducers'. In: *Nature Medicine* 18.10 (2012), pp. 1580–1585. DOI: 10.1038/nm.2933 (cited on page 10).

[52] C. Wang et al. 'Near-infrared light induced in vivo photodynamic therapy of cancer based on upconversion nanoparticles'. In: *Biomaterials* 32.26 (2011), pp. 6145–6154. DOI: 10.1016/j.biomaterials.2011.05.007 (cited on page 10).

[53] X. Wu et al. 'Dye-Sensitized Core/Active Shell Upconversion Nanoparticles for Optogenetics and Bioimaging Applications'. In: *ACS Nano* 10.1 (2016), pp. 1060–1066. DOI: 10.1021/acsnano.5b06383 (cited on page 10).

[54] S. Chen et al. 'Near-infrared deep brain stimulation via upconversion nanoparticle–mediated optogenetics'. In: *Science* 359.6376 (2018), pp. 679–684. DOI: 10.1126/science.aaq1144 (cited on pages 10, 11).

[55] A. Bansal et al. 'Quasi-Continuous Wave Near-Infrared Excitation of Upconversion Nanoparticles for Optogenetic Manipulation of C. elegans'. In: *Small* 12.13 (2016), pp. 1732–1743. DOI: 10.1002/smll.201503792 (cited on page 10).

[56] F. Vetrone et al. 'Temperature Sensing Using Fluorescent Nanothermometers'. In: *ACS Nano* 4.6 (2010), pp. 3254–3258. DOI: 10.1021/nn100244a (cited on page 10).

[57] D. Jaque and F. Vetrone. 'Luminescence nanothermometry'. In: *Nanoscale* 4.15 (2012), pp. 4301–4326. DOI: 10.1039/C2NR30764B (cited on page 10).

[58] M. You et al. 'Inkjet Printing of Upconversion Nanoparticles for Anti-Counterfeit Applications'. In: *Nanoscale* 7.10 (2015), pp. 4423–4431. DOI: 10.1039/C4NR06944G (cited on page 10).

[59] M. You et al. 'Three-Dimensional Quick Response Code Based on Inkjet Printing of Upconversion Fluorescent Nanoparticles for Drug Anti-Counterfeiting'. In: *Nanoscale* 8.19 (2016), pp. 10096–10104. DOI: 10.1039/C6NR01353H (cited on page 10).

[60] W. Zou et al. 'Broadband Dye-Sensitized Upconversion of Near-Infrared Light'. In: *Nat. Photonics* 6.8 (2012), pp. 560–564. DOI: 10.1038/nphoton.2012.158 (cited on page 10).

[61] Y. Tang et al. 'NIR-Responsive Photocatalytic Activity and Mechanism of NaYF4:Yb,Tm@TiO2 Core–Shell Nanoparticles'. In: *ACS Catal.* 3.3 (2013), pp. 405–412. DOI: 10.1021/cs300808r (cited on page 10).

[62] J. Wang and P. A. Tanner. 'Upconversion for White Light Generation by a Single Compound'. In: *J. Am. Chem. Soc.* 132.3 (2010), pp. 947–949. DOI: 10.1021/ja909254u (cited on page 10).

[63] K. R. Mun et al. 'Elemental-Migration-Assisted Full-Color-Tunable Upconversion Nanoparticles for Video-Rate Three-Dimensional Volumetric Displays'. In: *Nano Lett.* 23.7 (2023). PMID: 36939681, pp. 3014–3022. DOI: 10.1021/acs.nanolett.3c00397 (cited on page 10).

[64] X. Liu et al. 'Binary Temporal Upconversion Codes of Mn^{2+}-Activated Nanoparticles for Multilevel Anti-Counterfeiting'. In: *Nat. Commun.* 8 (2017), p. 899. DOI: 10.1038/s41467-017-00916-7 (cited on page 10).

[65] A. Bednarkiewicz et al. 'All-Optical Data Processing with Photon-Avalanching Nanocrystalline Photonic Synapse'. In: *Adv. Mater.* 35.42 (2023), p. 2304390. DOI: 10.1002/adma.202304390 (cited on page 11).

[66] Y. Wu et al. 'Dynamic upconversion multicolour editing enabled by molecule-assisted opto-electrochemical modulation'. In: *Nat. Commun.* 12.1 (2021), pp. 2022–2022. DOI: 10.1038/s41467-021-22387-7 (cited on page 11).

[67] A. Skripka et al. 'Intrinsic optical bistability of photon avalanching nanocrystals'. In: *Nat. Photonics* 19.2 (2025), pp. 212–218. DOI: 10.1038/s41566-024-01577-x (cited on pages 11, 14).

[68] Z. Zhang et al. 'Upconversion superballs for programmable photoactivation of therapeutics'. In: *Nat. Commun.* 10.1 (2019), p. 4586. DOI: 10.1038/s41467-019-12506-w (cited on page 11).

[69] S. He et al. 'Ultralow-intensity near-infrared light induces drug delivery by upconverting nanoparticles'. In: *Chem. Commun.* 51.2 (2015), pp. 431–434. DOI: 10.1039/C4CC07489K (cited on page 11).

[70] J. Sheng et al. 'Highly Efficient Near-Infrared Light-Driven Molecular Motor Rotation Enabled by Upconversion Nanoparticles as Nanoscale Light Sources'. In: *J. Am. Chem. Soc.* 147.30 (2025), pp. 26797–26803. DOI: 10.1021/jacs.5c07953 (cited on page 11).

[71] A. Bednarkiewicz et al. 'Photon avalanche in lanthanide doped nanoparticles for biomedical applications: super-resolution imaging'. In: *Nanoscale Horiz.* 4.4 (2019), pp. 881–889. DOI: 10.1039/C9NH00089E (cited on pages 11, 14).

[72] M. Pollnau et al. 'Power dependence of upconversion luminescence in lanthanide and transition-metal-ion systems'. In: *Phys. Rev. B* 61.5 (2000), pp. 3337–3346. DOI: 10.1103/PhysRevB.61.3337 (cited on pages 11, 12).

[73] J. Wang et al. 'Single-Band Upconversion Emission in Lanthanide-Doped $KMnF_3$ Nanocrystals'. In: *Angew. Chem. Int. Ed.* 50.44 (2011), pp. 10369–10372. DOI: 10.1002/anie.201104192 (cited on page 12).

[74] W. Wei et al. 'Cross Relaxation Induced Pure Red Upconversion in Activator- and Sensitizer-Rich Lanthanide Nanoparticles'. In: *Chem. Mater.* 26.18 (2014), pp. 5183–5186. DOI: 10.1021/cm5022382 (cited on page 12).

[75] R. Deng et al. 'Temporal full-colour tuning through non-steady-state upconversion'. In: *Nat. Nanotechnol.* 10.3 (2015), pp. 237–242. DOI: 10.1038/nnano.2014.317 (cited on page 12).

[76] E. S. Levy et al. 'Energy-Looping Nanoparticles: Harnessing Excited-State Absorption for Deep-Tissue Imaging'. In: *ACS Nano* 10.9 (2016), pp. 8423–8433. DOI: 10.1021/acsnano.6b03288 (cited on page 13).

[77] J. S. Chivian, W. E. Case, and D. D. Eden. 'The photon avalanche: A new phenomenon in Pr^{3+}-based infrared quantum counters'. In: *Appl. Phys. Lett.* 35.2 (1979), pp. 124–125. DOI: 10.1063/1.91044 (cited on page 13).

[78] A. W. Kueny, W. E. Case, and M. E. Koch. 'Nonlinear-optical absorption through photon avalanche'. In: *J. Opt. Soc. Am. B* 6.4 (1989), pp. 639–642. DOI: 10.1364/JOSAB.6.000639 (cited on page 13).

[79] W. E. Case, M. E. Koch, and A. W. Kueny. 'The photon avalanche in rare-earth crystals'. In: *J. Lumin.* 45.1 (1990), pp. 351–353. DOI: 10.1016/0022-2313(90)90191-D (cited on page 13).

[80] M.-F. Joubert. 'Photon avalanche upconversion in rare earth laser materials'. In: *Opt. Mater.* 11.2 (1999), pp. 181–203. DOI: 10.1016/S0925-3467(98)00043-3 (cited on page 13).

[81] C. Lee et al. 'Giant nonlinear optical responses from photon-avalanching nanoparticles'. In: *Nature* 589.7841 (2021), pp. 230–235. DOI: 10.1038/s41586-020-03092-9 (cited on pages 13–15).

[82] M.-F. Joubert et al. 'The photon-avalanche effect: review, model and application'. In: *Opt. Mater.* 4.1 (1994), pp. 43–49. DOI: 10.1016/0925-3467(94)90054-X (cited on page 13).

[83] A. Skripka and E. M. Chan. 'Unraveling the Myths and Mysteries of Photon Avalanching Nanoparticles'. In: *Mater. Horiz.* 12.11 (2025), pp. 3575–3597. DOI: 10.1039/D4MH01798F (cited on pages 13, 14).

[84] A. Skripka et al. 'A Generalized Approach to Photon Avalanche Upconversion in Luminescent Nanocrystals'. In: *Nano Lett.* 23.15 (2023), pp. 7100–7106. DOI: 10.1021/acs.nanolett.3c01955 (cited on page 14).

[85] J. Chen et al. 'Optical nonlinearities in excess of 500 through sublattice reconstruction'. In: *Nature* 643.8072 (2025), pp. 669–674. DOI: 10.1038/s41586-025-09164-y (cited on page 14).

[86] C. Wang et al. 'Tandem Photon Avalanches for Various Nanoscale Emitters with Optical Nonlinearity up to 41st-Order through Interfacial Energy Transfer'. In: *Adv. Mater.* 36.2 (2024), p. 2307848. DOI: 10.1002/adma.202307848 (cited on page 14).

[87] Y. Liang et al. 'Migrating photon avalanche in different emitters at the nanoscale enables 46th-order optical nonlinearity'. In: *Nat. Nanotechnol.* 17.5 (2022), pp. 524–530. DOI: 10.1038/s41565-022-01101-8 (cited on page 14).

[88] C. Wang et al. 'Giant Optical Nonlinear Response up to 60th-Order Induced by the Ytterbium Energy Relay Mediated Photon Avalanches'. In: *Laser Photonics Rev.* 18.10 (2024), p. 2400290. DOI: 10.1002/lpor.202400290 (cited on page 14).

[89] E. M. Chan. 'Combinatorial approaches for developing upconverting nanomaterials: high-throughput screening, modeling, and applications'. In: *Chem. Soc. Rev.* 44.6 (2015), pp. 1653–1679. DOI: 10.1039/C4CS00205A (cited on page 16).

[90] R. B. Anderson et al. 'Revisiting the NIR-to-Visible Upconversion Mechanism in β-$NaYF_4$:Yb^{3+},Er^{3+}'. In: *J. Phys. Chem. Lett.* 5.1 (2014), pp. 36–42. DOI: 10.1021/jz402366r (cited on pages 16, 17, 105, 109, 110, 130).

[91] M. T. Berry and P. S. May. 'Disputed Mechanism for NIR-to-Red Upconversion Luminescence in $NaYF_4$:Yb^{3+},Er^{3+}'. In: *J. Phys. Chem. A* 119.38 (2015), pp. 9805–9811. DOI: 10.1021/acs.jpca.5b08324 (cited on pages 17, 110).

[92] K. Zheng et al. 'Ultraviolet upconversion fluorescence of Er3̂+ induced by 1560 nm laser excitation'. In: *Opt. Lett.* 35.14 (July 2010), pp. 2442–2444. DOI: 10.1364/OL.35.002442 (cited on page 17).

[93] S. W. Hell and J. Wichmann. 'Breaking the diffraction resolution limit by stimulated emission: stimulated-emission-depletion fluorescence microscopy'. In: *Opt. Lett.* 19.11 (1994), pp. 780–782. DOI: 10.1364/OL.19.000780 (cited on page 18).

[94] T. A. Klar and S. W. Hell. 'Subdiffraction resolution in far-field fluorescence microscopy'. In: *Opt. Lett.* 24.14 (1999), pp. 954–956. DOI: 10.1364/OL.24.000954 (cited on page 18).

[95] T. A. Klar et al. 'Fluorescence microscopy with diffraction resolution barrier broken by stimulated emission'. In: *Proc. Natl. Acad. Sci. USA* 97.15 (2000), pp. 8206–8210. DOI: 10.1073/pnas.97.15.8206 (cited on page 18).

[96] S. W. Hell. 'Far-Field Optical Nanoscopy'. In: *Science* 316.5828 (2007), pp. 1153–1158. DOI: 10.1126/science.1137395 (cited on page 18).

[97] Y. Liu et al. 'Amplified stimulated emission in upconversion nanoparticles for super-resolution nanoscopy'. In: *Nature* 543.7644 (2017), pp. 229–233. DOI: 10.1038/nature21366 (cited on page 18).

[98] Q. Zhan et al. 'Achieving high-efficiency emission depletion nanoscopy by employing cross relaxation in upconversion nanoparticles'. In: *Nat. Commun.* 8.1 (2017), p. 1058. DOI: 10.1038/s41467-017-01141-y (cited on page 19).

[99] Y. Liu et al. 'Population Control of Upconversion Energy Transfer for Stimulation Emission Depletion Nanoscopy'. In: *Adv. Sci.* 10.20 (2023), p. 2205990. DOI: 10.1002/advs.202205990 (cited on page 19).

[100] R. Pu et al. 'Super-resolution microscopy enabled by high-efficiency surface-migration emission depletion'. In: *Nat. Commun.* 13.1 (2022), p. 6636. DOI: 10.1038/s41467-022-33726-7 (cited on page 19).

[101] M. Plöschner et al. 'Simultaneous super-linear excitation-emission and emission depletion allows imaging of upconversion nanoparticles with higher sub-diffraction resolution'. In: *Opt. Express* 28.16 (2020), pp. 24308–24326. DOI: 10.1364/OE.400651 (cited on page 19).

[102] S. Lamon et al. 'Lanthanide ion-doped upconversion nanoparticles for low-energy super-resolution applications'. In: *Light Sci. Appl.* 13.1 (2024), p. 252. DOI: 10.1038/s41377-024-01547-6 (cited on page 19).

[103] R. Wu et al. 'Optical depletion mechanism of upconverting luminescence and its potential for multi-photon STED-like microscopy'. In: *Opt. Express* 23.25 (2015), pp. 32401–32412. DOI: 10.1364/OE.23.032401 (cited on pages 19, 101, 105).

[104] X. Chen et al. 'Chromatic tuning of upconversion emission upon dual infrared wavelength co-excitation in Er^{3+} doped $Ba_3Lu_4O_9$ phosphor'. In: *Opt. Mater.* 157 (2024), p. 116266. DOI: 10.1016/j.optmat.2024.116266 (cited on page 19).

[105] H. Wanga et al. 'Luminescence property tuning of Yb^{3+}-Er^{3+} doped oxysulfide using multiple-band co-excitation'. In: *RSC Adv.* 8.30 (2018), pp. 16557–16565. DOI: 10.1039/C8RA02503G (cited on page 19).

[106] Z. Li et al. 'Structure design and modulation of dual-wavelength sensitive upconversion luminescence in RE_2MoO_6:Er^{3+}/Yb^{3+} materials'. In: *J. Mater. Sci.* 54.18 (2019), pp. 11913–11924. DOI: 10.1007/s10853-019-03697-0 (cited on page 19).

[107] P. Chen et al. 'Enhanced upconversion luminescence in $NaYF_4$:Er nanoparticles with multi-wavelength excitation'. In: *Mater. Lett.* 128 (2014), pp. 299–302. DOI: 10.1016/j.matlet.2014.04.179 (cited on page 19).

[108] O. Flasseur et al. 'Self-calibration for lensless color microscopy'. In: *Appl. Opt.* 56.13 (May 2017), F189–F199. DOI: 10.1364/AO.56.00F189 (cited on page 87).

[109] H. Lu, W. P. Gillin, and I. Hernández. 'Concentration dependence of the up- and down-conversion emission colours of Er^{3+}-doped Y_2O_3: a time-resolved spectroscopy analysis'. In: *Phys. Chem. Chem. Phys.* 16.38 (2014), pp. 20957–20963. DOI: 10.1039/C4CP02028F (cited on page 130).

[110] M. Pollnau and S. D. Jackson. 'Erbium 3 μm fiber lasers'. In: *IEEE J. Sel. Top. Quantum Electron.* 7.1 (2001), pp. 30–40. DOI: 10.1109/2944.924006 (cited on page 130).

[111] L. Gomes et al. 'Energy transfer rates and population inversion of $^4I_{11/2}$ excited state of Er^{3+} investigated by means of numerical solutions of the rate equations system in Er:$LiYF_4$ crystal'. In: *J. Appl. Phys.* 106.10 (2009), p. 103508. DOI: 10.1063/1.3259388 (cited on page 130).

[112] E. Madirov et al. 'Absolute quantum yield for understanding upconversion and downshift luminescence in PbF_2:Er^{3+},Yb^{3+} crystals'. In: *Phys. Chem. Chem. Phys.* 25.17 (2023), pp. 11986–11997. DOI: 10.1039/D3CP00936J (cited on page 130).

[113] F. Mselmi et al. 'Cross-relaxation induced efficient 1.55 μm emission in $La_{1.95}Er_{0.05}Ti_2O_7$ towards an application as an amplifier for silica-fibers'. In: *Opt. Mater.* 137 (2023), p. 113555. DOI: 10.1016/j.optmat.2023.113555 (cited on page 130).

[114] L. Liu et al. 'Upconversion mechanisms and thermal effects of Er^{3+} in Er^{3+} doped yttria nanocrystals'. In: *J. Lumin.* 132.6 (2012), pp. 1483–1488. DOI: 10.1016/j.jlumin.2012.01.052 (cited on page 130).

[115] J. Zhang et al. 'Observation of efficient population of the red-emitting state from the green state by non-multiphonon relaxation in the Er^{3+}-Yb^{3+} system'. In: *Light Sci. Appl.* 4.1 (2015). DOI: 10.1038/lsa.2015.12 (cited on page 130).